Near-Infrared Light Activatable Nanomiceller Chemo-Photodynamic Combination Therapy for Oropharyngeal Carcinoma

THESIS

Submitted in partial fulfillment

of the requirements for the degree of

DOCTOR OF PHILOSOPHY

By

MILAN PAUL

ID. No. 2019PHXF0453H

Under the Supervision of

Prof. Swati Biswas

BIRLA INSTITUTE OF TECHNOLOGY AND SCIENCE, PILANI

2024

BIRLA INSTITUTE OF TECHNOLOGY AND SCIENCE, PILANI

CERTIFICATE

This is to certify that the thesis titled **"Near-Infrared Light Activatable Nanomiceller Chemo-Photodynamic Combination Therapy for Oropharyngeal Carcinoma"** submitted by **MILAN PAUL** ID No **2019PHXF0453H**, for an award of a Ph.D. from the Institute, embodies original work done by him under my supervision.

Signature of the Supervisor:

Name in capital letters: SWATI BISWAS

Designation: Professor

Date: 16/04/2024

DECLARATION

I declare that this thesis has been composed solely by myself and that it has not been submitted, in whole or in part, in any previous application for a degree. The content of the thesis is original and is the outcome of my research work. Any relevant material taken from the open literature has been referred to and cited, as per established ethical norms and practices.

MILAN PAUL

Acknowledgment

The present piece of work would not have been possible without the assistance of several people for whom I am eternally grateful.

First and foremost, praises and thanks to the Almighty, for showering blessings throughout my research work which enabled me to successfully complete the research. I would like to express my deepest and sincere gratitude and respect to my supervisor Prof. Swati Biswas, Professor, Department of Pharmacy, Birla Institute of Technology & Science (BITS), Pilani, Hyderabad Campus, Jawahar Nagar, Kapra Mandal, Hyderabad - 500078, Telangana, India, for her constant and invaluable support, since I ever started working with her. It is a great privilege to work with her. She has introduced me to the fascinating field of "Nanomedicine". I am immensely grateful to her for channeling my thought process in science in the right direction and making me realize the true meaning of the words "Strive for Excellence". Her dynamism, vision, sincerity, and motivation have deeply inspired me. Respected Ma'am, I am privileged to complete my Ph.D. under your guidance. Your endless optimism, enthusiasm, and infectious energy toward breakthrough research will always be a source of inspiration for me.

I consider myself incredibly lucky to have had the chance to collaborate with another esteemed guide, Professor Balaram Ghosh, during my pursuit of a Ph.D. Respected Sir, our journey together has been delightful as you generously shared your extensive expertise and technical knowledge, which proved invaluable at various junctures. Your positivity and constant support in resolving significant and minor challenges have been incredibly motivating. Your ability to foster a friendly and supportive atmosphere in the laboratory made my time at BITS-Pilani truly memorable. Your

I would like to thank the central analytical laboratory of BITS-Pilani, Hyderabad Campus for providing me with a scientific platform to excel in my career.

I am fortunate to have met lovely colleagues and lab mates in BITS, where I got to work with them on various occasions. I am grateful to Dr. Soniya, Mr. Sanjay, Mr. Asif, Mrs. Sri Ganga, Mr. Nageswara Rao, Mr. Ganesh, Mrs. Sravani, Mr. Tarun, and Ms. Himaja. Thanks, all of you, for your remembrance and for being a source of happiness.

I express my sincere thanks to seniors Dr. Preeti Kumari, Dr. Vishnu Kiran, Dr. Himanshu Bhatt and Dr. Yamini Bobde, who were very supportive, their attention and timely concern I am thankful to Mrs. Sarita, Mrs. Rekha, Mrs. Sunita, Mr. Rajesh, Mr. Upalaiah, Mr. Mallesh, Mr. Kumar, Mr. Narsimha, and Mr. Tirumalaiah for their kind co-operation during the lab in the entire tenure of my Ph.D.

I am indebted to ICMR, and BITS-Pilani, Hyderabad Campus for providing me with a scholarship and necessary financial support to pursue my Ph.D. work without any hindrance. I would like to thank everybody who was necessary for the successful completion of this research work that I may have inadvertently failed to mention.

Finally, I take this opportunity to acknowledge my family, that has been my pillar of strength in the truest sense. It will never be enough to say thanks to my parents Late Nirod Paul and Mrs. Aunna Paul, for their unconditional love, support, and sacrifices.

Milan Paul

ABSTRACT

Nanocarriers possess distinct qualities that can augment their selective accumulation in tumor tissues, leveraging their nanoscale size, high surface-area-to-volume ratio, favorable drug release kinetics, and targeting capabilities. While most nanosystems for solid tumor treatment are delivered systemically and amass in tumor tissues through the enhanced permeability and retention (EPR) effect—commonly attributed to leaky tumor vasculature and inadequate lymphatic drainage—this interpretation oversimplifies the process. Various biological factors, including interactions with plasma proteins, blood circulation duration, extravasation, tumor tissue penetration, and uptake by cancer cells, influence the biodistribution of systemically administered nanosystems. Moreover, modifying nanosystems by conjugating them with drugs and polymers capable of bestowing specific targeting properties also significantly impacts their overall distribution.

First, Photodynamic therapy (PDT) is a promising method for treating oral cancer, utilizing photosensitizers, light, and molecular oxygen. However, the effectiveness of PDT can be hindered by the hydrophobic properties of certain photosensitizers. In this study, chlorin e6 (Ce6), a hydrophobic photosensitizer, was modified to become hydrophilic and loaded into pluronic F127 to enhance its solubility and improve tumor-specific targeting efficiency. The resulting Ce6@F127 Ms demonstrated significantly increased singlet oxygen generation (SOG) efficiency and fluorescence activity in aqueous media compared to free Ce6. Moreover, confocal imaging and fluorescence-activated cell sorting (FACS) analysis confirmed the enhanced internalization rate of Ce6@F127 Ms in murine melanoma cell lines (B16F10) and human oral carcinoma cell lines

(FaDu). Upon light irradiation, the cellular phototoxicity of Ce6@F127 Ms against B16F10 and FaDu was approximately three times higher than that of free Ce6 in vitro.

 In vivo therapeutic investigations conducted on a murine model of skin cancer demonstrated the ability of Ce6@F127 Ms, when combined with laser treatment, to effectively penetrate solid tumors. This resulted in a reduction in tumor volume, immunohistochemistry. Subsequent analysis of serum and blood components affirmed the safety and efficacy of Ce6@F127 Ms in mice. Consequently, the developed Ce6@F127 Ms exhibits significant potential for the concurrent treatment of solid tumors and prevention of metastasis.

Secondly, a nanomedicine with the ability to produce combination chemo- and photodynamic therapeutic effects in cancer was developed employing poly (D, L- lactic-co- glycolic acid) (PLGA) nanoparticles (NPs) using human serum albumin (HSA) as the surface modifier via emulsification technique to co-deliver both, a photosensitizer, chlorin e6 (Ce6) and the paclitaxel (PTX). The Ce6/PTX-H/P NPs were characterized for size, morphology, drug loading, entrapment efficiencies, drug release, hemolytic tendency, and kinetic/storage stabilities by using DLS, SEM, UV, IR, XRD, XPS, and DSC analysis. CD spectroscopy and SDS-PAGE was utilized to asses protein integrity. DMA, RNO, and SOSG were used to asses the the ability to generate ROS by Ce6. Next, the cell studies using murine melanoma (B16F10) and oral squamous cell carcinoma (FaDu) were performed to determine cellular uptake, laser irradiation-assisted cytotoxicity, combination index, and cell death mechanisms. In vivo therapeutic efficacy was analyzed using tumor (B16F10)-bearing mice. The NPs released both PTX and Ce6 sustainably with the enhancement of drug release at low pH of 4.6. The Ce6/PTX-H/P NPs exhibited photo- stimulated ROS production, resulting in enhanced cytotoxicity than monotherapies and induced synergistic

therapeutic response in FaDu cells (24 and 48 h treatment). The Ce6/PTX-H/P NPs exhibited extensive apoptotic induction, cell cycle arrest, DNA damage in the G2/M phase, and mitochondrial membrane perturbation than free Ce6, PTX, and the Ce6, or PTX-loaded NPs. The Ce6/PTX-H/P NPs reduced the tumor weight by 5.99 % in comparison to control and ~ 2.66 % than the free drugs, depicting the most effective treatment modality of all the tested formulations in the in vivo experiment using B16F10 tumor-bearing mice and in the immunohistochemistry analysis. Ce6/PTX-H/P NPs Third, Hypoxia is an important pathological hallmark of the tumor microenvironment, accompanying with metabolic alterations, cell proliferation, aggressiveness, metastasis, and therapy resistance in cancers. Hypoxia hampers the outcome of photodynamic therapy (PDT), largely reliant on on molecular oxygen to generate cytotoxic $^1O_2$. Here, a near-infrared light activatable, oxygen-generating nano micellar PDT- chemotherapy system (mPPCPN Ms) constituted of amphiphilic mPEG-PLA, photosensitizer Ce6, and tetravalent platinum prodrug Pt(IV)-diazide was developed for oral squamous cell carcinoma. The polymer conjugate self-assemble to nanosize (115 ± 2.35 nm) micelles, which, upon irradiation (660 nm laser), activated Ce6, and photodecomposed to produce cytotoxic Pt(II), azide radical, and molecular oxygen. The strategically fabricated PDT-chemotherapy produced a strong antitumor response in vitro using oral squamous cell carcinoma and in vivo in oral cancer- xenografted mouse models, revealing its significant potential in chemo- photodynamic combination therapy with the benefit of reversing hypoxia.

Fourth, This study involves the development of micelle-based nanoparticles by conjugating 2-nitrobenzyl-chlorin e6 (2NB-Ce6) with methoxy (polyethylene glycol) (mPEG) to increase the accumulation of the drug at the tumor site by passive targeting. NMR, SEM, XRD, X-ray

photoelectron spectroscopy, DSC, and SOG were used to characterize the conjugates. A hemolysis study was performed, which indicated that the synthesized micelles were not toxic to red blood cells and, hence, they were biocompatible. A cellular uptake study was performed, which has shown that Ce6 conjugation has improved the uptake of Ce6.

The cell viability assay revealed that the formulation had shown concentration-dependent cytotoxicity upon laser irradiation. mPNCe6 group plus laser irradiation has generated abundant ROS inside cells and exhibited strong green fluorescence indicating the efficient delivery of Ce6 by mPNCe6 micelles and its excellent ROS generation ability inside cells upon laser irradiation. Further, the in vivo efficacy study using MOC2 xenografted C57Bl6/J mice indicated that the mPNCe6 localized in tumor sections. mPNCe6 reduced the tumor growth significantly

developed micelle-based nanoparticles mPNCe6 can target the loaded drug to the tumor, and mPNCe6 can be utilized successfully in cancer treatment.

Fifth, The purpose of this research is to develop polymeric micelle-based nanoparticles by conjugating 2-nitrobenzyl with methoxy(polyethylene glycol)-poly(D,L-lactide) (mPEG- PLA) and then loading Ce6 to improve drug accumulation at the tumor location via passive targeting. Nuclear Magnetic Resonance (NMR), Scanning Electron Microscopy (SEM), X- ray Diffraction (XRD), X-ray Photoelectron Spectroscopy, Differential Scanning Calorimetry (DSC), and SOG techniques were employed to analyze and describe the properties of these polymeric micelles. A hemolysis study was performed, demonstrating that the produced micelles exhibited no toxicity towards red blood cells, thereby confirming their biocompatibility. A study on cellular absorption was conducted, revealing that the loading of Ce6 into the polymeric micelle has enhanced the

uptake of Ce6. The cell viability assay demonstrated that the formulation exhibited cytotoxicity that was dependent on the concentration when exposed to laser irradiation. The combination of Ce6@mPPN group and laser irradiation has produced a large amount of reactive oxygen species (ROS) within cells. This has been demonstrated by the bright green Fluorescence, suggesting the successful delivery of Ce6 via Ce6@mPPN micelles and its exceptional ability to generate ROS inside cells when exposed to laser irradiation. Moreover, the in vivo efficacy research conducted on MOC2 xenografted C57Bl6/J mice suggested that the Ce6@mPPN specifically accumulated in tumor sections. Ce6@mPPN showed a significant decrease in tumor growth compared to Ce6@mPP and free Ce6. Ce6@mPPN had a higher capability for inducing apoptosis. Therefore, the recently created polymeric micelle-based nanoparticles Ce6@mPPN have the capability to specifically deliver the loaded medicine to the tumor. Consequently, Ce6@mPPN holds promise for effective use in cancer therapy.

Table of Contents

Contents	Page No.

Chapter 1: Introduction

1.1 Cancer

1.2 Cell biology of cancer

1.3 Aetiopathogenesis

1.4 Cell biology of oral cancer

1.5 Hallmarks of cancer

1.6 Oral cancer treatments

1.7 Targeted drug delivery systems

1.8 Polymeric micelles as drug delivery systems

1.9 Albumin-based nanocarriers

1.10 Paclitaxel as anticancer agent

1.11 Cisplatin

1.12 Objectives

List of Tables

List of Figures

	vs. days during treatment (a); The average weight of tumors isolated from various treatment groups (b); Representative tumors isolated from mice post-treatment (c); Biodistribution of micelles and in vivo anticancer efficacy evaluation. time-dependent NIR fluorescence images of tumor- bearing nude mice after i.v. administration of free Ce6 and mPPCPN Ms (Ce6: 5 mg / kg) (d); Ex vivo NIR fluorescence images of major organs and tumor excised at 30 h post injection (e); The fluorescence intensity for the region of interest (tumor) was recorded as total photon counts per tumor (f); Mean fluorescent intensity of Ce6 in tumors, organs, at various time points after mice were i.v. injected with mPPCPN Ms (g); Assessment of therapeutic Efficacy of free Ce6 and mPPCPN Ms, Ce6:CDPP(1:1) formulations in FADU HTB-43 tumor-bearing female balb/c nude mice. Graphical representation of tumor volume vs. days during treatment (a); The average weight of tumors isolated from various treatment groups (b); Representative tumors isolated from mice post-treatment (c); Biodistribution of micelles and in vivo anticancer efficacy evaluation. time- dependent NIR fluorescence images of tumor-bearing nude mice after i.v. administration of free Ce6 and mPPCPN Ms (Ce6: 5 mg / kg) (d); Ex vivo NIR fluorescence images of major organs and tumor excised at 30 h post injection (e); The fluorescence intensity for the region of interest (tumor) was recorded as total photon counts per tumor (f); Mean fluorescent intensity of Ce6 in tumors, organs, at various time points after mice were i.v. injected with mPPCPN Ms (g);	
Figure 4.29	Immunohistochemical staining for FADU HTB-43 tumor from mice that received different treatments indicated for Tunel assay (a); KI67 activity (b); ROS generation assay (c); Quantify the intensity of the green fluorescence indicates ROS concentration in the tumor tissue. Data represented as the mean $\pm$ SE of three independent	185

LIST OF ABBREVIATIONS AND SYMBOLS

ACN	Acetonitrile
B16F10	Murine melanoma cell
CCD	Central composite design
CD	Circular dichroism
Ce6	Chlorin e6
$CDCl_3$	Deuterated chloroform
DAPI	4′,6-Diamidino-2-phenylindole dihydrochloride
DCFH-DA	2,7-dichlorodihydrofluorescein diacetate
DL	Drug loading
DLS	Dynamic light scattering
DMEM	Dulbecco's Modified Eagle Medium
DMSO	Dimethyl sulphoxide
DOE	Design of experiment
DSC	Differential scanning calorimetry
DTP	Drug: polymer
EE	Encapsulation efficiency
EDC	N-(3Dimethylaminopropyl)-N′-ethylcarbodiimide hydrochloride
EPR	Enhanced Permeability and Retention
FaDu HTB- 43	Homo sapiens pharynx squamous cell carcinoma
FITC	Fluorescein isothiocyanate
FTIR	Fourier transform infrared spectroscopy
GPC	Gel permeation chromatography
HEK	Human embryonic kidney cells
H & E	Hematoxylin and eosin
HPLC	High performance liquid chromatography
HSA	Human serum albumin
1H NMR	Proton Nuclear Magnetic Resonance
IC50	Half maximal inhibitory concentration
IVIS	In vivo imaging system
JC 1	5,5′,6,6′-Tetrachloro-1,1′,3,3′ tetraethylbenzimidazolocarbocyanine iodide

MCF-7	Human breast cancer cell line
MEM	Minimum essential medium eagles
MOC2	Mouse oral squamous cell carcinoma
mPEG	Methoxy polyethylene glycol
MTT	3-(4,5-dimethylthiazol-2-yl)-2,5-di-phenyltetrazolium bromide
MWCO	Molecular weight cut-off
mg	Milligram
min	Minute
mL	Millilitre
mm	Millimetre
mmol	Millimole
NHS	N-hydroxysuccinimide
nm	Nanometer
PBS	Phosphate buffered saline
PDI	Polydispersity Index
PI	Propidium iodide
PLA	Polylactic acid
RA	Retinoic acid
ROS	Reactive oxygen species
RT	Room temperature
SD	Standard deviation
SDS	Sodium dodecyl sulfate
SEM	Scanning electron microscope
SOSG	Singlet oxygen sensor green
TEA	Triethylamine
THF	Tetrahydrofuran
TUNEL	Terminal deoxynucleotidyl transferase mediated nick-End labeling
XRD	X-Ray Diffraction
4T1	Murine mammary carcinoma
µg	Microgram
µL	Microlitre
µM	Micromolar

Chapter 1

Introduction

1.1 Cancer

Cancer encompasses a group of diseases resulting from the uncontrolled proliferation of malignant cells capable of spreading to different parts of the body. It can originate anywhere in the human body and affects individuals of all ages and genders and involving billions of cells (Sriharikrishnaa S et al. 2023). Typically, human cells replicate through cell division to replenish the body's cell count as old or damaged cells die off and are replaced. However, this regulated process can malfunction, leading to inappropriate proliferation of abnormal or damaged cells, possibly resulting in the formation of tumors (Lee SY et al. 2018).

The World Health Organization (WHO) reports that cancer is a leading global cause of mortality, responsible for nearly 10 million deaths in 2020, equating to one in six fatalities. Predominant cancer types include breast, lung, oral, colorectal, and prostate cancers. Projections from GLOBOCAN 2020 indicate a 47% rise in new cancer cases, reaching approximately 28.4 million by 2040, up from 19.3 million in 2020 (Sung H et al. 2020) (Figures 1.1 and 1.2). In India, in 2018, cancer was responsible for an estimated 784,821 deaths. Notably, cancers of the oral cavity and lungs constitute over 25% of male cancer fatalities, while breast and oral cavity cancers account for 25% of female cancer fatalities in India (Dhillon PK et al. 2018) (Figure 1.3). The American Cancer Society has estimated that in 2023 there will be 54,540 new cases of oral cavity or oropharyngeal cancer and approximately 11,580 deaths from this disease. Since almost 70% of cases are reported in advanced stages, oral cancer is a much bigger concern in India than it is in the West (American Joint Committee on Cancer, Stage III- IV) it was found that the central region of India had the highest rate of oral cancer in both males and females. At 70 years of age, it was 37.2% for women and 64.8% for men whereas at 60 years of age, the west and northeast regions saw the next highest magnitude (58.4%) (Sharma S et al. 2018). Tobacco use, alcohol

consumption, high body mass index (BMI), low fruit and vegetable intake, and lack of physical activity contribute to nearly one-third of cancer-related deaths (Agarwal SK 2021). Globally, the incidence and mortality of cancer are on a rapid rise, attributed to factors such as aging, population growth, changes in risk factors, and socio-economic development (Zhang SZ, Zhang SZ, Xie L, Shang ZJ 2018). Nonetheless, throughout the last five years, there has been a decrease in death rates as a result of growing knowledge about the biology of tumors and improvements in diagnostic tools and therapies.

1.2 Oral cancer

The oral cavity is defined by anatomic boundaries, which include the vermillion border of the lip anteriorly, the junction of the hard palate and the soft palate posteriorly and superiorly, the circumvallate papillae inferiorly and the anterior tonsillar pillars laterally. Within this cavity are several subsites where cancers can grow including the lip, dentoalveolar ridge, oral tongue, retromolar trigone (RMT), floor of mouth (FOM), buccal mucosa, and hard palate (Figure 1.1).

Oral squamous cell carcinoma (OSCC) is a malignant neoplasm of the oral cavity and accounts for 95% of cancers in this anatomic site (Chamoli A et al. 2021). It is an invasive epithelial neoplasm with varying degrees of squamous differentiation and has the propensity to metastasize early and extensively to regional lymph nodes (LNs). OSCC is most commonly of the keratinising (conventional) type with three histological grades; well, moderately, and poorly differentiated. Other types of squamous cell carcinoma (SCC) include verrucous carcinoma, spindle cell SCC, basaloid SCC, adenosquamous carcinoma, and lymphoepithelioma-like carcinoma (Bugshan A, Farooq I 2020). There are associated premalignant surface epithelial changes called carcinoma in situ (CIS) that are characterized by cellular dysplasia involving the full thickness of the mucosa without compromise of the basement membrane. If the malignant cells penetrate the basement

membrane and infiltrate into the superficial compartment of the lamina propria, the lesion is termed micro-invasive carcinoma (Tilakaratne WM et al. 2000).
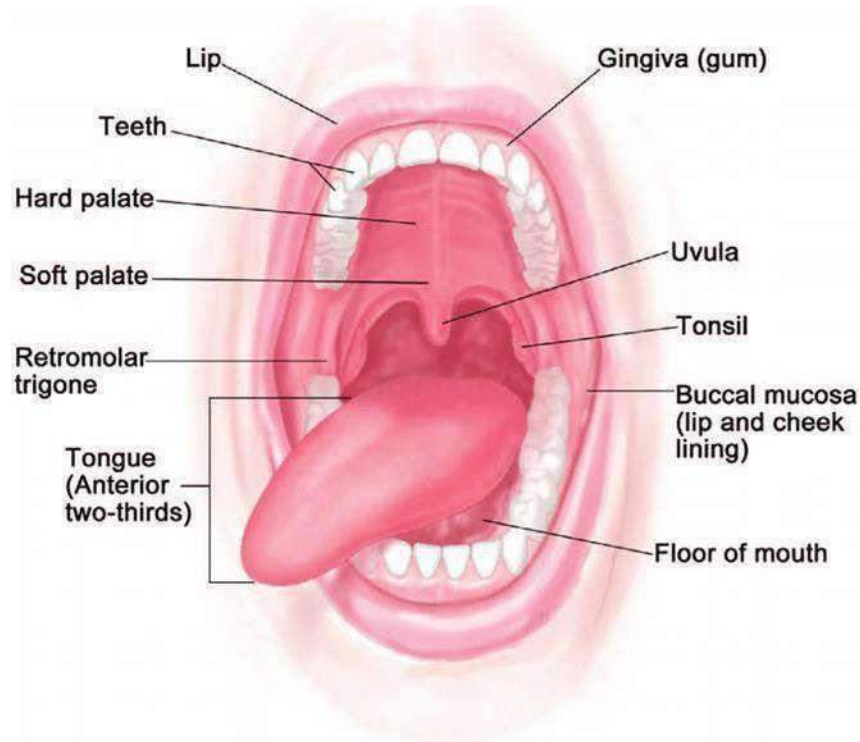
Figure 1.1 Subsites of the oral cavity

1.3 Aetiopathogenesis

The risk factors for OSCC are tobacco, spirits, sharp teeth, and, much more rarely now, syphilis. Smoking and alcohol increase the risk by four folds, and when consumed together have a super multiplicative effect (Chamoli A et al. 2021) (Johnson NW, Amarasinghe HK et al. 2016). In India and South East Asia, the practice of chewing betel nut with quid (lime and cured tobacco), is a common cause (Gunjal S et al. 2020). Other associations with the etiology of OSCC are chronic syphilis infection, ill-fitting dentures, and long-term immunosuppression (Imon AA et al. 2019).

The pathogenesis of OSCC is multifactorial and is thought to arise from a multi-step process within a clonal population of cells involving sequential activation of genes that have the potential to cause cancer (oncogenes), as well as inactivation of genes that prevent cancer (tumour suppressor genes) (Kyrgidis A, Antoniades K 2010). A molecular model for the pathogenesis of OSCC describes first a loss of chromosomal regions 3p and 9p21 followed by inactivation of the p16 gene leading to histological atypia (Towle R 2016) (Oliveira AC 2016). Subsequent mutation of the p53 tumour suppressor gene is associated with progression to dysplasia (Nathanson JW et al. 2008). Finally, gross gene alterations and deletions on 4q, 6p, 8p, 11q, 13q, and 14q are believed to lead to malignancy (Gollin SM 2014). A late event is the amplification and overexpression of the Cyclin D1 gene, which activates cell cycle progression and confers the ability of the tumour cells to invade (Qie S, Diehl JA 2016).
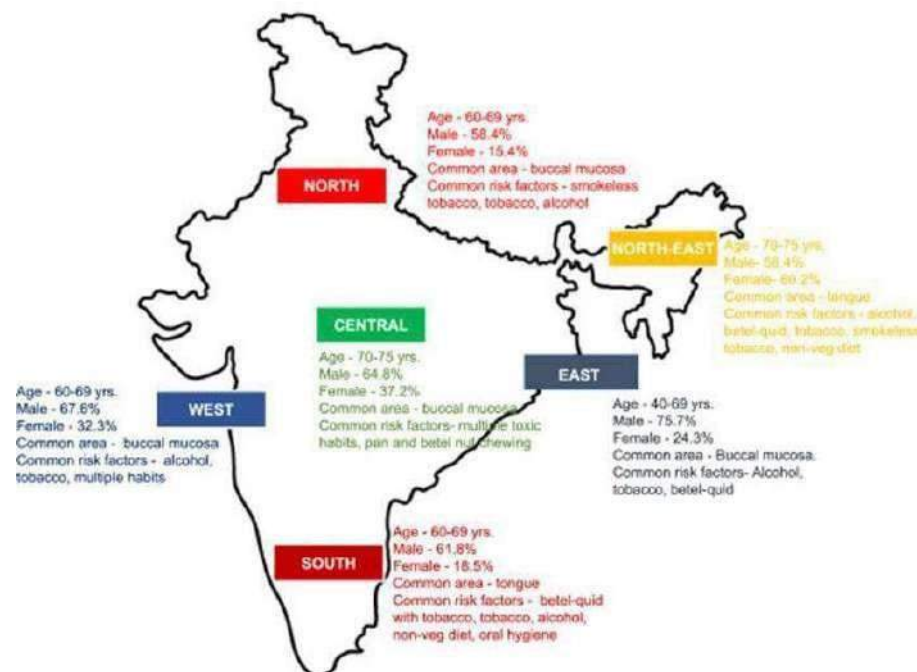
Figure 1.2 Distribution of oral cancer across the India. (Reference)
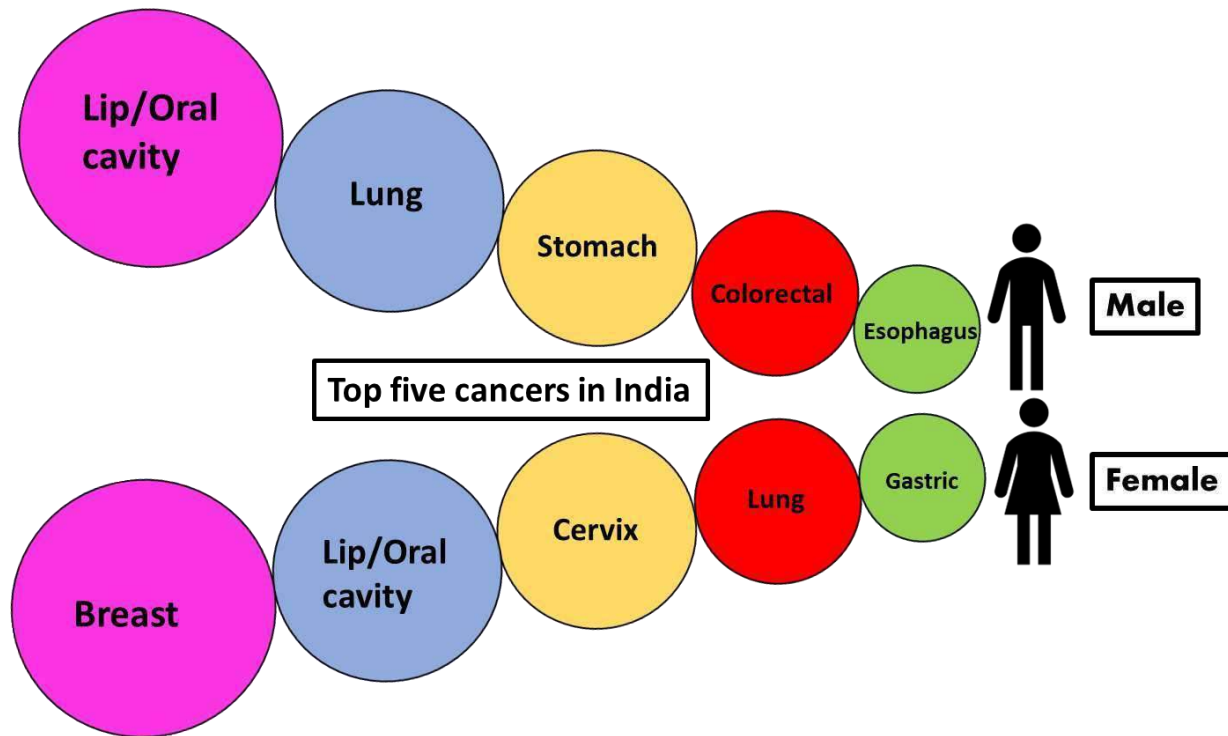
Figure 1.3: The five leading cancers for male and female in India (P. Mathur et al. 2020).

The structural building blocks of all living things are cells. Like a developing tree, each of us is composed of trillions of cells. Cells enable us to carry out all kinds of functions of life. The cell is the fundamental unit of life and the smallest component of the body that carries out all vital functions (Alberts B 2017). Each organ in the body, including the lung, breast, colon, and brain, is made up of specialized cells that perform the duties of the organ, including the movement of oxygen, digestion of nutrients, excretion of waste products, reproduction, thinking, etc. Each organ requires the replacement of damaged or worn-out cells as well as the growth of specific cell types in response to environmental changes to function properly (Alberts B 2017). For instance, in reaction to bleeding or high altitude, the bone marrow multiplies by seven or more the amount of oxygen-carrying red blood cells that are produced (Sandor GK et al. 2012). During an infection,

some white blood cells are produced more quickly. Similar to this, the liver or endocrine organs frequently repair damaged cells in response to injury (Baddour JA, Sousounis K, Tsonis PA 2012). Cell division is the process by which cells reproduce. Normal cell division is a well-controlled process. DNA(deoxyribonucleic acid) regulates the cell's growth, inheritance, and confinement. The "brain" of the cell is a highly complicated molecule called DNA, which is produced in the cell nucleus. DNA serves as the cell's operating manual. The DNA in a human cell is divided into 46 separate portions called chromosomes. The 23 chromosomes from each biological parent are organized in pairs. Together, the 46 chromosomes contain more than 100,000 genes (Keagle MB 2012). A gene is a section of DNA that defines a protein's structure. Proteins are necessary for growth and development as well as carrying out essential chemical processes in the body. Genes are grouped in pairs, just like chromosomes. Each gene has a defined chromosomal position. Each gene instructs a cell to produce a distinct protein through several biochemical processes. Some genes instruct the cell to manufacture structural proteins, which serve as building blocks (Choudhari SK et al. 2014). Other genes instruct the cell to make cytokines, hormones, or growth factors, which leave the cell and communicate with other cells. Other genes instruct the cell to make regulatory proteins that regulate the activity of other proteins or instruct other genes to become active or inactive (Iyama T, Wilson III DM 2013). When a gene is activated, it produces ribonucleic acid (RNA), a different complex molecule that has all the information a cell needs to produce new proteins (Lahtz C, Pfeifer GP 2011). Some genes give the cell instructions on how to make building-block proteins called structural proteins. Other genes instruct the cell to make cytokines, hormones, or growth factors, which leave the cell and communicate with other cells. Other genes instruct the cell to make regulatory proteins that regulate the activity of other proteins

or instruct other genes to become active or inactive. Every phase of the process has checkpoints to ensure that everything goes as it should (Yao Y, Dai W 2014).

A cell cannot divide successfully unless A cell cannot divide successfully unless several steps necessary for cell reproduction are carried out appropriately. If any of these intricate steps go wrong, a cell could become cancerous (Torgovnick A, Schumacher B 2015).

1.4 Cell biology of oral cancer

A cancer cell is a cell that grows out of control. Unlike normal cells, cancer cells ignore signalsto stop dividing, to specialize, or to die and be shed. Growing uncontrollably and unable to recognize its natural boundary, the cancer cells may spread to areas of the body where they do not belong, this process is termed as metastasis. In a cancer cell, several genes change (mutate) and the cell becomes defective (Ram H et al. 2011). There are two general types of gene mutations. One type, dominant mutation, is caused by an abnormality in one gene in a pair. An example is a mutated gene that produces a defective protein that causes the growth-factor receptor on a cell's surface to be constantly "on" when, in fact, no growth factor is present. The result is that the cell receives a constant message to divide. This dominant "gain of function gene" is often called an oncogene. The second general type of mutation, recessive mutation, is characterized by both genes in the pair being damaged. For example, a normal gene called p53 produces a protein that turns "off" the cell cycle and thus helps to control cell growth. The primary function of the p53 gene is to repair or destroy defective cells, thereby controlling potential cancerous cells. This type of gene is called an anti-oncogene or tumor suppressor gene. If only one p53 gene in the pair is mutated, the other gene can still control the cell cycle. However, if both genes are mutated, the "off" switch is lost, and the cell division is no longer under control (Leemans CR et al. 2011) (Jurel SK et al. 2014).

Abnormal cell division can occur either when active oncogenes are expressed or when tumor suppressor genes are lost. Several mutations are required for a cell to develop into a cancerous one (Figure 1.4). There are several situations in which both dominant and recessive mutations can occur. A gene mutation may enable an already abnormal cell to enter the healthy tissue where the cancer first appeared or to spread (metastasize) through the bloodstream to distant regions of the body, where it can continue to divide. A healthy cell can undergo injury in a variety of ways. A cell can develop an abnormality when a gene is partially lost (deleted) when a chromosome is rearranged and ends up in the incorrect position (translocation), or when a minor DNA error results in an abnormal DNA "blueprint" and the synthesis of an abnormal protein (Jurel SK et al. 2014). Viral diseases can also cause aberrant cell division. In this instance, genes may be healthy, but a cancer-causing virus in the cell may prevent the protein from functioning normally (Ahuja R et al. 2014). How a specific cancer cell behaves depends on which processes are not functioning properly. Some cancer cells simply divide and produce more cancer cells, and the tumor mass stays where it began. Whereas other cancer cells can invade normal tissue, enter the bloodstream, and metastasize to a remote site in the body (Akram N et al. 2017).
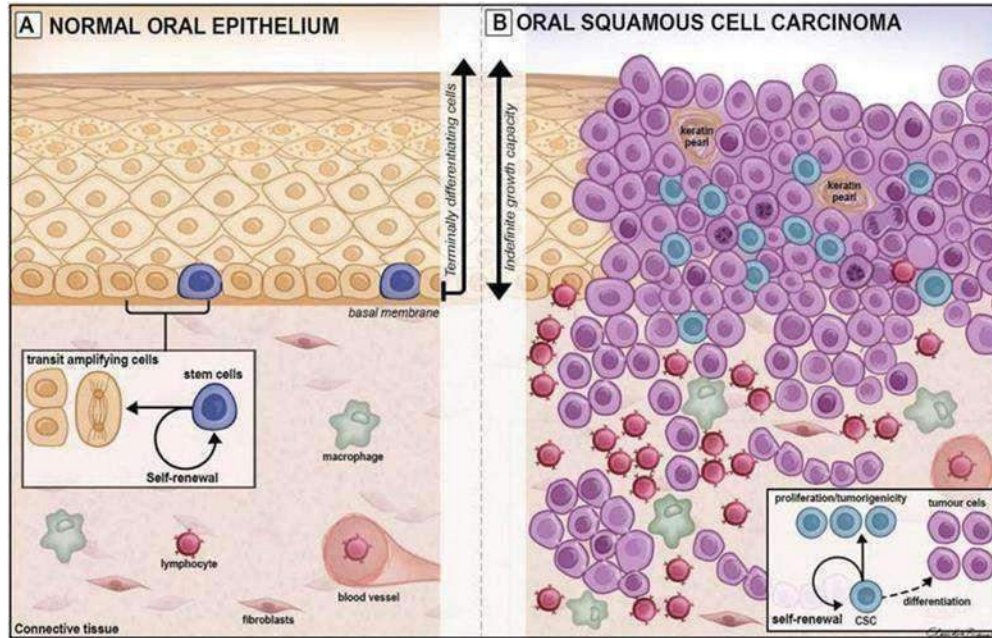
Figure 1.4 Diagrammatic representation of normal oral epithelium and oral squamous cell carcinoma

Cell division is the process by which cells reproduce (mitosis). The cell cycle is a series of changes the cell goes through from the time it is first formed until it divides into two daughter cells. It starts at mitosis (M-phase) and ends with mitosis. In between are the G-1, S, and G-2 phases. The duration of S, M, and G-2 are relatively constant in different tissues. Between the M-phase and the S-phase is a gap (G-l) where the production of RNA, proteins, and enzymes needed for DNA synthesis occurs. The duration of G-1 varies and determines the length of the cell cycle (Keagle MB 2012).

OSCC is characterized by aberrant activation of several pathways and regulators such as Wnt/β-catenin (Chen F et al. 2019), EGRF (Ohnishi Y et al. 2017), NOTCH 1, and PI3K/AKT/mTOR .
A study has shown, about 78 % of patients with OSCCs had high expression of EGFR. EGFR

aggravates oral cancer by enhancing stemness by inhibiting autophagic degradation of SOX2. Moreover, overexpression of EGFR is correlated with tumor aggressiveness and poor survival of patients with OSCC. Interestingly, EGFR expression in the nucleus of more than 5% of tumor cells was found in 24.3% of OSCC patients and was associated with poor survival (Lakshminarayana S et al. 2018).

Both activation and inactivation of NOTCH signaling are known to play a role in tumorigenesis and tumor progression. It was found that about 6 % of OSCC patients, had defective notch signaling contrary to the above findings, the overexpression of Nrf2 in OSCC cells was linked to promote pro tumorigenic phenotype (Tang D et al. 2017).

Two studies reported that the proteins, AKT and mTOR, were abundantly found in their active forms in OSCC tissues obtained from the gingiva, hard palate, and alveolar ridge, suggestive of AKT/mTOR pathway activation and its role in the development of OSCC. It profoundly impacts various cellular processes like proliferation, survival, invasion, EMT, and angiogenesis and is also responsible for driving chemoresistance and radio resistance in OSCC. Hence, upregulation of the PI3K/AKT/mTOR pathway induces tumor growth and development and results in poor prognosis (Cohen Y et al. 2011) (Johnson TL et al. 2010).

1.5 Hallmarks of oral cancer

Hanahan and Weinberg have proposed that six hallmarks of cancer together constitute an organizing principle that provides a logical framework for understanding the remarkable diversity of neoplastic diseases (Figure 1.5). The six major hallmarks: are self-sufficiency in growth signals, insensitivity to anti-growth signals, evading apoptosis, limitless replicative potential, sustained angiogenesis, and tissue invasion and metastasis (Hanahan D, Weinberg RA 2011). It was the notion that as normal cells evolve progressively to a neoplastic state, they acquire a succession of

these hallmark capabilities, and that the multistep process of human tumor pathogenesis could be rationalized by the need of incipient cancer cells to acquire the traits that enable them to become tumorigenic and ultimately malignant.
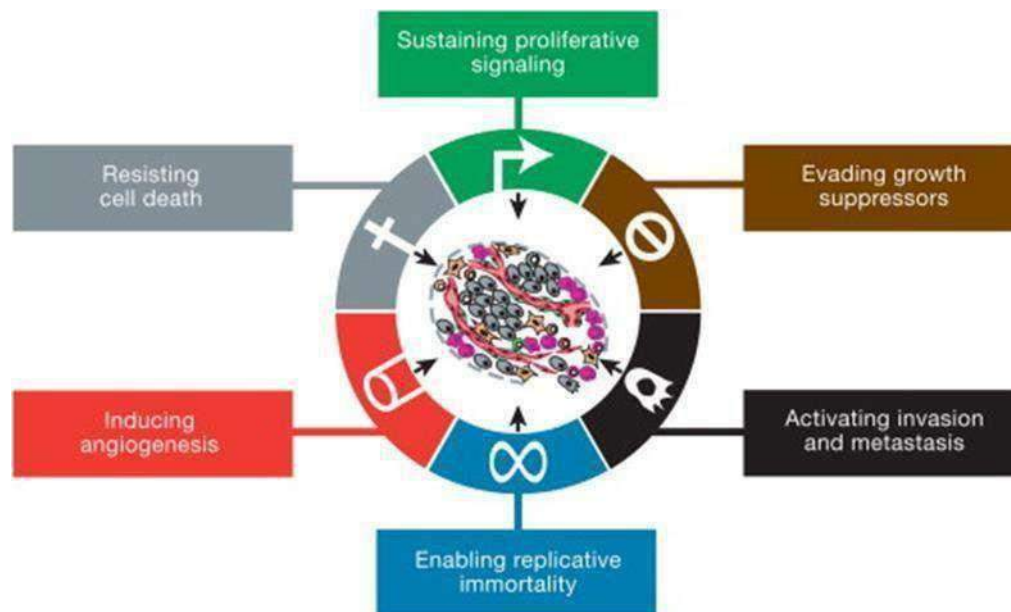
Figure 1.5 The biological hallmarks of cancer

The anti-cancer drugs targeting hallmarks have been developed which interfere with all six hallmarks including genome instability and tumor-promoting inflammatory markers. Some of these chemotherapeutic drugs are in the clinic, some are being tested in clinical trials while others are being tested pre-clinically. Eventually, the development of resistance during cancer treatment with these hallmark targeting drugs is apparent and co-targeting of multiple hallmarks with chemotherapeutics may prevent the emergence of drug resistance clinically and preclinically (Fouad YA, Aanei C 2017). Eventually, the development of resistance during cancer treatment with these hallmark targeting drugs is apparent and co-targeting of multiple hallmarks with

chemotherapeutics may prevent the emergence of drug resistance clinically and preclinically (Hanahan D, Weinberg RA 2011).
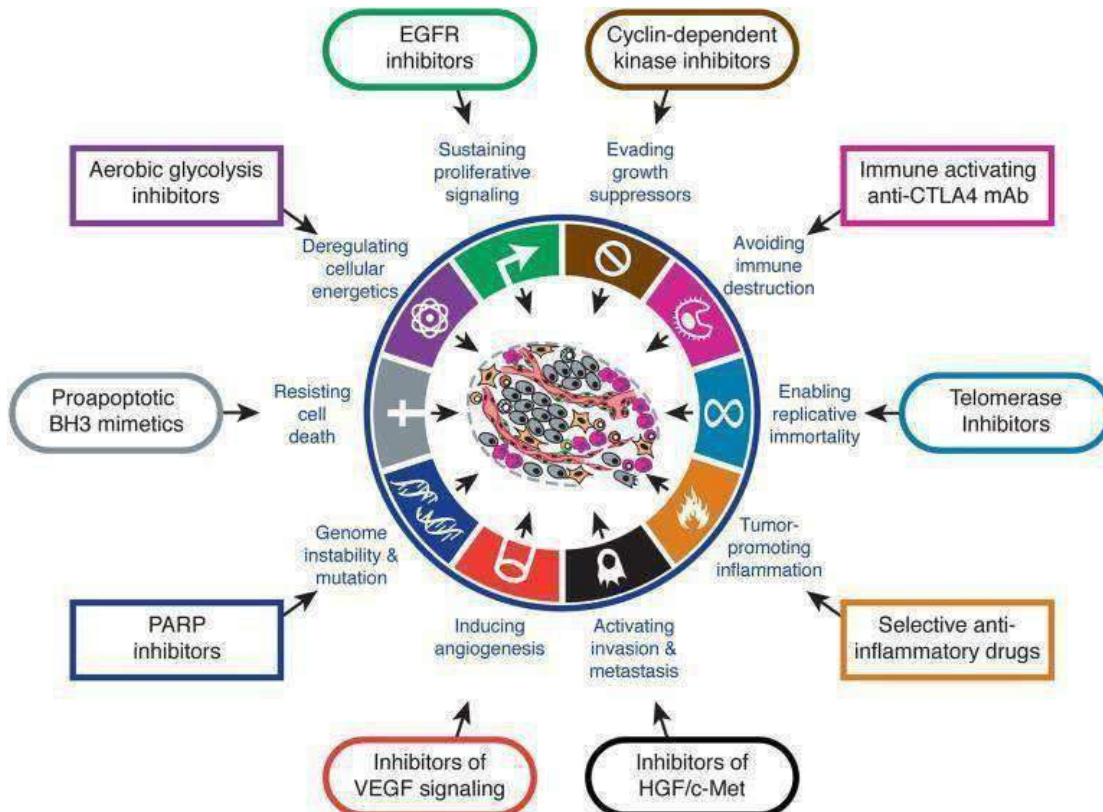
Figure 1.6 Therapeutic targeting of the hallmarks of cancer (Hanahan and Weinberg2011)

1.6 Oral cancer treatments

Surgery, radiation therapy, chemotherapy, or their combinations represent the prevailing methods for cancer treatment. The specific approach depends on the cancer type, its stage, progression speed, patient's condition, and response to treatment. Despite their widespread use, these treatments harbor notable drawbacks, leading to a grim prognosis and severe side effects.

Therefore, there's an imperative to innovate and develop improved therapies aiming to enhance current treatment outcomes (More Y, D'Cruz AK 2013).

1.6.1 Surgery

Surgery stands as the oldest cancer treatment method and remains a primary curative option, even as advancements in other treatment approaches have lessened its necessity in certain cancers. Despite enhancements in surgical techniques, its effectiveness in controlling cancer is limited, given that around two-thirds of cancer patients present tumors that have spread from their initial location by the time surgery is considered. Surgical oncologists grapple with numerous challenges when determining the best approach for solid tumor patients. Assessing whether local treatment suffices and, if so, identifying the surgical procedure that strikes the right balance between curing the disease and preserving the patient's quality of life are critical considerations. Adjuvant therapy often influences the extent of tumor resection in many cases, altering the removal of organ or tissue portions (Omura K, 2014). Additionally, therapy has progressed through the integration of surgery with other treatment modalities. While surgery is primarily aimed at cure, it can also serve palliative purposes by alleviating pain or dysfunction. Palliative surgery involves addressing issues such as intestinal obstruction or the removal of masses causing pain or disfigurement.

1.6.1 Radiation therapy

Ionizing radiation, encompassing X-rays, gamma rays, or subatomic particles like neutrons, serves as a method in cancer treatment to eliminate cancer cells. Approximately half of all cancer patients receive radiation therapy, where radiation induces cell death either by causing genetic damage that impedes cell reproduction or by triggering programmed cell death, known as apoptosis (Kondo T, 2013). Cancer cells, being continuously proliferating, are more susceptible to radiation compared to healthy cells, as they struggle to recover from radiation damage due to their constant replication,

unlike normal cells. Clinically, various radiation ranges or voltages are employed, with surface-level, orthovoltage, and super voltage representing the low, middle, and high ranges, respectively. Radiation therapy in clinics involves two primary methods: brachytherapy, or internal radiation therapy, where the radiation source is inserted into the tumor or nearby body cavities, and teletherapy, or external radiation therapy, utilizing devices like clinical linear accelerators to administer radiation from outside the patient (Huang SH, 2013).

The adverse effects of radiation therapy are categorized into acute and late effects. Acute effects manifest in rapidly renewing tissues such as the linings of the oral cavity, pharynx, intestine, urinary bladder, and vagina. Late effects, linked to the total radiation dose received, encompass scar formation (fibrosis), tissue damage, and the formation of abnormal passages (fistulae). Generally, secondary effects are less pronounced in brachytherapy compared to teletherapy (Sroussi HY et al., 2017).

1.6.2 Chemotherapy

The primary aim of chemotherapy is to impede the proliferation and multiplication of cancer cells, ultimately thwarting invasion and metastasis. Nevertheless, as chemotherapy affects normal cells, it leads to severe side effects. It acts at various levels, hindering tumor growth within the cell and its environment. Cancer treatments, ranging from hormones to targeted immunotherapy and the widely used cytotoxic agents, are classified based on their structure and function (Furness S et al., 2011). Cytotoxic drugs such as alkylating agents—nitrogen mustards (e.g., Bendamustine, cyclophosphamide, ifosfamide), platinum analogs (carboplatin, cisplatin, oxaliplatin), nitrosoureas (carmustine, lomustine), alkyl sulfonate like Busulfan, and triazenes (Dacarbazine, procarbazine, temozolomide)—generate an unstable alkyl group ($R\text{-}CH_2+$) that interacts with nucleophilic centers on proteins and nucleic acids. This action inhibits DNA replication and transcription (Kim

KW et al., 2016) (Bradshaw TD, 2013). Antimetabolites, another class of anti-cancer agents, hinder the synthesis of DNA, RNA, or proteins in cancer cells. Cytidine analogs (e.g., azacitidine, decitabine, cytarabine, gemcitabine), folate antagonists (methotrexate, pemetrexed), purine analogs (cladribine, clofarabine, nelarabine), and pyrimidine analogs (fluorouracil (5-FU), capecitabine (prodrug of 5- FU)) fall under this category (Tiwari M, 2012). Taxanes (paclitaxel, docetaxel, cabazitaxel) and vinca alkaloids (vincristine, vinblastine, vinorelbine) affect the spindle apparatus during cell division. They may be administered pre-surgery to reduce tumor size, post-surgery to impede metastasis, or combined with radiotherapy or hormonal therapy (Negi AS et al., 2015). Although cytotoxic drugs act swiftly on dividing cells, they cannot differentiate between cancer cells and labile healthy cells such as bone marrow, gastric lining, and skin cells. Administered at the maximum tolerated dose (MTD), they result in dose-limiting toxicity in healthy cells, causing myelosuppression, nausea, vomiting, mucositis, and alopecia (Monsuez JJ et al., 2010). Additionally, these drugs damage permanent tissues like the heart, kidneys, and brain. For instance, cyclophosphamide and ifosfamide can lead to cardiac failure and life-threatening arrhythmias at high doses (Livshits Z, Rao RB, Smith SW, 2014). Doxorubicin and cyclophosphamide contribute to neurocognitive deficits, affecting learning, attention, memory, and information processing speed in about 40% of treated breast cancer patients (Castel H et al., 2017). Consequently, chemotherapy's application in clinics is limited due to the decreased survival rates observed in patients.

1.6.3 Photodynamic therapy

Since the first successful demonstration of using PDT to ablate tumor cells in 1978 by Dougherty et al., research on PDT has improved substantially (Allison RR, Sibata CH 2010). This is an impressive technique having widespread benefits compared to traditional chemotherapy.

PDT may be repeated securely, if necessary, without incurring the risk of damaging nearby normal tissue. This makes PDT attractive option for treating malignancies wherein loco-regionally recurring therapy may be required. PDT might potentially provide dual specificity in tumor treatment by creating innovations that ensure light irradiation of the tumor only when necessary and PS deposition in the tumor. PDT has been extensively used for the local clinical therapy of several malignancies including stomach cancer, esophageal cancer, and head and neck cancers (Hu J et al. 2015). Despite its advantages, PDT still has poor therapeutic effectiveness owing to poor accumulation of PSs in tumor tissue following in vivo injection. The nonspecific absorption by other cells or tissues significantly reduces the therapeutic efficacy. Furthermore, the hypoxic tumor microenvironment limits its effectiveness. Moreover, PDT will result in a drop in oxygen concentration, thus jeopardizing the effectiveness of PDT (Saini R et al. 2016)

Developing nanoparticles (NPs) is thought to be a logical way to get over PDT's drawbacks due to the advancement of nanotechnology. PS can be incorporated into suitable nanocarriers either by chemical conjugation or by physical encapsulation. These methods alter the chemical properties of the PSs, namely solubility, prevent them from self-quenching, and increase the effectiveness of ROS generation. In contrast, NPs may also alter the biodistribution and pharmacokinetics of PSs in vitro and in vivo. NPs improve PS tumor specificity by the EPR effect or by altering their surface with targeted ligands (Andreadis D et al. 2016).
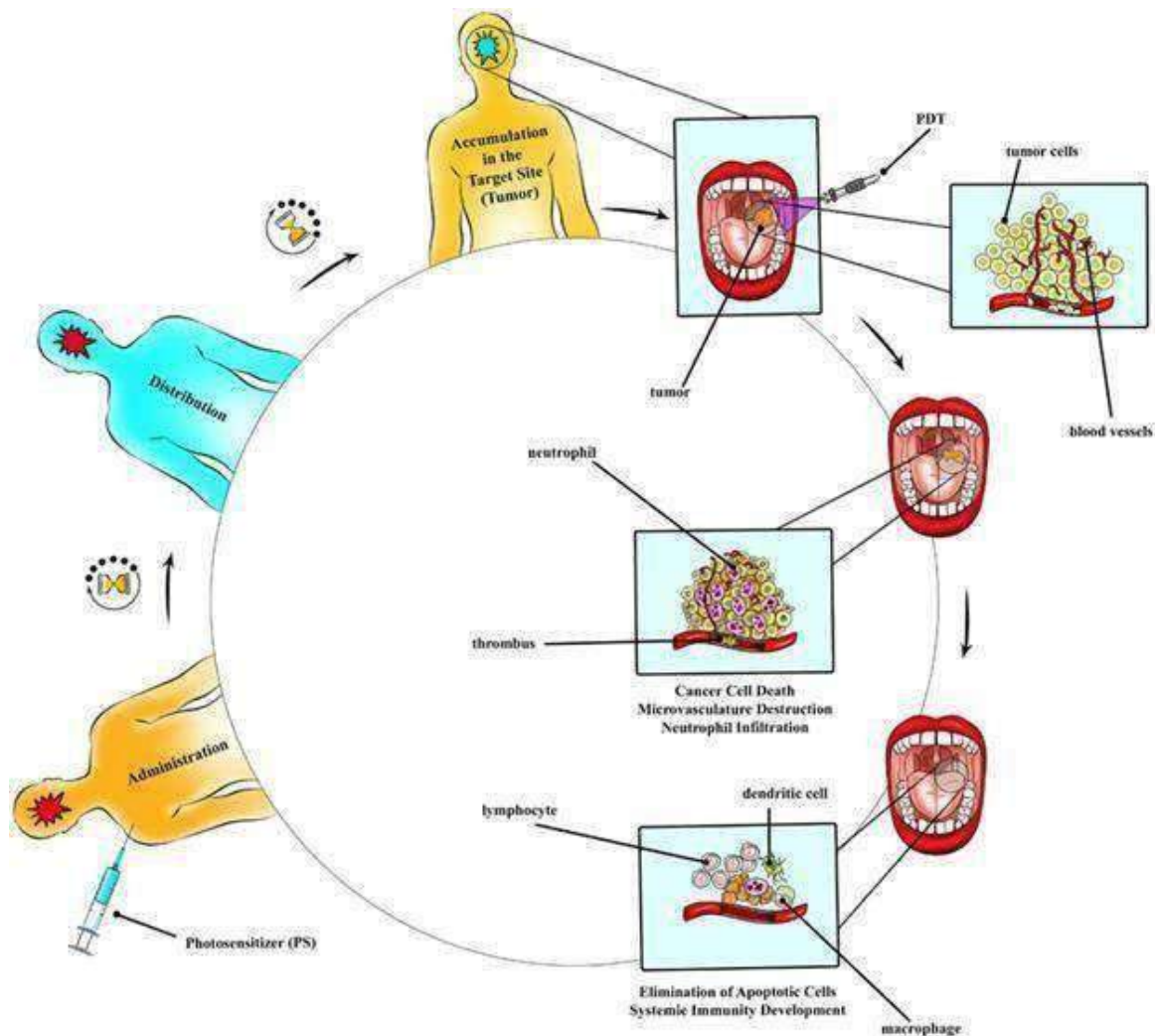
Figure 1.7 The principle of photodynamic therapy (PDT)

1.6.3.1 Mechanism of Reactive Oxygen Species (Ros) Generation in PDT

In PDT, tumors are eradicated by ROS generation, such as superoxide radical ($O_2 \bullet-$), hydroxyl radical ($OH\bullet$), and singlet oxygen ($^1O_2$) species, which are formed by the interaction of oxygen (O_2) and excited PSs. This effect is very localized owing to the short duration and high reactivity of ROS. Figure 1.6 shows a thorough breakdown of the photochemical mechanisms involved in PDT. A PS transitions from its ground state (S0) to the first singlet excited state (S1) or the second

singlet excited state (S2) after absorbing a photon of the proper wavelength. Internal conversion (IC) will cause S2 to decay ($\approx$ fs) fast to S1 (IC). S1 will either cease releasing light (fluorescence) or produce heat throughout the IC process since it is likewise unstable and has a lifespan of ns level. Intersystem crossover (ISC) of S1 may also occur in the meantime to create a more stable excited triplet state (T1). T1 has an extended lifespan ($\approx$ μs) and is capable of undergoing several photochemical processes such as phosphorescent emission and energy transfer to O2 to produce 1O2 (referred to as the type II PDT process). Additionally, T1 may generate radicals by reacting with intracellular substrates such as nucleic acids, proteins, and lipids via an electron transfer process. These radicals can then interact with O2 or H2O to generate additional ROS species like O2 $\bullet-$ and OH$\bullet$. This process falls under the category of type I PDT process. Under the influence of light, semiconductor nanomaterials may produce electron-hole pairs, and the subsequently separated electrons and holes can then interact with O2 or H2O to form O2 $\bullet-$ and OH$\bullet$. Heat-induced ROS production is a novel ROS-generating process that has just been identified (Lan M et al. 2019). Intense heat enhances the thermionic emission of electrons that further interact with the environment to generate ROS (Yang M, Yang T, Mao C 2019). Additionally, it has been shown that certain organic compounds with large π-conjugated structures may store 1O2 via the production of endoperoxide at low temperatures, whereas under hot conditions, the stored 1O2 can be liberated to annihilate cancer cells. It is also widely acknowledged that 1O2 is mostly to blame for the photodynamic destruction of cells and
 biological tissues, which occurs when PSs are employed, and that the majority of PSs now in use operate predominantly via the type II mechanism. However, a significant drawback of therapeutically used PSs, such as those derived from phthalocyanine (Pc) and porphyrin, is that their principal absorption band is in the ultraviolet−visible (UV-vis) region, where tissue receives

a small amount of light (Lucky SS, Soo KC, Zhang Y 2015). Because NIR light may penetrate deeper into normal tissues than UV and visible light and has lower phototoxicity, much work has been put into designing and synthesizing PSs that are activated by NIR light. Meanwhile, the majority of organic PSs with substantial absorbance in the 700−1000 nm region of the spectral region for PDT often exhibit hydrophobic character, leading to an agglomeration state and a decrease in 1O2 production and fluorescence quantum yields in aqueous solution. The two-photon excitation (TPE) method, which makes use of a NIR-pulsed laser as the excitation light source, is a very attractive solution to this problem (Lucky SS, Soo KC, Zhang Y 2015). During TPE PDT, a PS electron is stimulated from its ground state (S0) to an excited electronic state (i.e., S1 or S2) by absorption of two photons with the same frequency, which subsequently kills cancer cells through type I or type II procedure (Figure 1.7). The energy source of ITPE should be a quick (≈ 100 fs) laser pulse with high intensity to accomplish instantaneous absorption. The photon's energy may be lower than the energy difference between the two states, which is typically found in the NIR regime (Jungmann KP 2017). In addition to inheriting the benefits of conventional one-photon excitation (OPE) PDT, this strategy additionally provides the following notable features. TPE PDT may eliminate deeper tumors because NIR lasers can penetrate materials more deeply than visible or UV light. Compared to OPE PDT, TPE PDT provides more precise phototherapy and greater spatial resolution in fluorescence imaging since only the sample located in the laser beam focus may be stimulated (Shen Y et al. 2016). The upconversion nanoparticles (UCNPs) also include rare-earth metals and lanthanide dopants, which may absorb numerous photons owing to the extended lifespan and actual ladder-like energy levels of lanthanide ions, producing high energy anti-Stokes fluorescence in the process. UCNPs have been used in a variety of applications including bioimaging, biosensing, and PDT. Although TPE and UCNPs offer benefits in deep

tumor treatment, developing PSs with the following attributes is still quite difficult: high extinction coefficient in the optical window for PDT, the proper retention period in a live organism, high ROS generation efficiency, and excellent photostability and biocompatibility (Rafique R, Kailasa SK, Park TJ 2019).
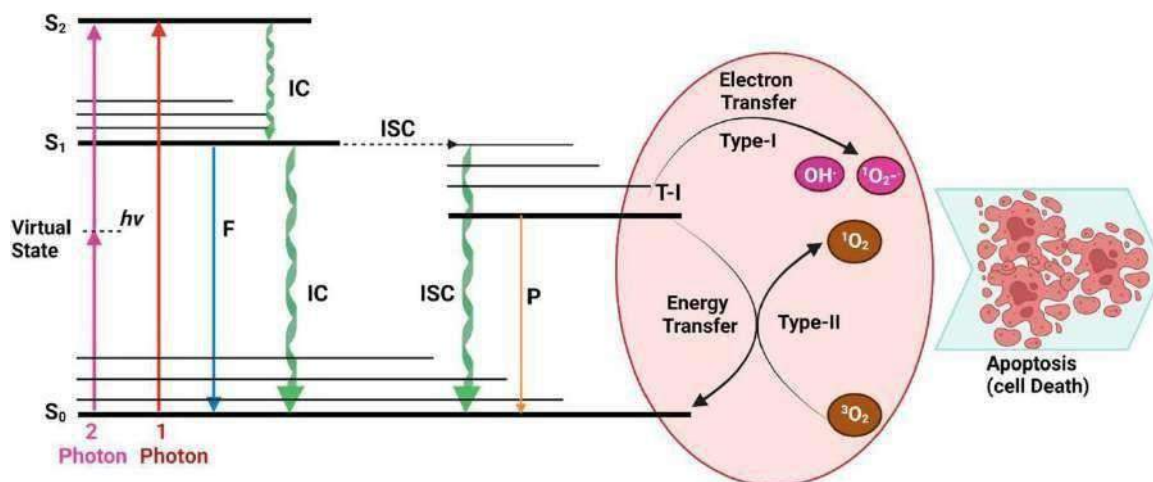
Figure 1.8 Jablonski energy level diagram for PDT.

1.6.3.2 Photosensitizers (PSs)

For PDT therapy to be effective, PS selection is essential. Light with a wavelength (600−700 nm) in the therapeutic window should ideally be used to activate the PS and to achieve maximum penetration. It has low solubility in bodily tissues and shouldn't damage cells in the dark or cause cell death in the absence of light. Additionally, the target cells must specifically capture and/or retain it. Lastly, It must also be capable of causing immunogenic cell death (ICD), which is characterized by changes in the cytosol's structure and the release of signaling molecules that activate T and dendritic cells and promote the development of a targeted immune response against

malignant tumors (Lan M et al. 2019). A few PSs that typically adhere to the above-mentioned requirements have been reviewed below.

1.6.3.3 Methylene Blue (MB)

It is a phenothiazine derivative dye that has both photosensitizing and fluorescent properties. MB is capable of killing cancerous cells, bacteria (in vivo), and viruses (in vitro). Owing to positive charge and low molecular weight of MB, it can interact with human cells and bacteria more favorably. Hence a PS of choice in PDT for cancer and infections. MB can freely traverse across biological membrane due to its net positive charge and hydrophilic/ lipophilic balance. It is widely used PS for antimicrobial PDT in infections caused by Enterococcus faecalis, Candida albicans, and Escherichia coli. The potential of MB in anticancer PDT is particularly intriguing because it is less expensive and more readily available than traditional PSs. MB has been used to study a range of NPs including apoferritin nanocages, polyacrylamide, and silica. Aerosol alginate NPs were fabricated by Khdair et al. to deliver MB and doxorubicin simultaneously for PDT−chemotherapy treatment approach (Khdair A et al. 2010). This approach effectively increased the cytotoxic effect in drug-resistant ovarian cancer cells while avoiding any active targeting domains. In a study, patients with basal cell carcinoma were treated with MB-PDT by Samy et al. where Out of the 17 patients, 11 had a complete recovery with favorable aesthetic results and only a few adverse effects (Samy NA, Salah MM, Ali MF, Sadek AM 2015). Despite of high water solubility of MB, it is rapidly eliminated from the body after intravenous injection because its converted into leucoMB in peripheral tissues and erythrocytes. LeucoMB has no photodynamic/PS activity; hence, it is critical to safeguard MB from peripheral and blood reduction when contemplating IV delivery. Chitosan and PLGA nanoparticles could be used to increase the stability of MB and improve its delivery.

1.6.3.4 Porphyrins

A significant class of PSs includes compounds of porphyrin. A member of this family, photofrin or porfimer sodium, has received clinical approval in the USA for PDT treatment of several premalignant lesions and tumors (Baskaran R, Lee J, Yang SG 2018). Although the present clinical formulation does not use an NP carrier, numerous encouraging preclinical investigations using nanoformulations of porphyrin photosensitizers have been conducted. In a study, Chen et al. delivered pheophorbides (chlorin derivatives) and 5,10,15,20-tetrakis- (m-hydroxyphenyl) porphyrin (mTHPP; a porphyrin derivative) to leukemia cells using human serum albumin NPs (Wacker M et al. 2010). It was discovered that the NPs were shown to be absorbed via lysosomal processes and resulted in around 50% of the cell's death from apoptosis. Several distinct NP systems, including gold NPs, silica, polymeric, chitosan, and metal oxide, have been used to manufacture porphyrin derivatives such as protoporphyrin IX and photofrin (Rabiee N et al. 2020). A few of the formulations have used receptor-mediated active targeting to improve cell-selective delivery, whereas the rest of them have the EPR mechanism being used to passively target solid tumors.

1.6.3.5 Phthalocyanine (Pcs)

Pcs structure can be elucidated as a tetra pyrrole structure consisting of four isoindole rings, where the connecting carbon is replaced by nitrogen atoms. The C−N bonds have similar lengths due to the uniform electron density distribution that provides a stable physicochemical property to the compounds. The molecular structures of phthalocyanine derivatives and cyanine derivatives are shown in Figure 1.8 These compounds intensely absorb the NIR and red light while vaguely absorbing the light of 400−600 nm. Pcs have been fabricated further with diamagnetic ions,

improving the tumor microenvironment's selectivity and inhibition by improvising the cytotoxic singlet oxygen quantum yields (Itoo AM et al. 2021).

1.6.3.6 Cyanine

The general structure of cyanine includes two nitrogen atoms linked by a polymethine chain. These nitrogen atoms are members of any heterocyclic molecule such as pyridine, pyrrole, indole, or imidazole. They exist in the zwitter ionic form and have both cationic and anionic moieties together. Cyanine and its derivatives have become one of the most widely used and researched dyes for chemo- sensors because of their high absorption coefficients, tunable light absorption throughout the visible and NIR regions, high biocompatibility, and relatively low toxicity. Recent studies have demonstrated the use of cyanine compounds as PSs in photodynamic therapies (Allison RR et al. 2004).

1.6.3.7 Chlorins

Bacteriochlorins and chlorins, present in natural substances, strongly absorb light between 640 and 700 nm. For instance, Rhodobacter capsulatus bacteria contain bacteriochlorins, and chlorins may be detected in chlorophyll-a (reported in certain species of Spirulina). Chlorins have a fundamental structural resemblance with porphyrins since they are hydrophilic reduced porphyrins. Numerous chlorin derivatives, such as mono-L-aspartyl chlorin e6 (NPe6), have been investigated for use as PSs. It has two crucial characteristics: a powerful light absorption in the therapeutic window between 650 and 680 nm, as well as a large quantum yield of $1O_2$ (0.70) (Calixto GM et al. 2016). The benzoporphyrin derivative BPDMA and meso-tetrakis (m-hydroxyphenyl) chlorin are two synthetic chlorins that have interesting biological effects. Photodithazine (PDZ) is the brand name of one more PS drug that originates in Russia and is part of the chlorins family. It is derived from the cyanobacterium Spirulina platensis, and its geometry has been amended by the inclusion of N-

methyl- D glucosamine (0.5%) as a stabilizing and solubilizing agent. It is a second-generation PS, and it has minimal to no effect on skin photosensitivity (Itoo AM et al. 2022). Chlorins' ability to cure oral cancer has been well-researched. In a study, Parihar et al. conducted both in vivo and in vitro studies to investigate the efficacy of chlorin-PDT as a potential treatment for oral squamous cell carcinoma. They observed full tumor shrinkage and significant cellular damage within a week of receiving the chlorin-PDT. When it comes to the treatment of lesions in the oral cavity, aqueous solutions are not always the most effective delivery vehicle for administering a PS, although chlorins demonstrate strong stability and water solubility (Calixto GM et al. 2016). In these situations, it is preferable to include the chlorins in a mucoadhesive delivery method. It prolongs the dosage form's duration at the absorption site and enhances the results. As an important category of PSs, chlorins have a chemical structure that is analogous to that of chlorophyll. The PS chlorin e6 (Ce6), which has been investigated for use in a variety of nano-based drug delivery systems, has the highest volume of clinical applications among the drugs in this category including hyaluronic acid, iron oxide, silica, human serum albumin, chitosan, and a variety of polymeric NPs. These chlorin-loaded NPs were mainly developed to exploit EPR-based passive targeting mechanisms in various cancers including those of the breast, colon, and cervical regions. Conversely, active receptor-mediated targeting has also been employed in a couple of these strategies. In a study, Benachour et al. developed silica NPs loaded with a targeting peptide neuropilin-I and 5-(4-carboxyphenyl)- 10,15,20-triphenylchlorin (TPC) to attack tumor angiogenic vasculature and accomplish near-complete cell killing in vitro (Wang C, Tao H, Cheng L, Liu Z 2011). Similarly, Yoon et al. designed CD44 tumor-targeting hyaluronic acid NPs (HANPs) to deliver Ce6 and accomplish almost 100% cell killing in two distinct human colon cancer cell lines (Yoon HY et al. 2012). In addition, Li et al. employed folate receptor targeting on

pheophorbide A-loaded heparin NPs for administration to cervical cancer (Li L et al. 2011). The primary emphasis of recent research using chlorin-based nano formulations has been on the development of NPs with the dual purpose of imaging and photodynamic treatment. For instance, concurrent PDT and magnetic resonance imaging of stomach cancer were performed by Huang et al. using Ce6-coupled magnetic NPs (Huang P et al. 2011). Another new nano vehicle preparation of chlorins involves a novel platform known as "up conversion NPs." This formulation of chlorins has been researched by a few different groups for PDT for breast, cervical, and glioma malignancies. Up conversion is a process that involves the successive absorption of numerous photons, which may then result in the emission of light at wavelengths that are shorter than the excitation wavelength. Typically, the excitation occurs in the infrared range, and the resulting emission occurs in the visible range. If up conversion components, such as rare earth metals like Er3+, are manufactured together with PSs inside the same vehicle, the produced light has the potential to activate the PS. As a result, this strategy has the potential to hold great promise in terms of tackling the issues associated with assuring light transmission in vivo (Cheng L, Wang C, Liu Z 2013).

1.6.4 Limitations of conventional cancer therapy

Traditional chemotherapy protocols remain a cornerstone in treating diverse cancers, either as standalone therapies or combined with other treatment approaches. However, these strategies face several limitations, as outlined below.

1.6.4.1 Limited aqueous solubility: The majority of anticancer medications have low water solubility, necessitating the use of solvents to create their dosage forms. This limitation often leads to low bioavailability, demanding frequent and high doses to attain therapeutic levels. For

intravenous administration, these agents need to be solubilized in aqueous media to remain within the biological system (Chidambaram M et al. 2011).

1.6.4.2 Lack of selectivity of anti-cancer agents: Conventional chemotherapeutic agents, when administered intravenously, circulate through the bloodstream, reaching both cancerous and healthy cells. These treatments often result in undesired toxicities due to their widespread distribution throughout the body, leading to significant side effects such as bone marrow suppression, systemic toxicity, anemia, hair loss, weight loss, nausea, diarrhea, infertility, cardiovascular issues, vomiting, and more. Moreover, the development of drug resistance to these single-agent therapies poses an additional challenge. Traditional chemotherapy lacks specificity in its mode of action as most anticancer drugs target mechanisms common to both normal and cancerous cells, rather than exclusively affecting cancer cells (Chidambaram M et al. 2011), (Greish K. 2010).

1.6.4.3 Uptake by the reticuloendothelial system (RES): The reticuloendothelial system, comprised of macrophages and monocytes within the reticular connective tissue, swiftly eliminates hydrophobic agents from the bloodstream. Its function involves phagocytosis, clearing cell debris, foreign substances, and pathogens from circulation. Given that many chemotherapeutic agents are hydrophobic, they become engulfed by the RES, leading to rapid clearance from the blood. Consequently, higher drug concentrations are required to achieve therapeutic levels at the intended site. The characteristics of the delivery system, such as its hydrophobicity, particle size, and surface charge, significantly impact its uptake by the RES (Greish K. 2010).

1.6.4.4 Multiple drug resistance (MDR): A significant challenge in traditional chemotherapy is the development of drug resistance within cells, which can arise from various mechanisms. Cellular resistance involves a plasma membrane protein known as P-glycoprotein (P-gp),

responsible for expelling drugs from the cell, hindering the accumulation of therapeutic agents within the cell. P-gp, a prominent efflux protein belonging to the ATP-binding cassette (ABC) transporter family, plays a key role in this process (Stavrovskaya AA, Rybalkina EY 2018)

1.6.4.5 Poor vascularization: The tumor environment significantly hinders drug accumulation within cancerous tissues due to poor vascularization, resulting in reduced drug efficacy. In acidic tumor environments, certain basic medications become ionized, impeding their passage through cell membranes. Additionally, high interstitial pressure and low microvascular pressure can restrict the extravasation of drug molecules. Alongside drug efflux pumps, cancer cells employ various mechanisms for drug resistance, including reduced drug uptake, heightened metabolism, modification of drug targets, disruption of apoptotic pathways, and interference with cell cycle checkpoints (Cameron AC, Touyz RM, Lang NN 2016).
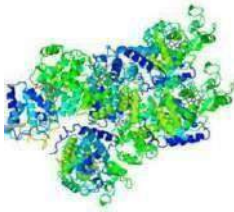
Effective cancer chemotherapy necessitates delivering the appropriate drug amount in a controlled manner for the required duration to the tumor while minimizing damage to normal cells. Achieving this goal involves a drug delivery system that not only maintains the necessary drug levels but also circumvents challenges such as drug resistance, non-specific toxicities, rapid clearance, poor bioavailability, and unfavorable biodistribution. Therefore, an ideal drug delivery system should circulate in the bloodstream for extended periods, exhibit tumor specificity, enhance drug accumulation in tumors, and enable modified drug release to maximize therapeutic efficacy (Biswas AK et al. 2014; Bhatia S 2016).
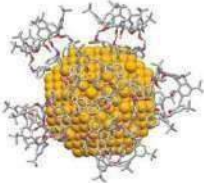
 Nanoparticles (NPs) have emerged as a promising solution in cancer therapy by overcoming limitations of conventional chemotherapy. Their nano-sized range, extensive surface area, and surface customization significantly influence in vivo biodistribution. Utilizing various materials like lipids, polymers, inorganic substances, and biological compounds, NPs can be formed and

engineered to co- deliver medications and imaging probes to targeted tissues (Kanwal U et al. 2018).

These NPs have shown promise in improving drug solubility, stability, circulation time, and targeting specific cells while reducing off-target effects. They hold potential for combination therapies by combining chemotherapeutic and photothermal effects or creating magnetic nanostructures for facilitated delivery under external magnetic fields (Torchilin VP 2012). Moreover, targeted nanocarriers have demonstrated enhanced drug uptake in cancer cells without causing harm to normal cells, presenting an avenue for more efficient drug/gene delivery and overcoming many issues associated with traditional chemotherapy.

Table 1.1: Nanoparticulate drug delivery system for chemotherapy

	Nanostructure	Drug	Advantages of nanoformulation	Indication	Company/approval year
Lipid based nanoparticles	Ameluz	5-aminolevulinicacid	sustaine drelease ↓ toxicity	Superficial and/or nodular basal cell carcinoma	Biofrontera Bioscience GmbH,EMA (2011)
	Marqibo	Vincristine	↑ blood circulation time ↑ tumor uptake (EPR) ↓ toxicity	Acute lymphoid leukaemia	Spectrum, FDA(2012)
	Onivyde	Irinotecan	↑ blood circulation time ↑ tumor uptake (EPR) ↓ toxicity	Pancreati cCancer, Colorect alCancer	Merrimack, FDA (2015)
	Vyxeos	Daunorubicin Cytarabine	↑ blood circulation time, ↑ accumulation in bone marrow	Acute myeloid leukaemia	Jazz Pharmaceuticals,EMA (2018)
Protein-drug conjugates	Abraxane	Paclitaxel	↑ Solubility ↑ blood circulation time ↑ tumor uptake (EPR) ↓ severe toxicity	Breast Cancer, Non-small lung Cancer, Pancreatic Cancer	American Biosciencem, Inc.,FDA (2005)
	Kadcyla	DM1 (or Emtansine)	↑ blood circulation time ↑ tumor uptake (EPR) ↑ selectivity ↓ toxicity	HER2+ breast Cancer	Roche Genentech, EMA(2013) FDA (2013)
	Pazenir	Paclitaxel	↑ Solubility ↑ blood circulation time ↑ tumor uptake (EPR) ↓ severe toxicity	Metastatic breast Cancer, metastatic adenocarcino maof the pancreas, non-small celllung Cancer	Ratiopharm GmbH, EMA (2019)

Metallic nanoparticles	NanoTherm	Fe_2O_3	↑ blood circulation time ↑ tumor uptake (EPR) -heat production under stimulation with EMF -teranostic properties	Glioblastoma, prostate, and pancreatic Ca.	Magforce, EMA (2013)
Micelles	Genexol PM	Paclitaxel	↑ drug loading and retention time	Breast, lung and ovarian cancers	Samyang Co., Seoul, Korea (2007)
	SP1049C	doxorubicin	↑ drug loading and retention time	Gastrointestinal cancer	US-FDA
	Nanoxel	Paclitaxel	Better safety profiles	NSCLC, ovarian cancer, and Kaposi's sarcoma	US-FDA
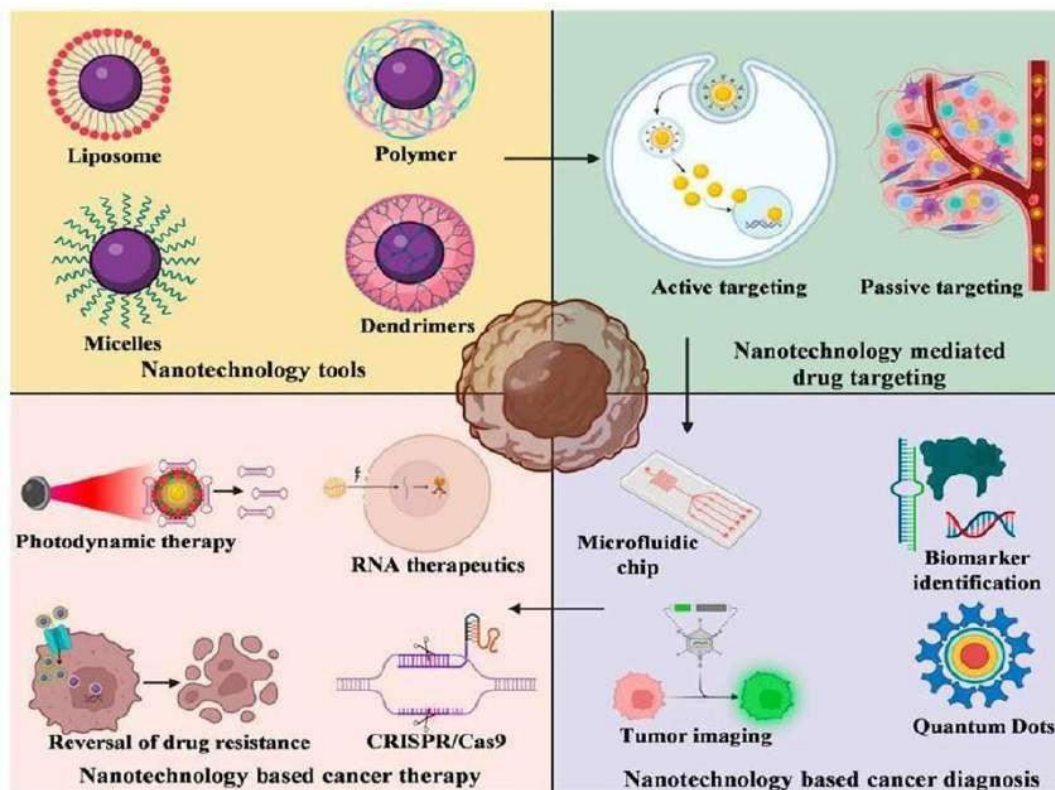
Figure 1.9: Schematic representation of different types of nanomaterials used in cancer therapy, along with key physical characteristics and surface chemistry required to transport drugs (Navya et al. 2019).

Advantages of nanoparticle drug delivery systems Nanoparticular drug delivery systems offer distinct advantages for cancer therapy over free drug administration such as (Saha RN et al. 2010):

• Improving the therapeutic index of the loaded chemotherapeutic agents compared to the drugs delivered via conventional dosage forms.

• Increasing drug efficacy by achieving steady state therapeutic levels of drugs over an extended period.

• Lowering drug toxicity due to controlled drug release and improving t h e drug's pharmacokinetics by increasing the drug's solubility and stability.

The development of nanotechnology-based formulations that improve drug pharmacokinetic parameters enables the resumption of research into potentially fruitful new chemical entities that were impeded during pre-clinical or clinical development due to their sub optimal pharmacokinetic or biochemical properties.

1.7 Targeted drug delivery systems (TDDS)

Traditional methods of tumor treatment often involve intravenous injections or oral administration. However, once drug molecules enter the systemic circulation, they are quickly eliminated from the body, resulting in low drug bioavailability and undesirable side effects. To mitigate these issues and efficiently target tumor sites, surface functionalization of nanocarriers or drugs with proteins, nucleic acids, enzymes, receptors, and other functional biological molecules is a commonly

employed strategy. Targeting drugs generally falls into two major categories: passive targeting and active targeting.

1.7.1 Passive targeting

Passive targeting operates through specific tissue pathophysiological traits that enable nanocarriers to remain in the targeted area and release drugs without relying on external stimuli or ligands (Kumari P, Ghosh B, Biswas S 2016) (Figure 1.10). The Enhanced Permeability and Retention (EPR) effect, a common characteristic in tumor pathophysiology, drives the targeted delivery of anticancer therapy using nanocarriers (Nakamura H, Jun F, Maeda H 2015). Tumors often feature poorly structured blood vessels with heightened permeability, facilitating the influx of nutrients and oxygen for rapid growth. The EPR effect allows macromolecules over 40 KDa to extravasate from tumor vessels into the interstitial space, leading to their accumulation. Conversely, normal endothelial cells' tight junctions restrict this extravasation. Consequently, the EPR effect holds promise for targeted drug delivery in anticancer treatments. Doxil®, a doxorubicin-loaded liposomal formulation, relies on passive targeting and is utilized in clinics for Kaposi sarcoma treatment, while numerous other nanomedicines using the EPR effect are undergoing clinical and pre-clinical studies (Green AE, Rose PG 2006).

Despite the successes of EPR effect-based anticancer drug delivery via nanocarriers, this approach encounters hurdles in effectively delivering drugs to tumors. First, interstitial fluid pressure poses a significant barrier by hindering nanocarriers from penetrating tissues. Tumor growth escalates fluid pressure due to plasma fluid and protein leakage from capillaries, creating colloidal pressure that prevents macromolecules in the bloodstream from entering. Second, fast-growing tumor cells compress lymphatic vessels, impeding interstitial fluid drainage and elevating fluid pressure. Third, tumor tissue heterogeneity is another challenge. The tumor's central region, primarily

composed of tumor stem cells, accumulates fewer nanocarriers compared to the rest of the tumor. This necrotic and poorly vascularized central area limits vascular leakage and impedes drug entry via the EPR effect (Danhier F, Feron O, Préat V 2010).
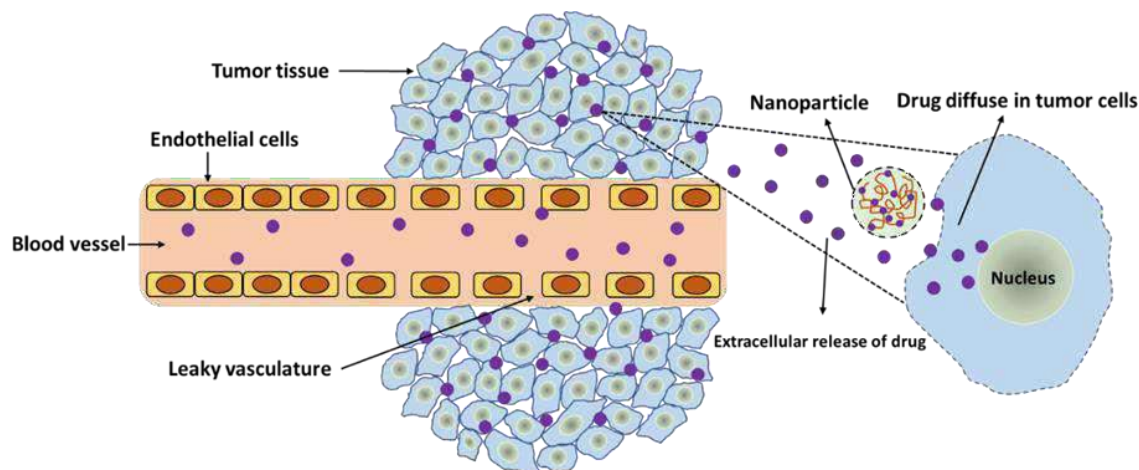
Figure 1.10: Schematic representation of the passively targeting drug delivery system and the EPR effect. Nanoparticles passively extravasate through the leaky vasculature and accumulate in tumors due to the damaged lymphatic drainage

1.7.2   Active targeting

In active targeting, molecular recognition processes guide the attachment of a homing moiety, such as a ligand or monoclonal antibody, to direct drug delivery to specific sites or bypass biological barriers. This method involves ligand-mediated or antibody (Ab)-mediated guidance of nanocarriers to cancer cells (Figure 1.11). Ligand-mediated targeting of nanocarriers significantly improves the drug's therapeutic potential by enhancing its effectiveness and reducing non-specific toxicity. Various targeting ligands—surface modifiers for nanocarriers—include proteins

(antibodies or antibody fragments), peptides (e.g., arginine-glycine-aspartic acid or RGD), vitamins (like folic acid), nucleic acids (aptamers), and glycoproteins (such as transferrin), which are extensively explored for cancer- targeted nanocarrier development (Torchilin VP 2010).

The efficacy of cytotoxic drugs against tumors can be boosted by creating intelligent nanocarriers that proficiently deliver chemotherapeutic drugs to the cytoplasm, triggered by diverse endogenous factors (pH, redox reactions, etc.) or exogenous stimuli (temperature, light, ultrasound, magnetic fields, etc.). Consequently, actively targeted nano systems have garnered more attention due to their superior performance compared to non-targeted nano systems, exhibiting enhanced cytotoxicity toward tumor cells while minimizing side effects.
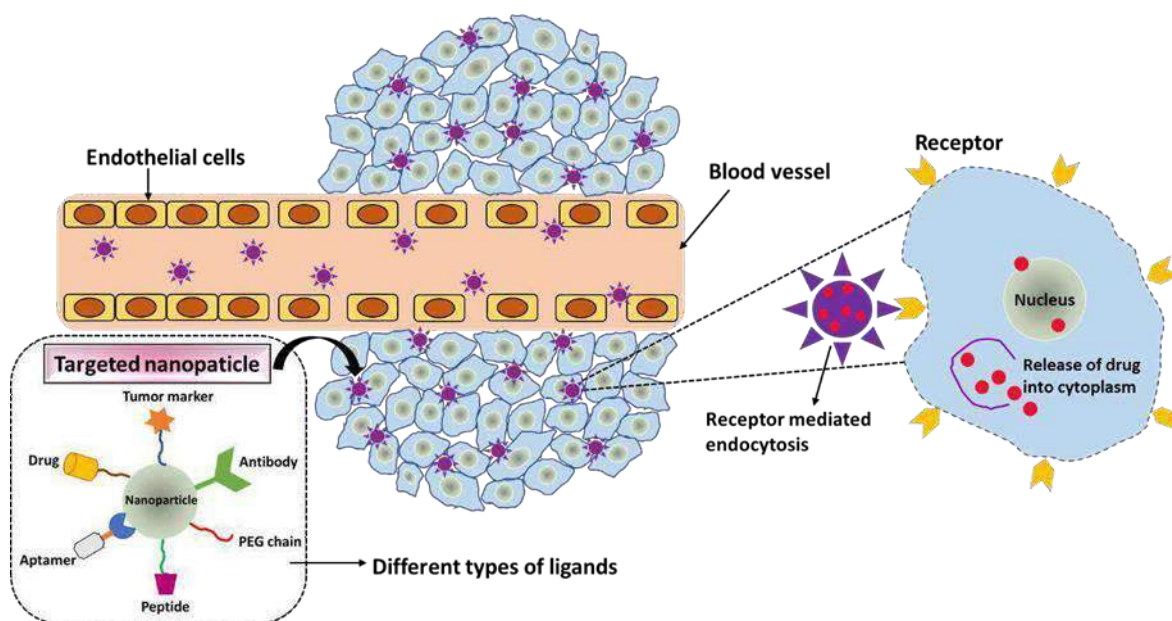
Figure 1.11: Schematic representation of the actively targeting drug delivery system. Targeting ligands grafted on the surface of nanocarriers bind to receptors overexpressed by tumor cells and facilitate internalization via receptor-mediated endocytosis.

1.8 Polymeric micelles as drug delivery system

Polymeric micelles are nanoscale drug delivery systems with a core-shell structure formed by the self- assembly of amphiphilic block copolymers in aqueous solution. Amphiphilic molecules exist independently in diluted aqueous solution, and amphiphiles operate as surfactants, lowering the surface tension at the air-water interface (Ghosh B, Biswas S 2021). As more chains are introduced to the system, the adsorption at the interface increases until unimers aggregation occurs due to the saturation of the bulk solution. The critical micellar concentration (CMC) is attained at this moment. As a result, the parameter is defined as the lowest concentration of polymers in solution that leads to the formation of micelles. According to this, micelles are stable at polymeric chain concentrations greater than the CMC, but the system disassembles after dilution below the CMC. The most important factor in assessing the thermodynamic stability of micelles is the CMC value. Above the CMC, the equilibrium is dynamic, with a constant interchange of unimers between the micelle and the bulk phase. In addition to thermodynamic stability, another important metric is kinetic stability, which measures the likelihood of micelles disassembling over time when the solution is diluted below the CMC (Oerlemans C et al. 2010).

Better kinetic stability and a lower CMC are the main advantages of polymeric micelles over low MW surfactant micelles. Indeed, disassembly happens in the range of microseconds for low MW surfactant micelles, but polymeric micelles retain their structure for significantly longer timeframes (Figure 1.12). Because polymeric micelles have better kinetic stability and less toxicity than low molecular weight surfactant-composed micelles, they are preferred as drug delivery vehicles (Majumder N, G Das N, Das SK 2020).

Amphiphilic di-block copolymers (e.g., polystyrene and poly (ethylene glycol)) and triblock copolymers (e.g., poloxamers) are the most often employed polymers for micelle formation, although graft (e.g., G-chitosan) and ionic (e.g., poly (ethylene glycol)-poly(-caprolactone)-g-

polyethyleneimine) are also used. The hydrophilic segment is typically composed of PEG (polyethyleneglycol), but other polymers such as poly (vinyl pyrrolidone), poly(acryloyl morpholine), or poly (trimethylene carbonate) are also used; the hydrophobic segment can be composed of poly (propylene oxide), polyesters such as poly(-caprolactone), or polymers and co-polymers of glycolic and lactic acid (Ghezzi M et al. 2021).

Depending on the preparation technique and the physicochemical properties of the medication, drugs can be encapsulated in the micelles during their formation or in a subsequent phase. Direct dissolution is the simplest way of preparation; additional processes include dialysis, emulsion with solvent (or co-solvent) evaporation, and solution-casting followed by film hydration. Method selection depends on both polymer and drug properties. Given that micelle features such as polarity and hydration degree are not uniform inside the carrier, the drug can be housed in a variety of locations, such as the surface or the inner core, based on its qualities. Hydrophobic drugs are often loaded and hosted in the inner core. In some cases, the drugs can also be covalently bonded to the polymer (polymer-drug conjugate) (Elzoghby AO, Samy WM, Elgindy NA 2012).
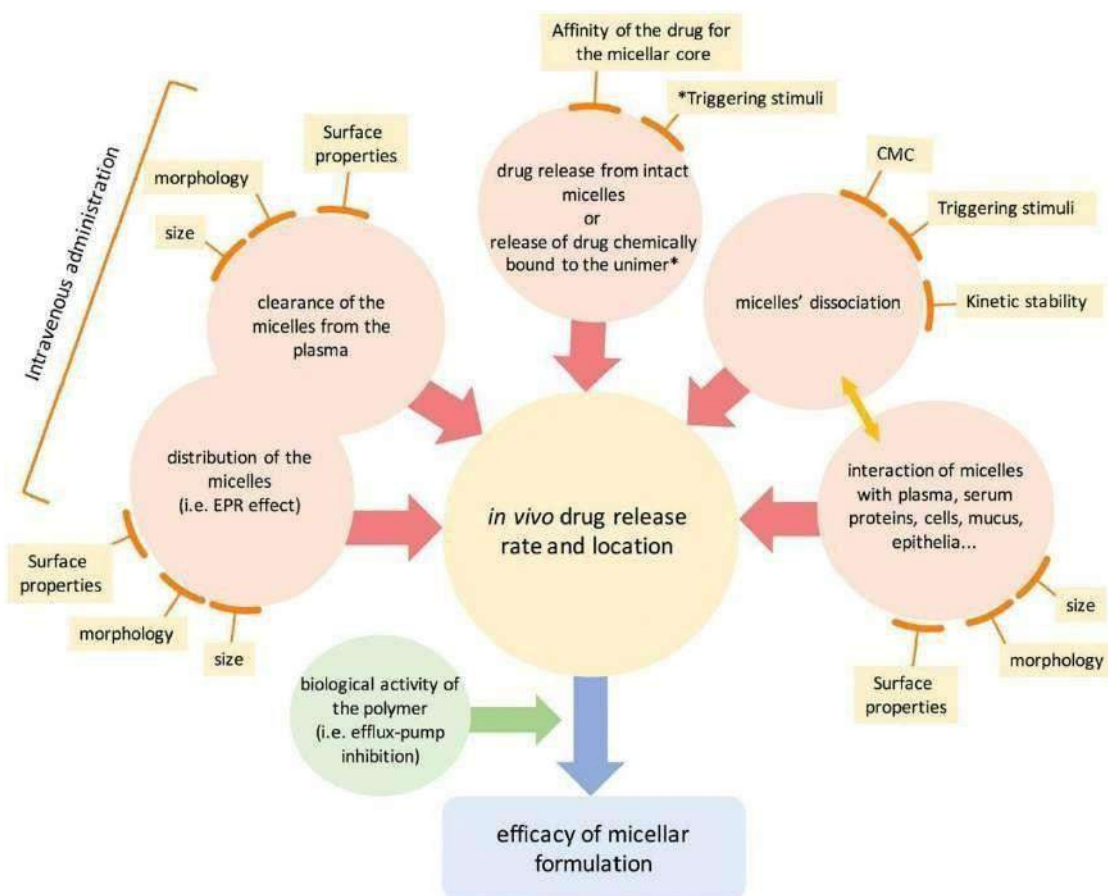
Figure 1.12: Schematic representation of the processes governing in vivo drug distribution from polymeric micelles, in terms of both rate and location. The characteristics of the micelles influencing these phenomena are also shown, as well as the potential impact of the constitutingblock- copolymer on the effectiveness.

1.8 Albumin based nanocarriers

Human serum albumin (HSA) is a globular plasma protein with a molecular weight of 66,500Dalton and a total of 585 amino acids. It is produced by the liver and has a half-life of around 19 days. HSA is a heart-shaped molecule consisting of three homologous domains. It is

stable against a wide range of factors including temperature, pH (4-9), and organic solvents. The albumin-based nanocarriers are one of the most efficient drug delivery vehicles, which use serum albumin as the carrier materials to encapsulate or conjugate the chemotherapeutic agents for tumor-targeted drug delivery (Elzoghby AO, Samy WM, Elgindy NA 2012). The albumin-bound formulation of paclitaxel (Abraxane) is composed of the combination of paclitaxel molecule and human serum albumin through hydrophobic interactions, which has already been approved by the United States Food and Drug Administration (FDA) for clinical treatment of metastatic breast cancer in 2005 (Desai N. 2016). The most abundant protein in plasma is serum albumin, which is important for regulating plasma colloidal osmotic pressure and transporting endogenous compounds. It has many advantages, including non- immunogenicity, nontoxicity, good biocompatibility, and high stability, making it an ideal candidate for drug delivery vehicle preparation, and loading chemotherapy drugs, hypoglycemic drugs, anti- inflammatory drugs, photosensitizers, photothermal agents, and a variety of other drugs. Serum albumin has both hydrophobic and hydrophilic domains, as well as a high number of functional groups, which makes it ideal for drug loading and functional modification (Hassanin I, Elzoghby A 2020).

Moreover, serum albumin can accumulate in tumor tissues or inflammatory areas. The accumulation of serum albumin in tumors is attributed to the efficient interaction of albumin with gp60 receptor (a glycoprotein with molecular weight of 60 kDa), a vascular endothelial membrane protein, and SPARC (secreted protein, acidic and rich in cysteine), an extracellular matrix glycoprotein that is overexpressed in a variety of tumors, which play a pivotal role in the transcytosis of albumin and promote the local concentration of the therapeutic agent-loaded albumin-based nano vehicles in tumors (Shen X et al. 2021).

1.9 Combination therapy against cancer

 In 1965, the concept of combination treatment was established for the first time (Moxley III etal. 1967; Falzone, Salomone, and Libra 2018). Since then, the effectiveness of this combined therapy strategy has dramatically altered the clinical oncology landscape. As a result, most cancer research has focused on studying combination therapies that target different pathways to provide beneficial anticancer activity. Combinational anticancer treatments can be combined with other targeted therapies or chemotherapeutic agents that have greatly expanded as a result of targeted therapies. A cornerstone of cancer therapy is the combination of two or more therapeutic agents to selectively target cancer-inducing or cell-sustaining pathways (Mokhtari RB et al. 2017). Although monotherapy is still a common treatment option for various forms of cancer, it is usually thought to be less successful than combination therapy. Traditional mono-therapeutic approaches target actively proliferating cells non-selectively, resulting in the death of both healthy and malignant cells. Chemotherapy can cause toxicity to patients with multiple side effects. It can also weaken a patient's immune system by affecting bone marrow cells and increasing vulnerability to host diseases. Although combination therapy can be toxic when one of the active ingredients used is a chemotherapy drug, the toxicity is significantly lower because different pathways are being targeted. Finally, this acts synergistically or additively, which is why a lower therapeutic dose of each drug is required. In addition, the combination therapy can prevent toxic effects on normal cells while producing cytotoxic effects on cancer cells (Bailly C, Thuru X, Quesnel B 2020). This can occur when one drug in the combination treatment is antagonistic to another drug in terms of cytotoxicity on normal cells, essentially protecting normal cells from cytotoxic effects.

For several reasons, the combination of cancer therapies is clinically attractive (Figure 1.10). First, combination therapy enhances treatment outcomes and produces greater therapeutic effects,

particularly when synergistic anticancer activity is achieved. Second, the combinatorial strategy reduces clonal heterogeneity, which is further associated with improved response rates. Third, combination therapies decrease therapy toxicity by allowing single drugs to be used in lower doses with sustained therapeutic efficacy. Another benefit of combination therapies is the reduction in the development of drug resistance (Bailly C, Thuru X, Quesnel B 2020). In this context, combination therapy allows for the simultaneous targeting of multiple molecular pathways essential for cancer cell survival and abrogates cellular mechanisms associated with adaptive resistance.
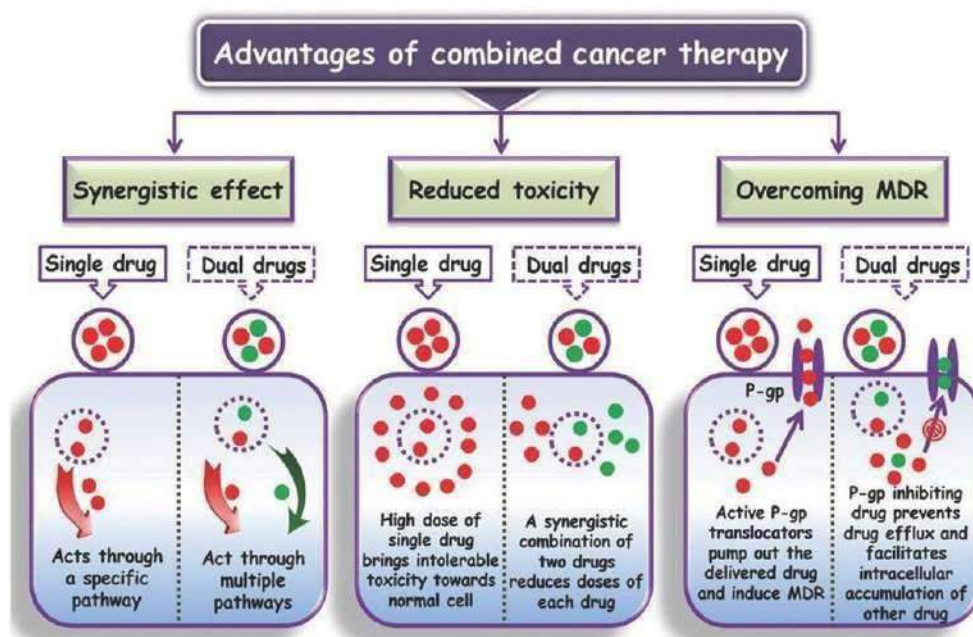
Figure 1.13: Advantages of combination therapy (Soni 2017)

1.10   Paclitaxel as anticancer agent

Paclitaxel is one of the most potent and effective chemotherapeutic drug which is active against a broad range of cancers like lung carcinoma, ovarian, and breast carcinoma (Ma P, Mumper RJ 2013). The PTX promotes and stabilizes microtubules and inhibits late G2 or M phases of cell cycle which results into the cell death (Singh S, Dash AK 2009). Paclitaxel (PTX), a white crystalline powder, was isolated from the bark of Pacific Yew tree Taxus brevifolia by Mrs. Monroe E. Wall and Mansukh C. Wani firstly (Sharifi-Rad J et al. 2021). The PTX also induces cellular processes which lead to programmed cell death. There are many genes e.g. Bcl-2 which are responsible in the regulation of the apoptotic pathways modulated by post- translational phosphorylation thereby targeting the microtubules. Although PTX has massive therapeutic potential, it suffers serious drawbacks of poor aqueous solubility, lack of cancer specificity, and substrate to P-gp efflux proteins (Fauzee NJ, Dong Z, Wang YL 2011). The low solubility problem was overcome by developing the PTX formulations based on Cremophor EL (e.g. Taxol®) and administered via slow intravenous infusion following dilution with normal saline (0.9% NaCl) or dextrose (5%) solutions. Nevertheless, the Taxol® shows serious side effects such as brain toxicity and kidney toxicity because of the excipient Cremophor EL which was used to solubilize PTX (Wang F et al. 2017). Therefore, Cremophor EL-free formulations of PTX have been investigated and numerous attempts were carried out to enhance its therapeutic potential by incorporating the PTX in different nanocarriers.

The various attempts were reported to enhance the solubility and efficacy of PTX. For example, PTX is encapsulated in PLA-b-mPEG diblock co-polymers (Paxceed®) which forms micelles with water. Presently, Paxceed® is in phase II clinical trials (Ehrlich et al. 2004). In 2005, Albumin-bound PTX- NPs (Abraxane®) was approved by US FDA to treat patients of metastatic breast

cancer who fail other chemotherapy or relapse and to treat non-small cell lung cancer approved in October 2012 (Mustafa G et al. 2023). Another micellar formulation is based on the co-polymer of PEG and polyaspartate (NK 105) by incorporating the PTX into the core of the micelles via hydrophobic interaction which is in phase III clinical trials. The most promising poly (L-glutamic acid)-PTX conjugate (CT-2103) was developed where PG is conjugated to 2′-OH position of PTX via an ester linker which is in phaseIII clinical studies currently (Singer JW et al. 2003). A PTX-Angiopep-2 conjugate (ANG 1005)is a novel drug-peptide conjugate, which consists of three PTX molecules conjugated to one molecule of an Angiopep-2 thereby targeting low-density lipoprotein receptor- related protein 1 (LRP1) receptor to facilitate PTX delivery across blood brain barrier for the treatment of brain cancer. The ANG 1005 is in phase II clinical trials recently (Regina A et al. 2008).

1.10.1 Physicochemical properties of paclitaxel

Paclitaxel ($C_{47}H_{51}NO_{14}$; molecular weight: 853.9 g/mol), is a cyclodecane derivative isolated from the bark of the Pacific yew tree, Taxus brevifolia and other Taxus spp. Sold under the brand name Taxol®, it is a fine, white to off-white crystalline powder which is poorly soluble in water. Paclitaxel is soluble in alcohols (methanol: 50mg/ml;ethanol: 1.5mg/ml) and DMSO (50mg/ml). Paclitaxel is rapidly degraded in weakly alkaline, aqueous solutions with minimum degradation observed between pH 3–5.

Paclitaxel melts at 213°C and has a logP~3, with the UV absorption maxima at 227 nm.The chemical structure of paclitaxel is shown in Figure 1.14. It has 4 hydrogen bond donors and 14 hydrogen bond acceptors ("National Center for Biotechnology Information, PubChem Compound Database; CID=36314").
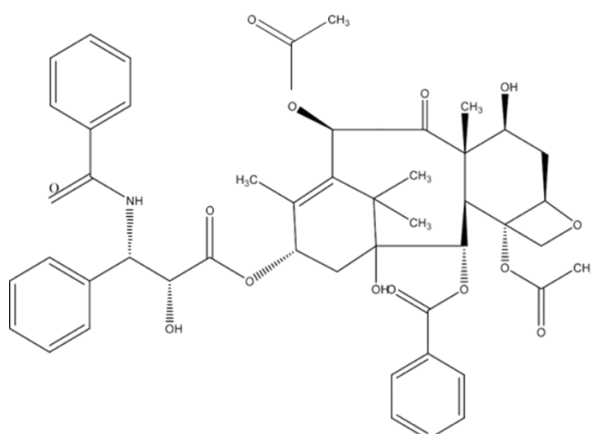
Figure 1.14: Chemical structure of Paclitaxel

IUPAC name: [4,12-diacetyloxy-15- (3-benzamido-2-hydroxy-3 phenylpropanoyl) oxy-1,9 dihydroxy-10,14,17,17-tetramethyl-11-oxo-6 oxatetracyclo [11.3.1.03,10.04,7] heptadec-13-en-2-yl] benzoate

1.11 Cisplatin

Cisplatin, scientifically recognized as cis-diamminedichloroplatinum(II), represents a pivotal platinum-based chemotherapy agent characterized by its square planar geometry. It was first synthesized in 1844 and its chemical structure was first elucidated by alifred werner in 1893. However, the true breakthrough occurred in the 1960s when Rosenberg et al. observed its remarkable ability to inhibit cell division in Escherichia coli. Cisplatin, found to be the key substance, became a crucial part of treating germ cell cancer throughout the body. It got approval from the FDA in 1978 (Dasari S, Tchounwou PB 2014).

Cisplatin demonstrates anticancer activity against various tumors, including ovarian, testicular, and solid tumors in the head and neck. Despite its efficacy, challenges persist due to drug resistance and side effects. To address these issues, researchers have adopted combination therapy with other

cancer drugs, introducing a novel strategy for enhancing treatment outcomes. The combination of paclitaxel, cisplatin, and fluorouracil has been found to be effective and well-tolerated in both first-line and second-line treatments in patients with advanced gastric and esophagogastric junction adenocarcinoma (Sun Q et al. 2009). Another successful combination includes oral UFT (tegafur and uracil) with cisplatin, proven to be effective in treating advanced non-small cell lung carcinoma (Surmont V et al. 2009). Encouraging results were observed in the combination chemotherapy of cyclophosphamide, doxorubicin, and cisplatin for advanced carcinomas originating from salivary glands (Sahara S, Herzog AE, Nör JE 2021)

1.11.1 Physicochemical properties of Cisplatin

Cisplatin possesses a molecular weight of 301.1 g/mol, a density of 3.74 g/cm3, and a melting point of 270 °C. It presents as a white or deep yellow crystalline powder, with slight solubility in water and solubility in dimethylprimanide and N,N-dimethylformamide. While stable under standard conditions, cisplatin can gradually transform into the trans-isomer over time. This inorganic and water-soluble platinum complex, following hydrolysis, interacts with DNA, forming intra and interstrand crosslinks. These crosslinks impede DNA replication and transcription, contributing to the cytotoxicity of cisplatin, which is associated with cellular arrest in the G2 phase of the cell cycle (Dasari S, Tchounwou PB 2014).
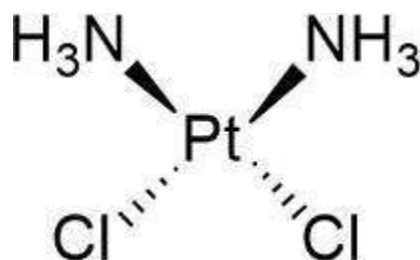
Figure 1.15: Chemical structure of cisplatin

IUPAC name: (SP-4-2)-diamminedichloridoplatinum(II)

1.12 Objectives

Our aim for the study is to develop nanomedical combination chemotherapy with superior efficacy compared to conventional therapy or monotherapies. We have adopted the strategy off abricating prodrug vehicles capable of incorporating a hydrophobic anticancer drug to achieve the goal. The following are the specific aim.

Objective 1: Utilizing Pluronic F127 micelles loaded with chlorin e6 for targeted photodynamic therapy in the treatment of metastatic melanoma

Specific aims:

(i) To prepare and optimize the doxorubicin-loaded micelles.

(ii) To characterize the micelles Zeta analysis, DSC, XRD, andencapsulation efficiency.

(iii) To evaluate the synthesized micelles in vitro in cancer cells.

(iv) To evaluate the efficacy of the targeted micellar formulations against 3D spheroids.

(v) To perform in vivo pharmacokinetic studies using wistar rats.

Objective 2: Concurrent Delivery of Paclitaxel and Chlorin e6 to Tumors Using Albumin/PLGA Nanoparticles for NIR Light-Triggered Chemo/ Photodynamic Therapy

Specific aims:

(i) To prepare Ce6/PTX coloaded PLGA nanoparticles.

(ii) To perform the physicochemical characterization of the nanoparticles , particle size, zeta potential, encapsulation efficiency, drug loading, FTIR, XRD, SEM, and GPCanalysis.

(iii) To evaluate nanoparticles in vitro against the cancer cells monolayers and 3D spheroids.

(iv) To perform in vivo pharmacokinetic studies using wistar rats.

(v) To evaluate the therapeutic efficacy of the nanoparticles in tumor-bearing mice.

Objective 3: Hypoxia alleviating platinum (IV)/chlorin e6-based combination chemotherapeutic-photodynamic nanomedicine for oropharyngeal carcinoma.

Specific aims:

(i) To synthesize Ce6-Pt(iv) conjugated mPEG-PLA micelles

(ii) To perform the physicochemical characterization of the conjugates using 1H NMR, particle size, zeta potential, encapsulation efficiency, drug loading, FTIR, XRD, SEM GPC analysis, spectroscopy, and SDS-PAGE analysis.

(iii) To evaluate micelles in vitro against the cancer cells monolayers and 3Dspheroids.

(iv) To perform in vivo pharmacokinetic studies using wistar rats.

(v) To evaluate the therapeutic efficacy of the micelles in tumor-bearing mice.

Objective 4: NIR-Light Degradable Chlorin e6 Pro-Drug Micelles for Oral Cancer Treatment

Specific aims:

(i) To synthesize Ce6 conjugated 2 nitrobenzyl micelles

(ii) To perform the physicochemical characterization of the conjugates using 1H NMR, particle size, zeta potential, encapsulation efficiency, drug loading, FTIR, XRD, SEM GPC analysis.

(iii) To evaluate micelles in vitro against the cancer cells monolayers.

(iv) To evaluate the therapeutic efficacy of the micelles in tumor-bearing mice.

Objective 5: Developing micelles containing a NIR light degradable of Chlorin e6 for the treatment of oral cancer.

Specific aims:

(i) To synthesize Ce6 loaded 2 nitrobenzyl micelles

(ii) To perform the physicochemical characterization of the conjugates using 1H NMR, particle size, zeta potential, encapsulation efficiency, drug loading, FTIR, XRD, SEM GPC analysis.

(iii) To evaluate micelles in vitro against the cancer cells monolayers.

(iv) To evaluate the therapeutic efficacy of the micelles in tumor-bearing mice.

Chapter 2

Utilizing Pluronic F127 micelles loaded with chlorin e6 for targeted photodynamictherapy
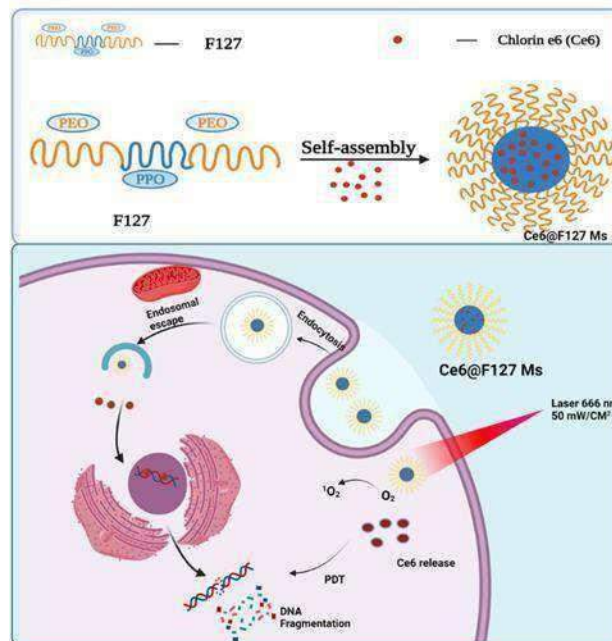
2.1 Introduction

Oral cavity and pharyngeal carcinomas significantly contribute to global morbidity and mortality (1,2). Among them, oral squamous cell carcinoma (OSCC) is a prevalent malignancy within the oral cavity and maxillofacial region, categorized under head and neck cancers. The treatment approach for oral cancers typically involves a combination of surgical procedures, radiation therapy, and chemotherapy, depending on the cancer stage. Advanced stages often require a combination of surgery or radiotherapy alongside chemotherapy as an adjuvant treatment (3). Commonly used chemotherapeutic agents include cisplatin, paclitaxel, docetaxel, and methotrexate. Photodynamic therapy (PDT) offers a novel strategy for tumor ablation, triggered by light activation of a photosensitizer (P.S.). PDT holds promise in oncologic intervention due to its potential for fewer side effects (4). This therapy is applicable in the treatment of various tumors, including early-stage lung cancer, head and neck cancer, bladder cancer, skin cancer, and endobronchial tumors. The efficacy of PDT depends on the photosensitizer, as it absorbs light energy, enters an excited state, and transfers energy to surrounding oxygen molecules, generating cytotoxic reactive oxygen species like singlet oxygen ($1O_2$) and hydroxyl radicals, leading to cell death. One of PDT's advantages is the ability to minimize damage to healthy tissues by illuminating only the tumor-specific area to activate the photosensitizer locally. Consequently, PDT differs from conventional cancer treatments that use chemotherapeutic agents, offering fewer side effects, high effectiveness, minimal invasiveness, and the potential for repeated administration without cumulative toxicity. Some photosensitizers, such as Photofrin and Laserphyrin, have received FDA approval for clinical cancer therapy (5). However, the clinical use of photosensitizers faces limitations due to issues related to poor solubility in aqueous media, cellular uptake, and limited tumor-targeting capabilities (6). To address these challenges, nanoparticle-

based systems, including micelles, liposomes, and solid lipid nanoparticles, have emerged to enhance the tumor specificity of photosensitizers through the enhanced permeation and retention (EPR) effect. In this study, we selected Chlorin e6 (Ce6) as our photosensitizer, offering advantages for clinical use, including activation by near- infrared wavelengths, the ability to penetrate deep into tissue layers, and efficacy against a wide range of cancers (7). Nevertheless, the utilization of PSs in clinical settings has been constrained by their inadequate solubility in water-based solutions, challenges in cellular uptake, and limited effectiveness in targeting tumors (8-12). In this study, Chlorin e6 (Ce6) was selected as the photosensitizer. Ce6 demonstrates significant advantages for clinical application, including responsiveness to near infrared wavelengths, strong tissue penetration capabilities, and efficacy against various cancers, notably lung cancer, metastatic breast cancer, and refractory ovarian cancer (10,13). Additionally, Poloxamers are non-ionic triblock copolymers of polyethylene glycol and polypropylene glycol. In aqueous solutions, poloxamers can self-assemble and form micelles. we employed Pluronic F127 (PF127) to create a water-soluble polymeric photosensitizer with improved cellular uptake and tumor-targeting potential when loaded with Ce6. PF127, an FDA-approved triblock copolymer consisting of poly(ethylene oxide)-block-poly(propylene oxide)-block-poly(ethylene oxide) (PEO-PPO-PEO), has been widely used as a pharmaceutical adjuvant (14-18). Notably, PF127 can interact with cell membranes, reducing microviscosity, creating membrane pores, and facilitating the rapid exchange of membrane components. Our hypothesis is that Ce6 loaded with PF127 can lower the HLB value, enabling efficient internalization into tumor cells. Consequently, Ce6-loaded PF127 micelles offer several advantages, including increased solubility in aqueous media, enhanced cellular uptake, and improved tumor-targeting efficiency through the EPR effect. In this study, we assessed the physicochemical properties and photoactivity of Ce6@F127 Ms using fluorescence intensity and

spectro-fluorophotometry. We also compared the cellular internalization behavior, generation of reactive oxygen species, mitochondrial membrane potential, and phototoxicity of Ce6@F127 micelles with that of free Ce6 using fluorescence microscopy. Significantly, our observations indicate that this treatment method holds promise in generating reactive oxygen species capable of reaching the lungs and hindering metastasis. As a result, this approach shows robust potential for addressing metastatic melanoma.

2.2 Materials and methods

2.2.1   Materials

N,N-Dimethyl-4-nitrosoaniline (abbreviated as RNO), anhydrous dimethyl sulfoxide (DMSO), 9,10- dimethylanthracene (DMA), propidium iodide, Paraformaldehyde, and DAPI (4,6- diamidino-2- phenylindole) were acquired from Sigma-Aldrich (located in Mumbai, India). Chlorin e6 (Ce6) was sourced from Frontier Scientific, Inc. (based in the USA). The Annexin V-FITC Apoptosis Detection Kit was obtained from Invitrogen Co. (USA). Spectra/Por dialysis membranes were procured from Spectrum Laboratories, Inc. (USA). Singlet oxygen sensor green (SOSG) and Calcein Blue AM were purchased from Thermo Fisher Scientific (USA). Trypan blue solution and Fluoromount-G were acquired from Himedia Laboratories (India).

Murine melanoma cell lines (B16F10) were obtained from the National Center for Cell Sciences (NCCS) in Pune, India. The hypopharyngeal carcinoma cell line (FaDu HTB-43) was acquired from the American Type Culture Collection (ATCC) in the USA. Dulbecco's modified eagle's medium (DMEM), fetal bovine serum (FBS), and penicillin/streptomycin were purchased from Himedia Laboratories (Mumbai, India). The complete growth media for culturing of cells was prepared by adding fetal bovine serum (10 %) and penicillin/streptomycin (100 IU/mL) to the DMEM and the cells were incubated at 37 °C with 5 % CO2.

2.3 Method

2.3.1 Development and Characterization of Ce6-Loaded Pluronic Micelles

A solution containing 10.0 mg/mL of polymer PF127 in DMSO (1.0 mL) and 2.0 mg/mL of the photosensitizer Ce6 in DMSO (0.1 mL) was prepared by thorough mixing and stirring for 20 minutes. Subsequently, water (5.0 mL) was added dropwise, and the mixture was continually stirred for an additional 4 hours. The resulting solution was then dialyzed using a dialysis bag (MW CO 3500 Da, Spectrum Laboratories, USA) against distilled water for a period of 2 days. The dialysate obtained was subjected to drying using a lyophilizer (Labconco, USA) and weighed. To determine loading and encapsulation efficiency, the product was redissolved in DMSO (19).

2.3.2   Characterization of Ce6@F127 Micelles

2.3.2.1 Physicochemical Characterization

The average particle size, polydispersity index (PDI), and zeta potential of Ce6@F127 Ms were measured using a Zeta-sizer instrument (Nano ZS3600, Malvern Instruments Ltd, UK) at a wavelength of 633 nm and a temperature of 25°C. The drug loading and entrapment efficiency are two important parameters used to evaluate the performance of drug delivery systems such as micelles. The drug loading and entrapment efficiency of Ce6@F127 Ms were determined using a UV/vis spectrophotometer (Spectramax, microplate reader, Molecular Devices, US) at a wavelength of 405 nm, and it was determined from a standard curve of free Ce6 concentrations in DMSO. This technique allows for the quantification of the drug in the carrier system and in the supernatant, which can be used to calculate the drug loading and entrapment efficiency by the given formula below:

E.E. (%) = (Weight of drug entrapped in the micelles) / (Weight of total drug added initially to prepare the micelles) x 100

DL (%) = (Weight of drug entrapped in the micelles) / (Weight of the polymer and drug) x 100

2.3.2.2 FTIR Analysis

The functional group identification and the study of interactions between functional groups on the surface of Ce6, Ce6@F127 Ms were performed using Fourier Transform Infrared Spectroscopy (FTIR) by KBR pellet technique (20). The analysis was conducted using a FTIR spectrometer (Jasco-4200, USA). The freeze-dried samples were mixed with potassium bromide (FTIR grade) and scanned over the frequency range of 4000-400 cm -1 at a resolution of 4 cm -1 , (64 scans) to obtain spectrum.

2.3.2.3 DSC Analysis

Thermal analysis of free drugs and micelles was performed. In brief, Ce6, F127, and Ce6@F127 Ms (lyophilized powder) was compressed into aluminum pans (21). The samples were analyzed under a nitrogen atmosphere in the temperature range of 30-300 °C with a flow rate of 20 mL/min by using a differential scanning calorimeter (DSC 60, Shimadzu, Japan).

2.3.2.4 Morphology Analysis by FESEM

Lyophilized powders of Ce6@F127 micelles were employed for the examination of morphology using Field Emission Scanning Electron Microscopy (NOVA NANOSEM 450). For SEM analysis, samples were prepared by uniformly applying a thin layer of micelles onto adhesive carbon tape attached to aluminum stubs. Subsequently, these stubs were coated with gold to the desired thickness and examined at 20 kV.

2.3.2.5 XRD Patterns

X-ray diffraction (XRD) analysis of Ce6, F127, and Ce6@F127 Ms were performed using the X-ray diffractometer (ULTIMA-IV, Rigaku). The samples were placed on glass substrates and small-angle XRD measurements were acquired using a super-speed X-ray diffractometer equipped with a nickel filter and a copper radiation source (Cu Kα radiations, k = 0.15405 nm). The instrument was operated at a tube voltage of 40 kV and a tube current of 30 mA, and the samples were scanned over a 2θ range of 2-60 °.

2.3.2.6 In Vitro Drug Release Studies

The NIR laser and pH dual-responsive drug release behavior of Ce6@F127 Ms was assessed using the dialysis method (22). Specifically, The NP solution were enclosed within a dialysis bag with a molecular weight cutoff of 2000 Da and submerged in different pH's (5.5, 6.5 and 7.4 PBS buffer solution, 100 mL). The entire setup was placed on a magnetic stirrer operating at 37 °C and 150 rpm for a predetermined duration. During the experiment, 1 mL of the release medium was sampled, and an equal volume of fresh medium was added to maintain sink conditions. After 12 hours, the sample was exposed to NIR (near- infrared) light 666 nm at a power density of 0.5 W/cm2 for 5 minutes. Prior to and after NIR irradiation, 1 mL of release medium was collected and replaced with fresh medium. As a comparison, a negative control group underwent the same process without NIR irradiation. The concentration of released Ce6 was quantified using a UV/vis spectrophotometer at 405 nm wavelength.

2.3.2.7 Hemolysis Assay

A hemolysis assay was conducted following established protocols (23). Various concentrations of Ce6@F127 micelles (500 µg/ml, 250 µg/ml, 10409µg/ml, 50 µg/ml, 25 µg/ml) were prepared.

Positive and negative controls were Triton X-100 (1%) and PBS at pH 7.4, respectively. Each sample was introduced to a red blood cell (RBC) suspension and incubated at 37°C for 1 hour. Following incubation, the samples underwent centrifugation at 7000 rpm and 4°C for 20 minutes. The hemoglobin released due to RBC hemolysis was present in the supernatant, and its absorbance at 576 nm was determined using a Spectramax Multiplate reader (Molecular Devices, USA). The hemolysis percentage was calculated utilizing the provided formula.

2.4 Biochemical Characterization

2.4.1 Evaluation of Singlet Oxygen Generation (SOG)

SOG assessment utilized 9,10-dimethylanthracene (DMA) as a fluorescent dye sensitive to singlet oxygen ($1O_2$), with its fluorescence intensity increasing upon exposure to $1O_2$. The study incorporated free Ce6, Ce6@F127 micelles in DMSO and PBS at pH 7.4. DMA (20 mM) was mixed with all Ce6-containing micelles at a concentration of 1.5 µg (in 1 mL DMSO) and equilibrated for 10 minutes. The mixture was irradiated with a 660 nm laser source at 0.5 W/cm2 intensity for varying time intervals. Post-irradiation, the reduction in DMA fluorescence intensity was measured at 360 and 380-550 nm, respectively, using a fluorescence spectrophotometer (SpectramaxTM, microplate reader, Molecular Devices, USA) and a UV−vis spectrometer (Jasco UV-670, Japan).

SOG was also determined using N,N-dimethyl-4-nitrosoaniline (RNO) in the presence of histidine, which aids in trapping $1O_2$. Aqueous systems of RNO (100 µL, 250 mM) and histidine (300 µL, 30 mM) were combined with solutions of free Ce6 and Ce6@F127 micelles (1 mL). From the aqueous system, 200 µL of sample solutions were taken in a 96-well plate and irradiated with 600 nm NIR laser irradiation. Post-laser irradiation, RNO absorbance at 440 nm was measured using a UV–vis spectrophotometer.

For the evaluation of 1O2 generation by Ce6@F127 Ms in distilled water, Singlet oxygen sensor green (SOSG) was used following a previously reported protocol. SOSG (2.5 mM) was introduced to measure the 1O2 generation of Ce6 (0.25 mM) loaded F127 micelles upon irradiation at a 666 nm wavelength. Control groups included free Ce6 and Ce6@F127 Ms. After irradiation, the level of SOG in the samples was evaluated by measuring the absorbance of SOSG (ex 494/em 534 nm). The yield of SOG was measured by the increased fluorescence intensity of SOSG compared to background or the control samples.

2.5 In Vitro Cell-Based Assays

2.5.1 Cellular Uptake Using Fluorescence Microscopy and Flow Cytometry

To visualize the internalization of the formulation into the cell monolayer, a fluorescence microscopic study was employed. B16F10 and FaDu cells were seeded onto a coverslip in a 12-well plate at a density of 50,000 cells/well and incubated overnight until reaching confluence. Upon reaching 80% confluence, the cells were treated with 100 µL of Ce6 and Ce6@F127 Ms, followed by further incubation for 1 and 4 hours. After incubation, the media was removed, and the cells were washed twice with PBS (300 µL). Subsequently, 50 µL of DAPI (6 µg/mL) was added and left for 5 minutes, followed by cell fixation with 4% paraformaldehyde for 20 minutes at room temperature. The coverslips were mounted on glass slides using fluoromount-G and observed under a fluorescence microscope.

A flow cytometry study was conducted to quantify the cellular uptake of micelles. Cells (0.2×10^6 cells/well) were added to a 12-well plate and incubated overnight. After 1 and 4 hours of incubation, the cells were washed with PBS, detached with trypsin, centrifuged, and resuspended in PBS. The internalization of the formulation in the cells was quantified using a flow cytometer (FACS ARIA III, BD Life Sciences), with the analysis of 10,000 cells from each group.

2.5.2 In Vitro Cytotoxicity Study

The MTT assay was utilized to estimate the combined chemo and photothermal therapy effects in vitro in B16F10 and FaDu cells (24). The experiment involved seeding cells in a 96-well plate at a density of 1 x 104 cells per well and incubated with 100 µL of DMEM medium. Following a 24-hour incubation period, the of Ce6 and Ce6@F127 Ms were introduced into the designated well and subjected to an additional 24- hour incubation period at a temperature of 37°C, 5 % CO2 to assess the potential for dark toxicity. In order to assess the phototoxicity induced by NIR laser, the Ce6 and Ce6@F127 Ms were subjected to a medium replacement with fresh DMEM medium after a 12-hour of incubation period. Subsequently, these wells were exposed to NIR laser irradiation (Shanghai MRTRADE International Co., LTD.). Each well was subjected to an 666 nm NIR laser with a power density of 0.5 W/cm2 for a duration of 5 min. Following a 24 and 48 h coincubation period, 50 µL of MTT (5 mg/mL in PBS) was introduced to each well and allowed to incubate for an additional 4 h. Subsequently, the medium was extracted and replaced with a 150 µL of DMSO to dissolve the formazan crystals. To estimate the relative cell viability, the absorbance at 570 nm was measured using a Spectramax TM multiplate reader (Molecular Devices, US).

The following formula is used to calculate % cell viability:

Cell viability % = (Absorbance of sample) / (Absorbance of control) $\times$ 100

Where Absorbance of the sample represents the absorbance of cells treated with free Ce6 or Ce6@F127 micelles, and Absorbance of the control is the absorbance of untreated cells. The determination of the half- maximal dosage (IC-50) was carried out using GraphPad Prism 9.0.2 software.

2.5.3 ROS detection assay

The intracellular sensor DCFH-DA dye was employed to observe ROS formation in the tested cell lines B16F10 and FaDu cells treated with Ce6 and Ce6@F127 Ms. B16F10 and FaDu cells were seeded in a 12- well tissue culture plate at a density of 50,000 cells/well (25). After 24 hours, the cells were treated with free Ce6, Ce6@F127 Ms formulations and incubated at 37°C with 5% CO_2 for 24 hours. Following incubation, the cells were washed using PBS 7.4, fixed with 4% paraformaldehyde (500 µl/well), stained with DCHFDA (5 µm, with excitation and emission wavelengths of 504 nm and 529 nm, respectively) for 20 minutes, washed, and observed under a fluorescence microscope. In the presence of ROS species and cellular esterases, the acetate group cleaves, and the molecule gets oxidized to form DCF, producing fluorescence.

2.5.4 Mitochondrial Membrane Potential Assay

B16F10 and FaDu cells, seeded at 50,000 cells/well in a 12-well tissue culture plate, were treated with free Ce6 and Ce6@F127 micelles and incubated for 24 hours at 37°C in a 5% CO_2 atmosphere. After incubation, the cells were washed three times with PBS (pH 7.4), fixed, and labeled with 5,5,6,6-tetrachloro-1,1,3,3- tetraethylbenzimidazolcarbocyanine iodide (JC1) dye (2 µM, with excitation and emission wavelengths of 504 nm and 529 nm, respectively) for 20 minutes. Following staining, the cells were washed and observed under a fluorescence microscope. JC1 dye aggreg5a2tes in the inner mitochondrial membrane, producing green fluorescence for depolarized mitochondria, indicating mitochondrial damage, and red fluorescence for normal polarized mitochondrial membranes.

2.5.5 Annexin-V Assay

The assessment of apoptosis induced by Ce6 and Ce6@F127 micelles in B16F10 and FaDu cells was conducted using the TACS® Annexin V-FITC Apoptosis Detection Kit. Following the incubation period of 12 h, cells were exposed to 666 nm NIR laser radiation for 5 min (0.5 W/cm 2). Cells were collected and subjected to cold 1× PBS solution for washing. Subsequently, the cells were suspended once more in cold 1× PBS and then re-centrifuged at 300 g for 5 to 10 minutes at 4 °C. The liquid portion containing non- cellular components was removed, and the cells were reconstituted in ice-cold 1× annexin binding buffer. The cell concentration was upheld at 1× 10 6 cells/mL with in the 1× annexin binding buffer. A volume of 100 μL of cell suspension, which had been reconstituted in 1× annexin binding buffer, was introduced into a fresh Eppendorf tube. To each 100 μL of cell suspension, 5 μL of Annexin V labeled with either Fluorescein isothiocyanate (FITC) was incorporated. Subsequently, propidium iodide at a concentration of 1 μg/mL was introduced into each 100 μL cell suspension. The mixtures were then incubated in dark at room temperature for a duration of 15 minutes. Then, cell analysis was performed using a flow cytometer (FACS Aria III, BD Biosciences, USA) with the examination of 10,000 viable cells within the gating strategy. Solely individual cells were selected for fluorescence analysis. The data were graphed in relation to Annexin V-FITC against PI, employing quadrant gating.

2.5.6 Cell Cycle Analysis

B16F10 and FaDu cells were appropriately placed and cultured (26). Subsequently, they were exposed to Ce6 and Ce6@F127 micelles at a concentration of 6 μg/mL for a duration of 24 hours. Following this exposure, the cells were harvested through centrifugation, washed, and then treated with 70% ethanol for fixation, which lasted 24 hours. After fixation, t h5 3e cells were again collected via centrifugation, rinsed, and suspended in 500 μL of PBS solution containing 200

μg/mL of RNAase. To stain the cellular DNA, Propidium Iodide (PI) was used at a concentration of 20 μg/mL in PBS. This staining process occurred at room temperature in darkness for 30 minutes. The quantification of DNA content in the cells was performed using a flow cytometer (BD Biosciences, USA). The Flow Jo Software was then utilized to analyze the data and determine the distribution of cells within the G1, S, and G2/M phases of the cell cycle.

2.6 To perform in vivo study using tumor-bearing mice

2.6.1 In Vivo Tumor Growth Inhibition Studies

The anti-tumor efficacy test adhered to protocols approved by the Animal Ethics Committee of BITS PILANI HYDERABAD CAMPUS. The therapeutic effectiveness of free Ce6 and Ce6@F127 Ms was assessed in female C57BL/6 mice (5–6 weeks, 18–20 g), sourced from Sai Life Sciences, India. The animals were acclimatized for one week in-house, maintaining an environment at 20–25°C with nocturnal-diurnal cycles and a relative humidity of 50–60%, with full access to food and water. For tumor induction, murine melanoma B16F10 cells (2.5×106 in 0.1 mL of PBS) were hypodermically injected to establish the xenograft tumor model (27). The animals were monitored daily for palpable solid tumor development. Upon the appearance of solid tumors, tumor volume was measured using a vernier caliper, and the volume was calculated using the formula (length × width2)/2. The in vivo therapeutic efficacy of Ce6 and Ce6@F127 Ms was evaluated in B16F10 tumor-bearing mice. When the tumor volume reached 50–100 mm3, the tumor- bearing mice were divided into three groups: (a) saline, (b) Ce6, and (c) Ce6@F127 Ms, each consisting of five animals. The formulations were intravenously administered to the mice at 5 mg/kg (equivalent to Ce6), followed by irradiation of the tumor region using a 666 nm laser at 0.5 W/cm2 for 6 minutes with a 5-minute interval. Tumor volume and body weight were monitored

throughout the study period. After the study period, the mice were euthanized by CO2, and their tumors and other organs were collected and weighed.

2.6.2 Immunohistochemistry

The excised tumor tissues were preserved by embedding them in optimal cutting temperature medium and subsequently frozen. Cryo-sectioning of the tissues was performed at a thickness of 5 μm using a cryotome (Leica CM1950, Leica Biosystems, Germany). T5h4e resulting tumor sections were then examined to evaluate the expression of cancer extracellular matrix (ECM) proteins, including TUNEL, Ki-67, and ROS, under a fluorescence microscope.

2.6.2.1 Detection of KI67 and Tunel assay

For the assessment of Ki-67, the tumor section was fixed with methanol, blocked in 3% BSA for 1 hour, and incubated overnight with the Ki-67 primary antibody (Rabbit mAb # A21861) at 4°C. On the following day, the tissue sections were washed with PBS and incubated with the secondary antibody Alexa Fluor® 488 for 2 hours at room temperature in the dark. After 2 hours, the tissues were washed with PBS, treated with DAPI for 5 minutes, and observed under a fluorescence microscope. The detection of apoptosis using the TUNEL assay (Click-iT™ Plus TUNEL Assay Kits for In Situ Apoptosis Detection Kit, ThermoFisher) followed the manufacturer's protocol. In brief, the terminal deoxynucleotidyl transferase (TdT) reaction buffer was applied to tumor tissues for 15 minutes at 37°C (28). Then, the TdT reaction mixture, consisting of EdUTP, TdT enzyme, and equilibration buffer, was added to the fixed tumor tissue and incubated for 60 minutes at 37°C in the dark. Slides were washed with deionized water, rinsed with 3% BSA and 0.1% Triton™ X-100 in PBS for 5 minutes. Subsequently, DAPI was added to the top of the tissue sections and left for 5 minutes. The sections were observed under a fluorescence microscope (Leica, Germany).

2.6.2.2 ROS generation in tumor tissue

In B16F10 tumor-bearing mice with a tumor volume of approximately 50 mm3, intravenous injections of Ce6 and Ce6@F127 Ms were administered with a Ce6 dose of 5 mg/kg (29). Subsequently, a laser was applied to the tumor region after 15 minutes for a duration of 6 minutes. After 12 hours, DCFH-DA was intratumorally injected at a concentration of 35 μM (50 μL) into the mice. Following 60 minutes of DCFH- DA administration, the mice were euthanized, and tumor tissue was collected and embedded in OCT media. The excised tumors were cryo-sectioned at a thickness of 5 μm using a cryotome and examined under a fluorescence microscope utilizing a FITC filter (ex/em 495/519 nm).

2.7 Lung metastasis - BrdU assay, collagen1A515and H&E in lung tissue

BrdU, also known as Bromodeoxyuridine or 5-bromo-2′-deoxyuridine, serves as a thymidine nucleoside analog in the BrdU assay for identifying proliferating cells in cancer. To create a sterile BrdU solution, it was diluted in PBS to achieve a concentration of 10 mg/mL. This solution (150 μL) was then intraperitoneally administered on the 20th day post-tumor inoculation to individual mice with tumors following each treatment. After a 2-hour interval, the lungs were resected and embedded in OCT media. The next day, the metastasized frozen lung was cryo-sectioned to a thickness of 5 μm. These sections underwent genomic DNA denaturation with 1 N HCl for 10 minutes, followed by an additional 10 minutes with 2 N HCl at room temperature. Subsequently, the sections were neutralized in 0.1 M borate buffer for 15 minutes to counteract the HCl, followed by three washes with 1% Triton X-100 in PBS 7.4 for 5 minutes each. The sections were then treated with 1.5% Triton X-100 in PBS for 1 hour, succeeded by an overnight incubation with anti-BrdU rabbit IgG at 4°C. The following day, the sections were washed with PBST and incubated with a secondary antiRabbit IgG (H + L) secondary antibody for 1 hour. After PBS washing, the

sections were examined using a fluorescence microscope. For collagen I staining in metastatic lung tissue, tumor tissue blocked with 1% BSA was exposed to Anti-Collagen I primary antibody (Abcam #ab138492) at a 1/1000 dilution overnight at 4°C. On the subsequent day, the tissue sections underwent PBS washing and were then incubated with the secondary antibody Alexa Fluor® 488 for 2 hours at room temperature in the dark. Following a 2-hour incubation, the tissues were rinsed with PBS, treated with DAPI for 5 minutes, and visualized under a fluorescence microscope. Hematoxylin and eosin (H&E) staining were employed for the lung tissue sections (4 μm thickness). Initially, the sections were exposed to xylene, followed by varying concentrations of alcohol (30 %–100 %) and water. Hematoxylin was used for nuclei staining, followed by tap water washing. Subsequently, eosin staining was applied for cytoplasm, followed by washing with dehydrated alcohol and xylene. The slides were fixed with mounting media and visualized under a microscope at 10× magnification.

2.8 Potential toxicity assessment of Ce6@F127 Ms

To evaluate the systemic toxicity of intravenously administered Ce6 and Ce6@F127 Ms in tumor-bearing mice, hematological and serum analyses were pe5r6formed. Blood samples were obtained three days post the last dosing via retro-orbital plexus puncture into heparin-coated tubes for plasma and non-heparinized tubes for serum. After centrifugation at 4500 rpm for 10 minutes, either plasma or serum was collected. Hematological parameters, including WBC, RBC, hemoglobin, platelets, and hematocrit value, were assessed using a blood analyzer (HEMAVET DREW) to identify any potential toxicity. Serum parameters such as total protein, blood urea nitrogen, creatinine, alkaline phosphatase, and alanine aminotransferase were measured with a chemical analyzer (Element-DC by HESKA) to evaluate liver and kidney function. The obtained results were presented graphically using GraphPad Prism software. For histological evaluation,

tumors and other organs were harvested from euthanized mice following each treatment. The collected tissues were frozen, sectioned at 5 μm, and subjected to hematoxylin and eosin (H&E) staining.

2.9 Statistical analysis

All the reported experiments were performed in triplicates, and the data were expressed as mean and standard deviation (mean ± S.D.). One-way ANOVA and student's t-test were conducted using graph pad prism software (GraphPad, Inc., California, USA) between the groups to determine the significance. The probability value of < 0.05, < 0.01 and < 0.001 represents statistically significant. *, **, and ***

2.10 Results and Discussion

2.10.1 Preparation and characterization of micelles

The Prepared micelles were characterized using particle size analysis, zeta potential measurements, differential scanning calorimetry (DSC), and X-ray diffraction spectroscopy (XRD). The particle size of the Ce6@F127 Ms was 167.45 ± 2.31 nm. Figure 1A illustrates a detailed particle size distribution curve of Ce6@F127 Ms produced from the Malvern zeta sizer. The representative SEM and TEM images of Ce6@F127 Ms were shown in Figure 2B&C, which exhibited co-relation with DLS data. The micelles had a narrow polydispersity index of 0.12–0.14, and a negative zeta potential was found (Table S1). The Ce6 loading was found to be 10.65 % in micelles. However, the Ce6 encapsulation efficiency of 84.15 % was observed in the case of Ce6@F127 Ms. The UV spectrum of Ce6 and Ce6@F127 is represented in Figure 1D. Moreover, Ce6@F127 Ms showed good solubility in aqueous media compared to free Ce6 molecules (Figure 1E). The solubility of Ce6@F127 Ms was confirmed using a fluorescence spectrophotometer,

which revealed that Ce6@F127 (1 mg/ml), regardless of whether it was dissolved in DMSO or distilled water, showed a similar intensity and trend in the range of 300- 800 nm due to its enhanced solubility in aqueous media (Figure 1F). These results suggest that Ce6@F127 Ms is a potential material for the clinical treatment of PDT via intra-venous (i.v.) injection.
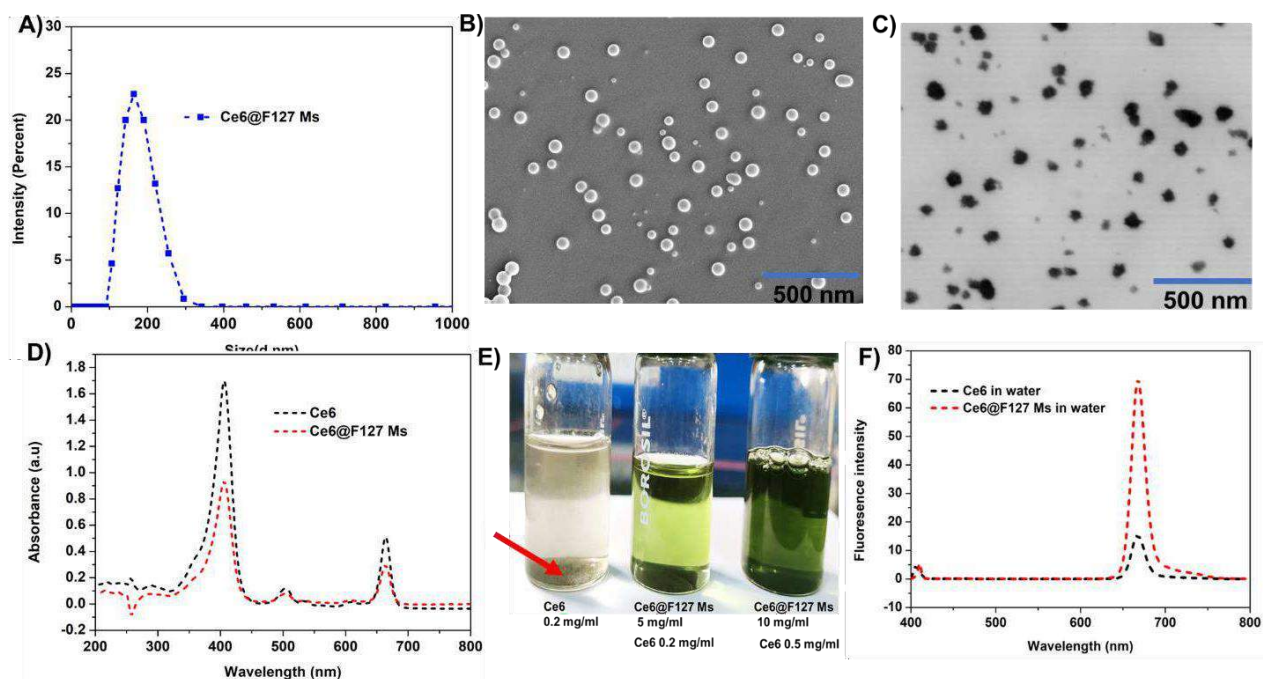
Figure 2.1 Particle size analysis of Ce6@F127 Ms (A); Scanning electron microscopy of Ce6@F127 Ms (B); Transmission electron microscopy of Ce6@F127 Ms (C); UV-visible spectroscopy of Ce6, Ce6@F127 Ms (D); Photographs of free Ce6 and Ce6@F127 Ms dissolved in distilled water. The red arrow indicates the precipitate (E); The fluorescence emission spectra of Ce6@F127 Ms and free Ce6 in distilled water, respectively (Ce6, 1 mg/ml).

The DSC thermograms were plotted simultaneously to compare the thermal characteristics of newly formed Ce6@F127 Ms. As represented in Figure S1A free Ce6, PF127, Ce6@F127 Ms

exhibited endothermic peaks at 260.89, 189.76, and 226.35 °C. The crystal properties of the Ce6@F127 Ms were better studied using wide angle X-ray powder diffraction to understand the Ce6 loading to the F127 miceller system. The diffractogram for Ce6 and Ce6@F127 Ms showed clear peaks that demonstrated the presence of crystalline phase in the native form, whereas Ce6@F127 M5 s8 showed identical peaks in the diffractogram, confirming the conjugation of Ce6 loaded F127 miceller system (Figure S1B). The stability testing data are illustrated graphically in Figure S1C. The particle size and drug loading of the Ce6@F127 Ms did not change significantly in a 30-day stability study at 4 °C, however, at room temperature, an increase in particle size and a decrease in drug loading were observed.

As shown in Figure 2D the Ce6 release from Ce6@F127 Ms was analyzed at different pH values (pH 7.4, 6.5, and 5) using the dialysis method. The amounts of Ce6 released from the micelles were all less than 50% after 48 h at pH 7.4, indicating that these systems were generally stable, and the release rate of Ce6 was rather slow under physiological conditions with or without laser. The released Ce6 from the Ce6@F127 Ms were increased to 65.12 %, significantly greater than at pH 6.5 with laser. The total Ce6 release from Ce6@F127 Ms was 82.41% for 48 h at pH 5.5. These Ce6-loaded micelles demonstrated considerable pH- dependent release behavior. When RBCs were treated with micelle solutions with polymer concentrations ranging from 0 to 500 µg/mL, the percentage of hemolysis was around 2.32 % (Figure S2). These findings indicated that the Ce6@F127 Ms did not cause hemolysis.
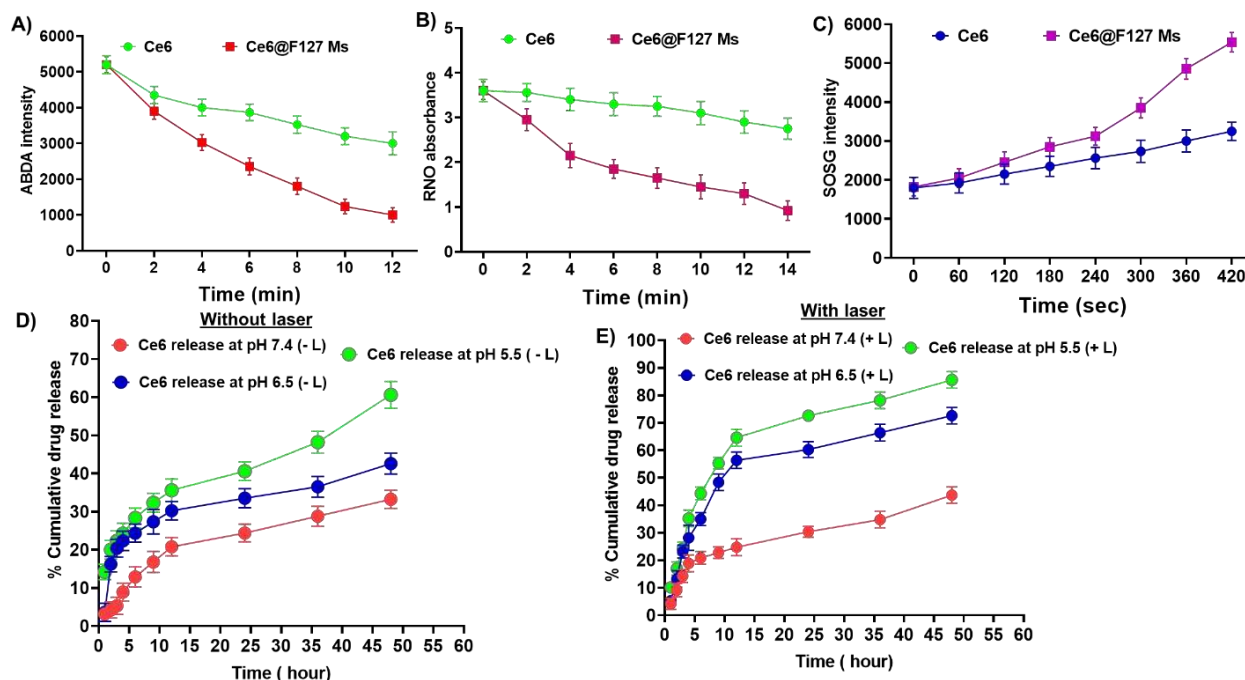
Figure 2.2 Change in ABDA, RNO and SOSG fluorescence due to the generation of singlet oxygen by free Ce6 and Ce6@F127 Ms in distilled water (A-C); In vitro release profiles of Ce6 from the Ce6@F127 Ms at pH 7.4, pH 6.5 and 5.5 without laser and with laser at 37 °C (D-E).

2.10.2 Cellular uptake of micelles

The distribution of Ce6-loaded micelles was analyzed using a confocal microscope. Ce6 fluorescence was distributed inside the cytoplasm and nuclei of the B16F10 and FaDu cells incubated with Ce6@F127 Ms for 4 h. This indicates that the Ce6-loaded micelles were rapidly taken up and gradually accumulated in the nuclei as the incubation time increased. Further, we have confirmed these observations using quantitative flow cytometry analysis. There is a significant increase in Ce6 fluorescence intensity in B16F10 and FaDu cells treated with Ce6@F127 Ms as the incubation time increases. Fluorescence intensity was represented in Figure

3E and F for B16F10 and FaDu cells treated with Ce6@F127 Ms were 2412.87 ± 321.11, 4025.20 ± 115.20 and 1912.79 ± 81.81, 3961.52 ± 35.20 and for 1h and 4h respectively. As shown in Figure 3, the fluorescence microscopy images exhibited that Ce6 and Ce6@F127 Ms were uptaken by all two cell lines in a time-dependent manner. The uptake of Ce6@F127 Ms in B16F10 and FaDu cells was greater than that of the free drug, indicating that the Ce6-loaded micelle is an effective drug delivery system for facilitat6i0ng drug internalization in B16F10 and FaDu cells. These micelles can be uptaken into cells via endocytosis, the size dimensions and homogeneity of the micelle particles are thought to be essential factors in determining cell uptake efficiency . The increased uptake of Ce6@F127 Ms into cells can be attributed to the targeting effects of Ce6 in addition to the small particle size and homogeneity. In contrast, the fluorescence intensity of Ce6@F127 Ms was as strong as that of Ce6@F127 Ms due to the presence of Ce6.
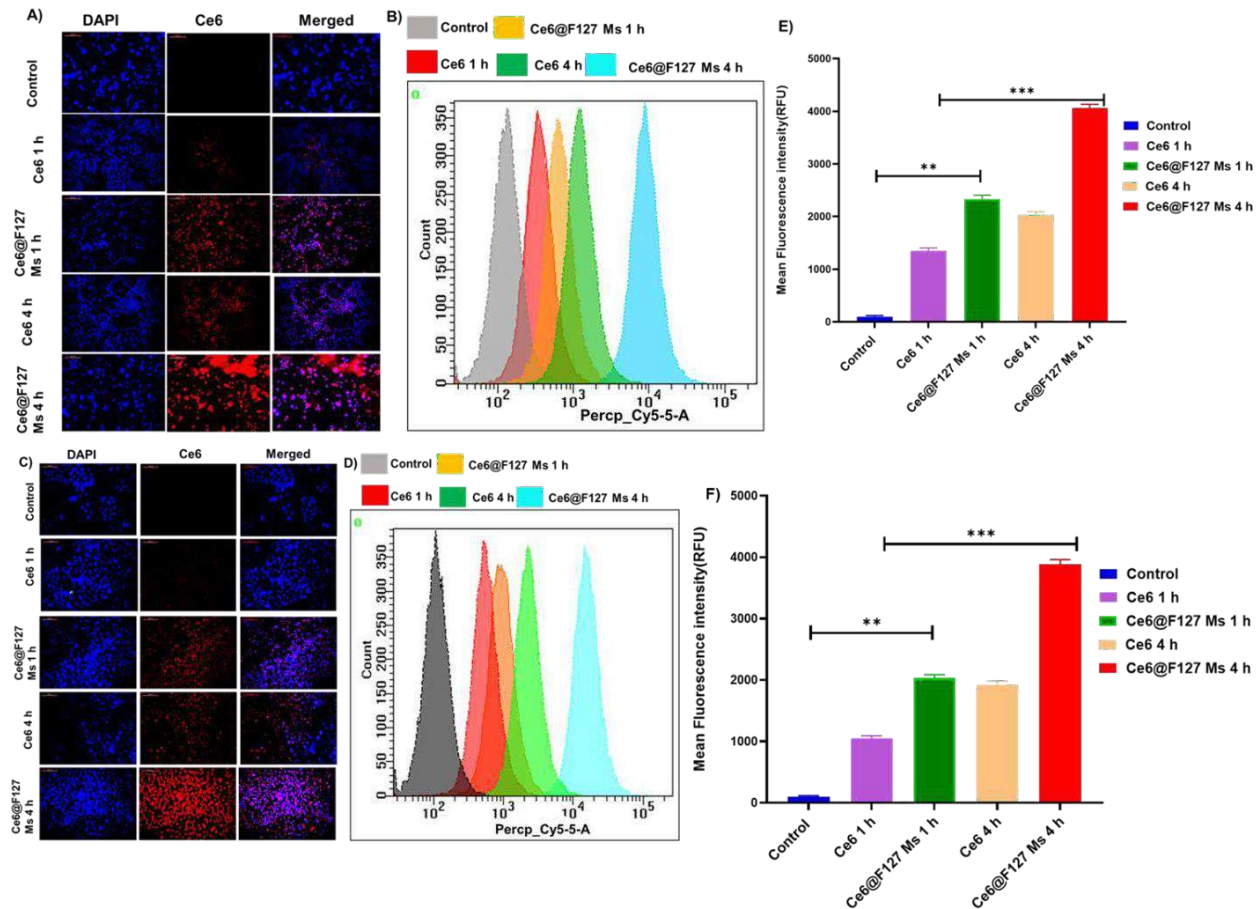
Figure 2.3 Time-dependent uptake of Ce6, Ce6@F127 Ms in B16F10 and FaDu cell line at 1 h and 4 h by the flow cytometer and fluorescence microscopy. (A-D) Qualitative uptake of Ce6, Ce6@F127 Ms at a concentration of 6 µg/ml and exposure time of 1 h and 4 h (E&F) in B16F10 and FaDu cells by the fluorescent microscopy. Mean ± SD, n = 3, n: not significant, p < 0.05, **p < 0.01; ***p < 0.001

2.10.3 In vitro cytotoxicity assay

To investigate the photocytotoxicity of Ce6, Ce6@F127 Ms treated in B16F10 and FaDu cells and compared after treatment with or without light at a dose of 0.5 W/cm2 at 666 nm. The toxicity was assessed using MTT assay 24 h after irradiation. No cytotoxicity was observed after

treatment with PF127, regardless of irradiation, and nearly all of the cells were viable in the case of both free Ce6 and Ce6@F127 Ms in the absence of irradiation. In comparison to the free Ce6 and Ce6@F127 micelles caused a higher level of cytotoxicity. The difference between Ce6@F127 Ms and free drug results was due to increased intracellular uptake that overcame drug resistance and increased solubility in micelle form. The IC50 values of all the formulations were calculated using GraphPad prism software (V. 8.0.1). According to the IC50 results, the drug-loaded micelles have the lowest IC50 for B16F10 cells (15.06 µg/mL, and 9.06 µg/mL respectively, with or without laser for 24 h) and (12.31 and

4.23 µg/mL, respectively with or without laser for 48 h). similarly, for FaDu cell lines IC50 value of 24 h (15.12 and 8.95 µg/mL, respectively, with or without laser for 24 h and 10.21 and 3.95 µg/mL, respectively, with or without laser for 48 h). The Ce6@F127 Ms caused more cytotoxicity than the corresponding free drug in B16F10 and FaDu cells. This difference between the result of Ce6@F127 Ms and free drug, Ce6@F127 Ms was due to the higher intracellular uptake and increased drug solubility in micelle forms. The results of the cell viability assay suggested that the cells treated Ce6@F127 Ms caused in much lower viability than those treated with either free drug.
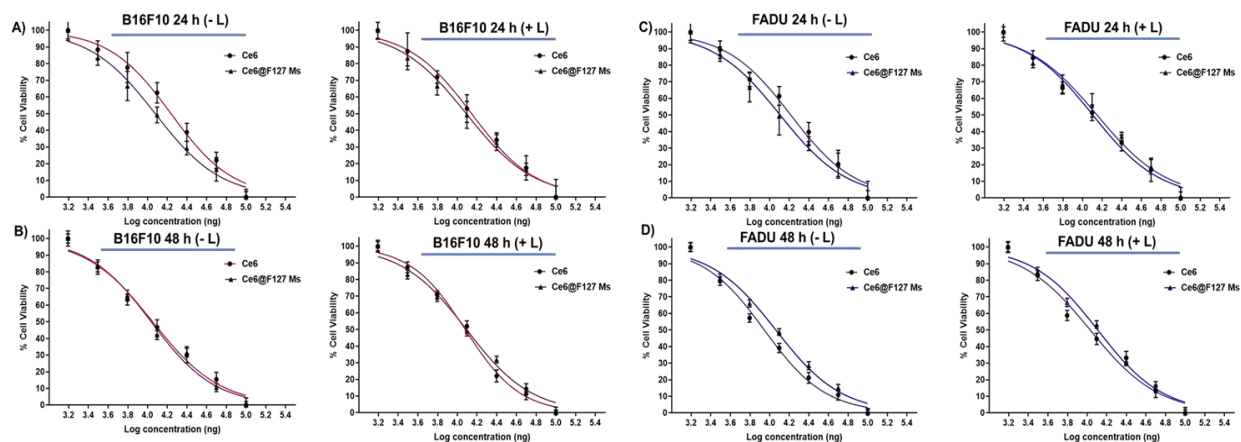
Figure 2.4 Percentage of cell viability of B16F10 and FaDu cells treated with different concentrations of Ce6, Ce6@F127 Ms at 24 h and 48 h (A-D).

2.10.4 Mechanism of micelles-induced Cytotoxicity

DCFH-DA (2',7'-Dichlorofluorescin diacetate) was used to measure the intracellular ROS generation in solid tumors. B16F10 and FaDu cells were seeded at a cell density of 1×10^4 cells /well in 6 well plates. The next day, the cells were treated free Ce6, Ce6@F127 Ms at a Ce6 concentration of 6 µg/mL for 24 h. Then, cells were stained with freshly prepared 5 µM of DCFH-DA for half an hour at 37 °C, washed three times with sterile PBS, and under a fluorescence microscope. Similarly, the detection of DCFH-DA fluorescence oxidized by ROS was also determined by using flow cytometry (FACS Aria III, BD Biosciences, USA). The phenomena suggested that FaDu and B16F10-treated cells with NPs produced higher intracellular ROS when exposed to laser radiation (Figure 5). As a result, the phenomenon demonstrated that Ce6@F127 Ms might be advantageous in improving chemo-photothermal combinational treatment results and killing cancer cells.
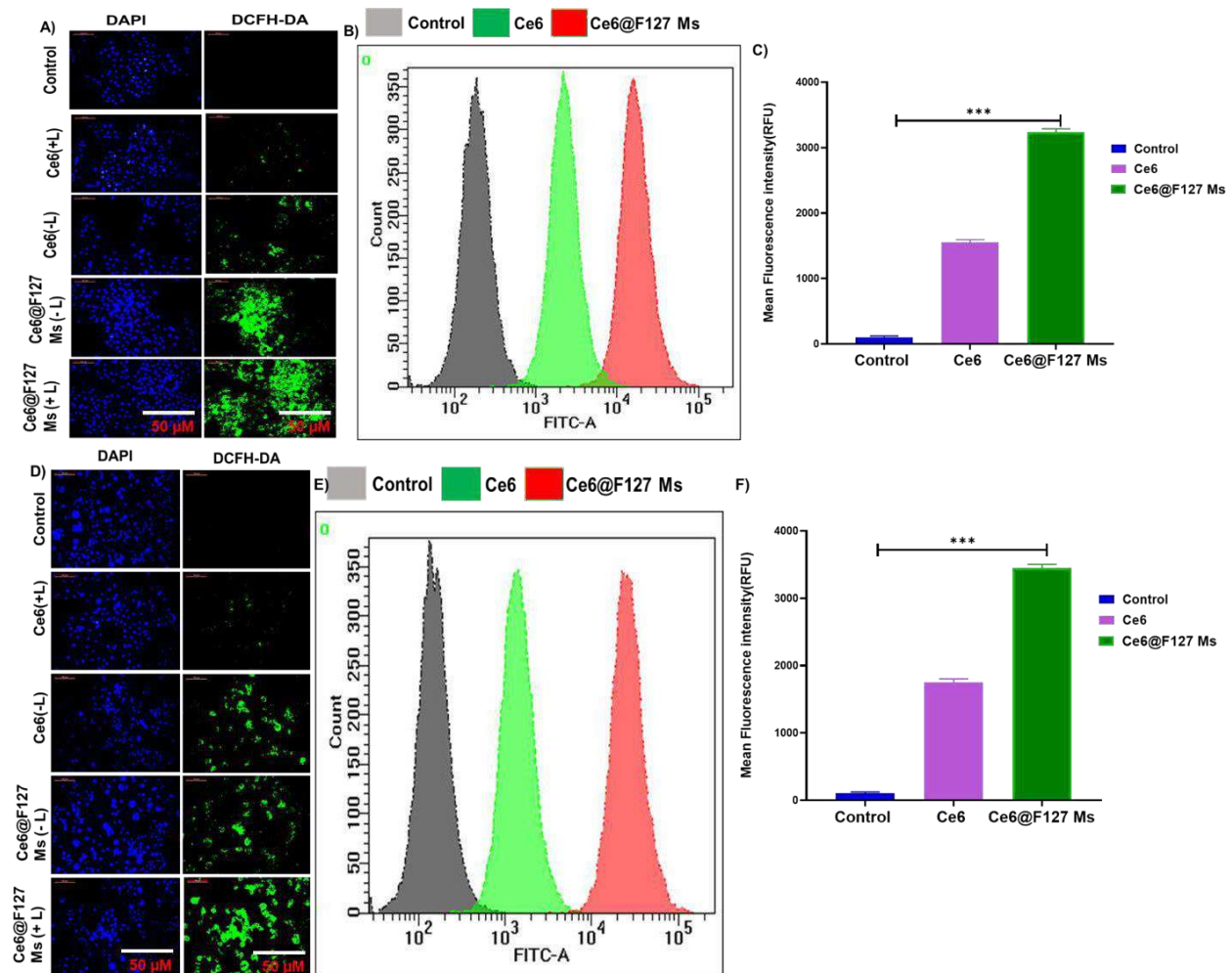
Figure 2.5 Confocal images of ROS generation by DCFH-DA staining in cells incubated with Ce6, Ce6@F127 Ms (with or without laser) (A&D); Flow-cytometry analysis of ROS generation in cells with different treatments (B&E); Quantitative analysis of the mean fluorescence intensity of ROS in B16F10 and FaDu cells (C&F). The data are shown as mean ± SD (n = 3)

Mitochondrial damage is exacerbated by producing reactive oxygen species (ROS), leading to cell apoptosis. Thus, we examined the impact of (±L) treatment on MMP in B16F10 and FaDu cells. The cationic JC-1 dye mainly indicates mitochondrial depolarization. This dye accumulates in

mitochondria in a potential- dependent way, as characterized by a shift in fluorescence emission from red (590 nm) to green (529 nm) when the mitochondrial membrane is disrupted. When compared to untreated cells, which look red (an aggregated form of the dye), Ce6@F127 Ms (+L) treated cells exhibited a higher green intensity (monomer- form of the dye) than Free Ce6 (red-green merged). These findings demonstrated that Ce6@F127 Ms (+L) caused mitochondrial membrane damage, lowering membrane potential. Flow cytometry analysis revealed that B16F10 and FaDu cells treated with of Ce6@F127 Ms (+L) exhibited more mitochondria membrane potential disruption.
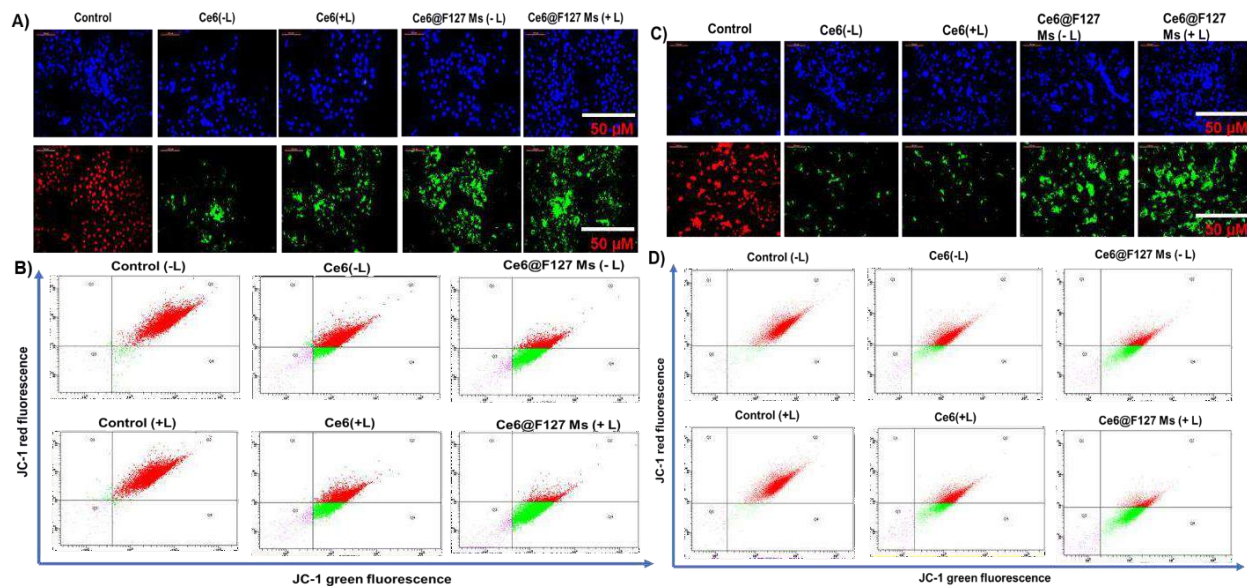
Figure 2.6 Mitochondrial membrane potential (MMP) measurement by JC1 dye on B16F10 Cells (A) FaDu cells (C), flow cytometry analysis of mitochondria membrane potential assay of Ce6, Ce6@F127 Ms (B & D).

Annexin-V was used to identify apoptotic cells, whereas propidium iodide (PI) was used to stain late apoptotic and necrotic cell nuclei. The proportion of normal cells (bottom left quadrant) in the control group (without NPs) was around 99.8 ± 1.2 %, and the proportion of viable cells was

drastically reduced when the cells were co-incubated with Ce6 and Ce6@F127 Ms. B16F10 and FaDu cells following treatment were evaluated using Annexin-V/PI double staining flow cytometry to show that Ce6@F127 Ms caused more significant cancer cell death than free drug. The free drug had no noticeable toxic effect on B16F10 (24.5 %) and FaDu cells (26.9 %). Ce6@F127 Ms showed apoptosis after laser irradiation 74.5 %.
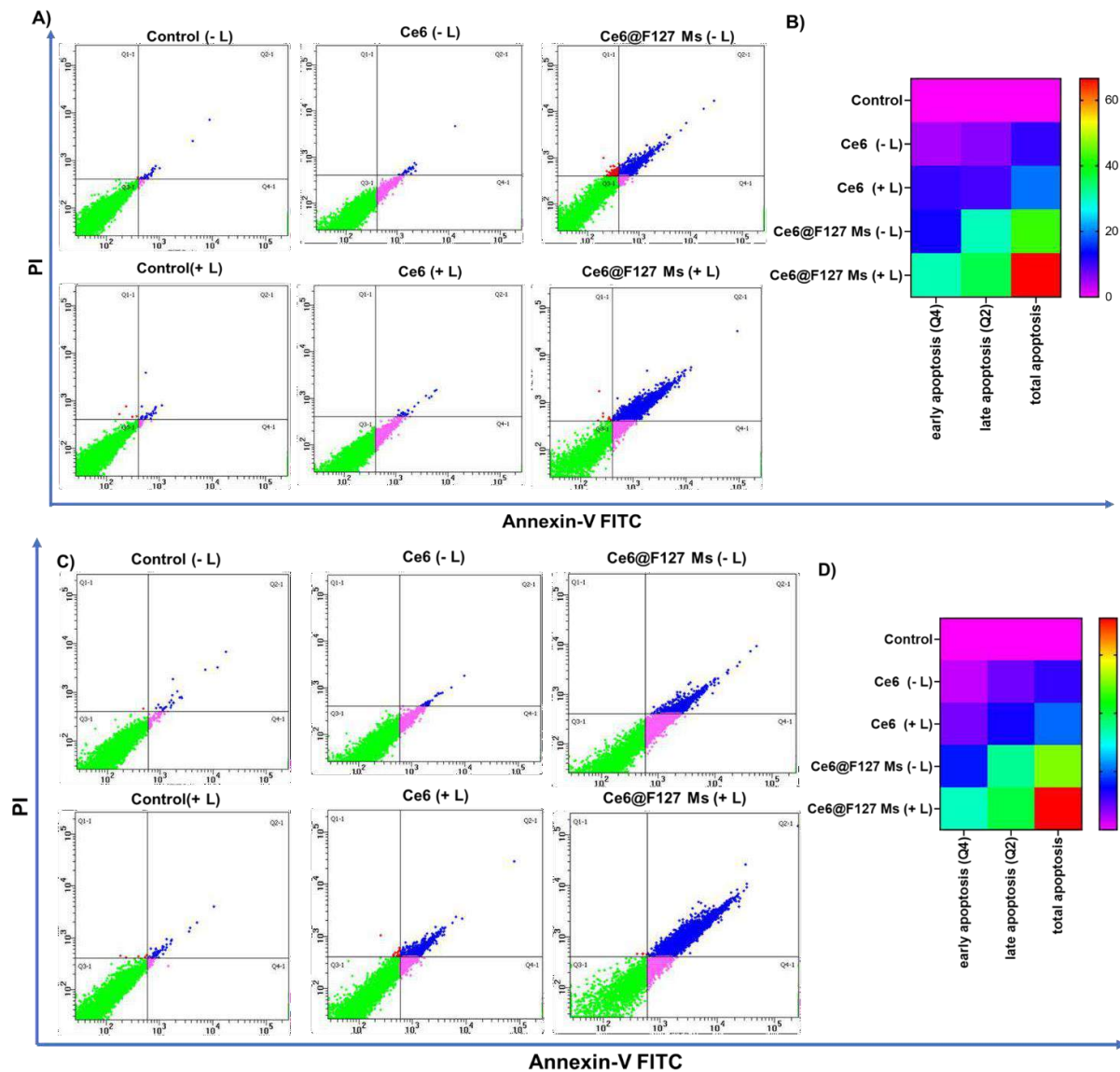
Figure 2.7 Flow cytometric analysis of B16F10 Cells (A) FaDu cells (C), apoptosis at 24 h induced by Ce6 formulations (+, -) laser irradiation, using Annexin V-FITC and PI staining. The concentration of Ce6 was 10 µg/mL. ∗ p < 0.05.

The various cell cycle stages, DNA duplication containing G1, S, and G2/M, are studied by cell cycle analysis. The free ce6 did not show noticeable changes in cell cycle pattern compared to the control group, which offers almost no toxicity to B16F10 and FaDu cells. The free Ce6 (G2/M: 34.8 & 28.59 %) in treated B16F10 and FaDu cells respectively (6 µg/mL) while, Ce6@F127 Ms showed S (4.58 & 5.58 %) and G2/M (52.04 & 41.18 %) arrest compared to control group (S: 21.11 & 34.88 %, G2/M: 8.17 & 6.49 %). Figure 8 depicts the most significant arrest in the G2/M phase for Ce6@F127 Ms (±L) against free Ce6, confirming the Ce6 mechanism of action, which arrests the cell in the early G2/M phase.
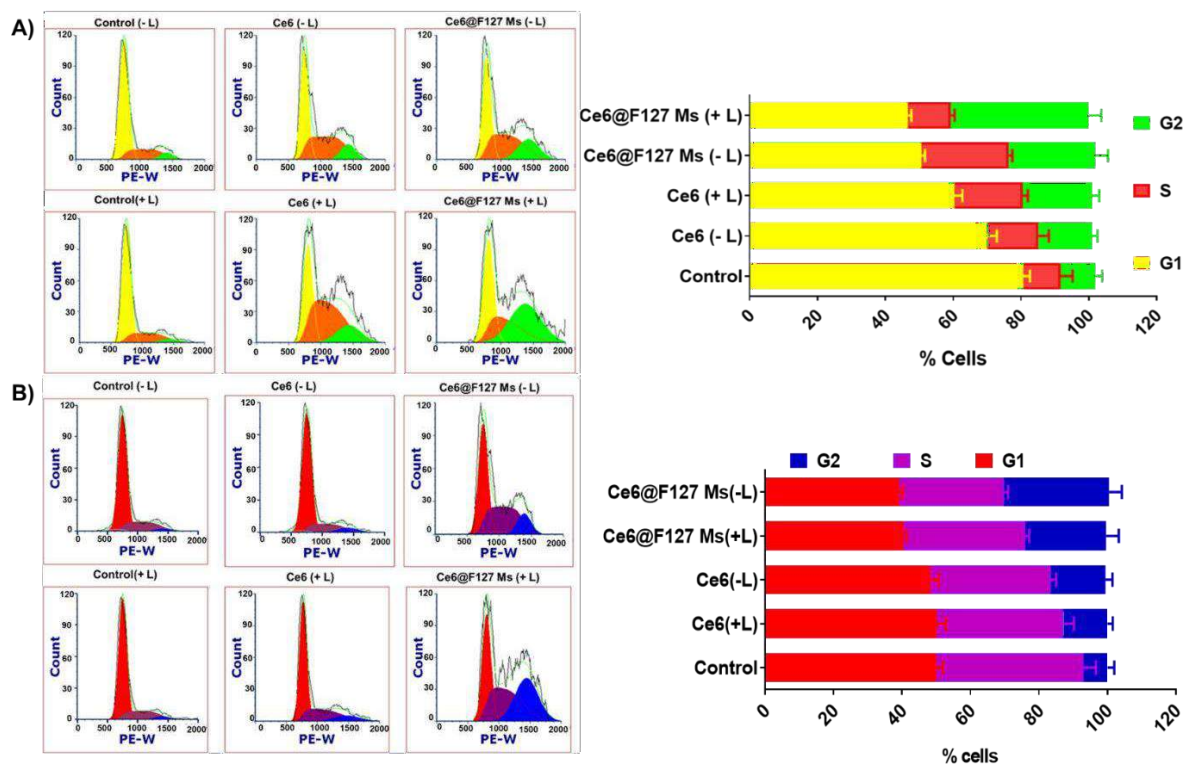
Figure 2.8 Cell cycle analysis and relative distribution of the cell population in B16F0 and FaDu cells by flow cytometry (A-B).

2.10.5 Antitumor Efficacy of Nanoparticles in Mouse Tumor Models

Motivated by the impressive in vitro therapeutic efficacy, we explored the in vivo anticancer potential of Ce6 and Ce6@F127 Ms. Intravenous administration of PBS, Ce6, and Ce6@F127 Ms was carried out in B16F10 tumor-bearing mice (initial tumor volume of 70 mm^3). The successful establishment of the tumor model was evident, as the tumor volume in the PBS-treated group reached 1125.6 ± 42.1 mm^3 at the end of 21 days, suggesting rapid tumor growth in u n6t6reat ed mice. Although the growth of B16F10 tumors showed a slight suppression within the first 10 days in the groups treated with free Ce6 and Ce6@F127 Ms, the tumor volume increased after the cessation of Ce6 treatment (1121.4 ± 57.2 mm^3 at 18 days) and Ce6@F127 Ms treatment (220.3 ± 23.4 mm3 at 21 days). Throughout the treatment period, there was a slight increase in mouse body weight. The average weights of tumors for the control, free Ce6, and Ce6@F127 Ms groups were 4.07 ± 0.21 g, 1.08 ± 0.14 g, and 0.50 ± 0.08 g, respectively.
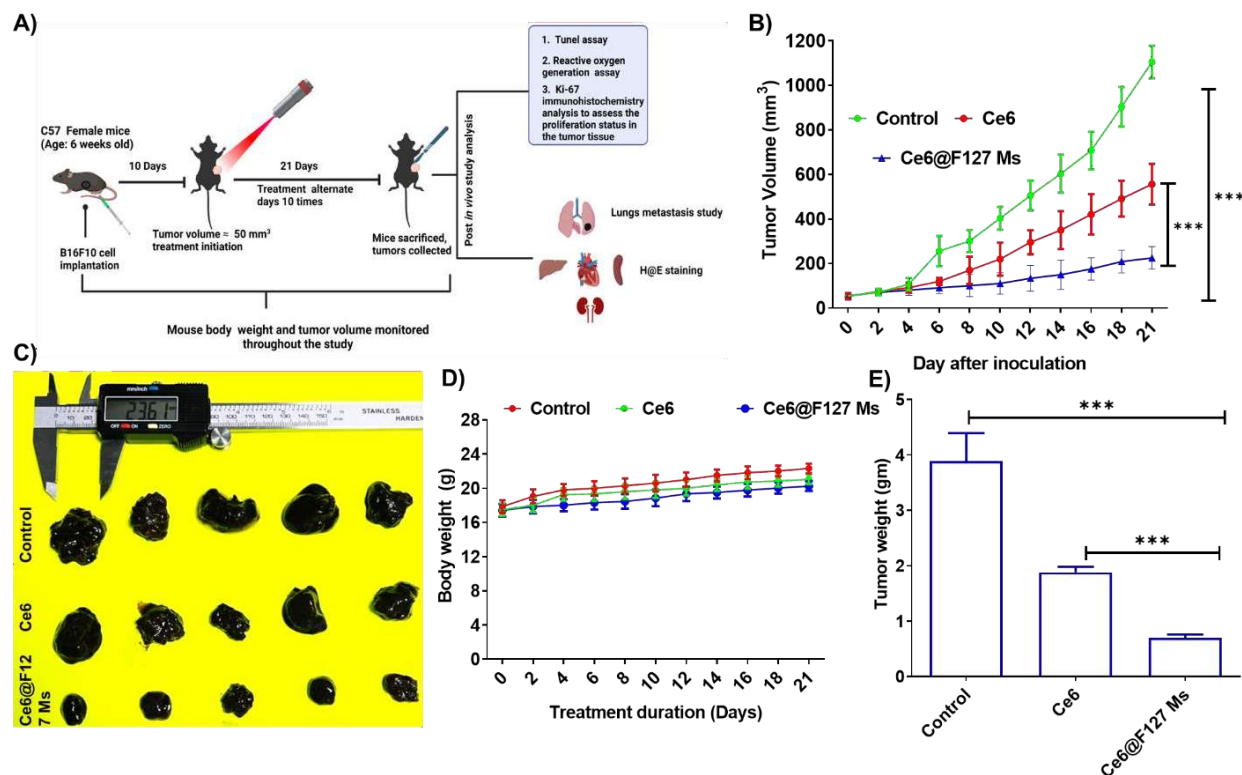
Figure 2.9 Schematic representation of the experimental protocol followed for the in vivo antitumor therapeutic efficacy of Ce6, Ce6@F127 Ms in the B16F10 cell implanted tumor-bearing mouse model (A); Tumor volume inhibition assay (B); Graphical representation image of B16F10 tumor-bearing mice(C); Body weight of B16F10 tumor-bearing mice (D); Tumor weight of B16F10 tumor-bearing mice (E).

2.10.6 Mechanism of Antitumor Effect Mediation by Nanoparticles in Mice

In the TUNEL assay, an increased number of TUNEL-positive cells (green) were evident in Ce6@F127 Ms subjected to laser treatment. This observation may be attributed to the nanosized nature of Ce6@F127 Ms, leading to an increased surface area, which, in turn, resulted in more TUNEL-positive cells. In the Ki-67 assay, the highest fluorescent signal was observed in the untreated and Ce6-treated groups, particularly in areas with a higher density of

blood vessels. Conversely, tumors treated with Ce6@F127 Ms, both with and without laser, exhibited low fluorescent signals, indicating a significant reduction in antigen presence in these tissues. Consequently, the enhanced antitumor activity led to a noticeable reduction in the number of proliferating cell populations.
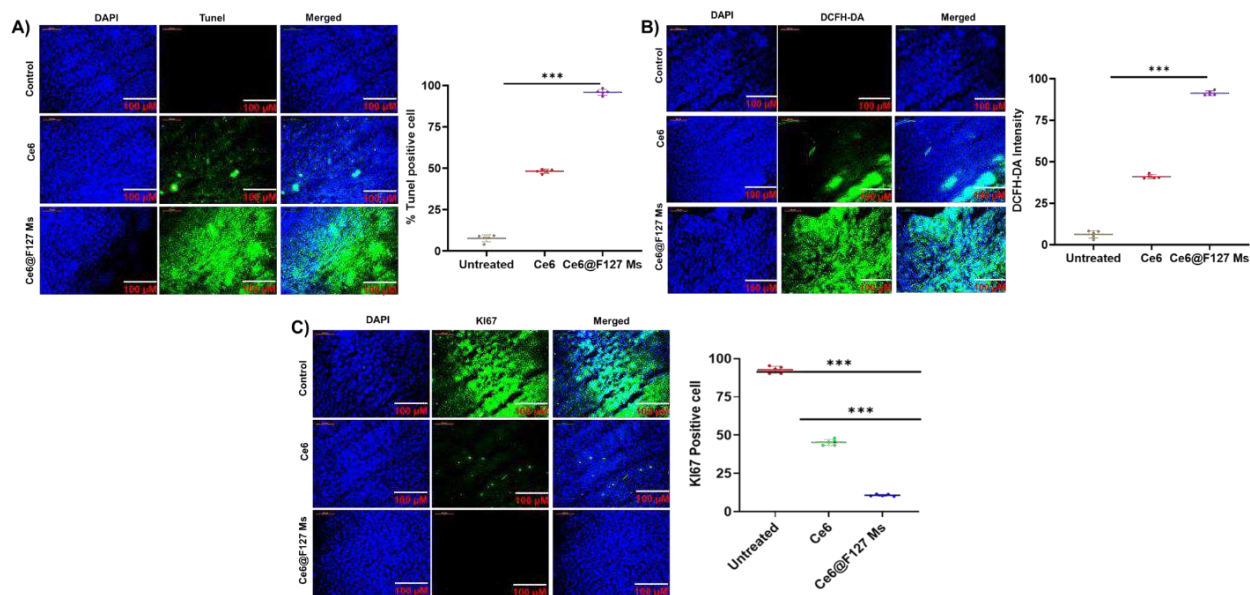
Figure 2.10 Immunohistochemistry analysis. Representative images of TUNEL assay in the tumor sections of isolated tumors (A); Ki67 assay (B); ROS generation assay (C);

2.10.7 Lungs metastasis

BrdU, an analog of the nucleoside thymidine, serves as a crucial marker in the BrdU assay for identifying proliferating cells. On examining BrdU-stained lung sections under a microscope, a notable finding revealed a significantly greater number of proliferating endothelial cells in metastasized lungs in the untreated and Ce6 group compared to Ce6@F127 Ms. This could be attributed to the entrapment of cancer cells in the vessels, leading to the formation of metastatic regions in the lungs. Another noteworthy observation in lung tissue pertained to lung

metastasis observed upon the demise of mice. Subcutaneous injection of nearly 1.5 million melanoma cells induced skin melanoma, resulting in visible melanoma black nodules on the lungs in the control and Ce6. The growth of cancer cells on the lungs significantly decreased in the treatment groups, as confirmed by reduced fluorescence intensity in the BrdU assay. Furthermore, the collagen level was reduced in the Ce6@F127 Ms treated group compared to the untreated group. The weights of the lungs were recorded as 1.2 ± 0.02 g, 0.51 ± 0.02 g, and 0.26 ± 0.04 g in the saline-treated, Ce6, Ce6@F127 Ms groups, respectively.
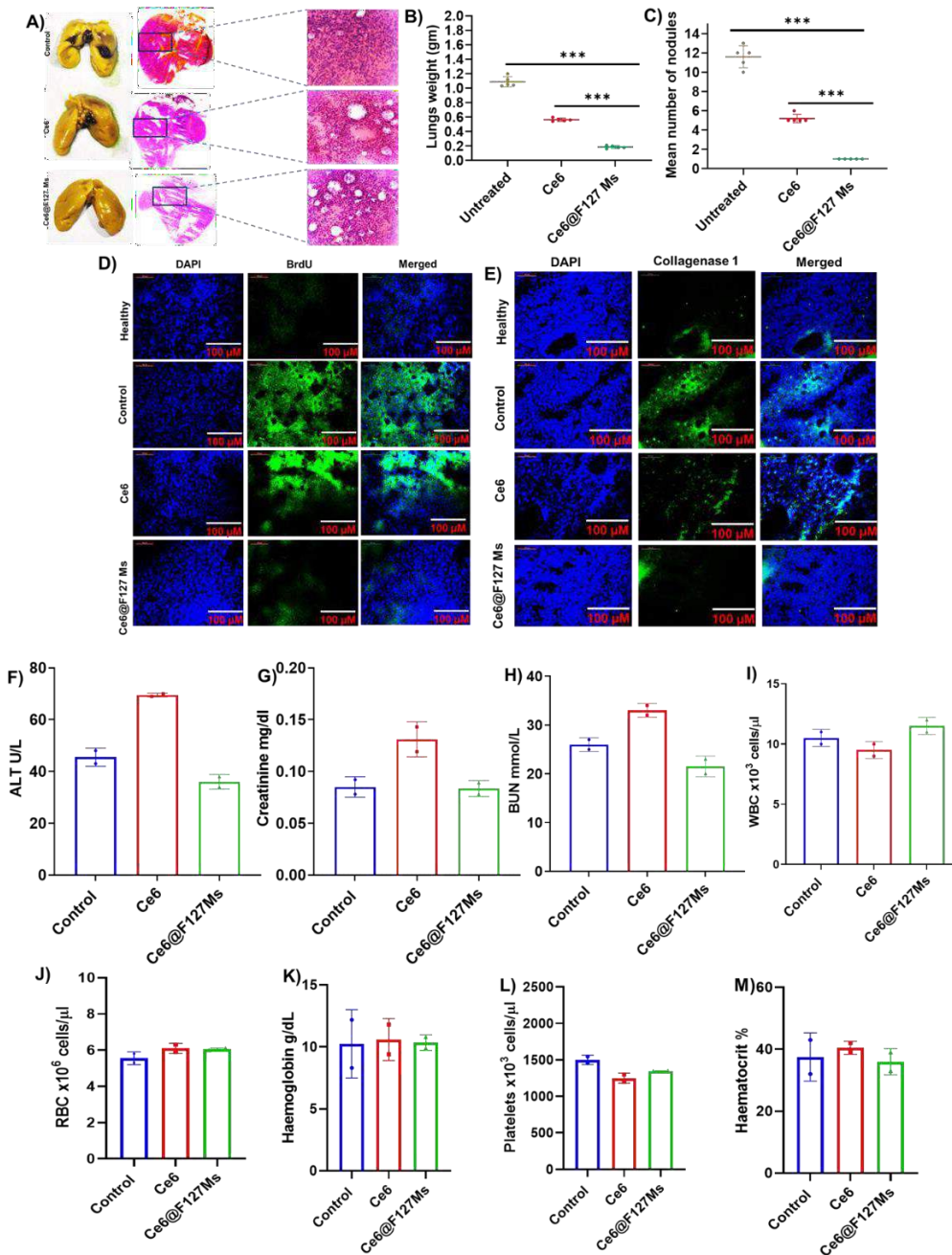
Figure 2.11 Suppression of lung metastasis. H&E staining of the lung section showed more proliferation of cells compared to treatment groups (A); Bar graph of lungs weight and lungs nodules (B &C); The proliferation of the metastatic cells in lung tissue was detected by injecting BrdU into the tail vein, followed by lung resection 2 h and stained with anti-BrdU

antibody (D); The section was stained with collagen1 antibody to see the collagen level in the lung (E); Blood biochemistry analysis of Ce6 and Ce6@F127 Ms (F-M).

2.10.8 Biosafety of Nanoparticles

Photodynamic therapy emerges as a minimally invasive and remarkably precise treatment method, circumventing the constraints linked with surgery, radiation, and chemotherapy. To gauge the safety of our devised photodynamic therapy, we conducted an analysis of diverse serum biochemical indicators, such as blood urea nitrogen, creatinine, alkaline phosphatase, alanine aminotransferase, and total proteins. Our findings indicate that all serum biochemical parameters measured post-treatment remained within normal ranges, affirming the non-toxic nature of the intravenous formulations to the liver and kidneys. Histological examinations of all organs post each treatment, as depicted in Fig. 11E, demonstrated no observable changes, indicating the safety of the combined modality. Notably, no inflammatory or immune responses were observed in isolated organs, further confirming the safety of the PDT approach.

2.10.9 Conclusion

Ce6@F127 Ms were prepared and their physicochemical characteristics, such as a solubility and photoactivity in aqueous media, cellular internalization and tumor targeting efficiency, were investigated. Ce6@F127 Ms exhibited high solubility and fluorescence intensity in aqueous media compared to free Ce6. Moreover, the ability of Ce6@F127 Ms to generate singlet oxygen was maintained in aqueous media. Ce6@F127 Ms demonstrated enhanced cytotoxicity against B16F10

and FaDu cells in vitro compared to free Ce6 due to its enhanced internalization rate. Moreover, due to its high tumor targeting efficiency, Ce6@F127 Ms strongly suppressed B16F10 xenograft tumor growth in after i.v. injection. On the basis of these results, we conclude that this Ce6@F127 Ms overcomes many of the problems associated with photosensitizers, such as poor solubility, cellular internalization and tumor targeting efficiency is towards late apoptosis side (almost 3-fold higher compared to free Ce6 treatment).

Chapter 3

Concurrent Delivery of Paclitaxel and Chlorin e6 to Tumors Using Albumin/PLGA Nanoparticles for NIRLight-Triggered Chemo/Photodynamic Therapy
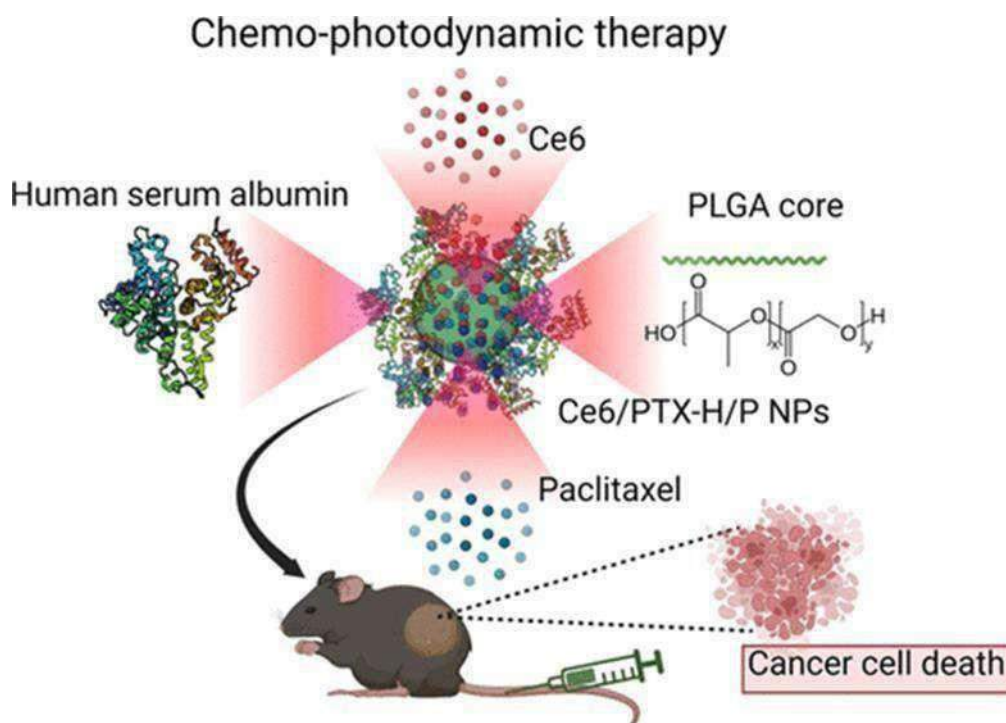
3.1 Introduction

Photodynamic therapy (PDT) is one of the emerging treatment options for neoplastic tumors. PDT employs two external components, a photosensitizer (PS) and light of a specific wavelength. Upon irradiation PS is activated and passes its energy to the nearby molecular oxygen. The photochemical reaction produces singlet oxygen ($^1O_2$) that causes cell death in PDT. Therefore, the presence of three components, light, PS, and intracellular oxygen, is essential for PDT to be effective. In their low-energy ground state, the photosensitizer molecules absorb light energy and transfer the energy to the excited singlet state. The excited state of the singlet photosensitizer is highly transient with a life span in the nanosecond range, which is stabilized either by radiating fluorescence or by transitioning into the triplet state via the nonradiative intersystem crossing process. The triplet-state PS stabilizes either by forming reactive oxygen species (HO•, O_2^-, H_2O_2) via the electron transfer type I reaction or $^1O_2$ via the energy transfer by type II reaction or by producing heat or light.

Porphyrin compounds are the widely used PSs, containing four pyrrole moieties that form a cyclic planar structure. The hematoporphyrin derivatives and Photofrins are the first-generation PSs. The molecules suffer the drawback of cutaneous phototoxicity, poor water solubility, and limited tumor accumulation. The second-generation PSs include benzoporphyrins, phthalocyanines, napthothiocyanines, and chlorins (Hak A et al. 2021), Chlorin e6 (Ce6) has multiple advantages to be used as a photosensitizing agent in cancer therapy, including water solubility, rapid clearance, near-infrared region (NIR) light-mediated activation, minimal dark toxicity, high $^1O_2$ production, and imaging capability via fluorescence emission. However, Ce6 tends to aggregate via π–π stacking, which quenches its PDT efficiency. Nanotechnological advancements enabled the preparation of various nanoparticles (NP) formulations of Ce6, either conjugated or loaded in

polymeric/macromolecular assembly. In our previous studies, Ce6 was physically entrapped or conjugated with the amphiphilic polymer, methoxy-poly(ethylene glycol)- poly- (lactide), which formed nanomicellar assembly and enhanced the photosensitizing ability of Ce6, as proven in the in vitro studies (Kumari P et al. 2017) (Kumari P et al. 2019). Poly(lactide) allows effective noncovalent interactions with Ce6 for optimal loading, and the final degradation product of poly(lactides), lactic acids, is safe and nontoxic.

Albumin NPs have been employed as a drug delivery system in cancer therapy due to albumin's excellent biocompatibility, ability to assemble into nanospherical structures, and active targeting toward tumor- associated endothelial cells and further extravasation in the tumor site. The albumin-binding 60 KDa- sialoglycoprotein gp60 is expressed in the endothelium involved in transcytoses of albumin (Schnitzer JE. 1992). Albumin-bound formulations bind to gp60 and activate caveolin-1, leading to membrane invagination and internalization of the protein-bound materials (Miele E et al. 2009). Secreted protein acidic and rich in cysteine (SPARC) is one of the matrix glycoproteins, marked as a cancer-specific biomarker that binds to albumin or albumin-bound formulations for tumor uptake. The overexpression of SPARC in breast cancer is linked to poor prognosis (Knauer D et al.2009). Like gp60, SPARC binds albumin complexes and enhances their endothelial cell internalization and transendothelial transport (Chlenski A et al. 2016). Therefore, SPARC-mediated active targeting of human serum albumin or albumin-bound nanocarriers is a promising approach for tumor-specific drug delivery.(Park CR et al. 2019).

Various nanoformulations have been fabricated recently, combining the benefits of chemotherapy and photodynamic therapeutic effects. Paclitaxel (PTX) and Ce6 were combined in various nanocarrier systems to achieve a synergistic therapeutic effect (Lee CS et al. 2013), (Zhou S et al. 2020). Human serum albumin (HSA) was used to prepare the NPs for Ce6/PTX codelivery. In

some studies, HSA had been conjugated with Ce6 to form NPs, loaded with hydrophobic PTX (Chen Q et al. 2015), (Chen Q et al. 2017), (Lee WT et al. 2022). A polylactide-core micellar system using mPEG-PLA-COOH was prepared to co-deliver paclitaxel and Ce6 in prodrug forms (Shi Y et al. 2020). The tumor inhibitory effect was significantly higher for dual drug treatment than for the monotherapies.

In our study, PTX and Ce6 were co-loaded in NPs with a hydrophobic core of poly(lactic-co-glycolic acid) (PLGA), stabilized by poly(vinylpyrrolidone) (PVP), and surface-modified with HSA. The NPs were prepared via the emulsion/solvent evaporation technique and thoroughly characterized to confirm drug loading, stability, and light-responsive drug release. Biochemical assays confirmed the reactive oxygen species (ROS) generation potential of the NPs. The in vitro cell studies were performed on murine melanoma (B16F10) and human oral squamous cell carcinoma (FaDu) using combination NPs, Ce6/PTX-H/P NPs, free Ce6 and PTX, Ce6-H/P NPs, and PTX-H/P NPs. The extensive DNA damage, ROS generation, arresting of cells in the G2/M phase, and mitochondrial destabilization induced by the Ce6/PTX combination nanomedicine led to a synergistic therapeutic response, further validated in the B16F10 in vivo anticancer mouse model.

3.2 MATERIALS AND METHODS

3.2.1 Materials

Poly(lactide)-co-glycolide (PLGA-50:50 (Lactide/ Glycolide)) (MW-15 KDa) and poly(vinyl alcohol) (PVA) (MW-30− 70 KDa, 78−90% hydrolyzed) were procured from Sigma- Aldrich (Mumbai, india). Chlorin e6 was obtained from Frontier Scientific, Inc. Human serum albumin (HSA) was purchased from the Baxter healthcare corporation was generously supplied by Dr. Reddy's Laboratory, India. Paclitaxel (PTX) was kindly gifted by Neon pharmaceuticals limited

(Mumbai, India). The cell culture media, including Dulbecco's modified Eagle medium (DMEM with high glucose), 10% heat-inactivated fetal bovine serum (FBS), trypsin, and 100 IU/Ml penicillin/streptomycin, were obtained from Himedia Laboratories (Mumbai, India). 4′,6-Diamidino-2-phenylindole dihydrochloride (DAPI) was obtained from Sigma-Aldrich (Mumbai, India).

3.2.2 Preparation of HSA-Modified Ce6/PTX-Loaded PLGA Nanoparticles

The nanoparticles were prepared using the O/W emulsification technique (Shen X et al. 2019). Briefly PLGA was dissolved in the organic phase dichloromethane (50 mg in 1 mL) and PTX and Ce6 dissolved in DMSO (1 mL) (0.4 and 0.75 mg, respectively). The above solutions were mixed. The aqueous phase contains HSA (2 mg dissolved in 3% w/v PVA). The O/W emulsion was obtained by slowly adding the aqueous phase to the organic phase dropwise and emulsified by ultra probe sonication (amplitude of 35% for 2 min) in an ice bath. The emulation was stirred overnight to evaporate the organic solvent. The obtained Ce6/PTX- H/P NPs were centrifuged at 1200 rpm for 15 min, washed with deionized water three times, and collected. The same procedure was followed to prepare the Ce6- or PTX-loaded HSA/PLGA nanoparticles, Ce6-H/P NPs, and PTX-H/ P NPs using either Ce6 or PTX.

3.2.3. Physicochemical Characterization of NPs.

3.2.3.1 Particle Size and ζ-Potential.

Particle size and ζ-potential of nanoparticles were determined using dynamic light scattering (DLS; ZetasizerZEN 3600 instrument, Malvern Instruments Ltd., U.K.). Samples were analyzed by placing 10 μL into specific cuvettes in DI water at 25 °C.

3.2.3.2 Drug Entrapment and Loading Efficiencies

The entrapment efficiency and loading percentages were calculated using the previously reported procedure. The nanoparticles were disassembled by dispersing them in ethanol/PBS. The concentrations of PTX and Ce6 were analyzed using an ultraviolet−visible (UV−vis) spectrophotometer (JASCO UV- 670, Japan) at a wavelength of 227 and 405 nm, respectively (He Z et al. 2020).

3.2.3.3 Morphology Determination by FESEM and Cryo-TEM

Lyophilized powder of the prepared NPs was used for the morphology study using field emission scanning electron microscopy (NOVA NANOSEM 450) and cryogenic transmission electron microscopy (Cryo-TEM, TEM, JEM-1200EX, JEOL, and Tokyo, Japan). The powder was evenly spread on adhesive carbon tape mounted on an aluminum stub for the SEM study. The stubs were then coated with gold of 10 nm thickness. Then, the stubs were placed at the sample holder and analyzed at a voltage of 20 kV. For the TEM study, the NPs were stained with uranyl acetate (2% w/v) and later were destained using distilled water. Furthermore, the samples were dried for 10 min by placing them on copper grids and then visualized under a microscope.

3.2.3.4 Analysis by Spectrophotometry

The kinetic stability of Ce6 in Ce6/PTX-H/P NPs was analyzed using UV−vis−NIR spectrophotometry (Jasco UV-670, Japan) for 30 days. Methanol was used to dilute free PTX and Ce6, Ce6- H/P NPs, PTX-H/P NPs, and Ce6/PTX- H/P NPs. The solutions were scanned over 200−800 nm wavelength range. FTIR analysis was performed using the KBr pellet method following the previously reported protocol using a FTIR spectrometer (Jasco-4200).The scanning range was 4000 to 400 cm $^{-1}$.

3.2.3.5 Differential Scanning Calorimetry (DSC)

The DSC analysis was performed using a thermal analysis system (DSC 60, Shimadzu, Japan) as per the previous procedure (Itoo AM et al. 2022). The analysis was carried out for Ce6, PTX, PLGA, and Ce6/PTX-H/P NPs. The samples were weighed (3−5 mg), kept in standard aluminum pans, and compressed. The pans were heated from 20−250 °C at a rate of 10 °C/min under a nitrogen atmosphere.

3.2.3.6 X-ray Diffraction (XRD) Analysis

The XRD analysis of the prepared NPs was determined using an X-ray diffractometer (ULTIMA-IV, Rigaku). The X-ray diffractometer was operated at 30 mA and 40 kV voltage. Samples were scanned at a 2θ angle.

3.2.3.7 Circular Dichroism (CD) Spectroscopy

The secondary structures of free HSA, Ce6-H/P NPs, PTX-H/P NPs, and Ce6/ PTX-H/P NPs were analyzed by circular dichroism (CD) spectroscopy (Shimadzu). The analysis was performed by dissolving the formulations at a HSA concentration of 50 μg/mL in sterile PBS (pH 7.4) and scanned at a range of 190−260 nm under a nitrogen atmosphere.

3.2.3.8 SDS-PAGE

Free HSA, Ce6-H/P NPs, PTX-H/P NPs, and Ce6/PTX-H/P NPs were subjected to gel electrophoresis studies (SDS-PAGE) to identify the presence of albumin in the NPS. Gel electrophoresis was performed by taking an aliquot of 15 μL from the prepared individual stock solutions and then mixed with 10 μL of loading buffer. The mixture was added to the gel wells and run for 180 min at 80 V along with the protein marker (Biorad, precision plus). The gel was stained

for 1 h with Coomassie brilliant blue and destained with acetic acid/methanol solution (100 mL of acetic acid and 200 mL of methanol/liter) overnight. After destaining, images were captured.

3.2.3.9 In Vitro Drug Release Study

The release study was performed for PTX/Ce6-loaded NPs before and after the laser irradiation (Kumari P et al.2020). The dissolution media were used at various pH conditions, including PBS, pH 7.4, 6.5, and 5.5. Cellulose ester membrane (MWCO 2 KDa) was used for dialysis. Ce6 or PTX at 50 μg/mL concentration was taken in the dialysis bag, laser-irradiated (660 nm) at a power density of 0.5 W/cm2 for 4 min, dipped in a beaker containing 250 mL of release medium, and stirred at 100 rpm. At predetermined time intervals, samples were collected and analyzed using an UV−visible spectrophotometer (JASCO-800, JAPAN) at 405 nm (Ce6) and 227 nm (PTX).

3.2.3.10 Evaluation of Singlet Oxygen Generation

Generation of singlet oxygen (1 O2) by Ce6, Ce6-H/P NPs, and Ce6/PTX-H/P NPs was evaluated using 9,10-dimethylanthracene (DMA), singlet oxygen sensor green (SOSG), and p-nitroso dimethylaniline (RNO) as a fluorescent dye (Paul M et al. 2023). The formulation containing Ce6 (1.5 μg) dissolved in 1 mL of DMSO/PBS solution (pH 7.4) was mixed with DMA (20 mM) and kept for equilibration for 10 min. The mixture was irradiated using a laser source of 660 nm at an intensity of 0.5 W/cm2 at various time intervals. The reduction in the fluorescence intensity of DMA was measured after irradiation at ex/em. 360/380−550 nm wavelengths. The change in the intensity at various time intervals was measured using a spectrofluorophotometer (SpectramaxTM, microplate reader, Molecular Devices). For SOSG, free Ce6 and the Ce6-H/P NPs and Ce6/PTX-H/P NPs at a concentration of 0.25 μM were dissolved in PBS pH 7.4. SOSG (2.5 μM) was mixed with the NP solution, and all the samples were irradiated using a laser source of 660 nm wavelength

at an intensity of 0.5 W/cm2. The samples were read using a spectrofluorophotometer at ex/em. 494/534 nm wavelengths of lights.

3.2.3.11 Hemolytic Toxicity Study

In vivo blood toxicity of the Ce6/PTX-H/P NPs was assessed by the hemolysis study (Kumari P et al. 2020). Briefly, blood (5 mL) was drawn from albino rats using capillaries by eye puncture and collected in heparinized tubes. The red blood cells (RBCs) were separated from the blood by centrifuging at 3000 rpm for 30 min at 4 °C. The RBCs were washed and resuspended in 0.9% w/v NaCl solution at 5% v/v suspension. The Ce6/PTX-H/P NPs in NaCl solution were incubated with RBC suspension at a concentration range of 0−250 µg/mL for 1 h at 37 °C. NaCl (0.9% w/v) and Triton-X 100 (1%) solutions were the negative and positive controls, respectively. After 40 min of incubation, the samples were centrifuged for 10 min at 4000 rpm. The absorbance of the supernatant was taken at the absorption maxima of hemoglobin at 540 nm using a microplate

$$\% \text{ hemolysis} = \frac{\text{Abs of sample} - \text{Abs of negative control}}{\text{Abs of positive control} - \text{Abs of negative control}} \times 100$$

reader (SpectramaxTM, Molecular Devices). The % of hemolysis was calculated using the equation given below

3.4 CELL-BASED STUDIES

The oral squamous cell carcinoma (FaDu) cell line and human embryonic kidney cells (HEK-293) were purchased from the American type culture collection (ATCC). The Eagle's minimum essential medium (MEM) was purchased from Himedia Labs (India). Murine melanoma cancer cells (B16F10) were procured from the National Center for Cell Sciences (NCCS, Pune, India). B16F10 cell lines were grown in the cell media (DMEM with high glucose added with 10% FBS and 100 IU/Ml penicillin/streptomycin) at 37 °C and 5% CO_2.

3.4.1 In Vitro Cytotoxicity Study

B16F10 cells, HEK-293 cells, and FaDu cells were seeded in a 96-well plate at a density of 1×10^4 viable cells/well overnight. Next, the cells were washed with PBS, pH 7.4, and incubated with PTX and PTXH/P NPs at PTX concentrations of 0−50 μg/mL and free Ce6 and Ce6/PTX-H/P NPs at Ce6 concentrations of 1.56−100 μg/mL. After 12 h, the cells were irradiated using a 660 nm laser (0.5 W/cm2) for 5 min and incubated for 12 h. The medium was discarded, and a solution containing 50 μL of MTT in PBS (pH 7.4) was added to each well, followed by 4 h of incubation. DMSO (150 μL) was added for solubilization of formazan crystals. The absorbance of the samples was measured using a microplate reader at a wavelength of 570 and 630 nm. The cytotoxicity (cell viability %) was calculated as per the following equation

$$\text{cell viability } (\%) = (\text{absorbance of treated cells} / \text{absorbance of control cells}) \times 100$$

3.4.2 Combination Index Analysis

Inhibitory concentrations (IC10−IC90) of Ce6 and PTX in Ce6/PTX-H/P NP-treated cells after 48 h of incubation were calculated using Graph Pad Prism 9.0.2. CompuSyn software was used to develop the graph between the combination index (CI) and fraction affected (Fa). A CI value below 1 is considered a synergistic effect, with 1 being an additive effect and above 1 being an antagonistic effect. combination index (CI) = D1/A1 + D2/A2 where A1: dose of free Ce6 to produce specific percent cell killing alone; D1: dose of free Ce6 to produce % cell killing in combination with PTX-H/P NPS; A2: dose of PTX to produce % cell kill alone; and D2: dose of PTX-H/P NPS to produce % cell kill in combination with Ce6 in Ce6/PTX-H/P NPs.

3.4.3 Cellular Uptake by Flow Cytometry.

The cellular uptake of free Ce6, Ce6-H/P NPs, and Ce6/PTX-H/P NPs was determined by flow cytometry (BD FACS). The study was performed on B16F10 and FaDu. Cells were cultured in a 6-well plate at a density of 0.8×10^6 cells/well. After cells were attached to the wells, the formulations at Ce6 equivalent concentrations of 6 µg/mL were added to each well and kept for incubation for 1 and 4h. After the incubation, the medium was discarded and washed with sterile PBS. Then, the cells were trypsinized, with centrifugation at 1000 rpm for 7 min at 4 °C, and the pellets were resuspended in 0.5 mL of sterile PBS. The samples were analyzed using flow cytometry. The gated cell population was 10,000 for the study. FlowJo software was used to analyze histograms and the geo mean fluorescence of the formulations was plotted as a bar graph. The experiment was conducted in triplicates.

3.4.4 Confocal Microscopy

B16F10 cells and FaDu cells were grown on a circular coverslip in a 12-well tissue culture plate at 50,000 cells/well density. After 48 h, cells were treated with free Ce6 and formulations containing 25 µg/mL Ce6 for 1−4 h. After washing, the cells were incubated with DAPI (1 µg/mL) solution for 5 min before fixing the cells with 4% paraformaldehyde for 15 min. After fixation, coverslips were mounted with Fluoromount-G and observed under a confocal microscope (TCS SP8, Leica Microsystems, Germany) using the Ce6 filter at excitation and emission wavelengths of 495 and 520 nm, respectively. The photographs were processed using Image J software.

3.4.5 DNA Fragmentation Assay

FaDu and B16F10 cells were grown in a 6-well tissue culture plate (1×10^6 cells per well) and incubated for 24 h. On the following day, cells were treated with Ce6, PTX, Ce6-H/P NPs, PTX-

H/P NPs, and Ce6/PTX-H/P NPs (Ce6 concentration of 10 μM) and incubated for 24 h. In between, the cells were irradiated using a 660 nm laser (0.5 W/ cm2) for 5 min after 12 h. The DNA was extracted using the GSure DNA genomic isolation kit and loaded on a 1.5% agarose gel containing ethidium bromide (1 μg/mL). The DNA was run in the gel electrophoresis apparatus using a mini submarine electrophoresis unit. The pattern of DNA fragments was observed and photographed by using a Fusion Pulse gel doc system (Vilber, Eberhardzell, Germany).

3.4.6 Nuclear Staining

Nuclear staining was performed on B16F10 and FaDu cells, incubated overnight at a density of 1 $\times$ 105/well on 6-well tissue culture plates, and treated with Ce6, Ce6-H/P NPs, and Ce6/PTX -H/P NPs at a Ce6 concentration of 10 μM and PTX and PTX-H/P NPs at a PTX concentration of 5 μM. After 12 h, cells were irradiated using a 660 nm laser (0.5 W/cm2) for 5 min and continuously incubated for an additional 12 h. The treated cells were rinsed with PBS, fixed, stained using 10 μg/mL DAPI and 100 μg/mL acridine orange solution, and visualized using a fluorescence microscope (Leica Microsystems, Germany).

3.4.7 ROS Detection Assay

Cells were seeded at a density of 1 $\times$ 104 cells/well in 6-well plates in the complete media (Kumbham S et al. 2022). On the following day, the cells were treated with Ce6, PTX, Ce6-H/P NPs, PTX-H/P NPs, and Ce6/PTX -H/P NPs at a Ce6 concentration of 10 μM. At 12 h post-incubation, cells were irradiated using a 660 nm laser (0.5 W/cm2) for 5 min and kept under incubation for an additional 12 h. Next, 2′,7′- dichlorofluorescein diacetate (5 μM) was added and incubated for 30 min at 37 °C, followed by visualization under a fluorescence microscope after thorough washing of the adherent cells with PBS, pH 7.4.

3.4.8 Mitochondrial Membrane Potential

B16F10 and FaDu cells were seeded in a 6-well tissue plate (cell density of 1×105 cells/well) in complete media. (Kumbham S et al. 2022). The cells were subsequently treated with Ce6, Ce6-H/P NPs, and Ce6/PTXH/P NPs at a Ce6 concentration of 10 µM with incubation. The free PTX and the PTX- H/P NPs were added at a PTX concentration of 5 µM. The incubation protocol was as follows: 24 h of incubation at 37 °C with laser irradiation (660 nm, 0.5 W/cm2) for 5 min after 12 h. Next, the cells were washed with PBS, dyed with JC1 (2 µM) for 30 min, and visualized under a fluorescence microscope (Leica Microsystems, Germany).

3.4.9   Apoptosis Assay

The seeded cells were exposed to Ce6 and Ce6 formulations (Ce6 concentration of 10 µM) and PTX and PTX-H/P NPs (PTX concentration of 5 µM) for 24 h. The cells were laser-irradiated using a 660 nm laser at a power of 0.5 W/cm2 after 12 h for 5 min and incubated for an additional 12 h. The assay was carried out by staining with PI and annexin V-FITC according to the protocol given in the TACS Annexin V assay kit and following the previously reported procedure (Vysyaraju NR et al. 2022). The extent of apoptosis was evaluated by flow cytometry (FACS Aria III, BD Biosciences, and the USA).

3.4.10 Cell Cycle Analysis

Cells were seeded (0.2×106 cells/wells) in a 12-well plate. On the next day, the cells were exposed to Ce6, Ce6-H/P NPs, and Ce6/PTX-H/P NPs at a Ce6 concentration of 10 µM for 12 h (Pulya S et al. 2022). The concentration of PTX added was 5 µM in free PTX- and PTX-H/P NP-treated wells. Next, the cells were irradiated using a 660 nm laser (0.5 W/cm2) for 5 min and further incubated for an additional 12 h. Then, the cells were fixed with ice-cold ethanol overnight.

Furthermore, the cells were collected by centrifugation and washed, and then, cellular DNA was stained for 1 h with RNAse (200 μg/mL) in PBS (pH 7.4). The progression of the treated cells through the cell cycle was analyzed by flow cytometry (FACS ARIA III, BD Biosciences).

3.5 IN VIVO STUDY

3.5.1 Pharmacokinetic (pK) Study.

The pK analysis of free Ce6 and Ce6/PTX-H/P NPs was performed in male Wistar rats (220 ± 20 g). The animals were housed in an environment that provided them with natural light and unfettered access to food and drink at a RH of 55% and a temperature of 25 °C. Prior to injection, the rats were randomly segregated into three groups (control, free ce6, and Ce6/PTX-H/P NPs, n = 3) and starved for 10 h but given free access to water. Each group of rats received the same quantity of Ce6 (5 mg/kg) via the tail vein. Subsequently, blood samples of about 0.5 mL each were withdrawn from the retro-orbital plexus at predetermined time periods into heparinized tubes. Plasma was obtained using centrifugation at 10,000 rpm for 5 min and stored at −20 °C for further examination. To determine the Ce6 concentration, 200 μL of frozen rat plasma was taken, put in a 1.5 mL plastic tube, and vortexed for 10 min with triple volume of cold acetonitrile to separate plasma protein, followed by centrifugation. Afterward, the supernatant (20 μL) was taken and examined for chromatographic analysis employing an HPLC system (Shimadzu) with a mobile phase of trifluoro acetic acid/acetonitrile (pH 2.6) (50/50, v/v) and a reverse- phase C18 Phenomenex column (150 nm × 4.4 nm, 5 μm) at a column oven temperature of 40 °C and eluted at a flow rate of 0.6 mL/min. pK solver software was used to calculate the pharmacokinetic parameters, and Student's t-test was used to establish the statistically significant difference (Bhatt H, Ghosh B, Biswas S.2020). The blood samples (10 μL) were collected from the eyes of the mice at different time points (1, 3, 6, 12, 24, 48 h), using a heparincoated capillary tube. The blood

samples were mixed with a detergent solution (1% Triton X-100, DMSO/PBS/DW = 5:4:1) at a ratio of 1:9, and the fluorescence intensity of Ce6 was measured using IVIS Lumina (Tan P et al.2021).

3.5.2 Tumor Inhibition Study

Male C57BL/6J mice weighing 18−20 g were obtained from the National Institute of Nutrition (NIN), Hyderabad, India. Mice were kept in a stable environment at a temperature of 19−23 °C with 12 h nocturnal−diurnal cycles and a relative humidity of 50−60% and given a week to adjust to the conditions before beginning the experiment. Animals had unrestricted access to food and water. The institute's Animal Ethics Committee approved the experimental procedures. The mouse melanoma model was created by injecting B16F10 cells subcutaneously into the right hind leg of mice at a cell density of 1×10^6 /100 µL of sterile phosphate buffer saline (pH 7.4) (Son J et al. 2019). A tumor inhibition study was performed after the tumor volume reached ~70 mm3 . The study was conducted by randomizing the mice into six groups, control (saline), Ce6, PTX, Ce6-H/P NPs, PTX-H/P NPs, and Ce6/PTX-H/P NPs, containing five mice in each group. After the intravenous tail injection of the drug/formulations, administered at a dose of 5 mg/kg, each mouse was subjected to laser irradiation using a diode having a wavelength of 660 nm with a power density of 0.5 W/cm2 for 5 min after 12 h. The mice's tumor volume and body weight were monitored regularly every other day for 21 days. At the end of the study period, mice were sacrificed by cervical dislocation, and the tumor mass was collected surgically and weighed.

3.5.3 Immunohistochemistry

3.5.3.1 TUNEL Assay

Frozen tumors were sectioned at 5 µm thickness with a cryostat (Leica Biosystems, Germany) and fixed with 4% paraformaldehyde for immunohistochemistry (Bhatt H et al. 2019). TUNEL assay was performed on the sectioned tumors by treating them with a TUNEL (FragEL DNA Fragmentation Detection Kit, Merck, and Darmstadt, Germany) reagent. The green fluorescence produced by TUNEL (+) cells was observed in the FITC filters using a fluorescence microscope. ImageJ software was used to capture and analyze the images.

3.5.3.2 ROS Generation

Mice were injected with free Ce6, Free PTX, Ce6-H/P NPs, PTX-H/P NPs, Ce6/PTX-H/P NPs, and NPs at an equivalent dose of 5 mg/kg intravenously; the development of ROS in tumors in tumor-bearing mice (60 mm3) was evaluated by intratumorally injecting the DCFH-DA fluorescence probe. At 24 h post-injection, tumors were irradiated for 5 min (660 nm, 0.5 W/cm2 for 5 min). The mice were sacrificed, and the collected tumors were frozen under tissue freezing OCT media. The tumor tissues were sectioned (5 µm thickness) and visualized under a fluorescence microscope using the FITC channel.

3.5.3.3 H&E Staining

Tissue sections of 4 µm thickness were subjected to hematoxylin and eosin (H&E) staining. Before staining, the sections were processed with xylene, different concentrations of alcohol (30−100%), and water. Hematoxylin was used to stain nuclei, followed by washing. Cytoplasm was stained using Eosin. Finally, after staining, sections were dehydrated with alcohol and xylene. The slides

were fixed with mounting media (Fluoromount-G) before visualization under a microscope with 10× magnification and bright field exposure (Leica, Germany)

3.6 Results and Discussion

3.6.1 Preparation and characterization of Ce6/PTX-H/P NPs NPs

Human serum albumin is an attractive drug carrier known for its biocompatibility, loading capacity for hydrophobic chemotherapeutic agents, and tumor-targeting via SPARC/gp60-mediated transcytosis. Our study utilized dual reservoirs, albumin, and PLGA, to physically entrap two hydrophobic drugs, paclitaxel and Ce6. The HSA constituting NPs surface would allow active targeting of NPs to the tumor, and the PLGA core would enhance the capability for dual drug incorporation to obtain a synergistic therapeutic response.

The PLGA NPs stabilized by HSA and the surfactant PVA on the surface loaded both drugs in a ratio of Ce6/PTX. ~1.1 displaying particle size and surface charge of 160.21 ± 2.32 nm and -11.05 ± 1.12 mV, respectively. The characteristic features of Ce6-H/P NPs, PTX-H/P NPs, and Ce6/PTX-H/P NPs, including particle size, polydispersity, zeta potential, percent drug entrapment, and loading, have been included in Table S1. Both Ce6 and PTX were encapsulated to greater than 70 %, with loading efficiencies of 3.06 ± 0.25 % (PTX) and 5.39 ± 1.15 % (Ce6). TEM and SEM micrographs revealed that all three, Ce6, PTX, and Ce6/PTX-loaded NPs were nano-sized and spherical structures. The NPs had negative zeta values, ascertaining their stability in an aqueous environment. The hydrodynamic diameter and surface potential of the NPs are shown. The Ce6/PTX-H/P NPs had a zeta potential of -11.05 ± 1.12 mV, while the Ce6-H/P NPs had a zeta potential of -9.17 ± 1.19 mV. There was no significant change in the Ce6 and PTX signals in the NPs. Ce6/PTX-H/P NPs at 4 °C from day 1 to day 24. The particle size of all the NP formulations was ~ 160-180 nm, with a

homogeneous distribution (PDI values 0.15-0.35) and a negative zeta potential. The NPs size and drug loading remained constant over 30 days at 4 °C. However, a two-fold decrease in particle size and drug loading was observed when stored at room temperature, indicating the recommended storage condition for NPs to be at 4 °C. The characteristic absorbance peak in the UV-vis spectra of PTX and Ce6 was at 261 nm and ~ 404 and 665 nm, respectively. The Ce6/PTX- H/P NPs in PBS displayed similar peaks, indicating their structural integrity after loading in the NPs.
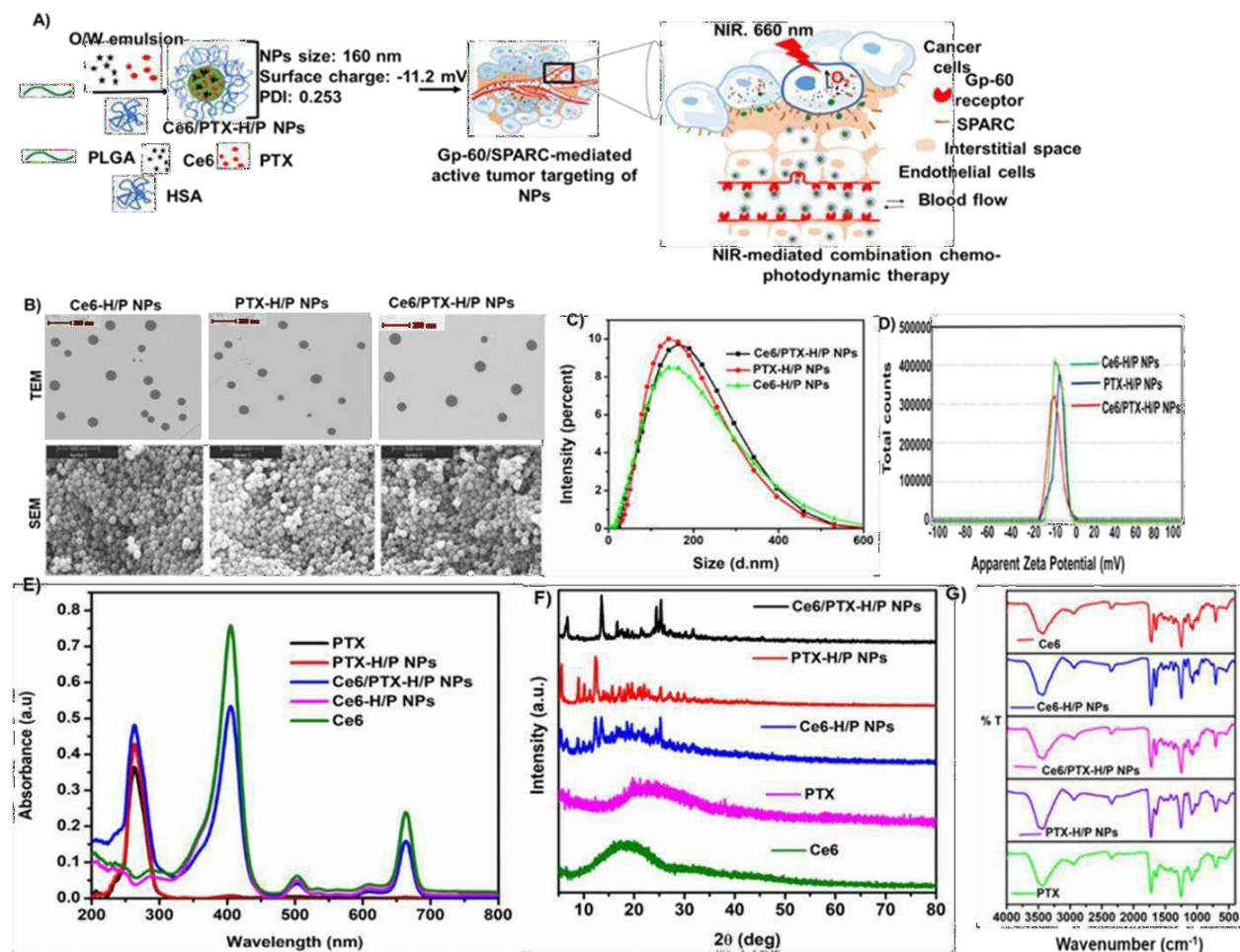
Figure 3.1 Schematic illustration for the preparation of PTX and Ce6-coloaded © nanoparticles (Ce6/PTX-H/P NPs), and cancer cell targeting to realize synergistic chemo-

PDT effect (A); transmission electron microscopic and scanning electron microscopic pictures of Ce6-H/P NPs, PTX-H/P NPs, Ce6/PTX-H/P NPs(B); particle size distribution of Ce6-H/P NPs, PTX-H/P NPs, Ce6/PTX-H/P NPs (C); zeta potential graph of Ce6-H/P NPs, PTX-H/P NPs, Ce6/PTX-H/P NPs, determined by dynamic light scattering technique (D); UV absorption spectra of PTX, Ce6, Ce6-H/P NPs, PTX-H/P NPs, Ce6/PTX-H/P NPs (E); XRD spectra of PTX, Ce6 Ce6-H/P NPs, PTX-H/P NPs, Ce6/PTX-H/P NPs (F); FT-IR Spectra of PTX, Ce6, Ce6-H/P NPs, PTX-H/P NPs (G).

In the FTIR spectra, the characteristic transmittance peak of Ce6 was found at 1715.9 cm−1 at the wavenumber corresponding to the carbonyl group. The FTIR spectra of PTX showed characteristic peaks at 1653 cm−1 (C-C stretching), 1225 cm−1 (C=N stretching), and 1070 cm−1 (C-O stretching). Ce6/PTX- H/P NPs showed peaks at 1236.1, 1744.2, and 3342.7 cm−1 wave numbers, representing amine and OH group stretching vibrations, respectively (Figure 3.1 G). The XRD analysis pattern, represented in (Figure 3.1F), demonstrated that PTX and Ce6 are amorphous as no characteristic 2θ peaks were observed. The diffraction pattern of the Ce6/PTX-H/P NPs demonstrated many characteristics peaks, ensuring drug encapsulation in the nanocarrier. X-ray photoelectron spectroscopy (XPS) analysis was conducted to determine the formulated nanoparticles' elemental composition and chemical states. The spectra show that the characteristic peaks of C 1 s, N 1 s, and O 1 s, are 284.9 eV, 399.3 eV, and 531.9 eV, respectively. The percentage of elements in Ce6/PTX-H/P NPs was 74.23 % (C1s), 23.52 % (O1s), 2.25 % (N1s); Ce6-H/P NPs contain 73.23 % (C1s), 26.77 % (O1s) and PTX-H/P NPs contain 70.30 % (C1s), 25.70 % (O1s), and 4.00 % (N1s) respectively (Figure 3.2C). The DSC thermograms of the free drugs, Ce6/PTX-H/P NPs, Ce6-H/P NPs, and PTX-H/P NPs formulation indicated the shift in the endothermic peak

in the final Ce6/PTX-H/P NPs, (50 ºC) from the endothermic peak obtained in free PTX (97 ºC)

and exothermic peak obtained in DTX (220 ºC) as represented in Figure 3.2D.
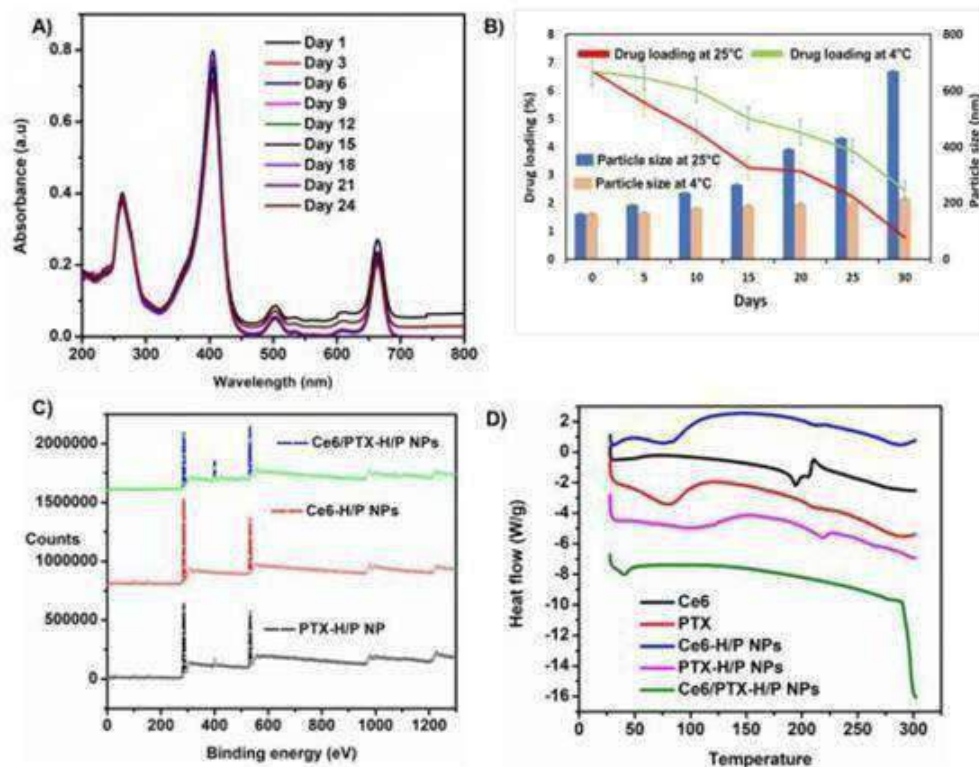
Figure 3.2 Kinetic stability study of Ce6/PTX-H/P NPs, at 4° C (A); storage stability study of Ce6/PTX-H/P NPs, at 4° C (B); XPS spectra of Ce6/PTX-H/P NPs. Ce6-H/P NPs, PTX-H/P NPs (C);DSC thermogram of PTX, Ce6, Ce6-H/P NPs, PTX-H/P NPs, Ce6/PTX-H/P NPs (D)

CD spectroscopy was employed to analyze protein structure (Figure 3.3A). The peaks at 208 and

216 nm indicated the α-helical and β-sheet structures, respectively, as reported previously (Wen Y

et al. 2016). There was hardly any difference between natural HSA, Ce6/PTX-H/P NPs in the

proportion of α-helix, β-sheet, and random coil, thus indicating that the protein nanoparticles

method did not alter the secondary protein structure. The decrease in the CD signal in all the NPs was attributed to the binding of other molecules that induced conformational changes in the structure. However, the protein secondary structure in the NPs remained predominantly α-helical. Further, distinct bands of albumin at ~66 KDa from disassembled NPs indicated the structural integrity of the protein in the NPs (Figure 3.3B).

The hemolysis study was performed to analyze the cytocompatibility of the NPs. The highest tested concentration of Ce6/PTX-H/P NPs (250 µg/ml) was 4.8 % hemolytic, less than the maximum tolerated hemolysis of 10 % wrt triton X treatment (Figure 3. 3C).

The in vitro release of Ce6 from the Ce6/PTX-H/P NPs at pH 7.4 was 36 % in 48 hours before irradiation, which improved to 56 % in 48 h (Figure 3.3D). Similarly, PTX release was enhanced from 40 % to 44 % after irradiation. At pH 4.6, Ce6/PTX-H/P NPs showed a release of 78 % at 48 hours (Figure 3.3E). The continuous release of drug from nanocarriers is an important criterion for nanomedicines effectivity, which would reduce the side effect and improve treatment efficacy. The release pattern was indicative of the fact that the drug was bound uniformly in the NPs core.
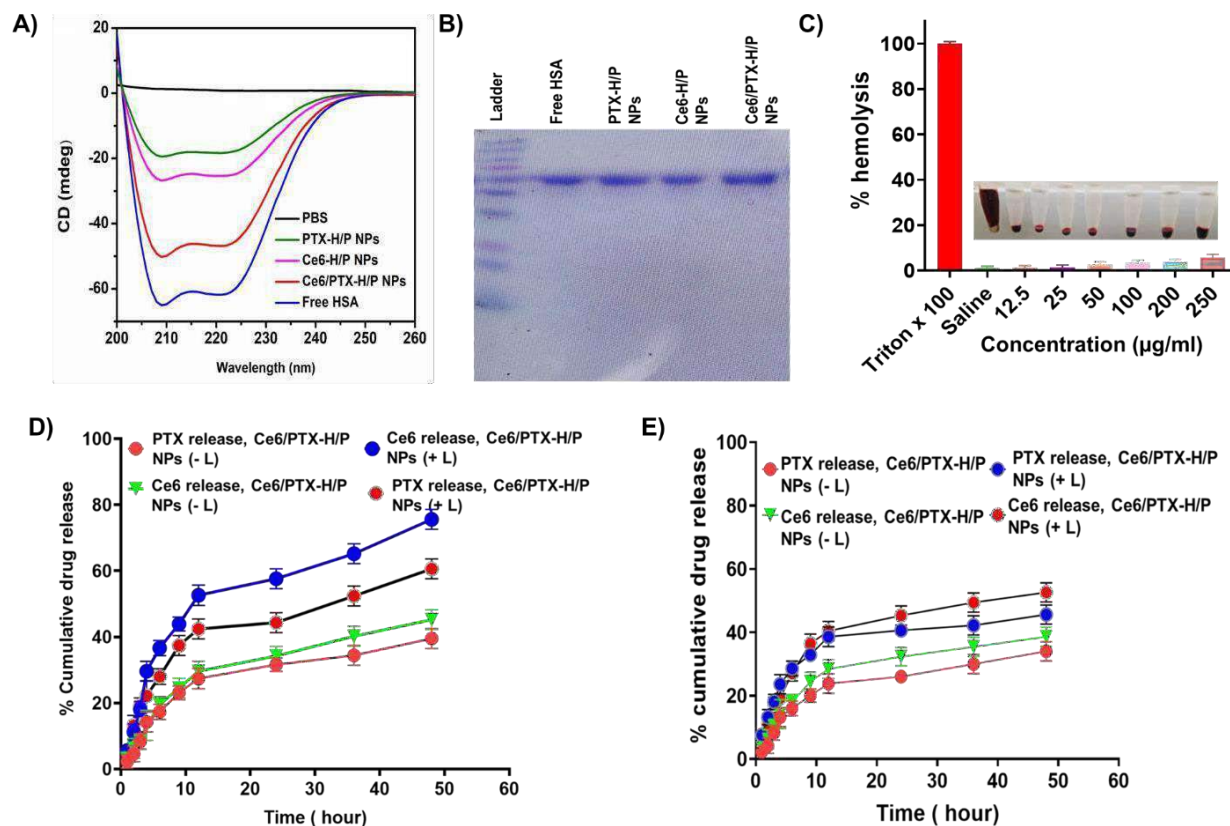
Figure 3.3 Circular dichroism spectra of free HSA, Ce6-H/P NPs, PTX-H/P NPs, and Ce6/PTX-H/P NPs (A); SDS PAGE of free HSA, Ce6-H/P NPs, PTX-H/P NPs, and Ce6/PTX-H/P NPs (B); hemolytic study of Ce6/PTX-H/P NPs (C); in vitro Ce6 and PTX release from Ce6/PTX-H/P NPs in phosphate buffer saline (pH 4.6) and (pH 7.4) (D) and (E).

3.6.2 Evaluation of the photoactivity and singlet oxygen generation

The free Ce6, Ce6-H/P NPs, and Ce6/PTX-H/P NPs showed DMA signals of 250000, 120000, and 90000 after laser irradiation (399 nm, 0.5 W/cm2) for 14 min (Figure 3A and 3B). The irradiation time- dependent decrease in DMA signals indicated an eventual increase in the production of 1O2. The free Ce6 in PBS is aggregated due to their strong π-π interaction, resulting in poor 1O2-

generating efficiency (Figure 3.4A). The 1O2 generation was the highest in Ce6/PTX-H/P NPs in all irradiation time points, indicating the non-aggregated amorphous presence of Ce6 in the NPs (Figure 3.4B). Next, 1O2 generation was evaluated using RNO in the presence of histidine. Upon irradiation, Ce6 generated 1O2, which caused the oxidation of RNO in the presence of histidine. The capture of 1O2 by the imidazole ring of histidine forms a transannular peroxide intermediate, which reacts further with RNO to realize photobleaching. The free Ce6 caused maximum bleaching of RNO absorbance than nanoformulations with increasing irradiation time (Figure 3.4C). The generated 1O2 could trap in the NPs, causing less interaction with histidine and less bleaching of RNO absorbance. The 1O2 yield of Ce6/PTX-H/P NPs was 3-fold higher than free Ce6 in the SOSG study (Figure 3.4D). The accessibility of free Ce6 and generated 1O2 in aqueous media could be one reason for its enhanced SOSG signal. The SOSG signal was less in the NPs, possibly due to their assembled structure in the buffer preventing the production of 1O2 and their release in aqueous media to react with SOSG.
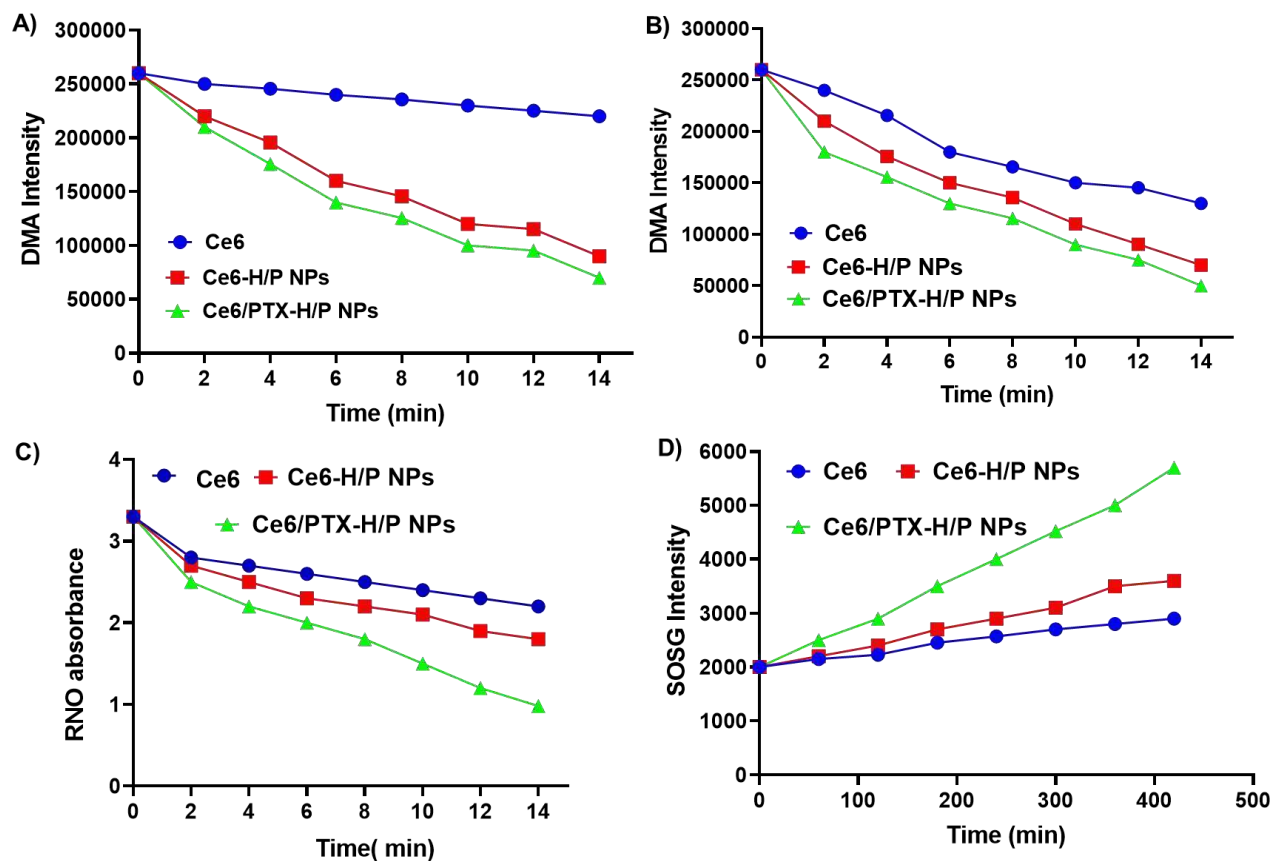
Figure 3.4 Biochemical analysis of Ce6-mediated ROS generation. Change in the fluorescence intensity of DMA (Ex. 360 nm; Em. 436 nm) with respect to time in the presence of SOG by Ce6, Ce6-H/P NPs, and Ce6/PTX-H/P NPs, in DMSO and phosphate buffer saline (pH 7.4), (A) and (B); time-dependent photobleaching of RNO by Ce6, Ce6/PTX-H/P NPs, Ce6-H/P NPs (C); changes in fluorescence intensity of SOSG in the presence of free Ce6, Ce6/PTX-H/P NPs, Ce6-H/P NPs in water (D)

3.6.3 In vitro cell line studies

3.6.3.1 Cellular uptake study

The cellular uptake was analyzed using fluorescence microscopy and flow cytometry analysis. Figures 3.5A and 3.5B represent examples of fluorescence micrographs. Further, the uptake was quantitatively analyzed using flow cytometry. A similar result was observed, with Ce6/PTX-H/P NPs displaying the highest cellular uptake (Figures 3.5C and 3.5D). Ce6/PTX-H/P NPs exhibited B16F10 cellular fluorescence intensities of 1900 ± 120 and 3520 ± 182 (AU) in 1 and 4 h, respectively, whereas free Ce6 showed a fluorescence increase from 900 ± 100 to 1200 ± 140 from 1 to 4 h. The Ce6 uptake in FaDu cells via Ce6/PTX-H/P NPs caused a significant increase in cellular Ce6 fluorescence intensity, 1620 ± 130 and 2850 ± 175 in 1 h and 4 h, respectively. In the contrary, the free Ce6 showed low uptake of 850 ± 90 (1 h) and 1250 ± 110 (4 h) (Figure 3.5E, 3.5F). Ce6/PTX-H/P NPs showed the highest cellular internalization than free Ce6 and Ce6-H/P NPs in both B16F10 and FaDu cell lines at 1 and 4 h. The result is in consistent with our previously published data that represented higher cellular uptake of Ce6 via nanoparticles than the free Ce6 (Kumari P et al. 2017).
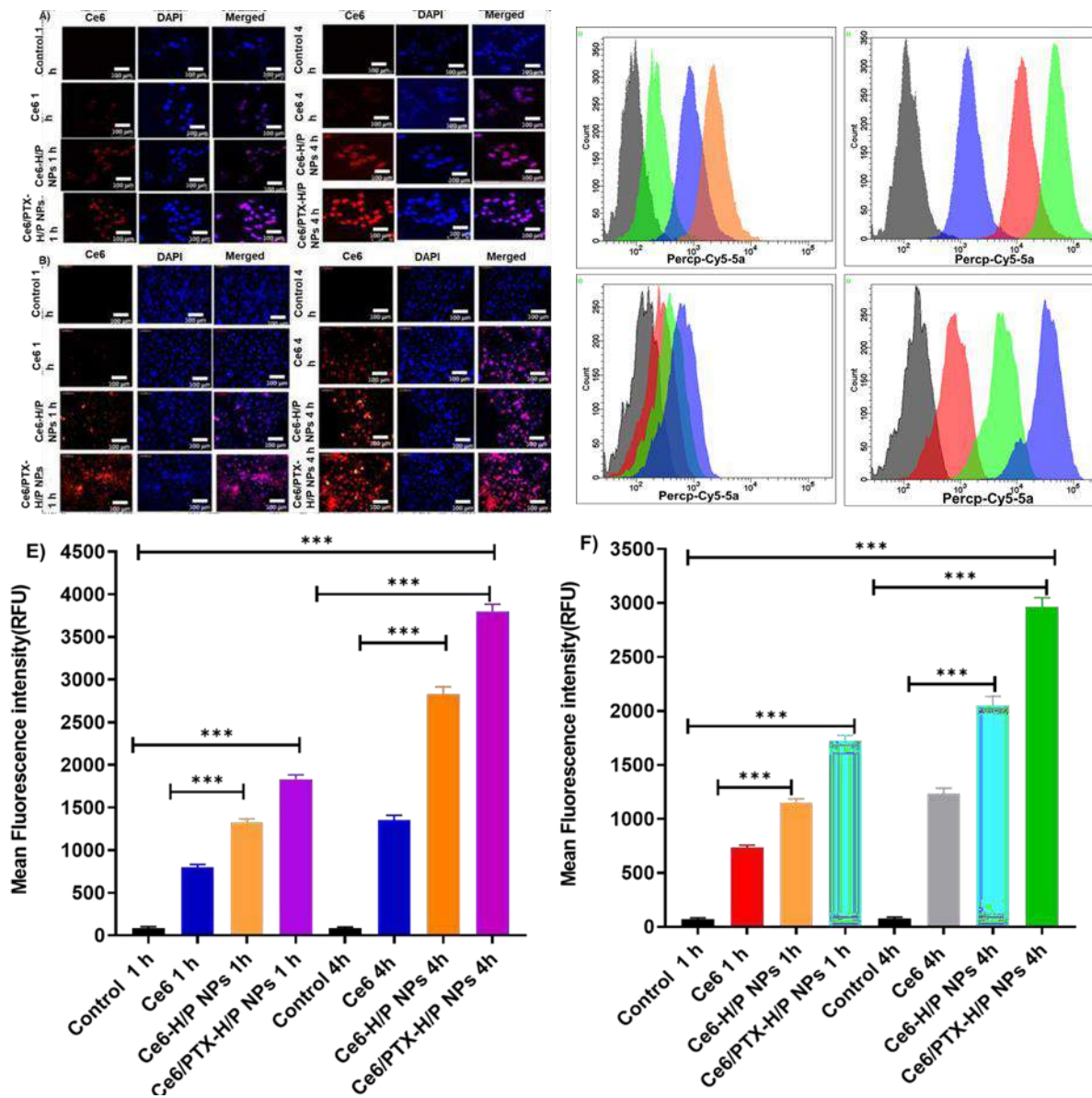
Figure 3.5 Cellular uptake study. Fluorescence microscopy images of B16F10 cells (A) and FaDu cells (B) treated with at PTX, Ce6, Ce6-H/P NPs, PTX-H/P NPs, Ce6/PTX-H/P NPs Ce6 concentration of 6 µg/mL; illustrative histogram plot achieved from statistics calculation by flow cytometer and assessment of the geo mean of fluorescence of the B16F10 cells for 1 h (left) and 4 h (right) (C); and FaDu cells for 1 h (left) & 4 h (right) (D). A bar graph were

used to demonstrate the amount of NPs taken up by B16F10 cells (E), and FaDu cells (F) cell lines using flow cytometry. The data represent mean ± standard deviation, calculated from three sets of experiments. The significance of the difference was assessed by the Student's t test, **, and *** indicate $p < 0.01$ and $p < 0.001$, respectively.

3.6.3.2 Cellular cytotoxicity analysis

 The nanoformulations, Ce6-H/P NPs, PTX-H/P NPs, and Ce6/PTX-H/P NPs exhibited B16F10 cell viability of 40.21%, 42.34 % and 36.10 % at the highest drug concentration (Ce6 50 µg/ml and PTX 100 µg/ml) after 48 h without laser condition, which was improved to 25.14 %, and 17.20 %, respectively for Ce6-H/P NPs and Ce6/PTX-H/P NPs after laser irradiation.

Table 3.1 IC50 value of B16F10 cells treated Ce6, PTX, Ce6-H/P NPS, PTX-H/P NPS, and Ce6/PTX- H/P NPs without laser irradiation.

Group	Without irradiation	With irradiation
Ce6	22.235	18.325
PTX	23.289	20.234
Ce6/PTX-H/P NPs	15.235	9.3256
Ce6-H/P NPs	17.325	12.2365
PTX-H/P NPs	18.2356	15.3256

Table 3.2 IC50 value of B16F10 cells treated Ce6, PTX, Ce6-H/P NPS, PTX-H/P NPS, and Ce6/PTX- H/P NPs with laser irradiation

Group	Without irradiation	With irradiation
Ce6	18.325	15.478
PTX	16.421	13.333
Ce6/PTX-H/P NPs	9.243	5.425
Ce6-H/P NPs	12.315	8.748
PTX-H/P NPs	10.421	7.635

Similarly, for FaDu cells, the Ce6-H/P NPs, PTX-H/P NPs, and Ce6/PTX-H/P NPs exhibited cell viability of 39.55 %, 41.02 %, and 36.20 % at the highest drug concentration (Ce6 50 µg/ml and PTX 100 µg/ml) after 48 h without laser condition, which was improved to 23.32 %, and 14.02 % respectively for Ce6-H/P NPs and Ce6/PTX-H/P NPs after laser irradiation.

Table 3.3 IC50 value of FaDu cells treated Ce6, PTX, Ce6-H/P NPS, PTX-H/P NPS, and Ce6/PTX-H/P NPs without laser irradiation

Group	Without irradiation	With irradiation
Ce6	19.235	14.325
PTX	18.125	15.234
Ce6/PTX-H/P NPs	12.235	7.3256
Ce6-H/P NPs	14.325	10.2365
PTX-H/P NPs	13.2356	10.3256

Table 3.4 IC50 value of FaDu cells treated Ce6, PTX, Ce6-H/P NPS, PTX-H/P NPS, and Ce6/PTX- H/P NPs with laser irradiation

Group	Without irradiation	With irradiation
Ce6	15.325	11.478
PTX	17.021	10.333
Ce6/PTX-H/P NPs	8.243	4.425
Ce6-H/P NPs	10.315	6.748
PTX-H/P NPs	10.421	8.635
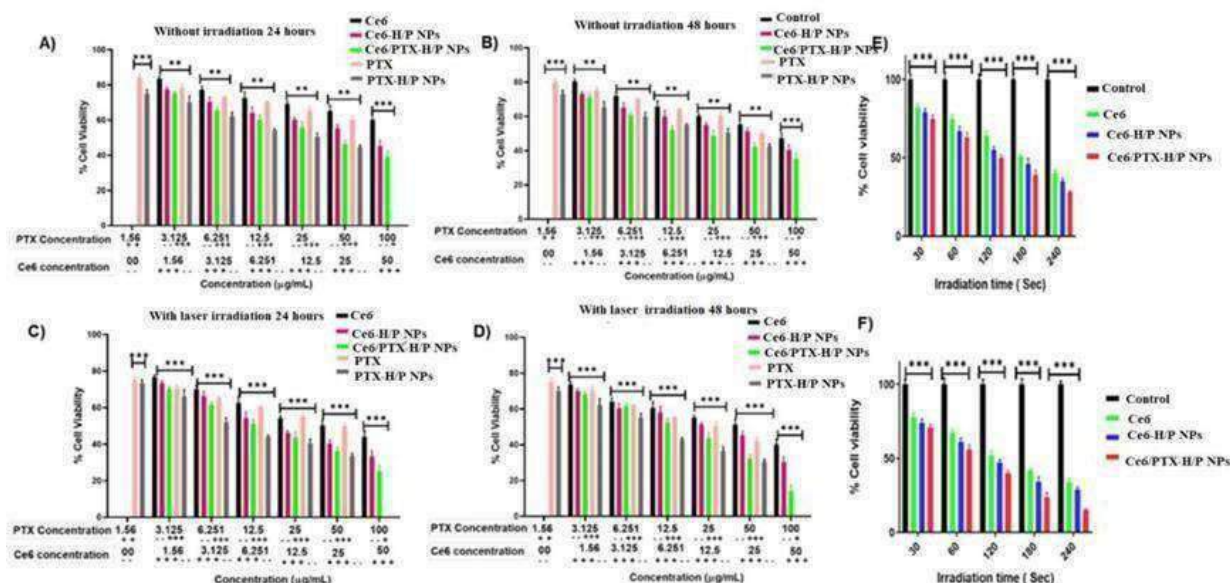
Figure 3.6 Assessment of cell viability of FaDu cells treated with Ce6, PTX, Ce6-H/P NPs, PTX-H/P NPs, Ce6/PTX-H/P NPs at PTX concentration of 0–100 μg/mL, and Ce6 concentration 0-50 μg/mL for 24 and 48h. with or without irradiation. (A, B, C, and D); Assessment of cell viability of B16F10 cells treated with Ce6, Ce6-H/P NPs, Ce6/PTX-H/P NPs at Ce6 concentration of 0–50 μg/mL for 24 and 48h, various time irradiation (E, F).

The time-dependent increase in cytotoxicity was observed by analyzing 24 h and 48 h cell viability data. The IC50 values in Table (S2-S4) display that Ce6/PTX-H/P NPs (+L) exhibited the highest cytotoxicity (lowest IC50 value) at both 24 and 48 h time points.
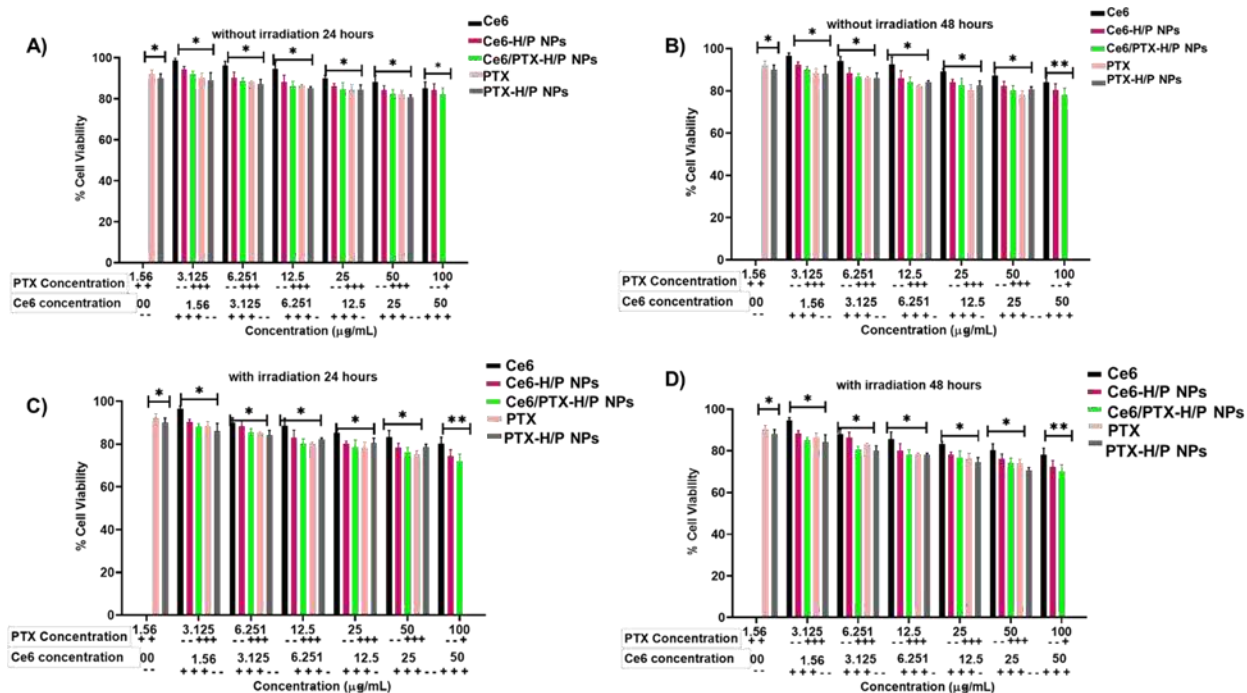
Figure 3.7 Assessment of cell viability of HEK 293 cells treated with Ce6-H/P NPs, PTX-H/P NPs, Ce6/PTX-H/P NPs at PTX concentration of 0–100 µg/mL and Ce6 concentration 0-50 µg/mL for 24 and 48h. with or without irradiation. (A, B, C, and D).

The NPs formulations displayed lower IC50 values than free drugs, indicating an enhanced accumulation of NPs in the cells than the free drugs resulting in a higher cytotoxic response. HEK-293 cells did not show any decrease in cell viability, which could be due to the Ce6/PTX-H/P NPs's targeting potential toward cancer cells. There could be a difference between the uptake mechanism of cancer cells vs. normal cells, contributing to the difference in cell viability.
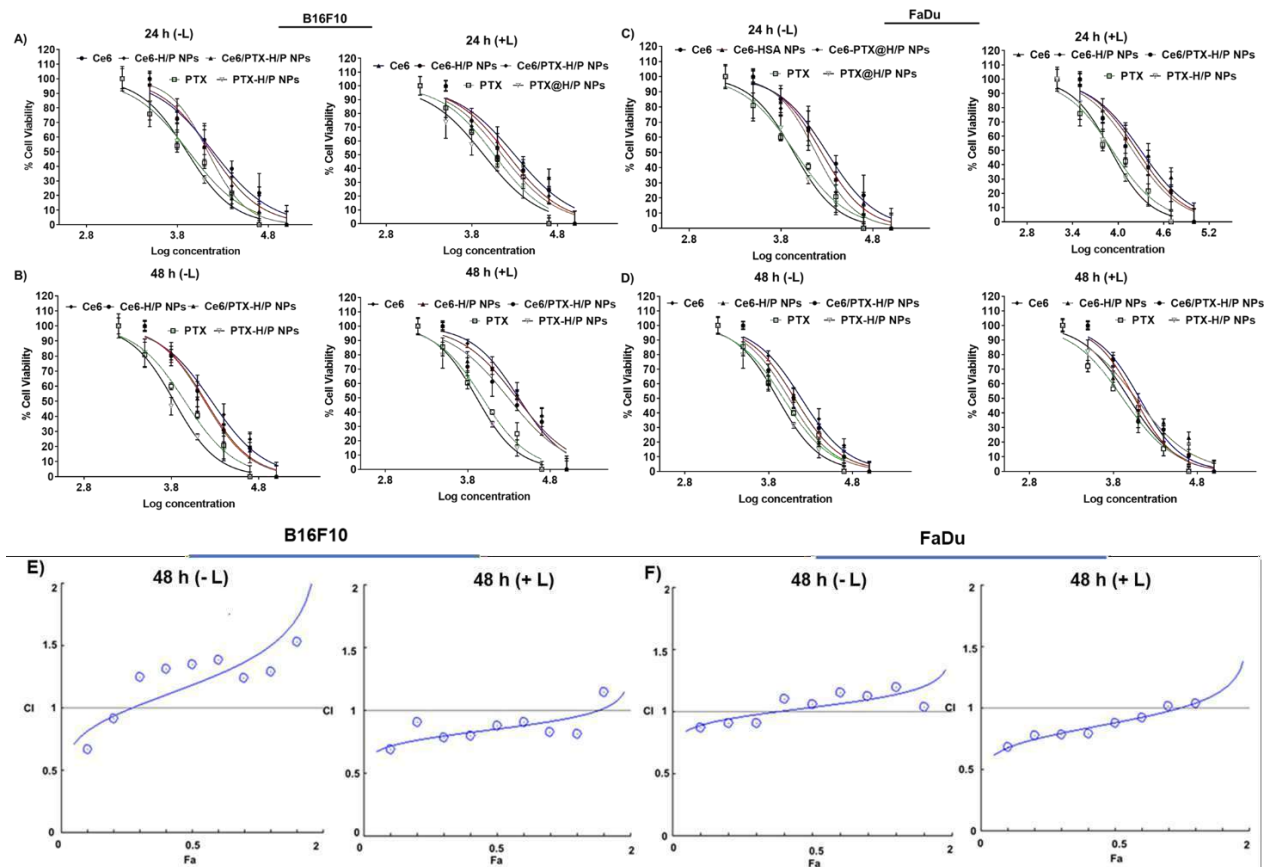
Figure 3.8 Viability of B16F10 cells pretreated with PTX, Ce6, Ce6-H/P NPs, PTX-H/P NPs, Ce6/PTX- H/P NPs and PBS-mediated PDT cultured for 24 h (- L, + L), (A); and 48 h (-L, +L), (B); Viability of FaDu cells pretreated with PTX, Ce6, Ce6-H/P NPs, PTX-H/P NPs, Ce6/PTX-H/P NPs and PBS- mediated PDT cultured for 24 h (- L, + L), (C); and 48 h (-L, +L), (D). Graphs representing combination index in B16F10 (E), and FaDu cells treated for 48 h (F).

A combination index analysis was performed to evaluate the effect of Ce6 and PTX-mediated combination therapy (Figure 5E). The combination index values at the majority of the fractions of 0.4, 0.5, and 0.6 were above 1, indicating an antagonistic effect. The CI values ranged between 0.5 -0.9 from fraction affected 0.1- 0.9 for B16F10 cell lines at 48 hours. Similarly, the CI ranged from 0.5 - 0.85 for FaDu cell lines indicating strong synergism between Ce6 and PTX at 48 hours while administering the drugs via Ce6/PTX-H/P NPs.

3.6.3.3 Apoptosis study

The flip of phosphatidylserine from the intracellular side to the outer membrane indicates the initiation of apoptosis. The process was captured using FITC-labeled annexin V, a ligand of phosphatidylserine. Over 97% of the cells treated with laser or blank micelles were annexin -, PI- and considered healthy with no apoptosis signal. The free Ce6 and Ce6/PTX-H/P NPs treated cells demonstrated higher late apoptotic cell populations in the flow cytometry analysis compared to control cell populations (Figure 3.9A). Ce6/PTX-H/P NPs mediated PDT increased the late apoptotic cell population to a much greater extent than the free Ce6 treatment. Free Ce6 exhibited apoptosis 8.75$\pm$ 0.25 (-L), 21.35$\pm$ 0.35(+L), Ce6- H/P NPs, 20.35$\pm$ 0.65 (-L), 36.52 $\pm$ 0.45 (+L), Ce6/PTX-H/P NPs 30.72$\pm$ 0.55 (-L), 44.65 $\pm$ 0.65 (+L), and PTX 10.2 $\pm$ 1.5, PTX-H/P NPs 28.1 $\pm$ 3.1 in FaDu cells. The data indicated that the PDT via Ce6/PTX-H/P NPs was efficacious compared to other treatments, which could be due to the enhanced cellular uptake of the Ce6, PTX, and the effect of synergistic combination therapy.

3.6.3.4 Cell cycle analysis

The cells treated with Ce6, PTX, Ce6-H/P NPs, PTX-H/P NPs, and Ce6/PTX-H/P NPs induced cell cycle arrest in G2/M and S phases with a significant decrease in G0/G1 phase compared to the control (Figure 3.9 B). Ce6/PTX-H/P NPs treated cell showed 4-fold greater accumulation than in

free Ce6 and PTX. More DNA damage was indicated by increased cell cycle arrest in G2/M of

Ce6/PTX- H/P NPs.
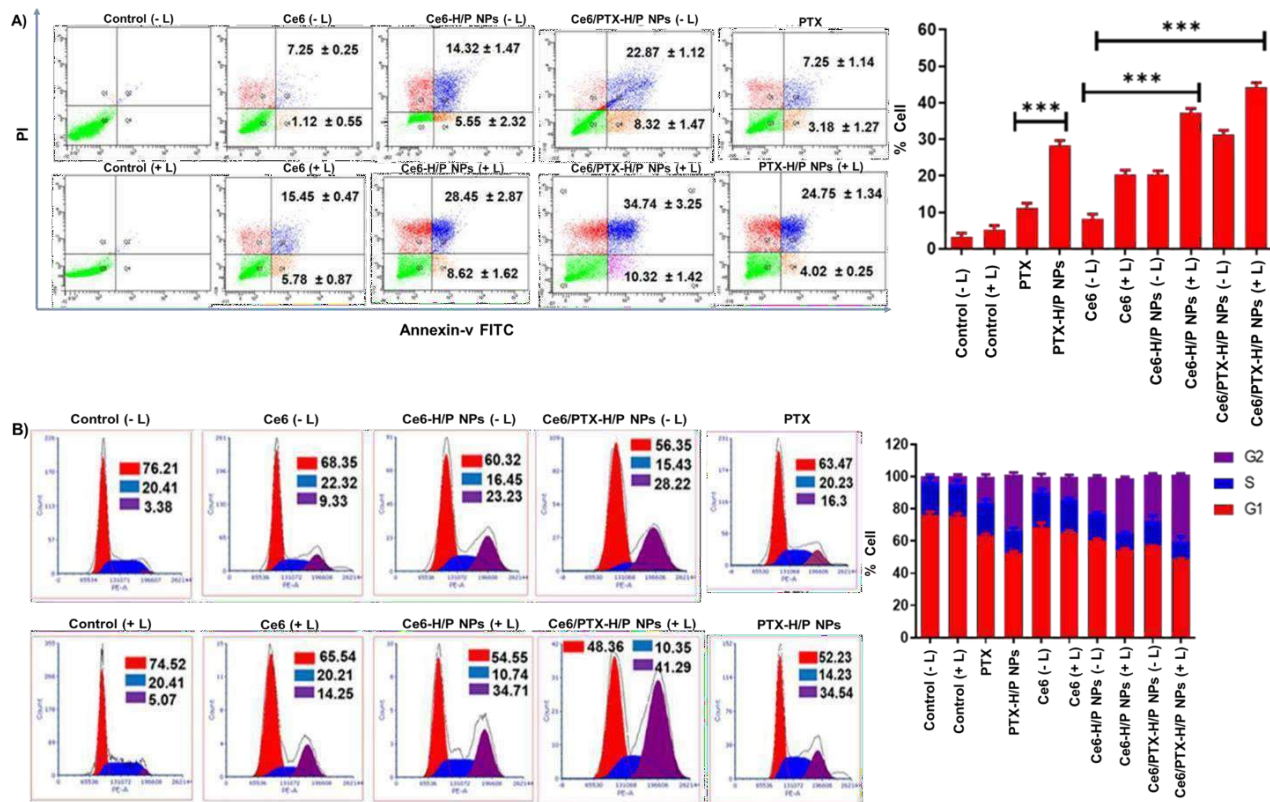
Figure 3.9 Annexin V assay (A) and cell cycle analysis (B). The extent of apoptosis was evaluated by analyzing FaDu cells treated with PTX, Ce6, Ce6-H/P NPs, PTX-H/P NPs, Ce6/PTX-H/P NPs at Ce6 concentration of 10 µM (incubation time. 24 h) by using flow cytometry. The Q3 and Q4 quadrants represent early and late apoptosis, respectively (gated cell number. 10,000); cell cycle arrest by PTX, Ce6, Ce6-H/P NPs, PTX-H/P NPs, Ce6/PTX-H/P NPs (B) as analyzed by flow cytometry. The histogram plots (left) and the representative bar graph (right) show cell populations in various stages of cell cycles.

3.6.3.5 DNA fragmentation study and nuclear staining

Electrophoresis was used for both cell lines to determine the extent of DNA damage. Compared to Ce6, PTX, Ce6-H/P NPs, and PTX-H/P NPs, Ce6/PTX-H/P NPs treated cells showed higher DNA fragmentation with a ladder-like pattern in both cell lines (Figure 3.10 A and B). The control DNA was undamaged and showed no signs of deterioration. To visualize the population of apoptotic cells and their cellular morphology after treatment, nuclear staining with DAPI and acridine orange (AO) was used (Figure 3.10). The cells undergoing apoptosis depicted blebbing nuclear fragmentation and cell shrinkage, which was the most prominent in Ce6/PTX-H/P NPs-treated cells.
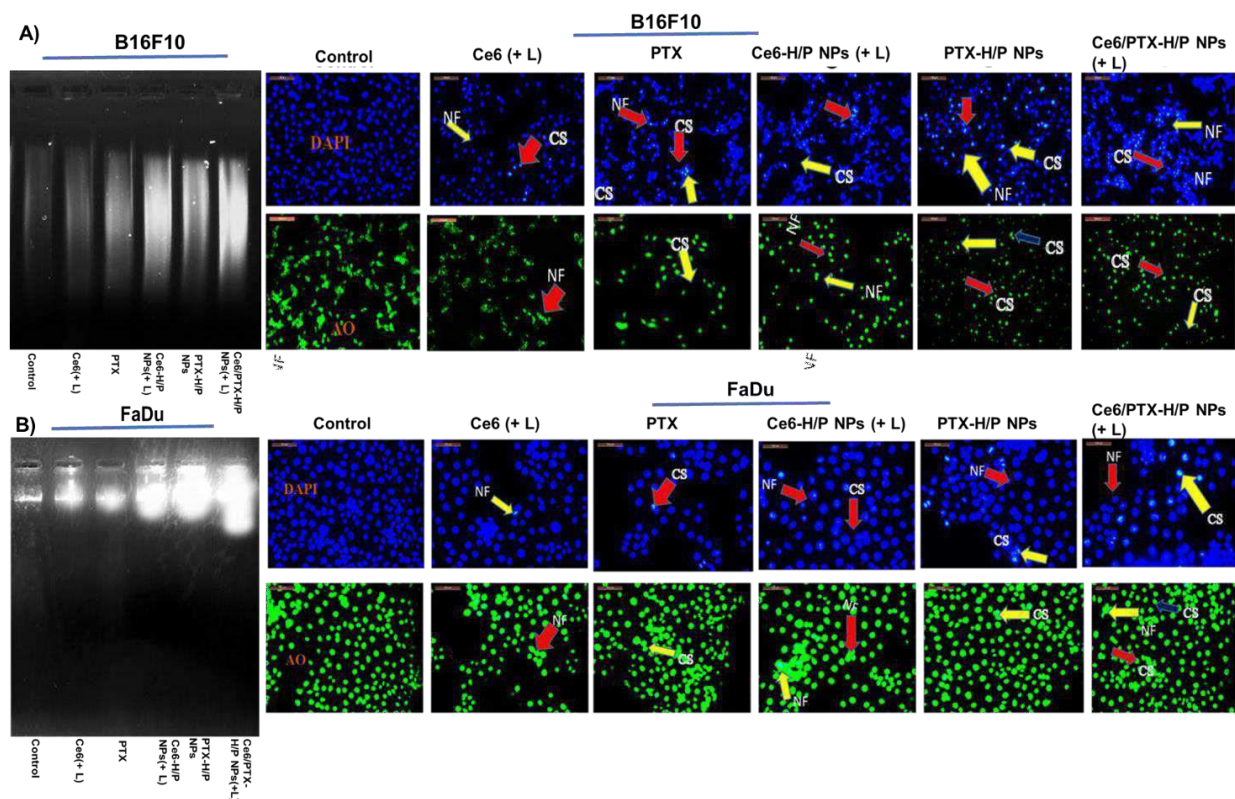
Figure 3.10 DNA fragmentation assay. DNA extracted from B16F10 and FaDu cells was viewed on ethidium bromide-stained gel. DNA from untreated cells (Control), PTX, Ce6, Ce6-H/P NPs, PTX-H/P NPs, Ce6/PTX-H/P NPs at Ce6 concentration of 10 µM. (A and B); nuclear staining of B16F10, FaDu cells with acridine orange (AO) (stained in green color) and DAPI (stained in blue color). Arrows indicate cytoplasmic shrinkage (CS) and nuclear fragmentation (NF) (upper and lower).

3.6.3.6 ROS detection/mitochondrial membrane potential assay

The intracellular ROS generation in B16F10 and FaDu cells after incubation with Ce6, PTX, Ce6-H/P NPs, PTX-H/P NPs, Ce6/PTX-H/P NPs was assessed using the fluorescence probe, DCFH-DA (Figure 3.11). The bright green signal in irradiated cells confirmed the ROS generation, resulting in the greatest extent of apoptosis and cell death.

The nanoformulations of PTX and Ce6 generated ROS, as visualized by their enhanced green fluorescence signal. In the mitochondrial membrane potential assay, the control cells emitted red JC-1 fluorescence from polymerized JC-1, which diffused to yellow in PTX or Ce6-treated cells due to the combined localization of red and green signals. However, Ce6/PTX-H/P NPs-treated cells emitted a bright green fluorescence, indicating the low mitochondrial membrane potential (Figures 3.12). Low membrane potentials are linked to mitochondrial dysfunction and apoptosis. The difference in the fluorescence indicated that the Ce6/PTX-H/P NPs caused the highest mitochondrial damage leading to apoptosis and cancer cell death.
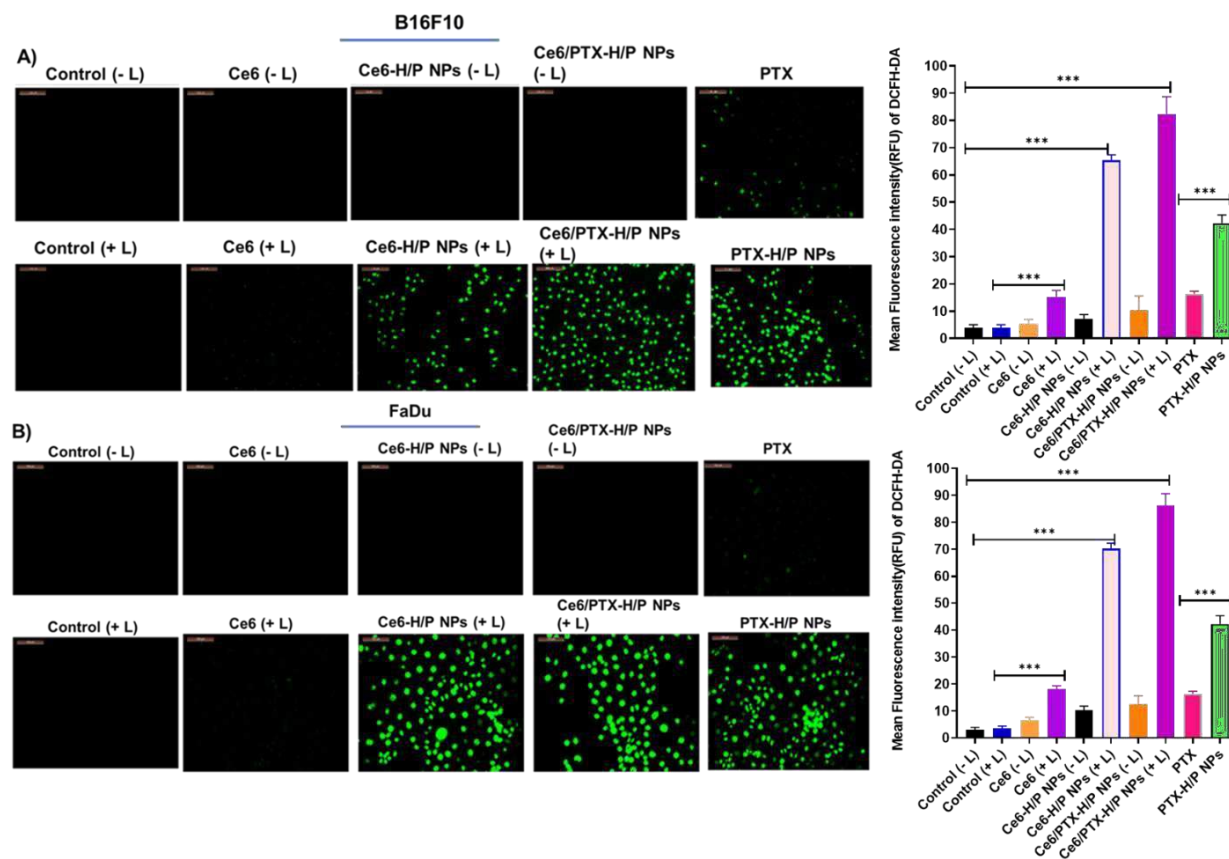
Figure 3.11 Intracellular ROS generation in B16F10 (A) and FaDu (B) cells treated within PTX, Ce6, Ce6-H/P NPs, PTX-H/P NPs, Ce6/PTX-H/P NPs at Ce6 concentration of 10 μM by fluorescence microscopy.
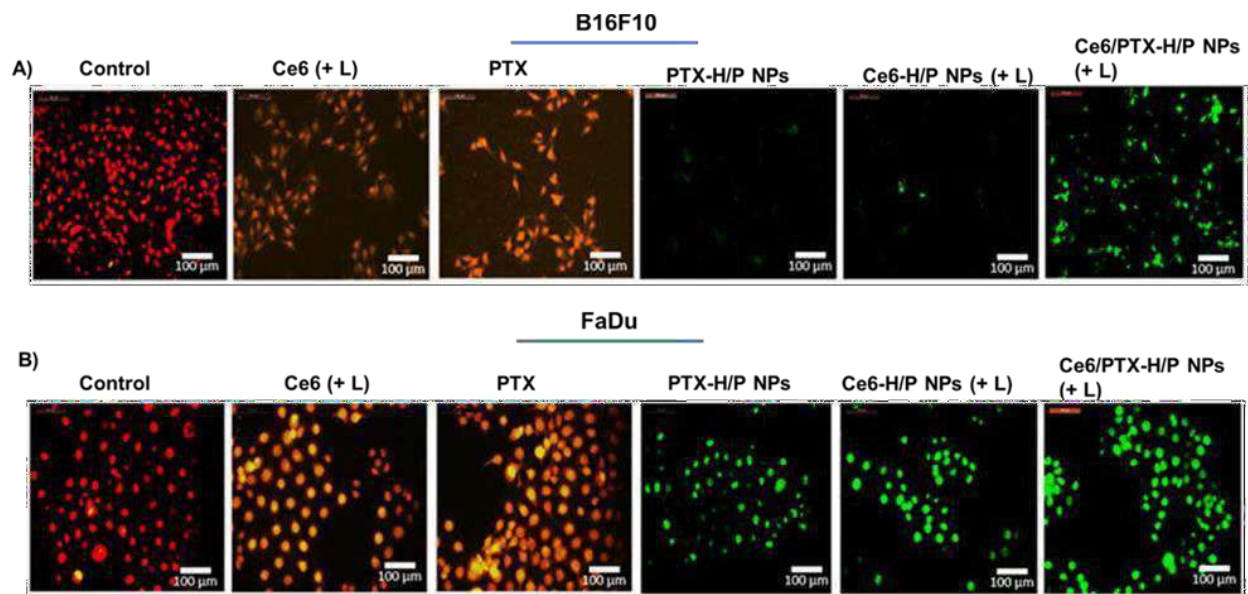
Figure 3.12 Qualitative assessment of mitochondrial membrane potential by JC-1 staining of PTX, Ce6, Ce6-H/P NPs, PTX-H/P NPs, Ce6/PTX-H/P NPs-treated B16F10 cells (A), and FaDu cells (B) by fluorescence microscopy.

3.7   In vivo study

3.7.1   Pharmacokinetic study

The pharmacokinetic (pK) characteristics were assessed by measuring drug concentrations at specific time points after IV injection of Ce6, Ce6-H/P NPs and Ce6/PTX-H/P NPs into the tails of female Wistar rats. (Figure 3.13) represent the pK parameters and plasma Ce6 concentration-time curves. The findings revealed that the free Ce6 and Ce6-H/P NPs level in blood was rapidly removed, with a blood retention T1/2 of 85 min and 367 min.

Table 3.5 Pharmacokinetic parameters for mice treated with Ce6-H/P NPs, Ce6/PTX-H/P NPs and free Ce6 by fitting the data to a non-compartment model by PKSolver 2.0 software

Parameter	Ce6	Ce6-H/P NPs	Ce6/PTX-H/P NPs
$T_{1/2}$ (min)	85.275	367.56	514.71
$AUC_{0-\infty}$(μg/mL·min)	2146	5375.27	10385.97
CL(mg/kg)/(μg/ml)/min	0.0023	0.0009	0.0003
$MRT_{0-\infty}$(min)	97.47	245.08	403.06

The Ce6/PTX-H/P NPs, on the other hand, had a blood retention T1/2 of 514 min, over 6 times higher than that of free Ce6 and 1.63 times that of Ce6-H/P NPs. As a result, the AUC values of the Ce6/PTX- H/P NPs increase to about 4.83 times those of free Ce6 and 1.93 that of Ce6-H/P NPs. The PK data revealed that Ce6/PTX-H/P NPs had the greatest t1/2, AUC, MRT, and lowest clearance compared to free Ce6 and Ce6-H/P NPs. The free Ce6 is promptly cleared out of the systemic circulation. Figure S6B showed that free Ce6 and Ce6-H/P NPs rapidly disappeared from the blood, but Ce6/PTX-H/P NPs remained in circulation longer and were cleared more slowly. The prolonged circulation time could contribute to Ce6/PTX-H/P NPs accumulation at the tumor site and enhance their therapeutic effects.
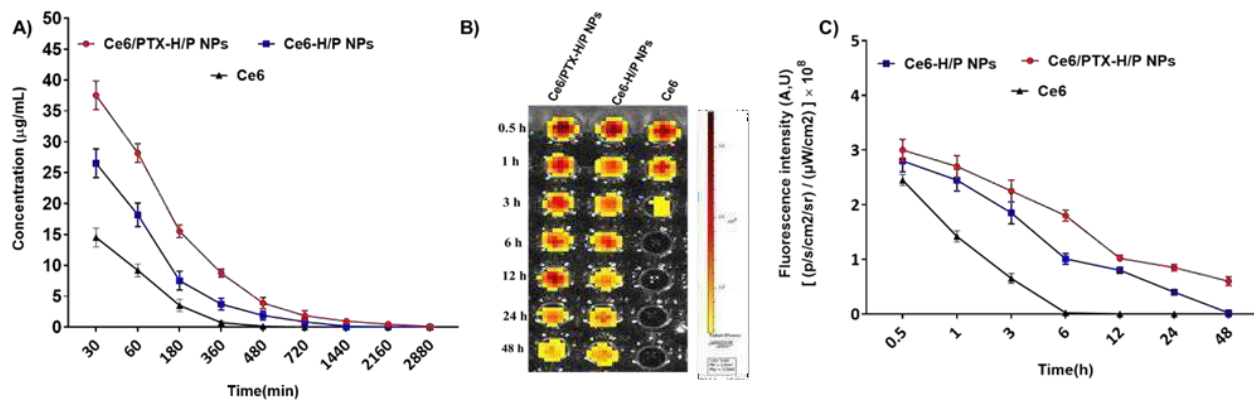
Figure 3.13 In vivo pharmacokinetic curves of the Ce6 concentration vs. time after intravenous injection of NPs and Ce6, respectively (Mean ± SD, n = 3) (A); NIRF images of blood samples from the mice (B); Quantification of fluorescence intensity (C).

3.7.2 Tumor inhibition assay

The tumor volumes on the 21st day following the initiation of treatment were 1470.56 ± 7.8, 850.75 ± 6.9, 810.75 ± 3.5, 620.39 ± 6.35, 450.35 ± 9.4 and 266.82 ± 5.3 mm3 for saline, Ce6, PTX, CE6-H/P NPs, PTX-H/P NPs, Ce6/PTX-H/P NPs-treated groups respectively (Figure 3.14A). The average weight of the isolated tumors for saline, free Ce6, free PTX, CE6-H/P NPs, PTX-H/P NPs, and Ce6/PTX-H/P NPs- treated animals were 4.72 ± 0.56, 3.66 ± 0.24, 3.75 ± 0.58, 0.95 ± 0.65, 1.15 ± 0.65, and 0.50 ± 0.42 gm respectively (Figure 3.14C). Moreover, no reduction in body weight endorsed nontoxic nature of the formulation to the mice. (Figure 3.14D).
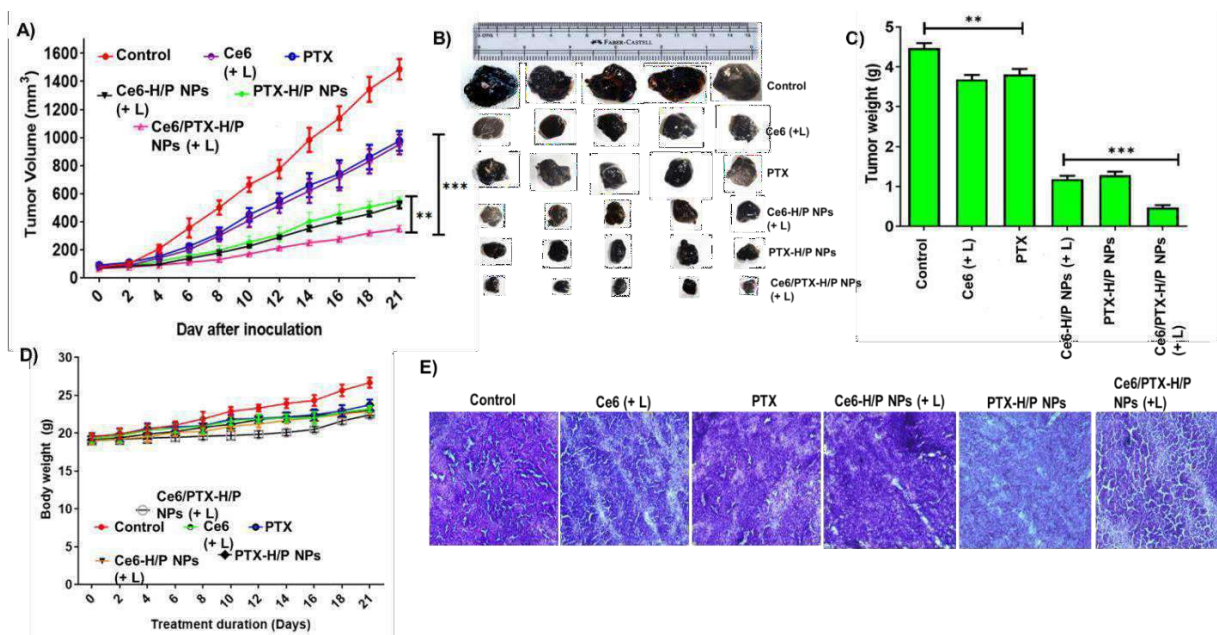
Figure 3.14 B16F10 tumor growth curves of mice treated with various formulations at a Ce6 dose of 5 mg/kg with 5 min laser irradiation (666 nm, 0.5 W/cm2, 12 h post-treatment) (mean ± SD, n = 5) (A); body weight monitoring of the mice that received treatments with various formulations (B); photographs of the tumors at day 21 of post-treatment (C); tumor weights at the end of the treatments (D); H&E staining of the tumor tissue (E).

3.7.3   Immunohistochemistry

Mice treated with Ce6/PTX-H/P NPs showed the highest green fluorescence from the DCFH-DA probe that determines the level of oxidative stress (Figure 3.16E). After cellular internalization, the dye oxidizes by the intracellular ROS to form 7'-dichlorodihydrofluorescein (DCF), emitting green fluorescence. The ROS generated following chemotherapy and PDT-insult to the cancer cells are superoxide anion, hydrogen peroxide, and hydroxyl radicals. The nanoformulations induced higher ROS generation in the tumor tissues in comparision to the free drug Ce6, PTX administration. The study verified the effectiveness of the Ce6/PTX-H/P NPs in producing a 4-fold higher amount of ROS than all other tested formulations.
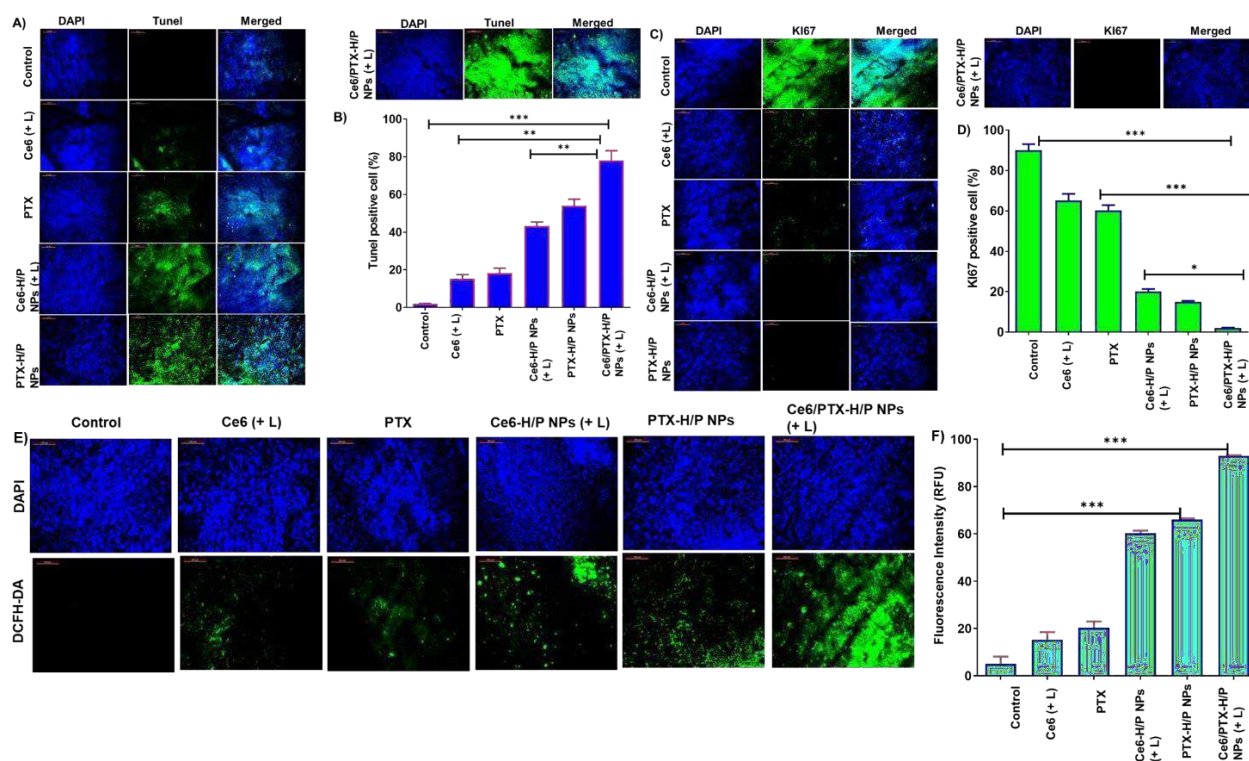
Figure 3.15 Evaluation of apoptosis in tumor tissues by TUNEL assay (A); Quantification of fluorescence from TUNEL assay (B); evaluation of cell proliferation in tumor tissues by Ki67 immunofluorescence assay (C); quantification of fluorescence from Ki-67 assay (D); intratumor ROS levels after intravenous injection of various formulations by fluorescence images of B16F10 tumor sections at 24 h. (E) ; quantification of fluorescence from ROS assay (F); (In all the panels, * represents $p < 0.05$, ** represents $p < 0.01$, * represents $p < 0.001$, **** represents $p < 0.0001$, and ns represents no significant difference).**

The high oxidative stress induced by the treatment led to an increase in apoptosis in cancer cells, as indicated by the TUNEL-positive cells showing green fluorescence (Figure 3.16A). Consistent

with the DCFH-DA data, the TUNEL-positive cells were more highly expressed in nanoformulation-treated cells than the free drugs, Ce6/PTX-H/P NPs showing the highest apoptotic cell population (Zhang W et al. 2021). Further, tumor sections are visualized for detecting the proliferation marker, Ki-67 expression (Figure 3.16C). The untreated tumor tissue shows the highest expression, indicating its high proliferation rate and the ability tometastasize (Shi G et al. 2023). The formulations showed decreased signal in corroboration with the ROS and TUNEL data, indicating the ability of the nanoformulations to produce ROS, induce apoptosis, and curb the proliferation rate.

The histopathological examination by H&E staining of tumor sections after the treatment with the formulations and the free drug has been conducted (Figure 3.17), where no histological damage to the other organs, such as the heart, liver, spleen, lungs, and kidney, was observed after treatment with all the formulations. The results indicate that the combination nanoformulation was safe without producing inflammation or immune reactions, warranting potential application in cancer treatment.
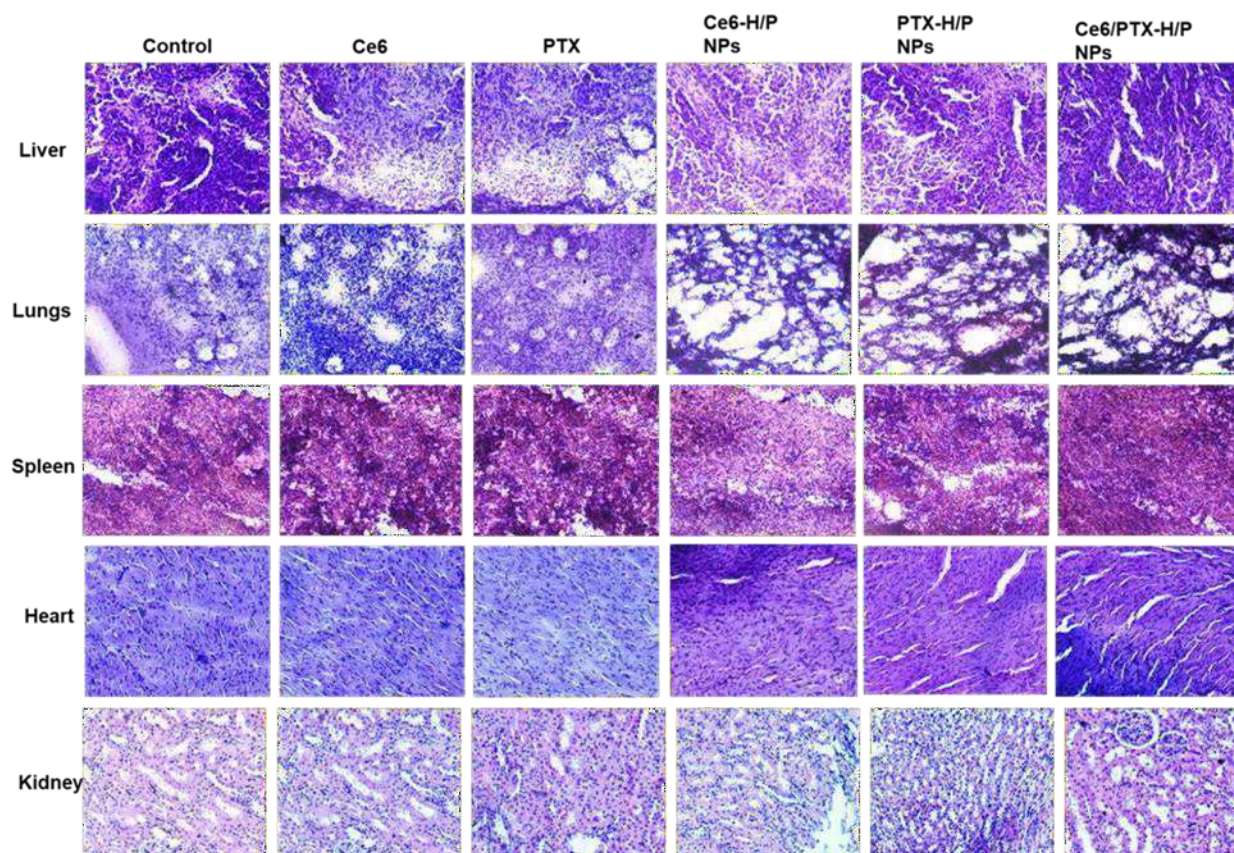
Figure 3.16 Histology examination of frozen mice organ slices (5 µm) utilizing hematoxylin and eosin (cytoplasm: pink, and nucleus: purple). Scale bar. 100 µm.

3.8 Conclusion

Here, we have prepared human serum albumin/poly(lactide)-co-glycolide (H/P) nanoparticles capable of incorporating dual drugs, the chemotherapeutic agent, paclitaxel and a photosensitizer, Chlroin e6 for a combination chemo-photodynamic therapy. The NPs were prepared via the emulsification technique, with PLGA and HSA as the corona and corona, respectively. The NPs were characterized thoroughly

for various physicochemical parameters, including particle size, surface morphology, charge, drug release rate, entrapment, loading efficiencies, protein integrity, and the ability for PDT-mediated generation of ROS in biochemical assays. Next, the effectiveness of formulations in killing murine melanoma and human oral squamous carcinoma cells was assessed in both in vitro and in vivo experiments. The cellular internalization data demonstrated the HSA-mediated active tumor targetability in both B16F10 and FaDu cell lines. The combination nanoformulations, Ce6/PTX-H/P NPs demonstrated the lowest IC50 in both the cell lines upon irradiation. The combination therapy demonstrated a synergistic effect. Ce6/PTX delivery to cancer cells induced apoptosis and cell cycle arrest in G2/M phase, causing DNA fragmentation and mitochondrial depolarization by inducing ROS. The in vivo study performed using B16F10 tumor-bearing mice indicated that the combination therapy effectively reduced the tumor volume and induced apoptosis and antiproliferative effect in the tumor. The newly developed laser- activatable nanoformulation could be an efficient chemotherapy and photodynamic treatment option for superficial cancers, including melanoma or head and neck cancer.

Chapter 4

Hypoxia alleviating platinum (IV)/chlorin e6- based combination chemotherapeutic- photodynamic nanomedicine for oropharyngeal carcinoma
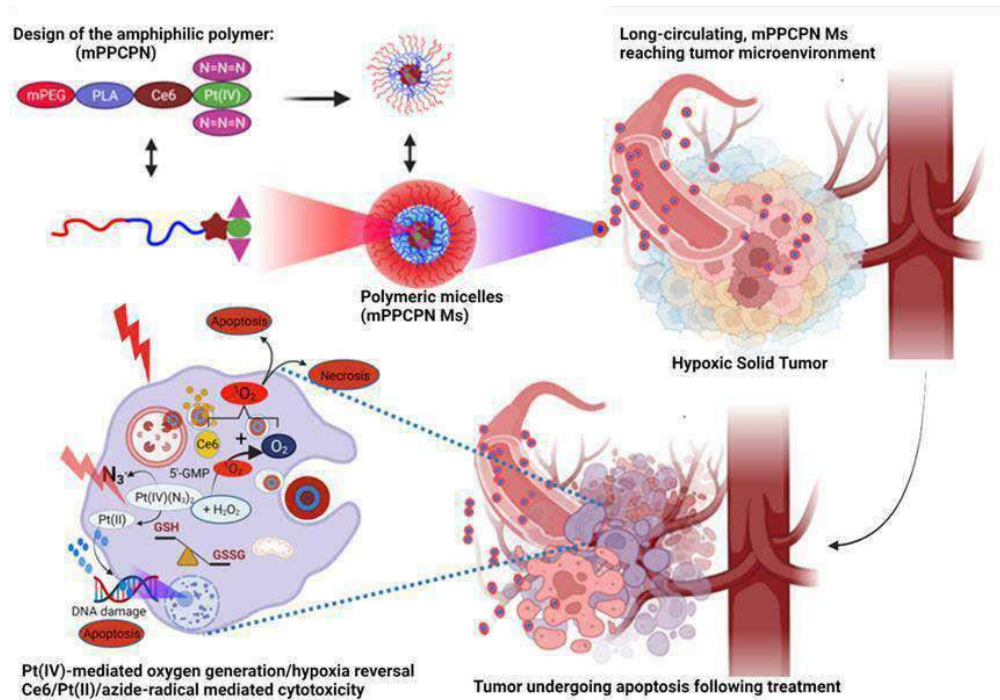
4.1 Introduction

Oral cancer is a malignant tumor of the oral cavity oropharynx, and oral squamous cell carcinoma (OSCC) is the most prevalent pathological form. Globally its incidence rate ranks 6th. (R.L. Siegel et al. 2017, A.C. Chi et al. 2015, H.W. Hsu et al. 2017, T. Naruseet al. 2016). OSCC emcompasses more than 90% of all diagnosed oral malignancies (A.C. Chi et al. 2015). Surgical elimination of the malignant tissue is the standard treatment (D. Guo et al. 2017). However, such surgeries lead to significant facial disfigurement, derogating the quality of life (Y. Yang et al. 2022, F. Ouyang et al. 2022). Photodynamic therapy (PDT) is a minimally invasive treatment option with spatiotemporal selectivity and low systemic toxicity (Y. Yang et al. 2022). PDT mandates the presence of a photosensitizers (PS), specific laser treatment, and molecular oxygen to exert a cytotoxic effect (M.D. Caverzán et al. 2020). Upon irradiation with a specific wavelength of light, photosensitizers transition to an excited singlet state and then to an excited triplet state via the intersystem crossing. The activated PS immediately transfers the energy to nearby triplet- state oxygen to form highly reactive singlet oxygen (1O2) via the type II process. Currently, PDT is used in head and neck cancer patients with superficial recurrence post-surgery and/or radiation to avoid morbidity or when re-surgery or re-irradiation posses an unacceptable risk (K. Chen et al. 2009). However, the potential of PDT in head and neck cancers is evident due to the successful experimental outcome in recent years (K. Chen et al. 2009). Hypoxia, a prominent feature of the solid TME induced by cancer cell proliferation and blood vessel deformation during tumor angiogenesis (X. Zhang et al. 2018, C.A. Robertson et al. 2009, J. Meulemans et al. 2019, G.L. Semenza et al. 2003) . Hypoxia hampers several treatments outcome, including radiation, chemotherapy, and photodynamic therapy (PDT) (X. Zhang et al. 2018, J.M. Brown et al. 2004,

W. Zhu, Z. Dong et al. 2016, A. Sahu, I. Kwon et al. 2020, W.R. Wilson et al. 2011, Y. Lou et al. 2011, Y. Liu et al. 2015). Specific treatment strategies have been established for reducing tumor hypoxia during PDT therapy. For example, in hyperbaric oxygen (HBO) treatment, pure O2 is administered to the patient in a pressure-enclosed chamber to enable O2 delivery in the tumor (K. Lu et al. 2015). Several O2- generating compounds, such as MnO2 (J. Meulemans et al. 2019, P. Therapy et al. 2013), perfluorohexane (H. Chen et al. 2015, P. Therapy et al. 2013), and catalase (J. Li et al. 2018, R. Ghasemi et al. 2018), have been employed to combat hypoxia in recent studies. MnO2 and catalase depend heavily on catalyzing endogenous H2O2 to produce O2.

Platinum-based anticancer drugs have transformed cancer chemotherapy with numerous applications in a varierty of cancers, namely head and neck, ovary, and testes. However, clinical translation with platinum drugs is limited due to the development of drug resistance, dose-limiting toxicity to the healthy organs, tumor relapse, and inadequate tumor accumulation. The newer generation non-classical platinum compounds are octahedral Pt(IV) prodrugs, demonstrating higher cellular uptake, quick DNA binding, and persistent inter-strand cross-linking. Here, a strategy of fabricating a nanomicellar system to produce a combination chemo-PDT effect, simultaneously capable of generating oxygen, has been shown. An amphiphilic polymer conjugate, methoxy(polyethylene glycol)(mPEG)-poly(D, L- Lactide)(PLA)- chlorin e6(Ce6)-cis, trans, cis-[-O-Pt(N3)2(NH3)2(OH)](Pt(IV)-diazide) (mPPCPN) has been synthesized, which self-assembled to form the nanomicellar structure. The PDT has been realized by the PS, chlorin e6. Achieving the therapeutic benefit of Ce6 via conventional therapy is uncertain due to its hydrophobicity and a strong tendency for aggregation (L. Ai et al. 2021). The amphiphilicity in the conjugate has been introduced by mPEG-PLA, which has been conjugated to Ce6. The mPEG would provide extended circulation ability causing eventual accumulation to the tumor tissues by

Enhanced Permeability and Retention (EPR) effect (H. Bhatt et al. 2019) and the PLA would provide sufficient hydrophobicity to form a stable micellar structure. Moreover, oxygen-generating potential, which was achieved by linking diazido moiety to Pt(IV)-moiety. Upon laser irradiation, the 1,2- diammino Pt(IV)-diazido complex was photoreduced to produce square planar Pt(II) species and two azidyl radicals. The Pt-azido causes light-mediated oxidation of 5'-GMP and produces singlet oxygen, nitrene intermediate, azidyl (N3.), and hydroxyl radicals (.OH). The hydroxyl and azidyl radicals cause injury to DNA, RNA, proteins, and lipids. The oxidation of 5'-GMP by platinum-diazide evolves nitrogen and oxygen gas in the presence of hydrogen peroxide via unknown reaction pathways. Another parallel mechanism for creating the oxidative equilibrium in the hypoxic condition is the conversion of Pt(IV) to Pt(II) mediated by upregulated Glutathione (GSH), which causes GSH depletion. Therefore, reducing GSH level and upregulated H2O2 transfers the hypoxia towards the oxidative environment, where molecular oxygen is produced from H2O2 by the enzyme catalase. The mPPCPN conjugate and the micelles were thoroughly characterized. The cell-based studies ascertained the cytotoxic potential of micelles, which was further validated in the in vivo oral cancer mice model.

4.2 Materials and methods

4.2.1 Materials

Chlorin e6 (Ce6) was sourced from Frontier Scientific, Inc. (USA). Methoxy polyethylene glycol, D, L, lactide, Stannous octoate, dimethylaminopyridine, N, N' dicyclohexylcarbodiimide, Acridine orange (AO), N, 4′, 6-Diamidino-2-phenylindole dihydrochloride (DAPI), Tetrahydrofuran (THF), 5,5′,6, 6′- Tetrachloro-1,1′,3,3′-tetraethylbenzimidazolocarbocyanine iodide (JC1 Dye), paraformaldehyde, Propidium iodide (PI), and dimethyl sulfoxide (DMSO) were procured from Sigma-Aldrich (Bangalore, India). Spectrum Laboratories, Inc. (the USA) provided the dialysis

membrane. GSure® DNA genomic isolation kit was purchased from GCC Biotech Pvt. Ltd. (India). Fluoromount-G, Methylthiazolyldiphenyl-tetrazolium bromide (MTT), and Trypan blue solution were bought from Himedia Labs (India). Cisplatin was obtained from Neon pharmaceuticals limited (Mumbai, India) as a free sample. TACS® Annexin V-FITC Apoptosis Detection Kit was received from R&D systems (Minneapolis, USA).

Cell lines: - Hypopharyngeal carcinoma cell line (FaDu HTB-43) were received from the American Type Culture Collection (ATCC, USA). Minimum Essential Medium Eagle (MEM), Penicillin Streptomycin, fetal bovine serum (FBS), and Trypsin-EDTA were sourced from Himedia Labs (India).

Animals: - For the antitumor study, the National Centre for Laboratory Animal Sciences, National Institute of Nutrition, Hyderabad, India, has supplied the Female BALB/c nude mice (18−22 g, 6-8 week-old). The hemolysis experiment was carried out on male Wistar rats, which were provided by Sainath Agency, Hyderabad, India. The work was authorized and carried out with the permission of the Institutional Animal Ethics Committee of BITS-Pilani, Hyderabad. The mice and rats were housed in normal mouse/rat cages (5/cage) in an air-conditioned environment (23-24 °C, relative humidity 50- 60%) with a 12-h light/dark cycle and free access to food and water.

4.2.2 Methods

4.2.2.1 Synthetic procedures

4.2.2.2 Synthesis and characterization of the mPEG –PLA- Ce6-Pt (IV) conjugate

The synthesis of mPEG –PLA- Ce6-Pt (IV) has been performed following a synthetic scheme shown in Figure 4.1 via a multi-step synthesis procedure as depicted below.

Step 1
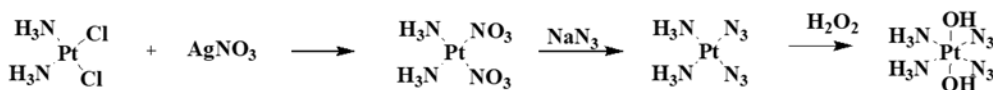
Step 2
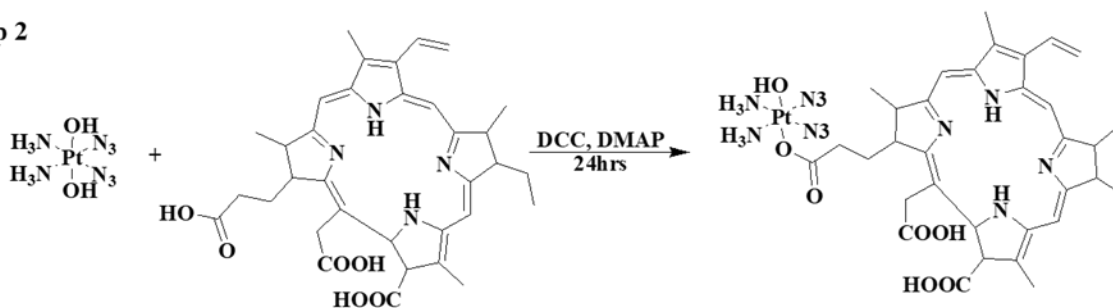
Step 3
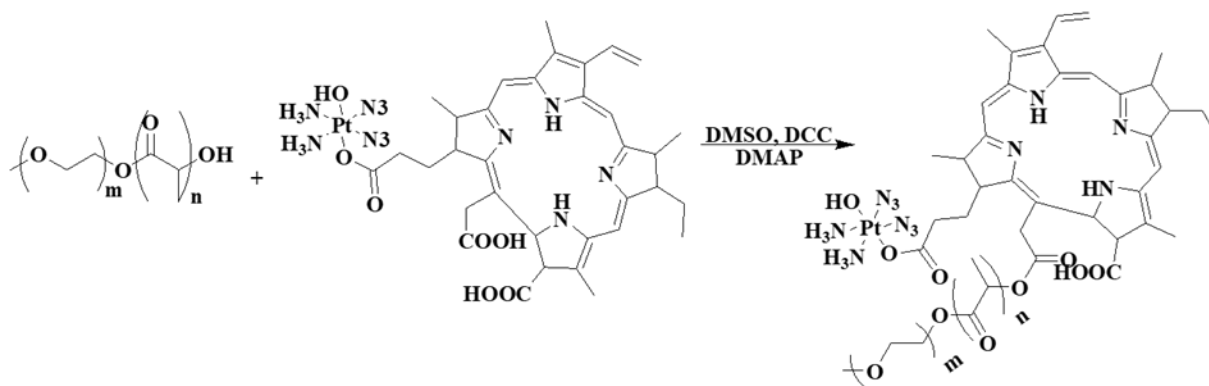
Figure 4.1 Synthetic scheme of mPEG-PLA-Ce6-Pt (IV)-(N3)2

4.2.2.3 Synthesis of cis, trans, cis-[Pt(N3)2(NH3)2(OH)2]

Cisplatin (cis-[PtCl2(NH3)2]) (1 moleequiv) was suspended in water. The cisplatin suspension was spiked with AgNO3 (2 moleequiv). For the next 24 h, the reaction mixture was kept in the dark and stirred. A membrane filter (Whatman, Anotop 10, 0.02 mm) was used to filter out the AgCl precipitate. 20 moleequiv of sodium azide (NaN3) was added to the solution and agitated for

30 min in the dark at room temperature, and the flask was kept at 4 °C overnight. The yellow precipitate was rinsed with diethyl ether and allowed to dry in the open air (yield: 70 %). In the dark, 40 moleequiv of H2O2 was agitated with the suspension of cis-[Pt (N3)2(NH3)2] in water. To get the yellow powder, the product was filtered, rinsed with diethyl ether and water, then centrifuged (yield: 45 %).

4.2.2.3 Synthesis of Ce6-Pt (IV) diazide

50 µL of N,N-diisopropylethylamine (DIPEA), 8.22 mg of 1-(ethyl3-(3-(dimethylamino) propyl) carbodiimide (DCC, 1.2 moleequiv) and 4-Dimethylaminopyridine (DMAP) was added into the solution of Ce6 (1 moleequiv) in dimethylformamide (DMF). Agitated the reaction mixture for 24 h at room temperature. Next, cis, trans, cis-[Pt(N3)2(NH3)2(OH)2] was added dropwise. The crude reaction mixture was refined by precipitation with ether after complete solvent evaporation (yield: 70 %).

4.2.2.4 Synthesis of methoxy-polyethylene glycol-poly (lactic acid) (mPEG-PLA) copolymer and conjugation with Ce6-Pt (IV) diazide to form mPEG-PLA-Pt(IV)-Ce6

Ring-opening polymerization reaction was employed to synthesize mPEG-PLA [41]. The Ce6-Pt(IV) diazide in DMF and 50 µL of triethylamine was agitated in the presence of DCC (10.5 mg, 3 moleequiv) and DMAP (3 moleequiv) at 25 °C for 4 h., mPEG-PLA was added to the reaction mixture dropwise, agitated overnight at 25°C. After evaporation of the solvent, deionized (DI) water was used to dialyze the crude reaction mixture against a dialysis bag (MWCO: 3.5 KDa). Every 6 h for 72 h, the dialyzing medium was changed with new DI water. The final amphiphilic polymer was generated by lyophilizing the dialysate (yield: 75 %).

KBR pellet method was employed to pperform FTIR analysis of Ce6, cis, trans, cis-[Pt(N3)2(NH3)2(OH)2], Ce6-Pt (IV) diazide, and mPEG-PLA-Pt(IV)-Ce6 at IR range of 400 to 4000 cm-1. The chemical structure of the conjugate in DMSO-D6 solution was characterized using proton nuclear magnetic resonance spectroscopy (1HNMR) (Bruker spectrometer-300 MHz, Bruker, USA and TMS as an internal standard at 25°C. Gel permeation chromatographic (GPC) technique was used to study the conjugation efficiency of mPEG-PLA, mPEG-PLA-Pt(IV)-Ce6 (mPPCPN) conjugate. ultra- hydrogel™ linear (7.8 × 300 mm) SEC was used to elute the samples in the GPC system. The flow rate of 1 mL/min, and water was used as a mobile phase with a RI detector. The Critical micelle concentration of mPPCPN conjugate was measured employing pyrene as a fluorescent probe, as described previously [42]. In the presence of pyrene, mPPCPN concentrations ranging from 3.125 to 200 µg/mL were agitated overnight in water at 25° C using Heidolph Shaker. Filtrated the test samples, kept in a fluorescence multi-well plate reader, and observed using SpectramaxTM multiplate reader (Molecular Devices, US) at λex 339 nm and λem 390 nm wavelengths, respectively. The pyrene spectra were obtained by scanning the solutions across a wavelength range of 190-600 nm.

4.2.3 Preparation and characterization of mPEG-PLA-Pt(II)-Ce6 micelles (mPPCPN Ms)

4.2.3.1 Preparation of mPPCPN Ms

mPPCPN conjugate was dissolved in DMF at a concentration of 10.0 mg/mL, and the organic solvent was removed by a rotary evaporator. The polymer film was hydrated in PBS 7.4 (500 µL), and stirred 5 h at 37˚C. The micellar solution was centrifuged (13,000 RPM, 20 min, 4 ˚C) and filtered through a 0.45 µm filter to remove the un-encapsulated Ce6.

4.2.3.2 Physico-chemical characterization of mPPCPN Ms

Before measuring the particle size distribution, the mPPCPN Ms was properly diluted in Milli-Q water. The polydispersity index (PDI) was calculated by dividing the standard deviation of the particle diameter distribution by the mean particle diameter. The average homogeneity of a particle solution is represented by PDI. Ce6 content in mPPCPN Ms was estimated by using UV–Visible spectrophotometer (Jasco UV- 670, Japan) at λmax of 405 nm. The SEM morphology of the lyophilized powder of mPPCPN Ms with cryoprotectant was examined by using a FESEM electron Microscope (Apreo Lo Vac, FEI, USA). The cryoprotected lyophilized mPPCPN Ms powder was placed on carbon tape and sputter-coated using a gold-palladium alloy for 30 min at a thickness of 10 mm. At a 20 kV accelerating voltage, the images were acquired with a resolution of 500 nm. Cryogenic Transmission Electron Microscopy (TEM, JEM- 1200EX, JEOL, Japan) also assessed the morphology of the mPPCPN Ms. Briefly, mPPCPN Ms was stained with Uranyl acetate (2% w/v) and later were de-stained using distilled water. Further, the samples were dried for 10 min by placing them on copper grids and then visualized.

The mPPCPN Ms were also stored at 4 oC, and room temperature for stability studies. The mPPCPN Ms samples were tested for particle size and drug loading % at specified time intervals for 30 days. The drug-loading, encapsulation efficiency, and triggered release behavior of mPPCPN Ms were determined using a UV−vis spectrometer (Jasco UV-670, Japan) at room temperature. The entrapment efficiency (EE) and drug loading (DL) of the mPPCPN Ms formulation were calculated using the formulae below.

$$\text{EE (\%)} = \frac{Weight\ of\ Ce6\ present\ in\ the\ \text{mPPCPN Ms}}{Weight\ of\ Ce6\ added\ initially} \times 100$$

$$DL\ (\%) = \frac{Weight\ of\ Ce6\ present\ in\ the\ \text{mPPCPN Ms}}{Weight\ of\ the\ \text{mPPCPN Ms}} \times 100$$

4.2.3.3 Differentialscanning calorimetry (DSC)

A Differential Scanning Calorimeter (DSC 60, Shimadzu, Japan) conducted the thermo-analytical characterization of Ce6, cisplatin, mPEG-PLA, and mPPCPN Ms. Samples were placed in an aluminum pan and hermetically sealed. Thermograms were recorded between ambient temperature and 500 °C at a heating rate of 10 °C/min.

4.2.3.4 XRD analysis

The X-ray diffraction spectra of Ce6, cisplatin, mPEG-PLA, and mPPCPN Ms were examined by an X - ray diffractometer (ULTIMA-IV, Rigaku) at 40 kV and 30 mA, respectively, using Cu Kα radiations (k= 0.15405 nm).

4.2.3.5 In vitro drug release study

The dialysis method was employed to examine the in vitro drug release of Ce6 from mPPCPN Ms. In Brief, 500 μg/mL mPPCPN Ms solution was poured in the dialysis bag of molecular cut-off 3.5 KDa (Spectrum Laboratories, USA). The dialysis bag was tightly sealed and suspended in PBS solution containing 0.1 % w/v Tween 80 at pH values of 5.5, 6.5, and 7.4. The whole system was held at 37 ± 0.5 °C under constant stirring at 100 rpm. 1 mL sample was removed at predetermined time intervals. To maintain sink conditions, a fresh medium was used to replenish the old medium of equivalent volume. The NIR laser (Shanghai Dream Lasers Technology Co., Ltd, China) triggered Ce6 release experiment was also conducted by exposing the sample to 660 nm laser irradiations (0.5 W/cm2) for 5 min. Then the accumulative release content of Ce6 from mPPCPN Ms was measured by UV−vis spectrometer (Jasco UV-670, Japan) at a specific wavelength of 405

nm. The % amount of the drug released at a specified time (t) can be computed using the following equation:

$$\text{Cumulative release (\%)} = \frac{Ct\, Vo + V' \sum_{i=1}^{t-1} Ci}{Mtotal} \times 100$$

Where M total denotes the total amount of Ce6 in the dialysis tubes prior to release; the initial volume of release media is represented as V0, and V′ represents the volume of the media taken out at a specified time (t), Ct denotes the measured Ce6 concentration in release medium at the specified time point.

4.2.3.6 Hemolysis study

In-vivo toxicity of the mPPCPN was assessed by a hemolytic toxicity study. Briefly, the Wistar rat blood (5 mL) was collected using capillaries by eye puncture method and collected in heparinized tubes. Then, Red blood cells (RBCs) were isolated from the blood by centrifuging at 3000 rpm for 30 min at 4 °C, and the supernatant was withdrawn. Then RBC was washed and resuspended with 0.9 % w/v NaCl and made to 5 % v/v suspension. 0.9 % w/v NaCl solution was used to dissolve mPPCPN and incubated with RBC suspension for 1 h at 37 °C. In this study, NaCl (0.9% w/v) and Triton-X 100 (1% solution) were mixed with RBC suspension as a negative and positive control, respectively. The % of hemolysis in the supernatant was quantified by measuring the hemoglobin (Hb) content in the supernatant. The SpectramaxTM multiplate reader (Molecular Devices, US) has been used to measure Hb content (at 576 nm), and the following formula was used to calculate it:

$$\% \text{ Hemolysis} = \frac{\text{Absample} - \text{Ab}(-)}{\text{Ab}(+) - \text{Ab}(-)} \times 100$$

Where Ab sample = sample absorbance, and Ab (+) = Triton-X 100 absorbance, and Ab (−) = 0.9 % w/v NaCl absorbance.

4.2.3.7 Biochemical characterization

4.2.3.7.1 Evaluation of singlet oxygen generation (SOG)

The Assessment of SOG was evaluated by using 9, 10-dimethylanthracene (DMA) as a fluorescent dye which is mainly used for the observation of singlet oxygen ($1O_2$). The release of $1O_2$ increases the intensity of fluorescence. This study was performed for the free Ce6, mPPCPN, mPPCPN Ms in DMSO and PBS at pH 7.4. DMA (20 mM) was mixed with all Ce6-containing formulations containing Ce6 at a concentration of 1.5 µg (1 mL DMSO) and allowed to equilibrate for 10 min. The irradiation to the mixture (Ce6 & DMA) was done by a laser source of 660 nm and exposed at an intensity of 0.5 W/cm2 at various time intervals. The reduction in the DMA fluorescence intensity was measured after the irradiation at Excitation and Emission wavelength 360 and 380-550nm, respectively. The change in the intensity at various time intervals was examined using a fluorescence spectrophotometer (SpectramaxTM, microplate reader, Molecular Devices, US) and UV−vis spectrometer (Jasco UV-670, Japan).

The $1O_2$ assessment for free Ce6, mPPCPN, and mPPCPN Ms was also evaluated by using N, N-dimethyl-4-nitrosoaniline (RNO) in the presence of histidine, which helps in the entrapment of $1O_2$. The aqueous systems of RNO (100 µL, 250 mM) and histidine (300 µL, 30 mM) were mixed with solutions of free Ce6, mPPCPN, and mPPCPN Ms (1 mL). From the aqueous system, 200 µL of sample solutions were plated in a 96-well plate and exposed to 600 nm NIR laser irradiation. After laser irradiation, the RNO absorbance at 440 nm was examined using a UV–vis spectrophotometer.

The determination of SOG for the Free Ce6, mPPCPN, and mPPCPN Ms was also determined by employing Singlet Oxygen Sensor Green (SOSG). Briefly, mPPCPN Ms containing 0.25µM of Ce6 concentration were dissolved in PBS pH 7.4. Then SOSG (2.5µM) was mixed with the micelle formulation, and all the samples were irradiated using a laser source of 660 nm (0.5 W/cm2) for 5 min. After the irradiation, the samples were determined for SOG by measuring the change in the fluorescence intensity at 494ex and 534em nm wavelength, respectively. The generation of singlet oxygen indicates the efficiency of the formulation to produce phototoxicity.

4.2.3.7.2 In situ oxygenation assay

To test our nanoformulations oxygen production capacity, we used OxiVision Green, an H2O2-responsive fluorescence nanoprobe, to evaluate H2O2 quenching capabilities. 5mM OxiVision Green dye- containing H2O2 (10 mM) was added to free Ce6, Ce6:CDPP (1:1), mPPCPN , and mPPCPN Ms (0.5 mg/mL) and incubated at 25 °C for 20 min. UV light at 365 nm wavelength was used to capture fluorescence photographs. The O2 production capacity of free Ce6, Ce6:CDPP (1:1), mPPCPN , and mPPCPN Ms was also measured in real-time using an oxygen dissolving meter (HANNA, India). PBS was used to disseminate free Ce6, Ce6:CDPP (1:1), mPPCPN , and mPPCPN Ms at a concentration of 50 µg/mL. Then 1 mL of liquid paraffin was added to separate the fresh PBS from the air.

4.2.3.7.3 Photothermal effect

The photothermal effect was evaluated by exposing the various concentrations of Ce6, mPPCPN Ms to 660 nm NIR laser (Shanghai Dream Lasers Technology Co., Ltd, China) radiations at a power density of (0.8 W/cm2) for 5 min to check the temperature variations.

4.2.4 Cell culture studies

4.2.4.1 In vitro Cell Cytotoxicity Assay

The MTT assay was used to test the in vitro cytotoxicity of free Ce6, Ce6:CDPP, and mPPCPN Ms on FaDu HTB-43 cells. Briefly, FaDu HTB-43 cells were cultured at a number of 1x104 viable cells/well in a 96-well plate. The plates were incubated overnight to enable the cells to adhere. The media was removed after the incubation and washed the cells with PBS pH 7.4 immediately. Then, the cells were incubated with free Ce6, Ce6:CDPP (1:1), and mPPCPN Ms at different Ce6 concentrations (i.e., 1.56 to 100 µg/mL equivalent Ce6 concentrations) followed by 12 h incubation . After 12 h, cells were exposed to 660 nm NIR laser (0.5 W/cm2) irradiation using a 660 nm laser for 5 min and then placed for another 12 and 36 h incubation. After discarding the media, each well was filled with a solution containing 50 µL of MTT in PBS (pH 7.4) and incubated for 4 h. Next, the MTT solution was discarded. In order to dissolve the MTT formazan crystals, 150 µL of dimethyl sulfoxide (DMSO) was poured into each well. A microplate reader was used to detect the absorbance of these specimens at a wavelength of 570 nm. The in-vitro cytotoxic effects on FaDu HTB-43 cells were also analyzed at different irradiation times (0–10 min). The % cell viability was computed as per the following equation:

$$(\%) \text{ Cell viability} = \frac{Abs_{Sample}}{Abs_{Control}} \times 100$$

4.2.4.2 Cellular uptake studies

Flow cytometry and Confocal microscopy were used to analyze the qualitative and quantitative uptake of free Ce6, Ce6:CDPP (1:1), and mPPCPN Ms in FaDu HTB-43 cells. For flow cytometry analysis, 1 x 106 cells of FaDu HTB-43 were cultured in 12 well plates at 37 °C in a 5 % CO_2 humidified environment containing 10% FBS and kept for 12 h incubation. The MEM media was then withdrawn and replaced (500 µL) with a new media possessing free Ce6, Ce6:CDPP (1:1), and mPPCPN Ms at a concentration of 6 µg/mL. After 1 and 4 h of incubation, the cells were irradiated with 660 nm laser (0.5 W/cm2) for 5 min, while cells without NIR laser exposure were considered control. Following incubation, the cells were processed, harvested, and suspended in PBS to be studied employing a flow cytometer (BD FACS Area III). For the investigation, ten thousand cells were gated and captured utilizing the Ce6 channel (ex/em. 461/650 nm). For the Confocal microscopy study, FaDu HTB-43 cells were injected with free Ce6, Ce6:CDPP (1:1), and mPPCPN Ms (6 µg/mL) for 1 and 4 h. Following incubation, the cells were irradiated for 5 min to a 660 nm NIR laser (0.5 W/cm2), and the cells without light irradiation served as control. Washed the cells with PBS and stained the cell nuclei with DAPI for 5 min followed by washing with PBS to remove free DAPI, fixed the cells with 4 % paraformaldehyde, and imaging captured by Confocal microscope.

4.2.4.3 Annexin V Assay

In a 6-well plate, 1 ×106 FaDu HTB-43 cells were plated and cultured overnight. After incubation, the cells were given free Ce6, Ce6:CDPP (1:1), and mPPCPN Ms at a Ce6 concentration of 50 µM. Following 12 h of incubation, the cells were exposed to a 660 nm laser (0.5 W/cm2) irradiation for 5 min. Rinsed the cells with PBS pH 7.4 following 12 h of incubation and centrifuged to yield a cell pellet. The method provided by TACS® Annexin V-FITC Apoptosis Detection Kit was

followed in which the cell pellet was resuspended in 100 µL of binding buffer and labeled with 1 µL of Annexin-V FITC and 10 µL of PI. After 15 min, all test samples and control tubes received binding buffer. Flow cytometry was used to examine the cells (gating 10,000 live cells) [43,44].

4.2.4.4 Cell cycle analysis

In a 12-well plate, 1×106 FaDu HTB-43 cells were plated and cultured overnight. For 12 h, cells were treated with free Ce6, Ce6:CDPP (1:1), and mPPCPN Ms at a 50 µM concentration. The treated cells were exposed to 660nm NIR laser (0.5 W/cm2) intensity laser radiation for 5 min. The cells were centrifuged at 1000 rpm for 7 min. The cells were collected after treatment, rinsed in 1 mL PBS (pH = 7.4), and centrifuged at 1000 rpm for 7 min. The supernatant was removed, and the cells were fixed with ethyl alcohol (70 %, ice-cold) for 30 min at 20°C. Cells were fixed and centrifuged at 1200 rpm for 5 min. The fixed solution was aspirated, added 1 mL of ice-cold PBS, and centrifuged the cells at 1500 rpm for 5 min. The cells were resuspended in a staining solution (50 µL of 1 mg/mL RNase, 50 µL of 1 mg/mL propidium iodide, and 400 µL of PBS7.4). A flow cytometer was used to examine the cell cycle arrest (BD FACS ARIA, Germany).

4.2.4.5 DNA Fragmentation and Nuclear staining assay

DNA fragmentation assay was studied on FaDu HTB-43 cells. Briefly, In a 12-well plate, 1×105 FaDuHTB-43 cells were plated and cultured overnight. After the incubation, cells were treated with free Ce6, Ce6: Pt (1:1), and mPPCPN Ms (Ce6 concentration of 50 μM), incubated overnight, and afterward, treated cells were exposed to 660nm NIR laser (± L) (0.5 W/cm2) intensity laser radiation for 5 min, respectively. The cells were rinsed in PBS 7.4, trypsinized, harvested, and DNA was extracted using GSure DNA genomic isolation kits following incubation. The isolated DNA was checked for absorbance at 260 nm and 280 nm, and the ratio was obtained. A ratio of

1.8 is considered to be pure DNA. DNA was extracted and ran on a 1.5 % agarose gel containing 0.5 µg/mL ethidium bromide. The gel was then observed for DNA fragmentation under the microscope using the Fusion Pulse gel doc system (ChemiDocTM Gel Imaging System).

For Nuclear staining, FaDu HTB-43 cells were cultured overnight at a density of 1×105/well in six- well tissue culture plates. Treated the cells with free Ce6, Ce6: Pt (1:1), and mPPCPN Ms. After incubation, the cells were exposed to 660 nm laser ($\pm$ L) (0.5 W/cm2) for 5 min, respectively. The cells were then rinsed in PBS, fixed, and labeled with acridine orange (10 µg/mL) and DAPI (10 µg/mL) before being viewed under a fluorescence microscope.

4.2.4.6 Mitochondrial membrane potential

In a 6-well plate, 1×106 FaDu HTB-43 cells were plated per well and cultured overnight. Following that, the cells were injected with free Ce6, Ce6: Pt (1:1), and mPPCPN Ms at a Ce6 concentration of 50 µM for 24 h. After that, the cells were exposed with or without a 660 nm laser at a power density of 0.5 W/cm2 for 5 min, respectively. Following treatment, the cells were rinsed in cold PBS and labeled with 5,5,6,6tetrachloro1,1,3,3 tetraethylbenzimidazolcarbocyanine iodide (2 µM, JC-1 dye, Sigma-Aldrich, USA) for 30 min under incubation. The cells were observed using red and green channels on a fluorescence microscope. A flow cytometer was also used to examine the mitochondrial membrane potential (BD FACS ARIA, Germany).

4.2.4.7 ROS detection assay

1×104 cells of FaDu HTB-43 cells were grown per well in 6 well plates. The cells were subsequently subjected to free Ce6, Ce6: Pt (1:1), and mPPCPN Ms at a Ce6 concentration of 50 µM for 24 h. Following incubation, cells were exposed to 660 nm laser irradiation ($\pm$ L) (0.5 W/cm2) for 5 min. The cells were labeled for 20 min at 37 °C with 5 µM of 2',7'-Dichlorofluorescin

diacetate (DCFH-DA), washed three times with sterile PBS and examined under a fluorescence microscope for qualitative analysis. For quantitative analysis, flow cytometry analysis was examined on 1 x 106 of cells FaDu HTB- 43 using an analytical flow cytometry device (BD FACS Area III). The tests were carried out three times.

4.2.5 Spheroid study

4.2.5.1 Penetration in spheroids

\Ten thousand cells of FaDu HTB-43 were cultured as spheroids using the liquid overlay technique as per earlier reported literature [45] and subjected to free Ce6 and mPPCPN Ms for 1-4 h. The z-stacked pictures (10 µm intervals at z-axis) were acquired using a confocal microscope (TCS SP8, Leica Microsystems, Germany) at 10X magnification after being gently cleaned once with PBS. During the visualization of spheroids through the z-axis, the X and Y axes are fixed. Image J software was used to process the pictures of spheroids.

4.2.5.2 Growth inhibition in spheroids

Spheroids were incubated with free Ce6, Ce6: Pt (1:1), and mPPCPN Ms at a Ce6 concentration of 6 µg/mL to evaluate growth inhibition. The images of the spheroids were taken for different time periods (0, 2, 4, and 6 days), the dimensions of the spheroids were evaluated, and the spheroids were imaged using a fluorescence microscope (Leica Microsystems, Germany) at 10X magnification under bright- field conditions.

4.2.5.3 Live/dead cell assay

For 24 h, the spheroids were loaded with free Ce6, Ce6: Pt (1:1), and mPPCPN Ms. The spheroids were then labeled with 2 µM of Calcein blue and 4 µM of PI and incubated for 30 min at 37 °C.

Finally, the dyed spheroids were examined using a fluorescence microscope equipped with a rhodamine (540/570 nm) filter and a FITC (Ex/em. 495/519 nm).

4.2.5 In vivo anticancer efficacy Study

The subcutaneous xenograft tumor in nude mice was developed by injecting FaDu HTB-43 cells (1.5×106) into the right flank. The tumor inhibition study was carried out once the tumor volume reached ~50 mm3, and the mice were segregated into four groups: negative control (saline), Free Ce6 group, Ce6:CDPP (1:1) group, and mPPCPN Ms group, each group with five mice. Each mouse was exposed to laser irradiation by a diode with a wavelength of 660 nm (0.5 W/cm2) for 5 min after receiving an intravenous tail injection of the drug at a dosage of 5 mg/kg, and tumor volume was measured. The tumor volume and body weight of the mice were measured every other day for 21 days, after which the animals were euthanized by cervical dislocation, and the tumor mass was weighed surgically[46]. The in vivo biodistribution was studied using optical imaging. Mice with FaDu HTB-43 tumors (~50 mm3) were given an intravenous injection of 100 µL mPPCPN Ms through the tail vein at a Ce6 dosage of 5 mg/kg. Following injection at 0, 1, 3, 6, 12, 24, and 30 h, the mice were anesthetized and monitored using an IVIS in vivo imaging system (IVIS® Lumina III, PerkinElmer, USA). Furthermore, the treated animals were slaughtered at 36 h after injection for the tissue micelles distribution study. The heart, liver, spleen, lung, kidney, and tumor were among the principal organs obtained for IVIS observation [47]. The mice were slaughtered following treatment, and the tumors were collected, frozen, sectioned into slices for histological investigation using hematoxylin and eosin (H&E), TUNEL, Ki67 staining, and ROS (DCFHDA) assay in each group of treated animals according to the manufacturer's instructions (Y. Nakamura et al. 2022).

4.2.5.1 In vivo overcoming hypoxia study

PBS, Free Ce6 (+L), Ce6: CDPP (1:1) (+L), and mPPCPN Ms (+L) were injected into the tail veins of FaDu HTB-43 tumor-bearing mice (100mm3). Ce6 and cis-Pt (IV) doses were maintained constant in these groups at 5 mg per kg body weight. Light irradiation of the tumor locations was given to mice 12 h after injection. Mice were slaughtered, and tumors were collected for immunofluorescence investigation 24 h after they had been irradiated. For HIF-1α (F.S. Mackay et al. 2007) and CD31 labeling, the tumors of mice were fixed in 4% formalin (dilution 1:1000, CST36169, and CST3528). DAPI was used to label the tumor cells' nuclei. fluorescence microscope (Leica Microsystems, Germany) was used to get the pictures.

4.2.5.2 Western blotting

In tumor tissues, apoptotic protein markers such as caspase 3, 7, hypoxia-inducible factor-1α (HIF-1α), CD31, epidermal growth factor receptor (EGFR), and Ki-67 were measured. The tumor tissues were disrupted and homogenized using MINILYS® after being suspended in RIPA buffer supplemented with protease inhibitor/PMSF (Bertin Technologies, France). The supernatants were obtained after centrifuging tumor tissues at 16000 g for 20 min at 4 ° C. A BCA protein assay kit (TaKaRa Bio Inc., USA) was used to quantify the isolated proteins. For electrophoresis, identical amounts of proteins were added to 15 % and 10 % sodium dodecyl sulfate-polyacrylamide gels (lower/higher mol weight proteins) (SDS-PAGE). The proteins were then deposited for 3 h at 60 V in Tris-glycine buffer on nitrocellulose membranes (Bio-Rad, USA). In Tris-buffered saline containing 0.1 percent (v/v) Tween-20, primary antibodies for Caspase-3, Caspase-7, HIF-1α, CD31, EGFR, and Ki-67 were used to block the membranes overnight at 4 °C (TBST). The isolated proteins were normalized using β-actin. Following treatment, the membranes were rinsed 3 times with TBST and incubated with secondary antibodies for 2 h at room temperature. After completely

rinsing the membranes, the blots were developed using Bio- enhanced Rad's chemiluminescence (ECL) solution. The ChemiDocTM Gel Imaging System was used to identify the blots, which were subsequently quantified using Image J software (Version 6.0).

4.2.5.3 Glutathione level in tumor tissues

To evaluate GSH levels in vivo, GSH and GSSG assay kit (Thermo-Fisher) was used. Mice with 200 mm3 FaDu HTB-43 tumors were exposed to PBS, Free Ce6 (+L), Ce6:CDPP (1:1) (+L), and mPPCPN Ms (+L) at a Ce6 dose of 5 mg/kg body weight with the laser by intravenous injection. The tumor of each group was rinsed with cold PBS to remove the blood. The tumor (10 mg) was homogenized in 250 µL of ice-cold PBS (100 mM, pH 7), followed by centrifugation at 14000 rpm for 10 min at 4 °C. 1 mL of cold 5 % SSA was added to the homogenized pellet, mixed thoroughly, and incubated for 10 min. The sample was centrifuged at 14000 rpm for 10 min at 4 °C, and the supernatant was collected for analysis using UV-Vis spectroscopy at λmax. 405 nm.

4.2.6 Statistics

All of the tests were carried out three times, and the findings are shown as mean and standard deviation (mean SD). Student's t-test and one-way analysis of variance (ANOVA) were used to compare the groups. Values of $p < 0.05$ were considered to be statistically significant (*$p < 0.05$, ** $p < 0.01$, *** $p < 0.001$). The data were analyzed using GraphPad Prism 6 software.

4.3 Results and Discussion

4.3.1 Physicochemical Characterization of the mPPCPN Ms

The mPPCPN conjugate was synthesized following the steps outlined in Figure 4.1 The cis-dichloro leaving groups were substituted with azide via intermediate nitrate substitution using silver nitrate followed by sodium azide. The square planar cisplatin derivative at its +II oxidation

state was oxidized to Pt(IV) via dihydroxyl derivatization by the reaction with hydrogen peroxide. The Ce6 was derivatized with the platinum compound via esterification reaction followed by conjugation with the preformed polymer, mPEG-PLA. The newly synthesized mPPCPN conjugate was physiochemically characterized by 1H NMR, FTIR spectroscopy, UV absorption, and GPC analysis. Figure 4.1a depicts the 1H NMR spectrum of mPPCPN conjugate. The proton peaks at δ0.8 ppm, 2.3 ppm, 6.5 ppm belong to Ce6 protons, δ8.2 ppm, 8.5 ppm relate to ammine protons of Pt(IV), and the peaks at δ4.3 ppm, 4.2 ppm, and 3.7 ppm belong to mPEG-PLA protons. These findings suggested that Pt(IV) and Ce6 have been effectively conjugated to mPEG-PLA. Moreover, the 1H NMR spectra of the intermediates, cis, trans, cis-[Pt(N3)2 (NH3)2 (OH)2, and Ce6-Pt(IV) diazide is shown in Figure 4.1b and c, respectively. The conjugation of Ce6-Pt(IV) and mPEG-PLA was further verified by FTIR spectroscopy Figure 4.1d. The -CH vibrations and -C=O stretch of PLA on mPPCPN conjugate are responsible for the peaks at 2958 cm-1 and 1722 cm-1, while the –C-O-C- stretch of mPEG and PLA on the mPPCPN chain is responsible for the bands at 1079 cm-1 and 1248 cm-1, respectively. The distinctive peaks at 1722 cm-1 and 1248 cm-1, corresponding to the ester bonds (O-C=O), verified the successful conjugation of Pt(IV) and Ce6.

Furthermore, the presence of vibration frequencies at 3432 cm-1 (-OH stretching), 2946 cm-1 (-CH stretching), 1722 cm-1 (-C=O), 1648 cm-1 (-NH), 1259 cm-1 (-C-O-C), and 2160 cm-1 (N=N=N stretching) corroborated the conjugation of Ce6-Pt(IV) to mPEG-PLA.
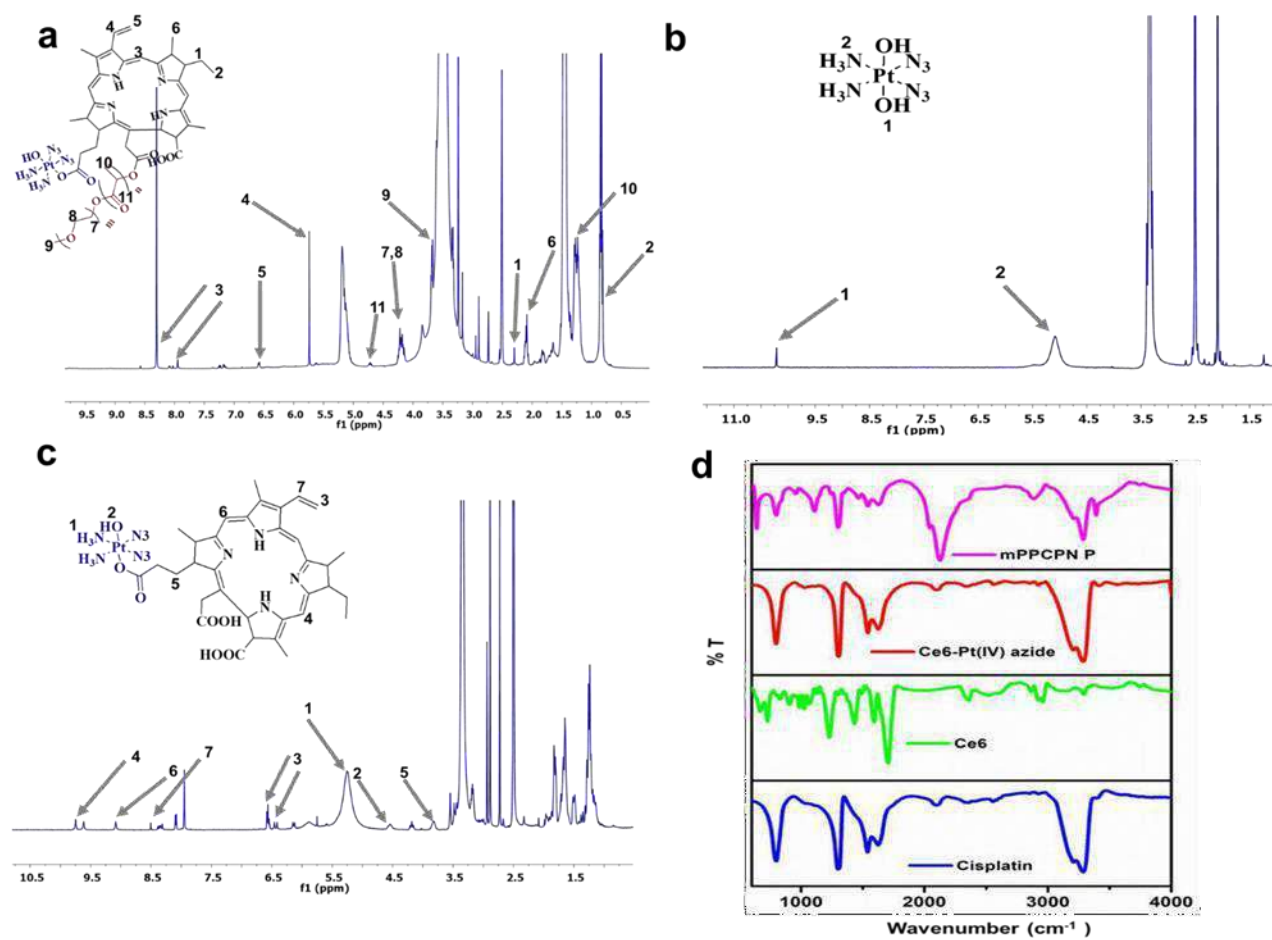
Figure 4.2 1H NMR spectra of mPEG-PLA-Ce6-Pt (IV)-(N3)2 in DMSO-d6; cis, trans, cis-[Pt(N3)2 (NH3)2 (OH)2 in DMSO-d6; Ce6-Pt (IV) azide in DMSO-d6.
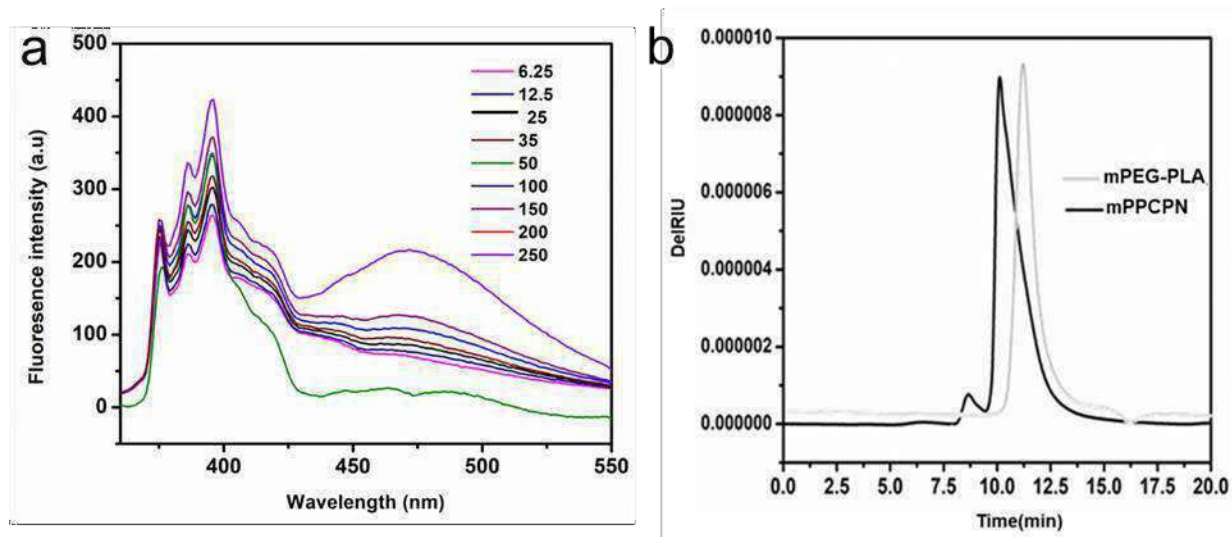
Figure 4.3 Determination of critical micelles concentration (CMC) by pyrene incorporation technique (inset. Excitation spectra of pyrene detected at the emission wavelength (λem). 390 nm) at various mPPCPN conjugate concentrations (0-250 µg/mL) (a); GPC chromatogram of mPEG-PLA and mPPCPN (b).

Further, the UV-vis absorption spectra of free Ce6, cisplatin, and mPPCPN Ms in aqueous solution at pH 7.4 were analyzed to obtain insight into the structural properties of the conjugate. The bathochromic shift of mPPCPN Ms absorption peaks from 663 nm for free Ce6 to 668 nm for micelles is illustrated in Figure 4.3a. The bathochromic shift might be due to changes in the Ce6 environment, indicating that Ce6 was successfully conjugated with Pt(IV) and mPEG-PLA. The mPPCPN Ms exhibited a wide absorption band extending from 300 to 600 nm obtained from fluorescence spectroscopy, as illustrated in Figure 4.3b. The mPPCPN Ms showed fluorescence at 440 nm after excitation at 360 nm and 665 nm after excitation at 405 nm, which belongs to Ce6

typical fluorescence, respectively. The fluorescence analysis confirmed the effective encapsulation of Ce6 in mPPCPN Ms. Ce6 drug loading content and entrapment efficiency in mPPCPN Ms were found to be around 10.23 % and 70 %, respectively. The Ce6 characteristic absorption peak at 405 nm in the UV was used to quantify the proportion of Ce6 loaded on mPPCPN Ms.
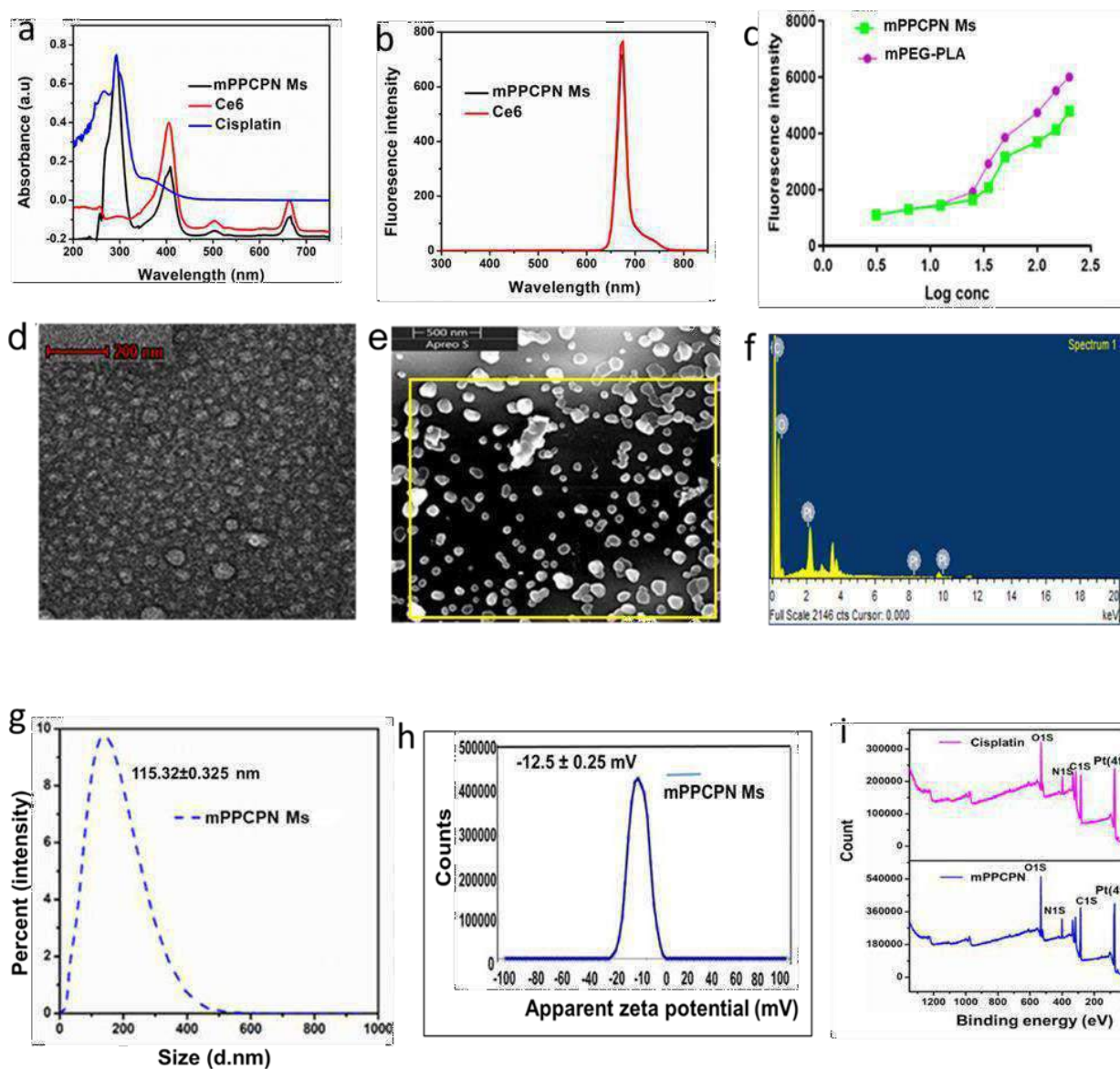
Figure 4.4 Physicochemical characterization of mPPCPN Ms. UV/Vis absorption spectra (a); fluorescence spectra (b); determination of critical micelles concentration (CMC) by pyrene incorporation technique (Excitation spectra of pyrene detected at the emission wavelength (λem). 390 nm) at various mPPCPN conjugate concentrations (0-250 µg/mL) (c); examples of mPPCPN Ms images from TEM (d) and SEM (e); Elemental analysis (EDX) of mPPCPN Ms (f); size distribution by dynamic light scattering technique (g); zeta-potential (h); XPS spectra of cisplatin and mPPCPN conjugate (i).

The increase in the molecular weight of the mPPCPN conjugate following conjugation of mPEG-PLA with Ce6-Pt(IV) diazide was evaluated using size exclusion chromatography (SEC). SEC analysis revealed that one molecule of mPEG-PLA was covalently bound to the Ce6-Pt(IV) polymer under the specified reaction environment (Figure 4.2b). Further, pyrene was used as a fluorescent probe to estimate the CMC of the mPPCPN copolymer. The CMC value for mPPCPN conjugate was determined to be 35 µg/mL (Figure 4.2a). The low critical micelle concentration (same as mPEG-PLA) indicated that the mPPCPN copolymer could easily form a core-shell structure in an aqueous environment and maintain the micellar structure in vitro and in vivo under diluted conditions.

The mPPCPN Ms, prepared using the thin-film hydration technique, were physiochemically examined by particles size analysis, zeta potential measurements, XRD spectroscopy, DSC, XPS analysis, drug loading, and encapsulation efficiency determination experiments. The morphology of mPPCPN Ms was comprehensively investigated using transmission electron microscopy (TEM) and SEM. TEM scans revealed that the mPPCPN Ms had a 2D spherical form with an average diameter of ~100 nm (Figure 4.3d). Furthermore, SEM micrographs revealed that mPPCPN Ms

were nanosized with spherical shapes exhibiting the size of 100-200 nm (Figure 4.3e). Elemental analysis was performed to evaluate the elemental composition of the mPPCPN Ms using EDX spectroscopy. The EDX spectrum of the mPPCPN Ms exhibited the peaks corresponding to C, O, and Pt, as shown in Figure 4.3f. Dynamic light scattering (DLS) was used to verify the particle size of mPPCPN Ms, which was found to be 115 ±2.35 nm with a polydispersity index (PDI) of 0.136 (Figure 4.3g), indicating a reasonably narrow size distribution and good dispersity in aqueous solution. The zeta potential of mPPCPN Ms was -12.9 mV, indicating that the nanocarrier possessed good colloidal stability (Figure 4.3h). The mPPCPN Ms displayed stable dispersity in various solutions, including PBS buffer, cell culture medium (MEM), and 10% fetal bovine serum (FBS), as shown in Figure 4.4c, with no evident aggregation over 7 days, indicating potential applicability in the biological context. The particle size, drug loading (%), and the fluorescence intensity of Ce6 in mPPCPN Ms were also examined for 30 days upon storing at 4 °C. As shown in Figure 4.4d, the size of the mPPCPN Ms did not increase much and retained the size of ~110 nm upon storing at 4 °C, which confirmed the micellar stability. In addition, the fluorescence intensity of Ce6 was quenched negligibly, and the % drug loading content was also found stable upon storage at 4 °C. UV-absorption and fluorescence spectra were used to investigate the optical characteristics of mPPCPN Ms (Figure 4.4a and b).
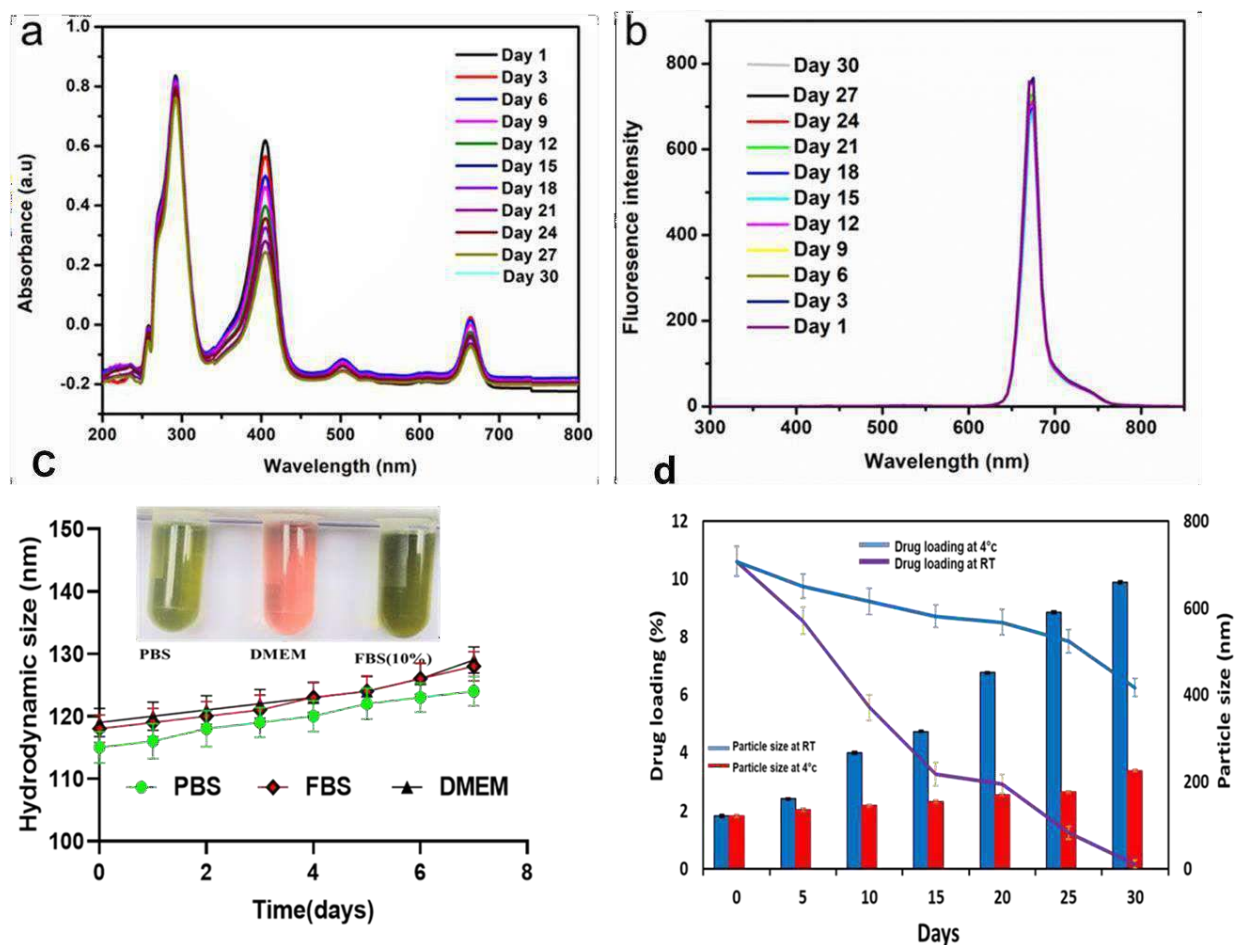
Figure 4.5 Kinetic stability of mPPCPN Ms using UV-Visible spectroscopy (a); fluorescence spectroscopy (b); Changes in particle size of mPPCPN Ms in DMEM media, PBS pH 7.4, FBS (10%) at 4 °C for one week (C); Changes in particle size, polydispersity, and drug loading of mPPCPN Ms in aqueous solution at 4 °C and 25 °C for 30 days. Data are expressed as mean SD (n=3).

DSC thermograms were plotted simultaneously for thermal analysis of free Ce6, cisplatin, mPEG-PLA, and mPPCPN Ms (Figure4.5a). Exothermic melting peaks were observed for Ce6 at 65.87

°C, mPEG- PLA at 64 °C, and cisplatin at 95 °C and 173 °C, respectively. mPPCPN Ms showed a melting point in the range of 47.74-61.93 °C, with a peak maxima at 55.43 °C. The XRD spectra of pure Ce6, cisplatin, mPEG-PLA, and mPPCPN Ms are shown in Figure 4.5b. No distinctive strong peaks were identified in XRD analysis, but a very smooth curve of pure Ce6 was observed. Cisplatin displayed 2θ peaks at 23.15°, 25.70°, 28.24°, 34.39°, 35.45°, 43.94°, 48.81°, 52°, 54°, 57°, and 65° indicating the crystalline structure. The XRD pattern of mPEG-PLA exhibited typical high-energy diffraction peaks at 2θ, 19°, and 23°. mPPCPN Ms showed 2θ peaks at 13.60°, 16.78°, 24.64°, 25.48°, and 31.85° revealing the crystalline structure of mPPCPN conjugate. X-ray photoelectron spectroscopy (XPS) was used to quantify the chemical state of the surface elements in cisplatin and mPPCPN Ms formulation.
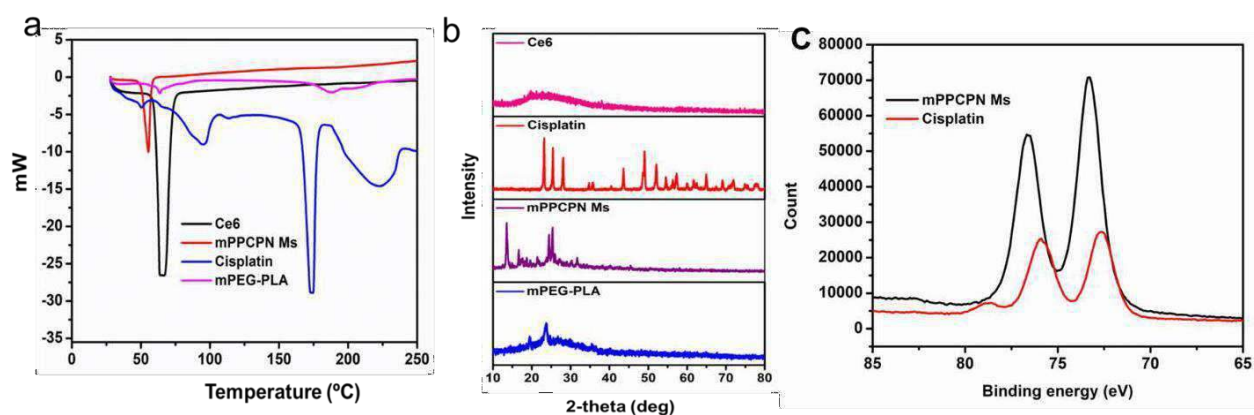
Figure 4.6 DSC thermogram of Ce6, Cisplatin, mPEG-PLA, mPPCPN Ms (a); XRD spectral analysis of Ce6, Cisplatin, mPEG-PLA, mPPCPN Ms (b). High-resolution XPS spectra (Pt 4f) of CDDP and mPPCPN Ms

The complete survey and core-level spectra of cisplatin and mPPCPN Ms samples are shown. Elements C, N, O, and Pt(II) are predominated in free cisplatin, whereas the elements C, N, O, and Pt(IV)are predominated in mPPCPN. The element content was higher in mPPCPN conjugate (C1s 20.14%, O1s 59.64 %, N1s 14.32 % , Pt4f 5.9 %) than in cisplatin (C1s 16.82 %, O1s 55.32 %, N1s 12.25 % , Pt4f 15.61%). The binding energy of platinum in cisplatin and mPPCPN conjugate were calculated using a deconvolution method of corrected XPS spectra (Figure4.3i). Based on the XPS spectra, Pt(II) in cisplatin exhibited characteristic binding energy at 72.23 eV and 76.16 eV, respectively, while Pt(IV) 's binding energy in mPPCPN was shifted to 74.83 eV and 77.82 eV. This result indicated the change in the oxidation state from Pt(II) to Pt(IV) in mPPCPN conjugate.

Next, the Ce6 release behavior from the mPPCPN Ms was then measured using a UV-spectrophotometer (JASCO-800, Japan) at a specified wavelength of 405 nm in pH 7.4, 6.8, and pH 5.5, with or without NIR laser irradiation (±L). The sustained in vitro release for Ce6 was observed for many hours (h) in mPPCPN Ms. The quantity of Ce6 released from the mPPCPN Ms displayed a pH-dependent and laser irradiation-dependent release characteristic (Figure 4.6). The hydrolysis of Ce6 from the conjugate was rapid at lower pH, and the laser irradiation dissociated platinum diazide leading to faster Ce6 release than without laser treatment. A best-fit model for drug release kinetics was established based on the r2 values. The regression values for drug release from mPPCPN Ms at pH 5.5, 6.5, and 7.4 were 0.9664, 0.9827, and 0.9659, respectively, as calculated using kinetDS 3.0 software. The Ce6 release from mPPCPN Ms at pH 5.5 and pH 6.8 followed the Higuchi kinetic model, while the release at pH 7.4 followed the Korsmeyer Peppas kinetic model. The Ce6 release mechanism model for mPPCPN Ms was super case II transport at pH 5.5 based on the 'n' values of the Korsmeyer–Peppas equation (Figures 4.6). Further, the blood compatibility of the mPPCPN micelles was evaluated using PBS and TRITON- X 100 as negative

and positive controls (Figure 4.7a). The percent hemolysis induced by the mPPCPN polymer was less than 3% at a concentration as high as 0.4 mg/mL. Following treatment, the hemoglobin showed similar morphology as the untreated hemoglobins under SEM, indicating no significant damage (Figure 4.7b).
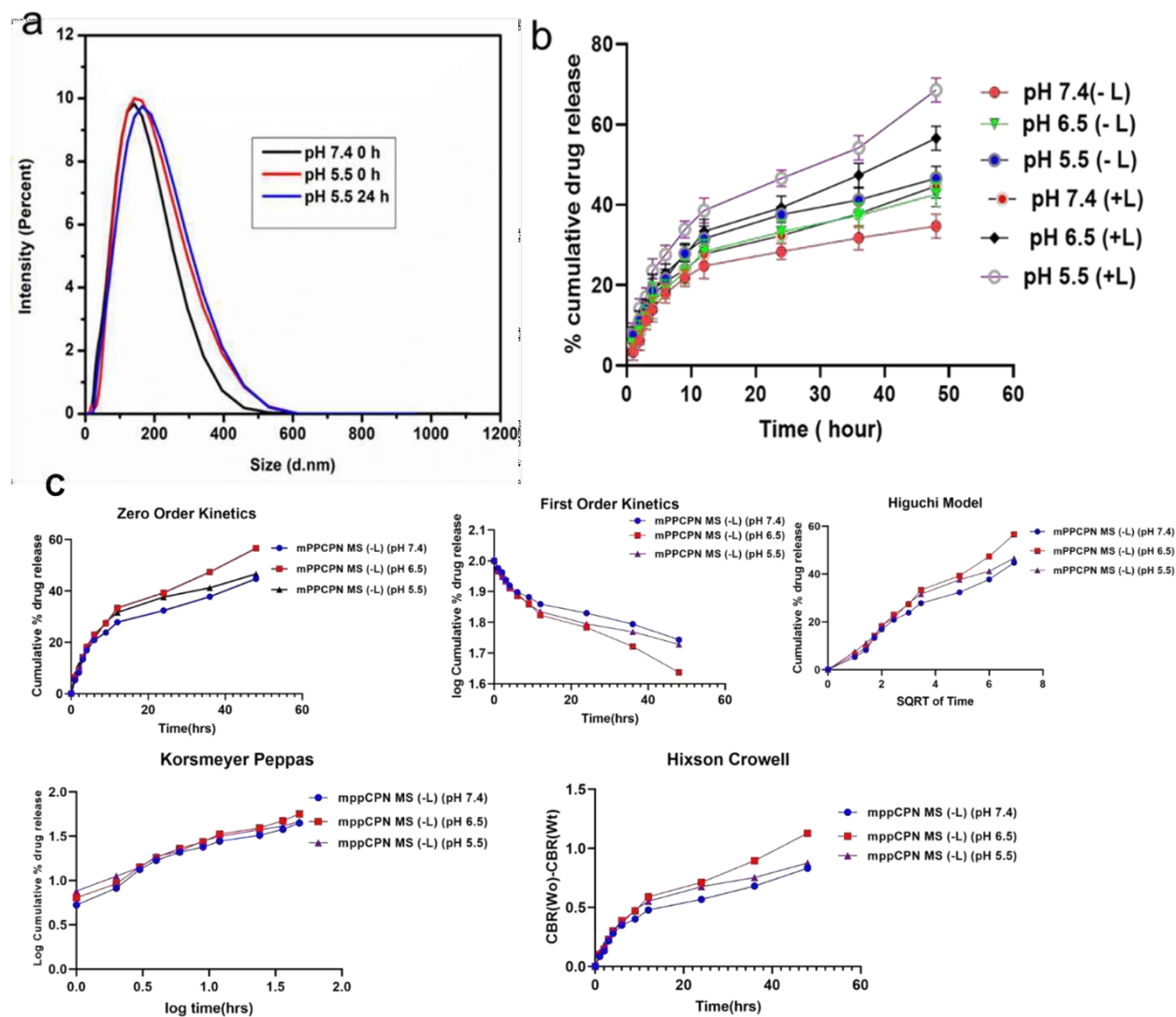
Figure 4.7 Size distribution of mPPCPN Ms at pH 7.4 or pH 5.5 for different time (a). In vitro drug release study of mPPCPN Ms at pH 7.4, pH 6.5, pH 5.5, with or without laser irradiation (b). Kinetic release study of mPPCPN Ms(-L) at various pH (7.4, 6.5, and 5.5)
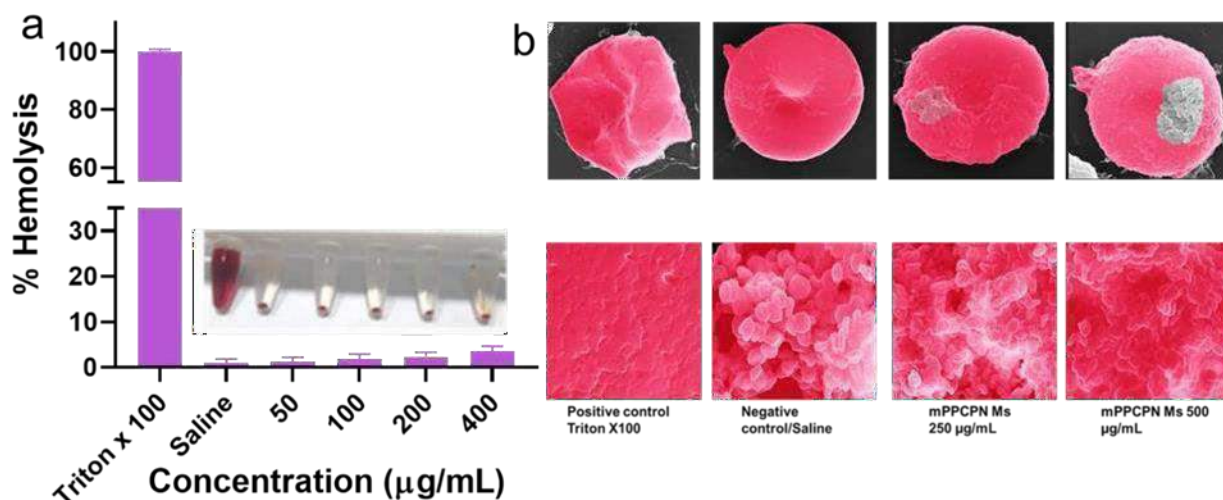
Figure 4.8 Haemolytic study of mPPCPN (a); RBC aggregates observed by scanning electron microscopy under normal conditions and influencing by 250 µg/ml, 500 µg/ml of polymer concentration (b). Scale bar 10 µm.

4.3.2 Evaluation of the Photoactivity and Singlet Oxygen Generation

The potential of free Ce6, Ce6, and cisplatin (CDPP) mixture at the molar ratio, 1:1, Ce6:CDPP (1:1), and mPPCPN Ms to generate singlet oxygen ($1O_2$) under laser irradiation was investigated using 9, 10- dimethyl anthracene (DMA), singlet oxygen sensor green (SOSG), and N,N-dimethyl-4-nitrosoaniline (RNO). DMA reacts selectively with $1O_2$, resulting in a reduction in its distinctive absorbance peaks. When a solution of free Ce6, Ce6:CDPP (1:1), and mPPCPN Ms containing DMA was exposed to a 660 nm laser (0.05 W/cm2), the relative absorption intensities of DMA at 399 nm reduced rapidly over time, indicating the generation of $1O_2$. There were no spectrum changes in the pure DMA solution (Figure 4.15). The $1O_2$ production capacity of mPPCPN

conjugates was much greater than that of free Ce6 in DMSO, suggesting that the Ce6 conjugated polymer prevented Ce6 aggregation and retained phototoxicity. The potential of free Ce6 to generate 1O2 gets reduced on aggregation due to the pi-pi stacking.
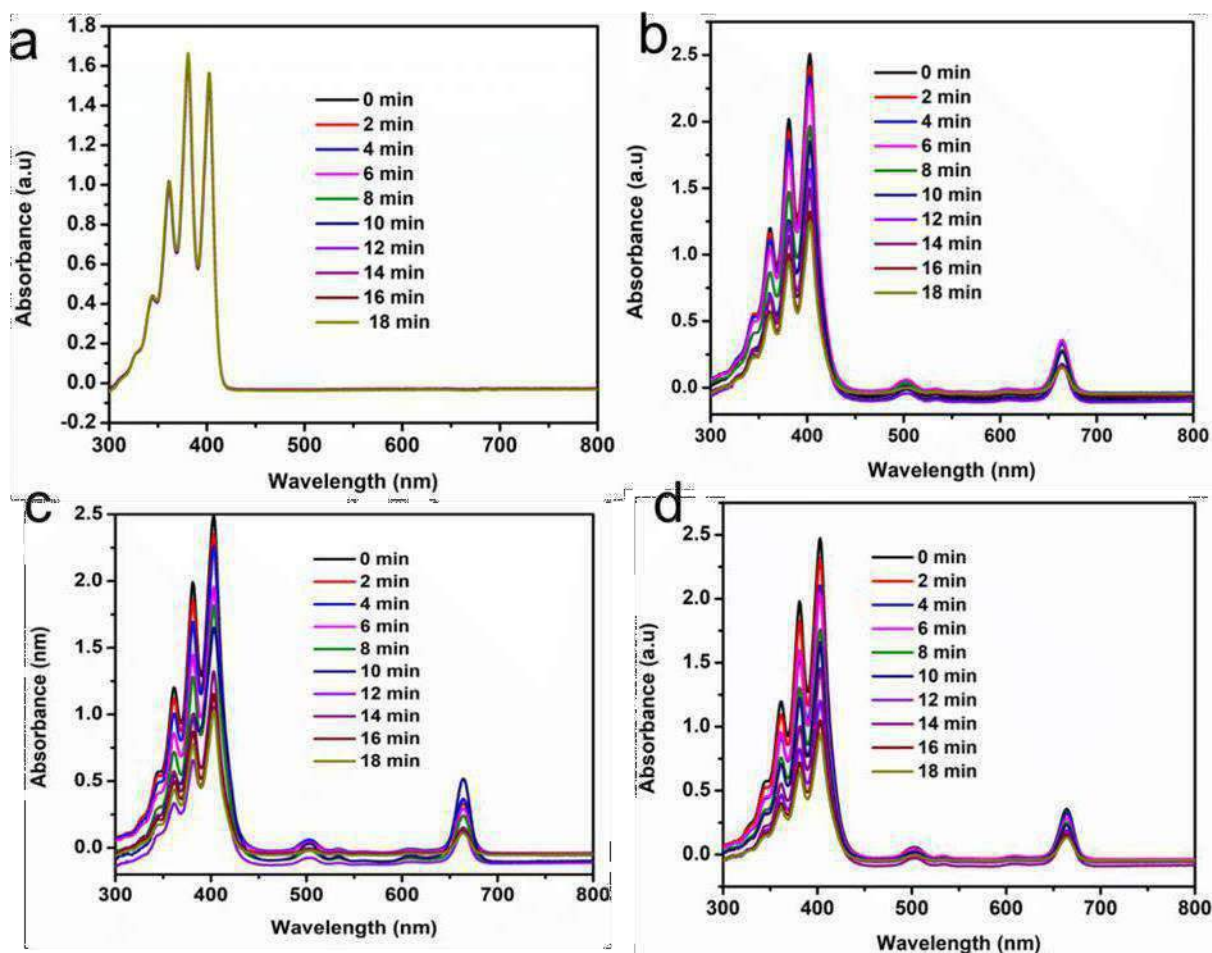
Figure 4.9 Time-dependent UV-Visible absorption spectra of ABDA (a); ABDA mixing with free Ce6 (b); mPPCPN (c); and mPPCPN Ms (d); after irradiation with a 660 nm lamp (0.5 W/cm-2) for 18 min.

The fluorescence signal of a 1O2-sensor green has also been used to detect 1O2 production levels (SOSG). Interestingly, the ability to produce singlet oxygen by mPPCPN Ms was lower than free Ce6. The presence of Ce6 in the micellar core could prevent it from interacting with molecular

oxygen to form 1O2, leading to decreased SOSG signal. Moreover, the lowering of the SOSG signal by mPPCPN Ms could be due to the absorption/quenching of the fluorescence signal of SOSG by the polymer conjugate itself. A similar observation was reported for Ce6-nanoformulations in previously reported articles. (Figure 4.9).
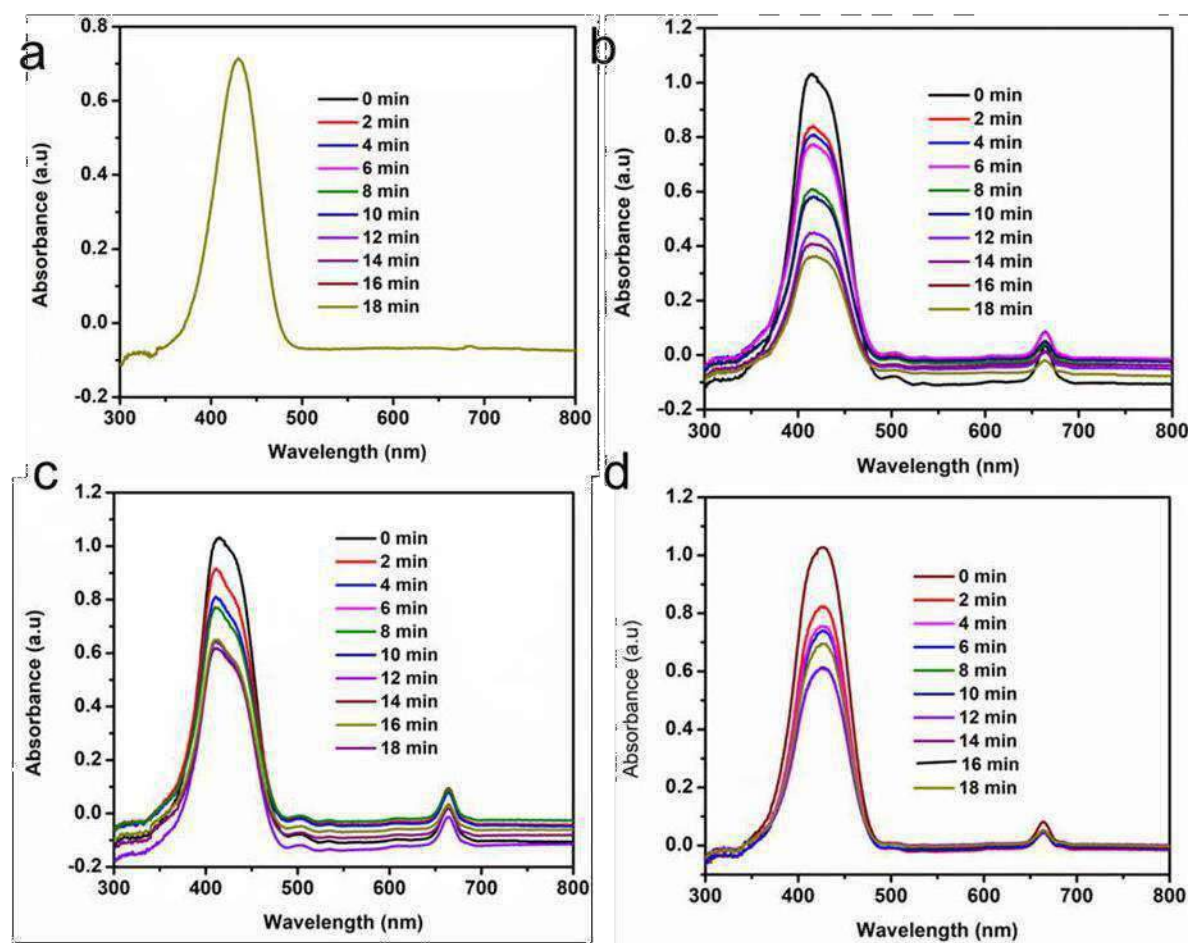
Figure 4.10 Time-dependent UV-Visible absorption spectra of RNO (a); and RNO mixing with Ce6 (b); mPPCPN (c) and mPPCPN Ms (d) after irradiation with a 660 nm lamp (0.5 mW/cm-2) for 18 min

Further, RNO was also used to evaluate the 1O2 generation ability of mPPCPN conjugate in the presence of histidine. The generated 1O2 gets trapped in the imidazole ring of a histidine, which reacts with RNO to form a photo-bleached transannular peroxide intermediate. The RNO bleaching measured at 440 nm wavelength of light in the presence of PS indicated their 1O2-generation potential (Figure 4.11c and d).
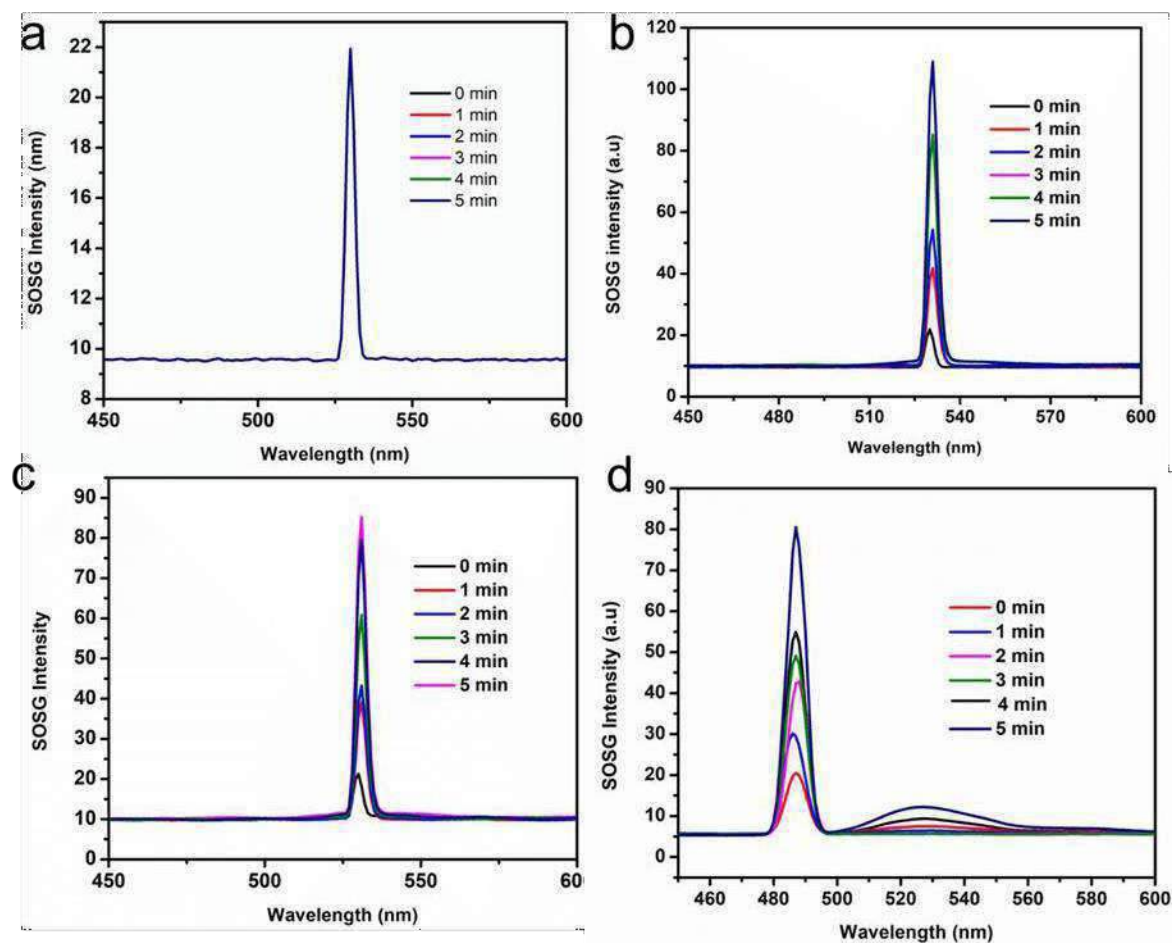
Figure 4.11 Time-dependent fluorescence spectra of SOSG (a); SOSG mixing with Ce6 (b); mPPCPN (c); and mPPCPN Ms (d) after irradiation with a 660 nm lamp (0.5 W/cm-2) for 5 min
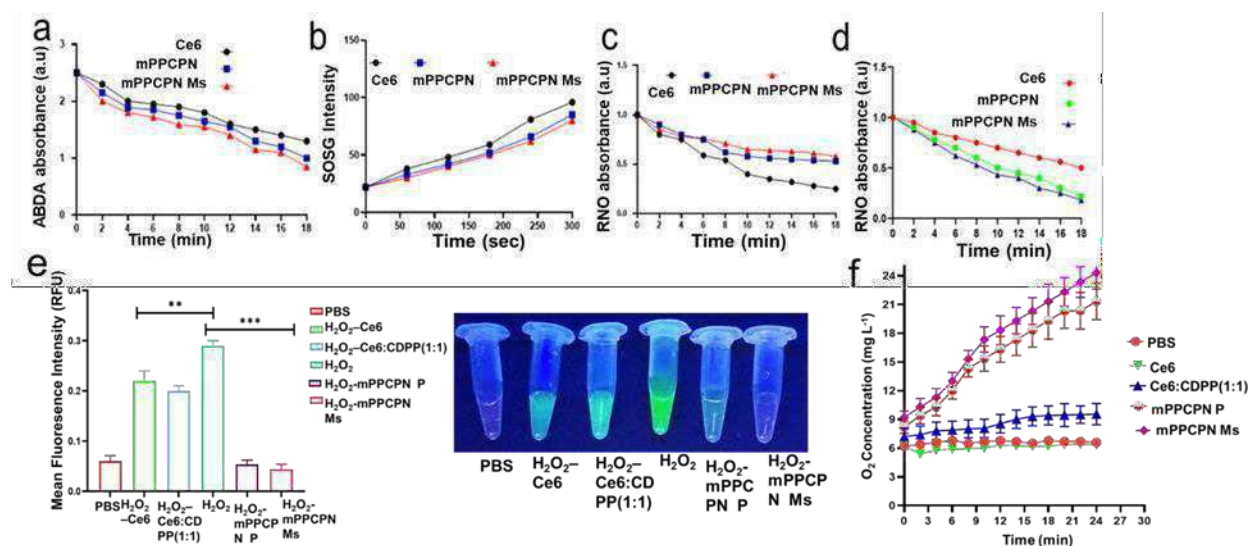
Figure 4.12 Normalized absorbance of 9,10-dimethylanthracene (ABDA) during photodecomposition by the generated ROS at variable laser (660 nm, 0.5 Watt/cm2) irradiation times (0-18 min) (a); variation of SOSG intensity as a function of irradiation time in free Ce6, mPPCPN conjugate, and mPPCPN Ms in water (b); irradiation time-dependent ROS generation-mediated oxidative degradation of RNO, as measured by the loss of absorbance at 440 nm (ROS production by laser irradiation of free Ce6, mPPCPN conjugate, and mPPCPN Ms in water and DMSO (c) and (d); Evaluation of H2O2, a c, quenched by micelles (20 μg/mL of Ce6) using OxiVision Green, a H2O2-sensitive fluorescent probe, mean fluorescence intensity of free Ce6 and mPPCPN Ms , Ce6:Pt (1:1) using OxiVision Green, a H2O2- sensitive fluorescent probe (e); Oxygen generation or consumption of Ce6, Ce6:CDPP (1:1) mPPCPN and mPPCPN Ms under 660 nm irradiation (0.5 W cm−2) (f);

With increasing irradiation periods, free Ce6 generated a higher amount of 1O2 than mPPCPN Ms, as determined by the abrupt drop in RNO absorbance. The externalization of Ce6 from the micellar

core is restricted below CMC, resulting in less interaction to produce singlet oxygen. Moreover, the micellar assembly could complicate the chain reaction between 1O2, histidine, and RNO by physically entrapping any one of them. However, these studies validated the 1O2-generation potential of Ce6, either as conjugate or as the micellar form. There was no significant difference in the effects between polymer and micelles. The effect was slightly lowered for micelles than for conjugates, which showed lower 1O2- generation potential due to their self-assembly in an aqueous environment.
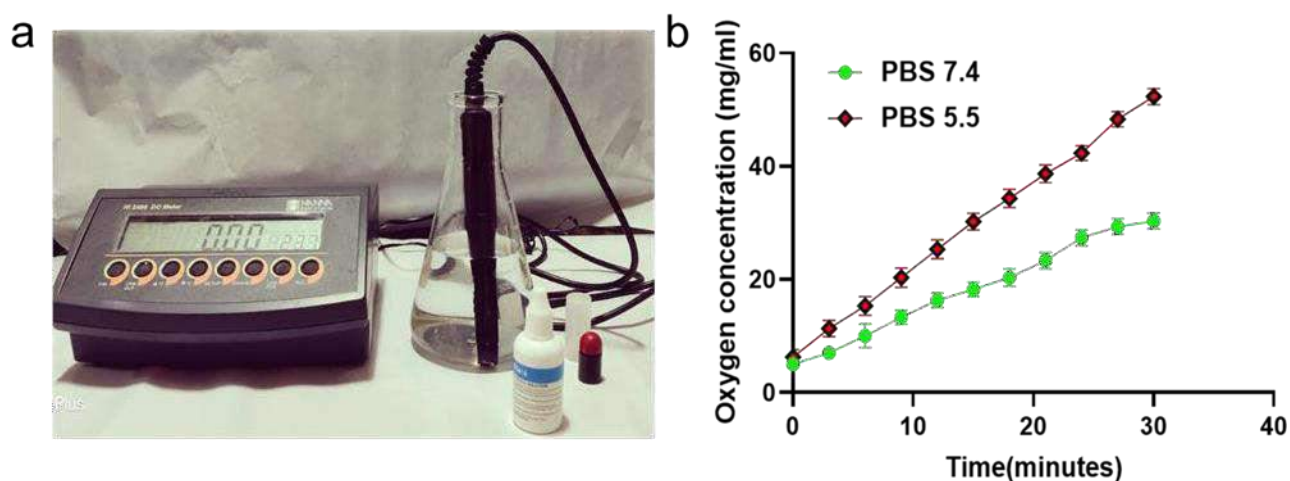
Figure 4.13 HI-2400 bench-top dissolved oxygen meter (a). The O2 concentration of mPPCPN Ms in PBS at pH 7.4 & 5.5 (b)

The ability of mPPCPN conjugate/Ms to deplete hydrogen peroxide to produce 1O2 was examined using the hydrogen peroxide sensor, OxiVisionTMGreen. H2O2 exhibited a high fluorescence intensity without the micelles. However, on mixing mPPCPN conjugate/Ms with H2O2, the fluorescence intensities were significantly quenched, compared to the PBS samples indicating the

depletion of H2O2 to produce 1O2 (Figure 4.11e). Other tested samples, including free Ce6, Ce6:CDPP (1:1), showed a slight decrease in H2O2 signals due to the photosensitizing ability of Ce6 by depleting H2O2. The oxygen gas generating ability of free Ce6, Ce6:CDPP (1:1), mPPCPN conjugate/Ms from hydrogen peroxide was evaluated using a dissolved oxygen meter. Figure 4.12b shows the data, indicating that the oxygen generation was much more efficient in mPPCPN Ms. The mPPCPN micelles showed a higher oxygen-generation potential at pH 5.5 than pH 7.4, according to the previous report. Based on these findings, we conclude that the mPPCPN Ms would effectively produce 1O2 and quench H2O2 to produce molecular oxygen in the tumor microenvironment resulting in improved PDT effectiveness by tilting the redox balance towards more oxidative equilibrium.

4.3.3 Photothermal effect

The photothermal effect of free Ce6 and mPPCPN Ms was also observed by exposing the different concentrations of samples at 660 nm NIR-laser (0.8 W/cm2) irradiation for 5 min using DI water control. The temperature of mPPCPN Ms (200 µg/mL) was increased up to 46.8 °C following laser irradiation due to the significant photothermal conversion effectiveness of mPPCPN Ms, as shown in Figure 4.13. A concentration and laser irradiation time-dependent photothermal effect were also evident in the free Ce6 sample. However, the intensity was much less than mPPCPN Ms at the same Ce6 concentration.
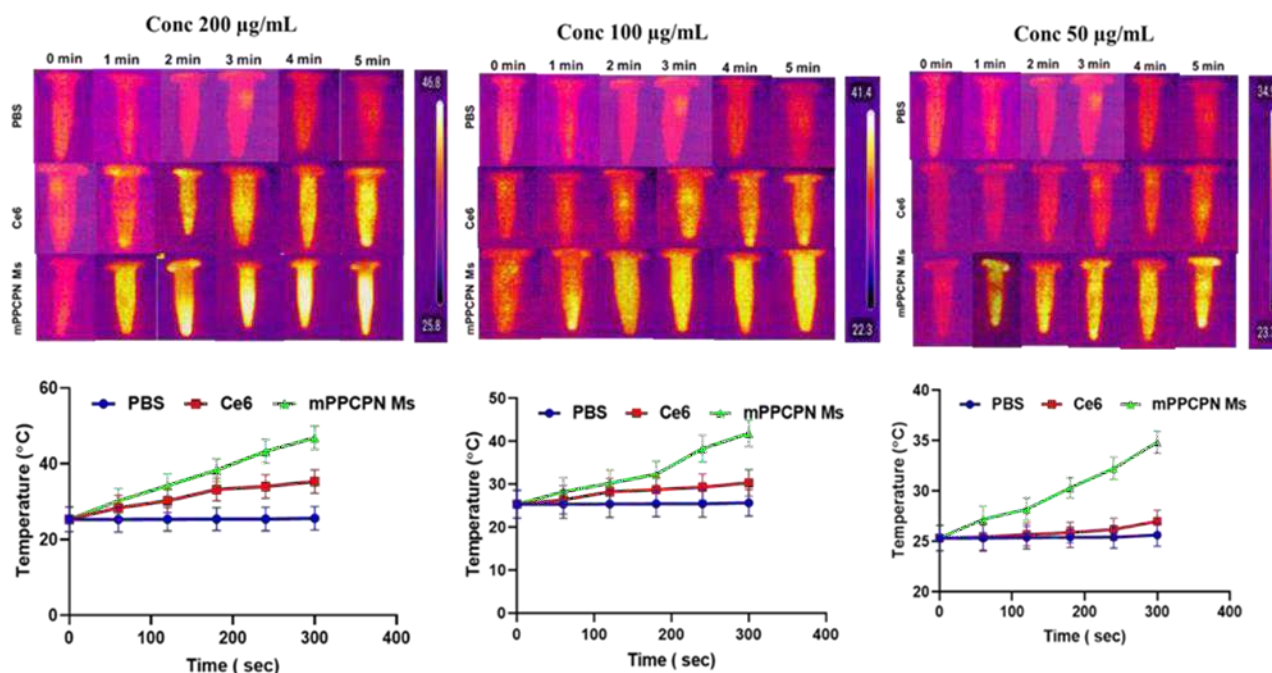
Figure 4.14 Temperature variation in the PBS, Ce6, mPPCPN Ms dispersion under NIR laser (660 nm, 0.5 W/cm-2) irradiations with different time intervals.

4.3.4 In vitro assays

4.3.4.1 Cellular Uptake study and intracellular ROS generation of mPPCPN Ms

The cellular uptake of free Ce6 and mPPCPN Ms was investigated qualitatively and quantitatively by confocal microscopy and flow cytometry analysis, respectively. In FaDu HTB-43 cells, clear brighter fluorescence in the cytoplasm and nuclei was observed in mPPCPN Ms-treated cells, suggesting quick internalization of mPPCPN Ms. From 1 to 4 h, the red fluorescence intensity of free Ce6 and mPPCPN Ms groups was increased, demonstrating time-dependent cellular uptake for FaDu HTB-43 cells. Flow cytometry studies were performed to corroborate further the

increased cellular uptake (Figure 4.14). The mean fluorescence intensity values for mPPCPN Ms and Free Ce6 were shown to increase from 1 to 4 h in the flow cytometer's histogram, which was displayed as a bar graph (Figure 4.14, right). The geometric mean fluorescence of mPPCPN Ms (+L)-treated cells rose from 1413.2 ± 54.22 to 3045.54 ± 16.27 from 1 to 4 h, whereas the geometric mean fluorescence of free Ce6-treated cells was increased from 751.4 ± 19.7 to 1515.7 ± 23.67. The time-dependent increase in fluorescence intensity was observed in FaDu HTB-43 cells.

The potential of mPPCPN Ms to generate reactive oxygen species (ROS) in FaDu HTB-43 cells was then examined by treating the cells with a cell-permeable ROS-detecting fluorescent probe DCFH-DA and subsequently estimating the cell-associated fluorescence by fluorescence microscopy and flow cytometry analysis. The mPPCPN Ms group (+L, 660 nm, 0.5 W/cm-2) has generated abundant ROS inside cells and exhibited strong green fluorescence when compared to the control group, free Ce6 ($\pm$ L), Ce6:CDPP(1:1) ($\pm$ L), and mPPCPN Ms (-L), as shown in Figure 4.14, indicating that mPPCPN Ms efficiently delivered Ce6 and had excellent ROS generation ability inside cells upon laser irradiation. Flow cytometry studies also revealed that mPPCPN Ms (+L) produced abundant ROS compared to other groups Figure 4.14. Based on the preceding findings, the resultant mPPCPN Ms could penetrate inside cells and produce ROS more effectively in response to irradiation than free Ce6, facilitating the Ce6- mediated cytotoxic response to the treated cells.
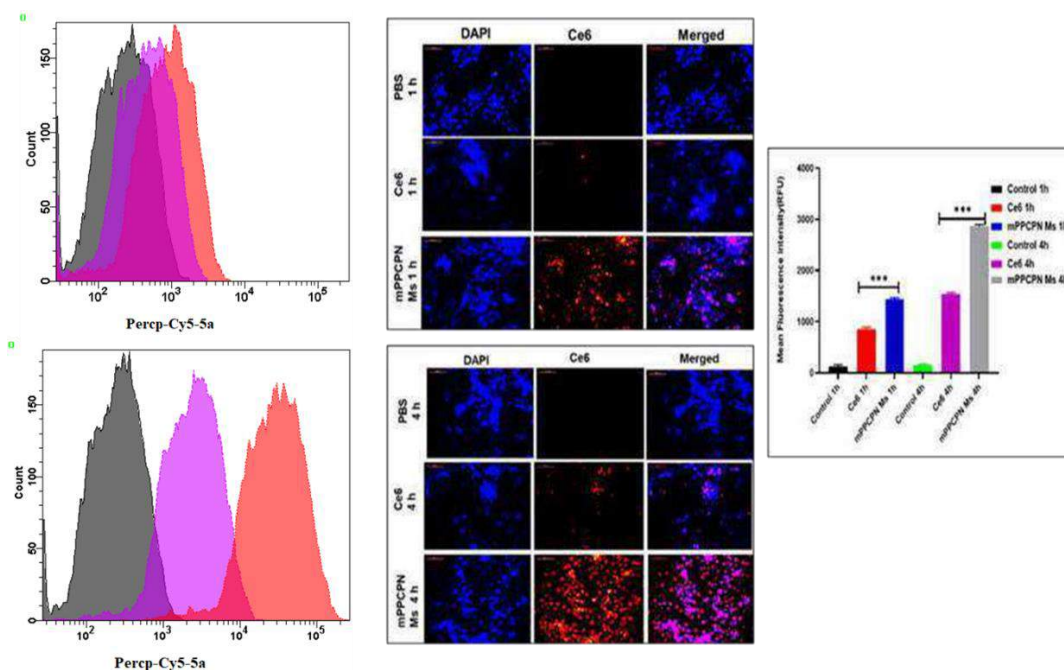
Figure 4.15 Uptake of free Ce6 and Mppcpn Ms by FADU HTB 43 after incubation for 1 h, 4 h at 37°C. Scale bar, 100 μm.

4.3.4.2 MTT assay

Furthermore, the cytotoxicity of mPPCPN Ms in FaDu HTB-43 cells was evaluated by MTT assay in vitro for 24-48 h. The anticancer impact of Free Ce6, Ce6:CDPP (1:1), and mPPCPN Ms were tested in vitro using FaDu HTB-43 cancer cells. The positive control group (laser alone) had comparable cell viability to the negative control group (PBS), demonstrating that laser irradiation alone was not cytotoxic. Overall, the laser-irradiated cells (+L) showed cell death greater than the laser-non-irradiated (-L) cells in both the time points (24 and 48 h) (Figure 4.15).
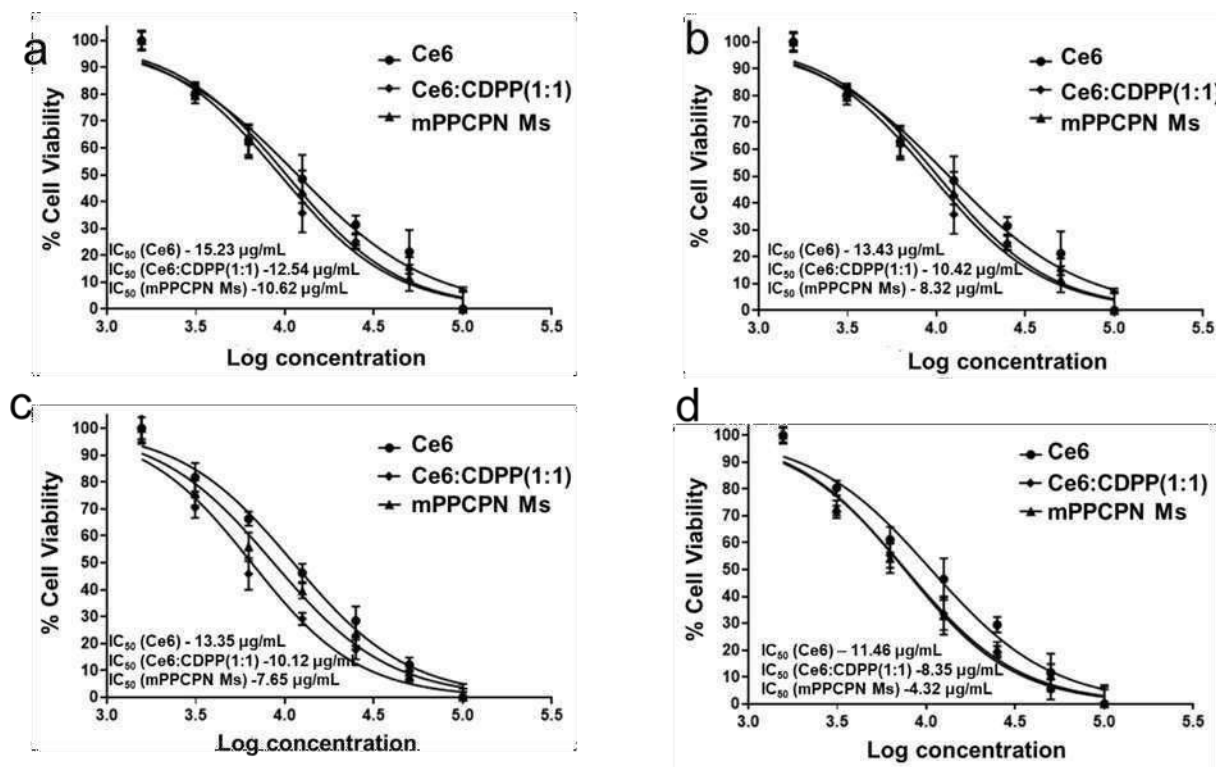
Figure 4.16 In vitro cell cytotoxicity of free Ce6 and mPPCPN Ms, Ce6:CDPP (1:1) against FADU HTB-43 after incubation for 24 h , 48 h without irradiation 24 h (a) and with irradiation 24 h (b) or without irradiation 48 h (c) and with irradiation 48 h (d) under light irradiation (666 nm, 0.5 Wcm-2 5 min) in the dark.

The percentages of viable cells were 19.12 % (+L) and 40.32 % (-L) following 24 h incubation period for mPPCPN micelles, which was further reduced to 8.63 % (+L) and 21.35 % (-L) after 48 h at the highest equivalent Ce6 concentration of 100 µg/mL. Similarly, free Ce6 (100 µg/mL) displayed cell viability of 38.65 % (+L) and 56.63 % (-L) for 24 h , and 32.56 % (+L) and 43.35% (-L) for 48 h, respectively.
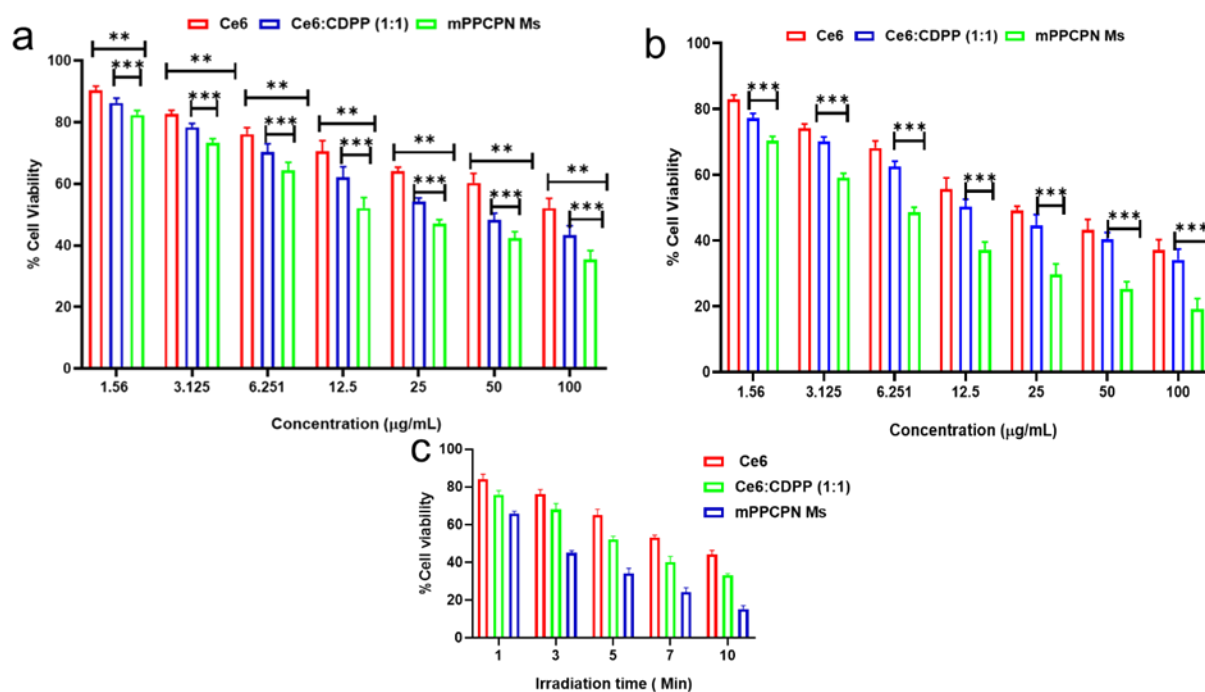
Figure 4.17 In vitro cell cytotoxicity of free Ce6 and mPPCPN Ms, Ce6: CDPP (1:1) against FaDu HTB-43 after incubation without irradiation 24 h (a) and without irradiation 48 h (b) under light irradiation (660 nm, 0.5 W/cm-2 5 min) in the dark. Various irradiation time for 24 h (c). - L: without irradiation

The increase in laser irradiation time enhanced the cytotoxicity at 24 and 48 h post-irradiation incubation, indicating energy dependency to exert the photodynamic effect. The equimolar amount of Ce6 and cisplatin mixture, referred to as Ce6:CDPP (1:1), displayed reduced cell viability compared to free Ce6, indicating the combination effect. Promisingly, the mPPCPN micelles, at Ce6 equivalent amount, displayed much-decreased cell viability than free Ce6 and Ce6:CDPP (1:1) at all tested concentrations and time points, mainly due to the cytotoxic effect of Ce6 (+L),

Pt(IV), and azide. Moreover, the receptor-mediated endocytic internalization of micelles allows longer intracellular retainment with less efflux than the free drugs undergoing diffusion for cell entry/exit. Interestingly, the mPPCPN micellar treatment exhibited the lowest IC50 values at all tested conditions, 10.62 (-L), 8.32 (+L) for 24 h, and 7.65 (-L), and 4.32 (+L) for 48 h incubation. The ~2.7-fold decrease in IC50 values of mPPCPN micelles than free Ce6 at 48 h (+L) indicated the longer retention of micelles intracellularly reaching optimal concentration to exert cytotoxic action.
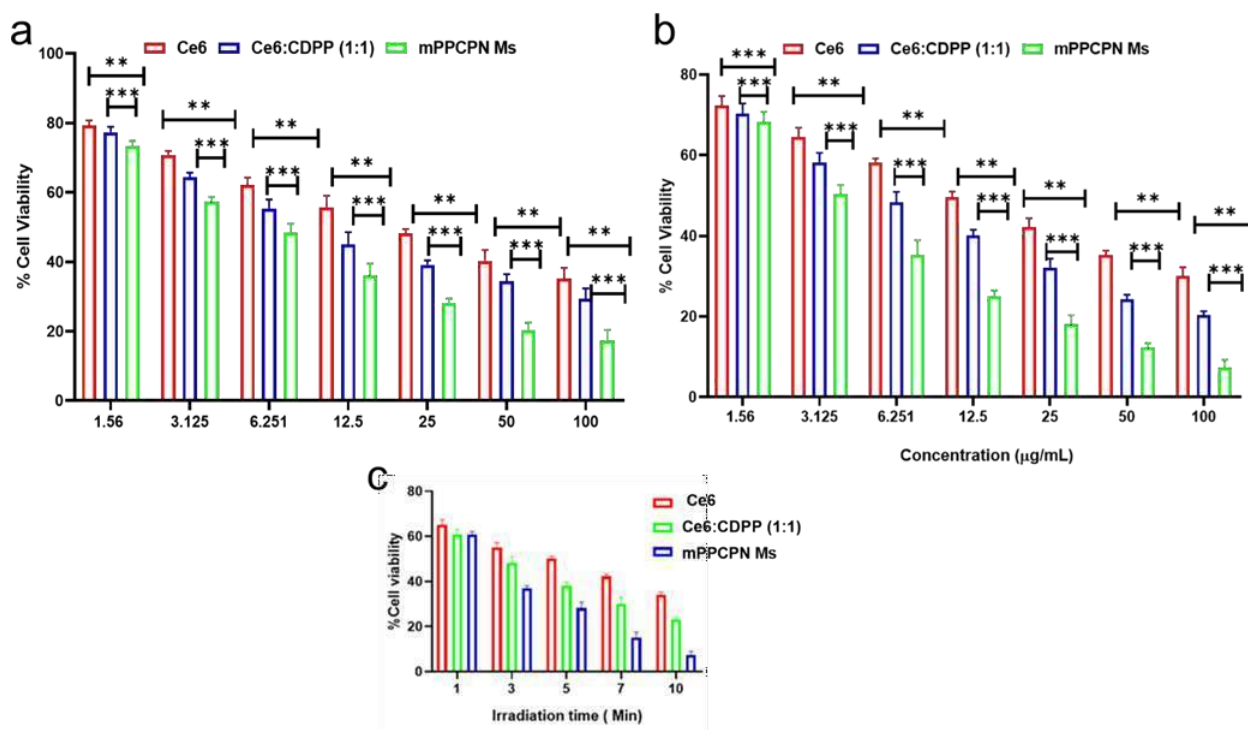
Figure 4.18 In vitro cell cytotoxicity of free Ce6 and mPPCPN Ms, Ce6: PCDPP (1:1) against FaDu HTB-43 after incubation with irradiation 24 h (a) and with irradiation 48 h (b) under

light irradiation (660 nm, 0.5 W/cm-2 5 min) in the dark. Various irradiation time for 48 h

(c). + L: with irradiation

4.3.4.3 Nuclear staining and DNA fragmentation assay

Various staining procedures visualized the dying cancer cells under the fluorescence microscope. The nuclear staining by DAPI showed the frequent presence of chromatin condensation (CS) and nuclear fragmentation (NF) at mPPCPN Ms (+L)-treated cells, which was further confirmed by staining nuclei with acridine orange (Figure 4.18).
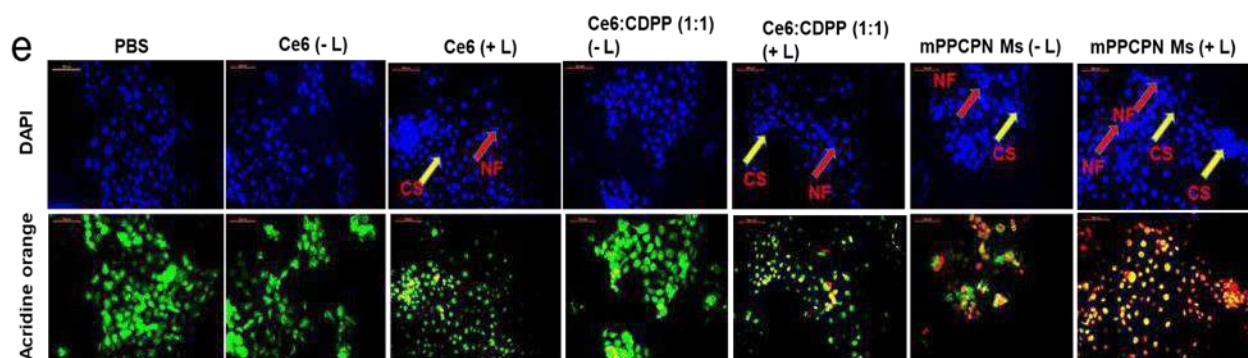
Figure 4.19 Nuclear staining of FADU HTB-43 cells using DAPI, acridine orange (AO) following cellular treatments. The mPPCPN Ms treated cells showed more nuclear fragmentation (NF) compared to Ce6, Ce6:CDPP (1:1) as shown by arrows whereas untreated cells showed the presence of intact nuclei (e).

The green signal indicated healthy double-stranded DNA, which turned to a red signal following mPPCPN (+L) treatment, indicating the emergence of fragmented, single-stranded DNAs. The equimolar C6:CDPP (1:1) (+L) showed some green-red-merged yellow signals. Further, the live/dead staining experiment was utilized to assess the anticancer response of free Ce6, Ce6: Pt (1:1), and mPPCPN Ms after laser irradiation.
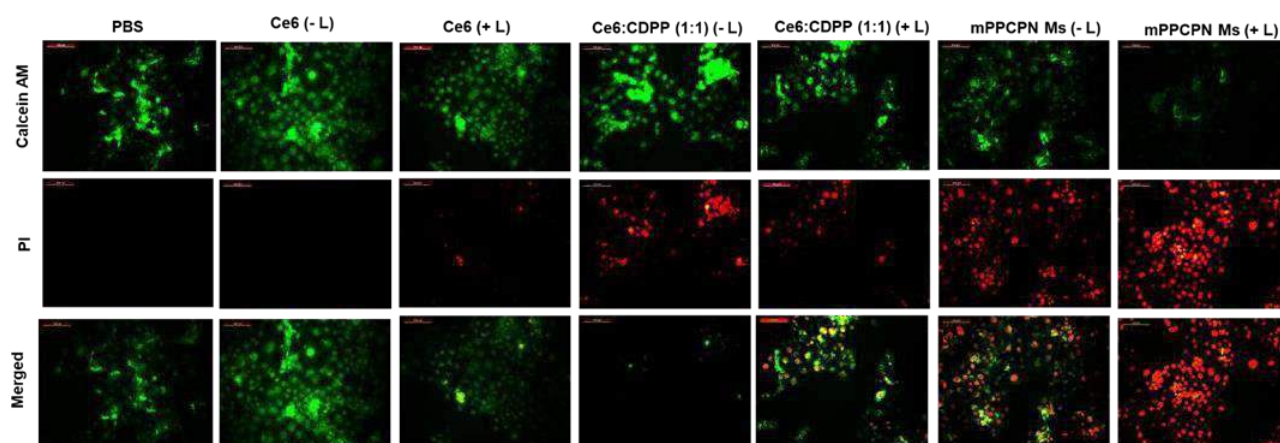
Figure 4.20 Fluorescence microscopy images of FaDu HTB-43 cells stained by Calcein-AM/PI dyes after Ce6, Ce6: CDPP (1:1), mPPCPN Ms Light dose: 660 nm, 0.5 W/cm-2 5 min.

As demonstrated in Figure 4.24, the control cells (PBS without Ce6 doping) remained healthy and alive with abundant green fluorescence even after irradiation, indicating that no visible cell death occurred. The merged red fluorescence images, on the other hand, revealed that nearly all cancer cells were in the state of undergoing apoptosis after treatment with mPPCPN Ms (+L). The effectiveness of mPPCPN in exerting a strong anticancer response has been proven in these

staining experiments and following subsequent experiments, including annexin V assay, cell-cycle

analysis, DNA fragmentation, and mitochondrial membrane potential assays.
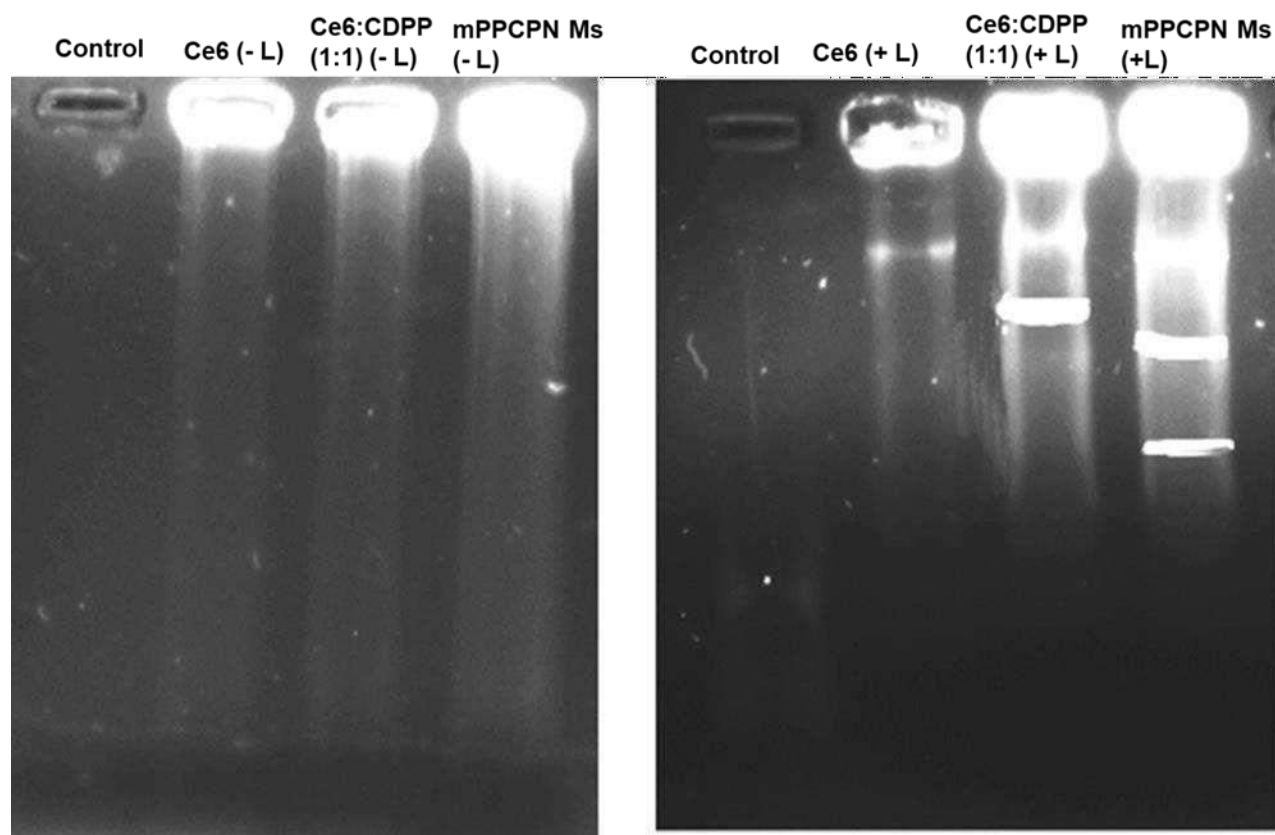
Figure 4.21 Representation of DNA isolated from FaDu HTB-43 cells after treatment Ce6, Ce6: CDPP (1:1), mPPCPN Ms Light dose: 660 nm, 0.5 W/cm-2 5 min, performed on agarose gel electrophoresis.

4.3.4.4 Annexin-V assay

Annexin V–FITC/PI staining was used to evaluate the extent of initiation of apoptosis in FaDu

HTB-43 cells (Figure 4.20). The percentages of normal cells (lower left quadrant) in the control

group were about 99.6%; however, when the cells were coincubated with free Ce6, Ce6:CDPP (1:1), and mPPCPN Ms with or without laser irradiation, the percentages of living cells were substantially reduced. FaDu HTB-43 cells, treated with free Ce6 displayed a total apoptosis of 7.34 ± 1.32 % (-L), 15.49 ± 1.02 % (+L), Ce6:CDPP (1:1) showed total apoptosis of 30.64 ± 1.22 % (-L), 40.35 % ± 2.10 (+L), and mPPCPN Ms exhibited total apoptosis of 38.86 ± 1.22 % (-L), 56.66 ± 1.12 % (+L), respectively, as shown in Figure 4.20. The highest apoptotic response of cells treated with mPPCPN Ms (+L) could be due to various factors, including enhanced cellular uptake, retention of formulations in cellular compartments, and Ce6/platinum/azide-mediated combination chemo-photodynamic therapy. Cellular DNA fragmentation pattern as visualized by performing agarose gel electrophoresis indicated that the Ce6:CDPP (1:1) and mPPCPN Ms treatment (+L) caused higher DNA fragmentation compared to free Ce6 (+L) . Laser irraiation increased the extent of DNA damage.
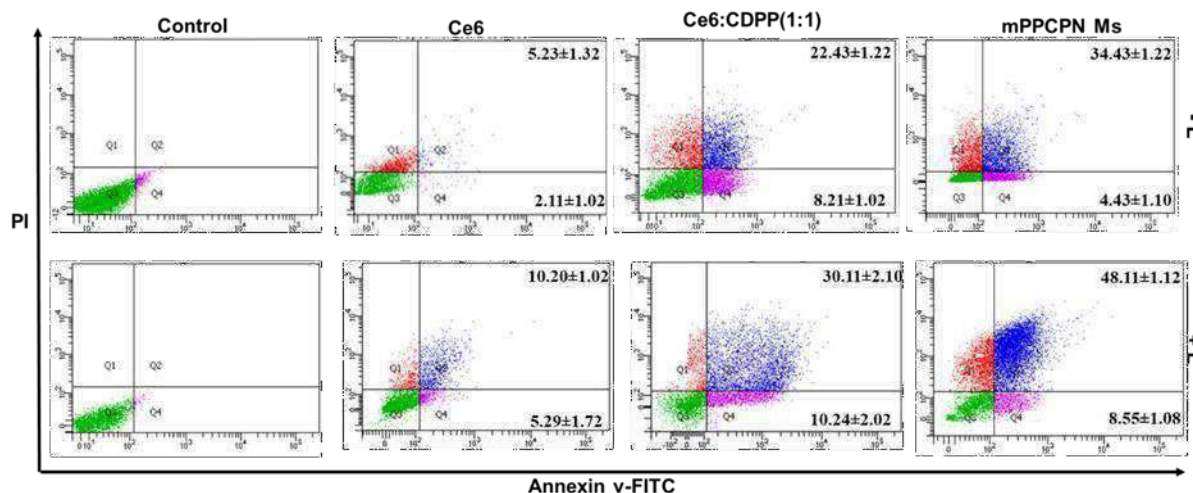
Figure 4.22 Apoptosis assay of FADU HTB-43 cells using Annexin V/PI double staining method. Apoptotic populations of FADU HTB-43 cells after exposing to different

formulations: culture medium plus NIR irradiation, Ce6 solution, Ce6 solution plus NIR irradiation, Ce6: CDPP (1:1), Ce6: CDPP (1:1) plus NIR irradiation, mPPCPN Ms, mPPCPN Ms plus NIR irradiation. Cell counts (%) of necrotic cells (Q1), late apoptotic cells (Q2), early apoptotic cells (Q3), normal cells (Q4), and total apoptotic cells (Q2 & Q3) after different treatments.

4.3.4.5 Cell cycle analysis and Mitochondria membrane potential study

Cell cycle analysis was carried out on free Ce6, Ce6:CDPP (1:1), and mPPCPN Ms (+L, -L)-treated FaDu HTB-43 cells using a flow cytometer to determine if the treatment caused cell cycle arrest. The proportion of cell populations in the G2/M phase was increased from 9.66 to 41.45 %, and 8.56 to 26.34 % without and with laser irradiation, respectively, following treatment with mPPCPN Ms. This increment was followed by a reduction in the percentages of mPPCPN Ms in the G1 and S cell populations, respectively. The plot represents (Figure 4.21) maximum arrest in the G2/M phase for mPPCPN Ms (+L) compared to free Ce6 and Ce6:CDPP (1:1) (+ and –L), thus abiding with the mechanism of action of Ce6, which arrests the cell in the early anaphase stage (M-phase).
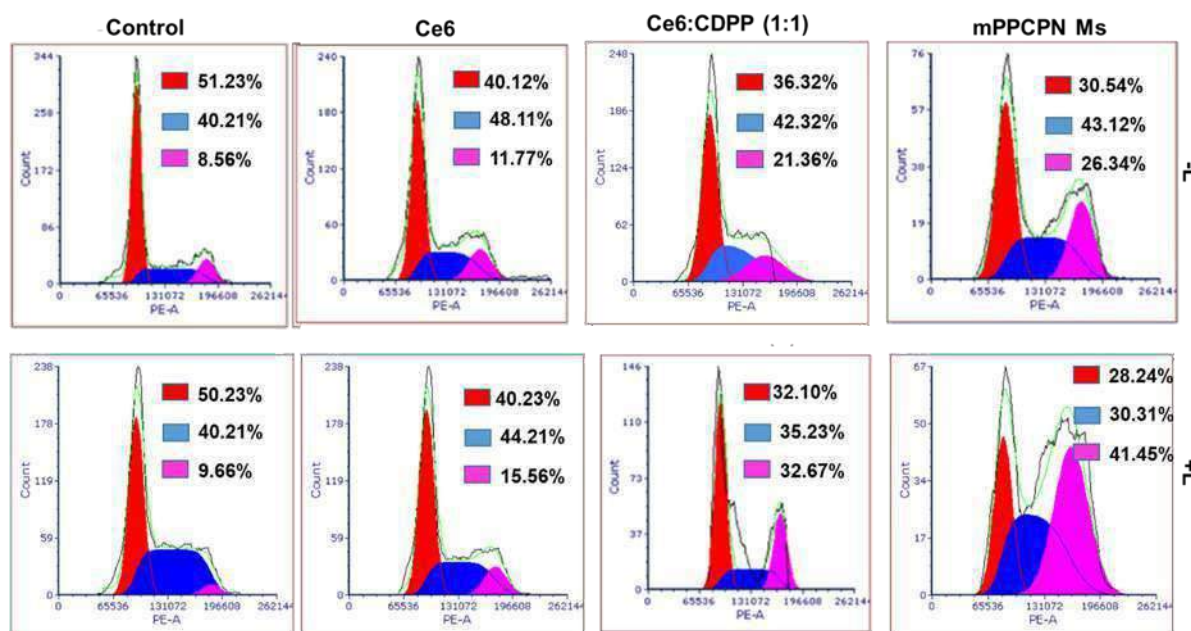
Figure 4.23 Cell cycle analysis of FADU HTB 43 cells after 24 h of treatment with free Ce6, Ce6:CDPP (1:1) and mPPCPN Ms.

The results validated the previous cytotoxicity results that the mPPCPN Ms treatment (+L) had a stronger therapeutic effect than the free Ce6, Ce6: Pt (1:1), and mPPCPN Ms treatments (-L). Mitochondria membrane potential (MMP) fluctuation has been associated with mitochondrial dysfunction leading to apoptosis. JC-1 (carbocyanine cationic dye) aggregates in the electronegative core of mitochondria at high concentrations and emits red fluorescence (590 nm). As mitochondria get depolarized, the amount of dye accumulating in them decreases; the dye remains in monomer form and emits green fluorescence (529 nm). The control cells produced red fluorescence due to the accumulation of JC-1 in aggregated form in the healthy mitochondria, which diffused to yellow (red-green merged) in free Ce6-treated cells (Figure 4.22).
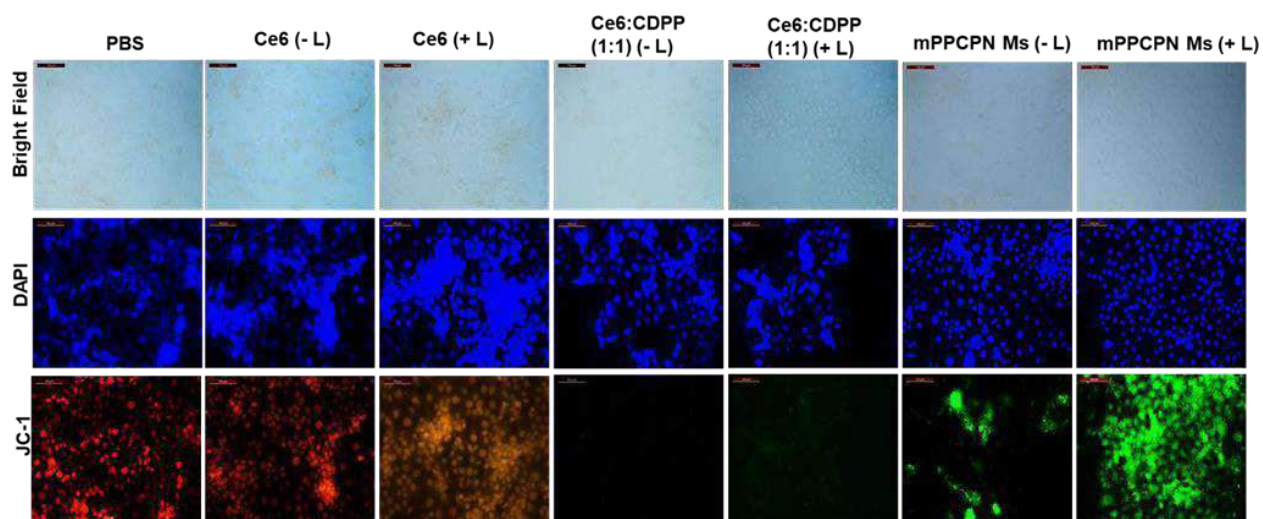
Figure 4.24 Analysis of mitochondrial membrane potential FaDu HTB-43 cells in different groups Ce6, Ce6: CDPP (1:1), mPPCPN Ms. Light dose: 660 nm, 0.5 W/cm-2 5 min by fluorescence microscopy.

The cells that were treated with mPPCPN Ms (+L) produced a stronger green fluorescence than the cells treated with free Ce6 (±L), Ce6:CDPP (1:1) (±L), and mPPCPN Ms (-L). As shown in Figure 4.21, flow cytometry analysis also revealed that FaDu HTB-43 cells treated with mPPCPN Ms (+L) had higher mitochondria membrane potential disruption.
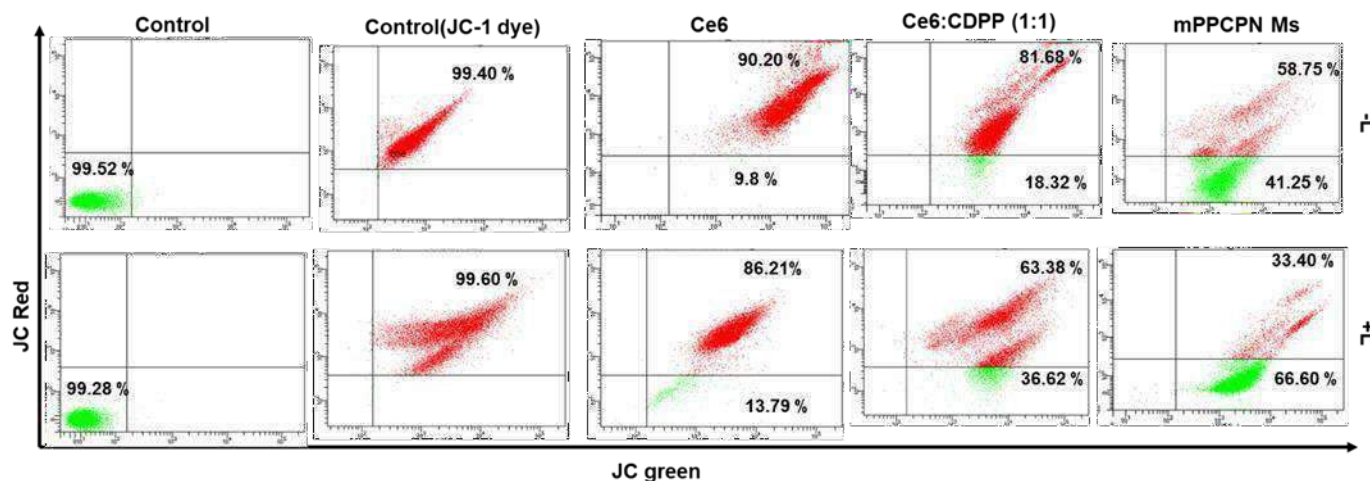
Figure 4.25 Analysis of mitochondrial membrane potential FaDu HTB-43 cells in different groups Ce6, Ce6: CDPP (1:1), mPPCPN Ms. Light dose: 660 nm, 0.5 W/cm-2 5 min by flow cytometry.

4.3.4.6 Spheroid study

3D-cell culture systems using FaDu HTB-43 spheroids were used to assess the potential of in vivo application of the formulations. The Ce6 signal was recorded in spheroids at 80 µm depth along the Z- axis in the spheroid uptake studies. The mPPCPN Ms had the greatest Ce6 penetration efficiency than free Ce6 and Ce6:CDPP (1:1) (Figure 4.22). The blue Calcein signal was highest in the control spheroids and gradually faded in the other spheroids treated with free Ce6, Ce6:CDPP (1:1), and mPPCPN Ms (Figure4.22c). On the other hand, the high intensity bright red PI signal was observed in the mPPCPN Ms-treated spheroids. The PI signal was also evident in spheroids treated with free Ce6 and Ce6:CDPP (1:1). Compared to the untreated spheroids and spheroids treated with free Ce6, Ce6:CDPP (1:1), the mPPCPN Ms-treated spheroids displayed

the highest reduction of the volumes (Figure 4.22a). On the sixth day, the mean diameters of spheroids were observed as 852.6 ± 128, 678.9 ± 135.95, 511.14 ± 29.94, and 389.6 ± 231.84 for the control, free Ce6, Ce6:CDPP (1:1), and mPPCPN Ms (+L) treatments, respectively.
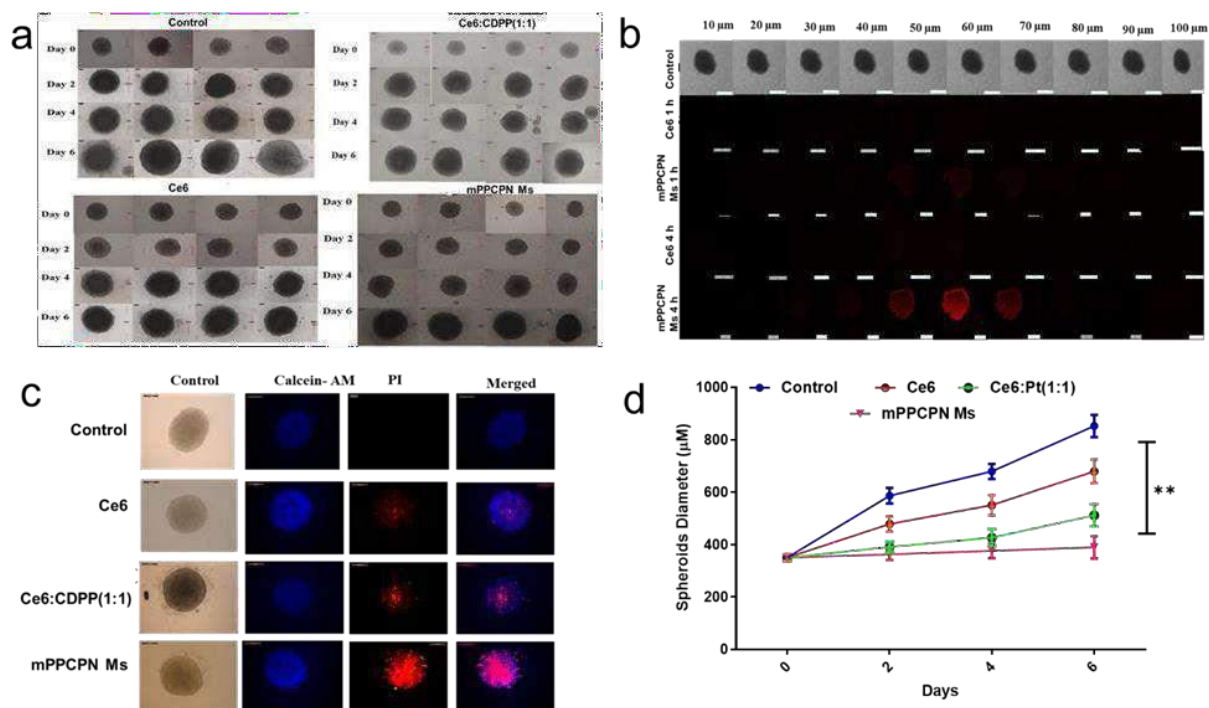
Figure 4.26 Growth inhibition study in spheroids (a and d); Confocal microscopic Z stacked images of FaDu HTB-43 spheroids treated with mPPCPN Ms, Ce6 at Ce6 concentration of 6 µg/mL for 1 h and 4 h (b); Live-dead cells assay in spheroids (c).

4.3.4.7 In vivo studies

Following the encouraging in vitro results, we looked into the possibility of using the mPPCPN Ms (+L) treatment in vivo. The FaDu HTB-43 tumor-bearing mice were administered with several

formulations, including PBS (+L), free Ce6 (+L), Ce6:CDPP (1:1) (+L), and mPPCPN Ms (+L). The formulations were administered to each mouse through the tail vein, and after 12 h, the mice were exposed to 660 nm NIR laser irradiation (0.5 W/cm2) for 5 min.
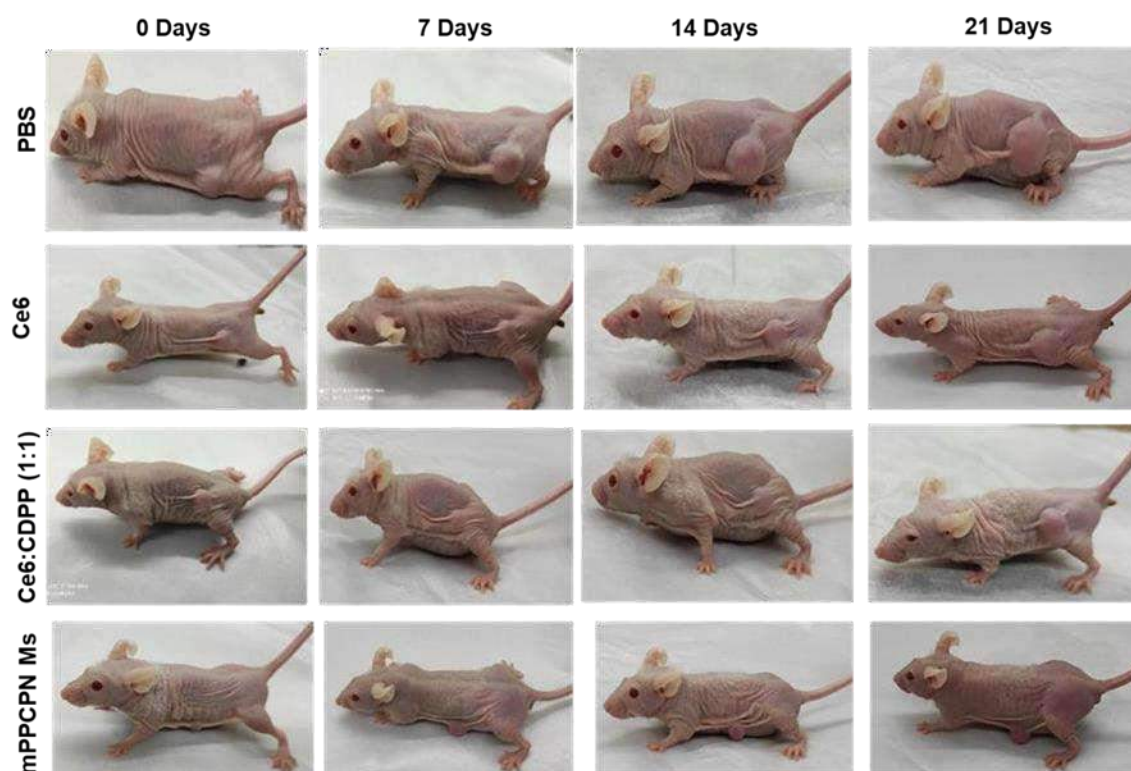
Figure 4.27 Tumor volume images of FaDu bearing nude mice

Figures 4.27 a-c show the tumor progression over 21 days in different treatment groups. The increase in tumor volume was more rapid in PBS-treated control animals than other treatment groups with mPPCPN Ms (+L), displaying the lowest rate of increase. The average tumor volumes post 21 days were 1185±108 mm3, 555±42 mm3, 380±22 mm3, 202± 25 mm3, for control, Ce6 (+L), Ce6:CDPP (1:1) (+L), and mPPCPN Ms (+L), respectively. The Ce6:CDPP (1:1) Ms (+L) treated group demonstrated a significant degree of tumor suppression as compared to the PBS or

free Ce6 (+L) treatment groups. The mPPCPN Ms (+L) group showed the most significant reduction in tumor development as the treatment offers multiple therapeutic benefits, including offering chemo (Pt(IV))-PDT (Ce6)-combination therapeutic effect, reversal of hypoxia, reduction of glutathione, and a cascade of other intracellular events favoring cellular apoptosis.
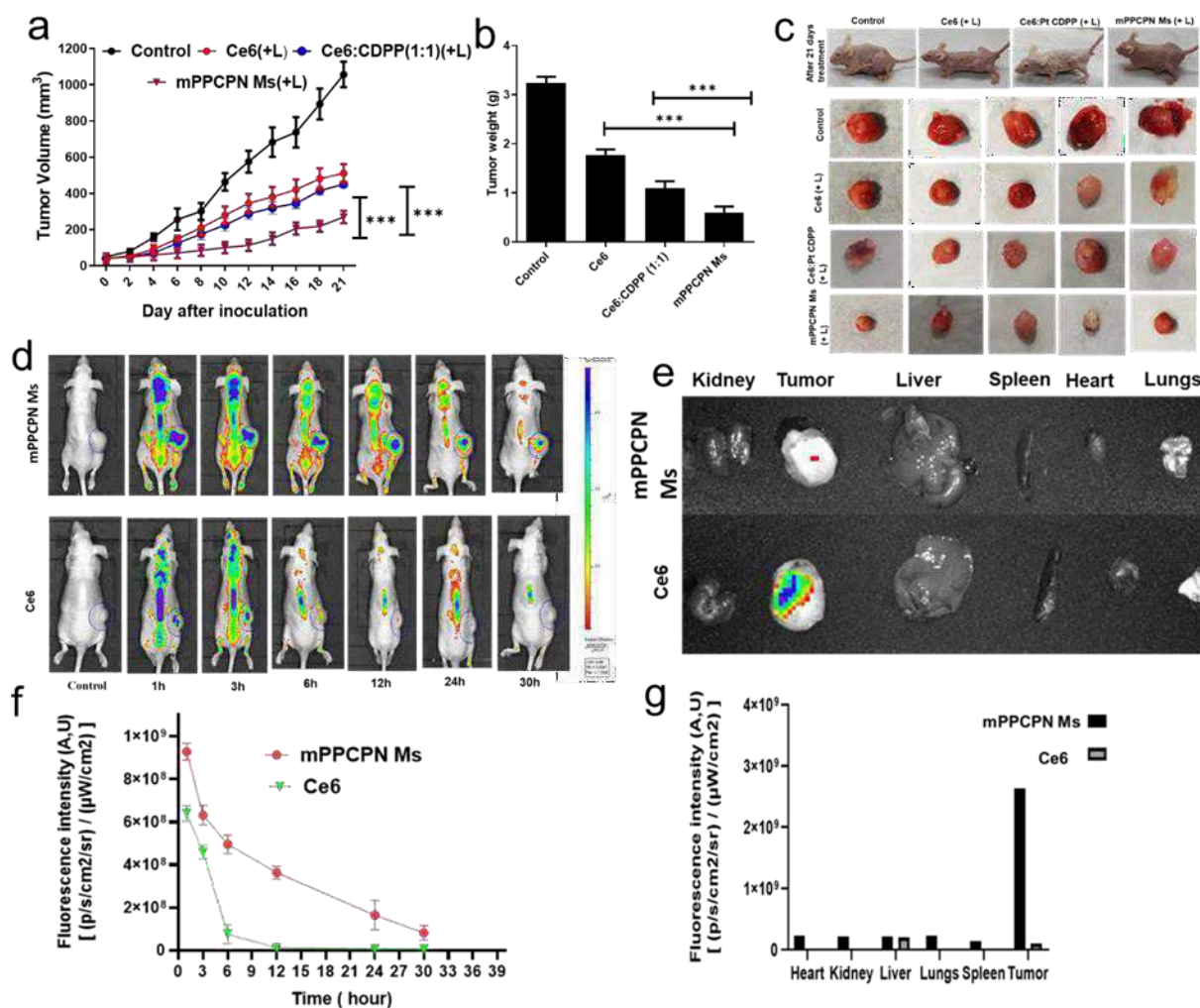
Figure 4.28 Assessment of therapeutic Efficacy of free Ce6 and mPPCPN Ms, Ce6:CDPP(1:1) formulations in FADU HTB-43 tumor-bearing female balb/c nude mice. Graphical representation of tumor volume vs. days during treatment (a); The average weight of tumors isolated from various treatment groups (b); Representative tumors isolated from mice post-

treatment (c); Biodistribution of micelles and in vivo anticancer efficacy evaluation. time-dependent NIR fluorescence images of tumor-bearing nude mice after i.v. administration of free Ce6 and mPPCPN Ms (Ce6: 5 mg / kg) (d); Ex vivo NIR fluorescence images of major organs and tumor excised at 30 h post injection (e); The fluorescence intensity for the region of interest (tumor) was recorded as total photon counts per tumor (f); Mean fluorescent intensity of Ce6 in tumors, organs, at various time points after mice were i.v. injected with mPPCPN Ms (g);

The Hematoxylin and eosin (H&E), Antigen KI-67 (Ki67), ROS generation, glutathione detection, terminal deoxynucleotidyl transferase dUTP nick end labeling (TUNEL) staining tests were also performed to evaluate the therapeutic effectiveness of the various treatments. Herein, the Ki67 staining was used to assess the growth percentage of a specific cell population, TUNEL labeling was employed to determine DNA fragmentation and detect apoptotic cells, H&E staining was utilized to analyze the structure of cells, DCFH-DA probe was employed to identify ROS generation in tumor cells, and aqueous 5-sulfosalicylic acid dihydrate was used to detect the level of GSH in tumor tissue homogenates. As shown in Figure 4.24e, the H&E pictures following specified treatment with mPPCPN Ms (+L) demonstrated pycnosis and karyolysis of the tumor tissue under laser irradiation. More significant necrosis was observed compared to the other groups. There was no histological damage to the other organs such as the liver, lungs, spleen, heart, and kidney, which confirms the low toxicity of the formulation. Studies using H&E staining revealed that the developed combination therapy modality was safe, with no evidence of inflammation or immune response activation in isolated organs. As a result, mPPCPN Ms formulation is a safe and effective therapeutic regimen for synergistically treating oropharyngeal

carcinoma or other solid tumors, with much-decreased recurrence rates. The immunostaining studies revealed repressed cell proliferation (Ki67 staining, Figure 4.24a) and the highest percentage of apoptotic cells (TUNEL staining, Figure 4.24a) in the tumor tissues of mice administered with mPPCPN Ms followed by laser irradiation. The inclusion of Ce6 and Pt(IV) in mPPCPN Ms caused greater ROS generation, leading to apoptosis shown in Figure 4.24c.

Generally, drugs in nanoparticles have a prolonged retention period in the circulation, facilitating drug accumulation at the tumor site by Enhanced Permeability and Retention (EPR) effect [53]. Micelles were observed by in vivo imaging to validate their tumor retention ability. The free Ce6 was rapidly cleared from the body, and the fluorescence intensity at the tumor location was extremely low (Figure 4.24d). On the other hand, the fluorescence signal of mPPCPN Ms steadily grew near the tumor location over time, even up to 30 h (Figure 4.24e). After the animals were sacrificed, ex vivo biodistribution of Ce6 in various organs and tumors indicated that the mPPCPN Ms accumulated at the tumor site.
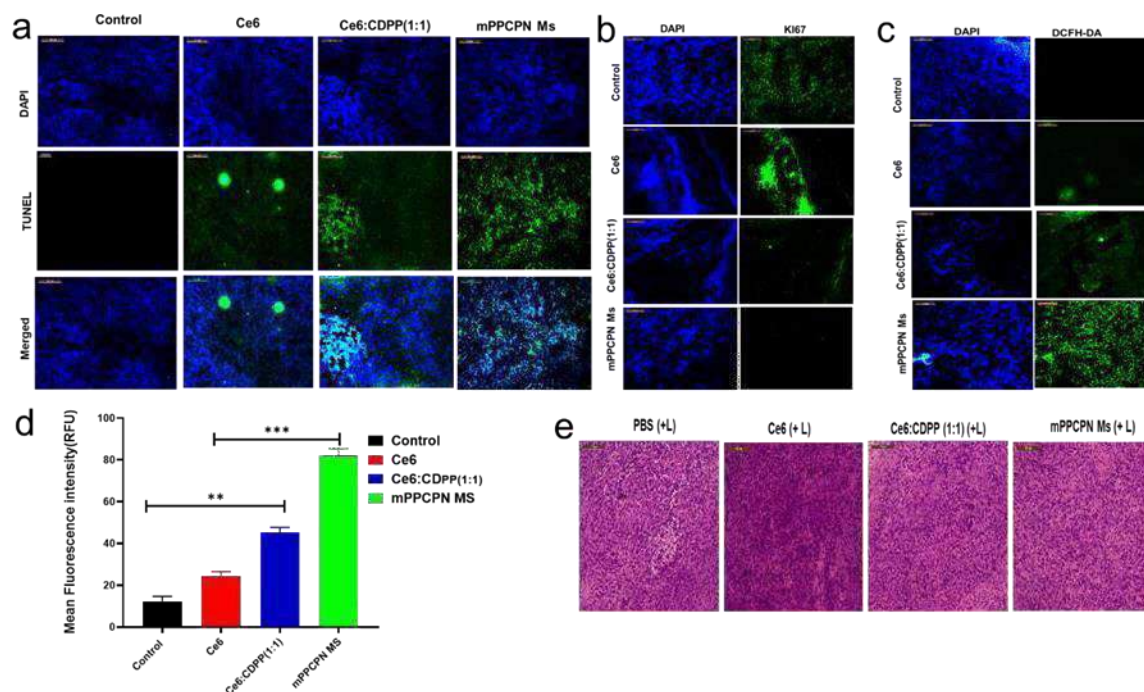
Figure 4.29 Immunohistochemical staining for FADU HTB-43 tumor from mice that received different treatments indicated for Tunel assay (a); KI67 activity (b); ROS generation assay (c); Quantify the intensity of the green fluorescence indicates ROS concentration in the tumor tissue. Data represented as the mean ± SE of three independent experiments (statistically significant differences, ** $P < 0.01$, *** $P < 0.001$) (d); H&E stained images of tumor slices collected at the end of the experiment (e); Scale bar, 100 μm.

4.3.4.8 In vivo overcoming hypoxia study

Further, to confirm the capacity of mPPCPN Ms to alleviate tumor hypoxia, FaDu HTB-43 tumor slices from mice were stained with FITC-labeled antibody to detect the expression of hypoxia-inducible factor- 1 (HIF-1α green) and CD31 (red). The reduction in HIF-1α and CD31 levels is a

common sign of hypoxia reversal [54,55]. Tumor slices in Free Ce6 (+L) and Ce6:CDPP (1:1)

(+L) displayed significantly increased green and red fluorescence when compared to the mPPCPN

Ms (+L) treated group, indicating that the mPPCPN Ms suppressed tumor hypoxia (Figure 4.36 a,

b).
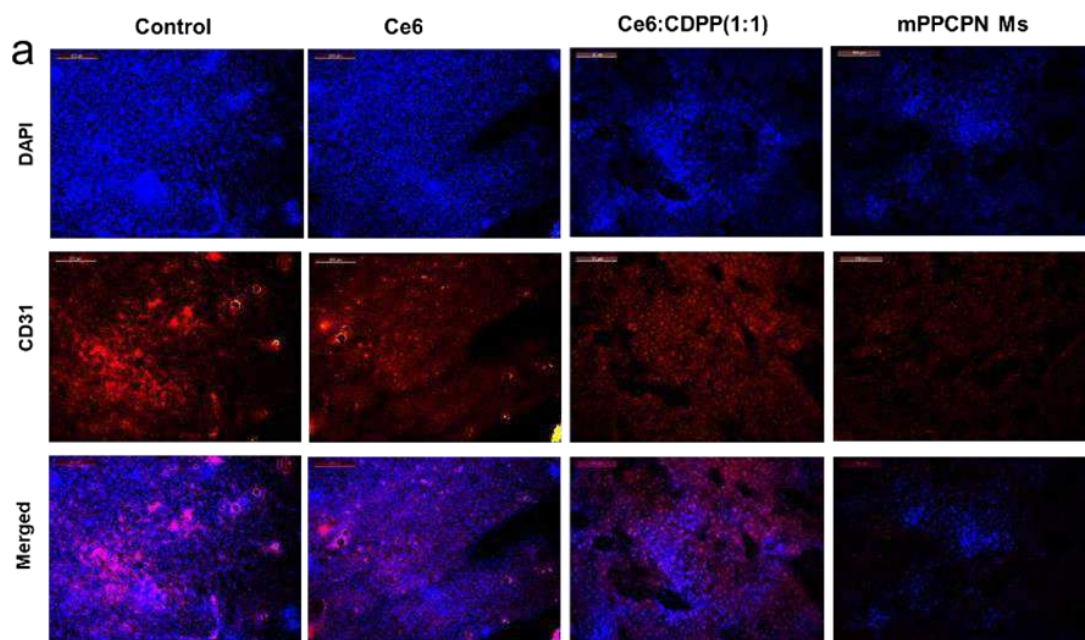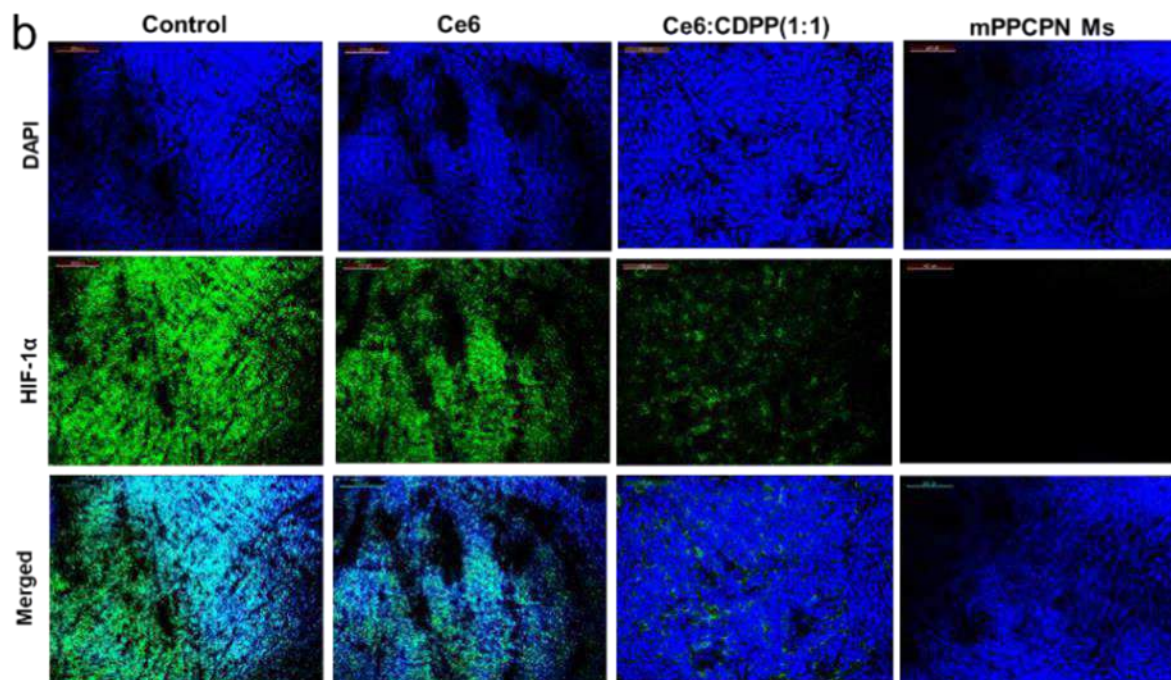
Figure 4.30 In vivo studies of anticancer efficacy and hypoxia reversion. Representative immunofluorescence staining of CD31 (a); HIF-1α (b); The scale bars represent 100 µm.

Reduced expression of HIF-1α and CD31 in mPPCPN Ms (+L) therapy is related to the Pt(IV)-azide- mediated O2-generation upon irradiation. The hypoxic condition in the tumor arises due to the high rate of proliferation of the cancer cells and poor vascularization. The activated HIF-1α in hypoxic tumors regulates genes that facilitate responses to the hypoxic environment, including angiogenesis, erythropoiesis, cell cycle, metabolism, and apoptosis. Reversal of hypoxia by aerobic mPPCPN Ms resulted in a decreased level of HIF-1α in the tumor microenvironment, which could reverse the expression of other cancer biomarkers. Angiogenesis is crucial in tumor progression and invasion.
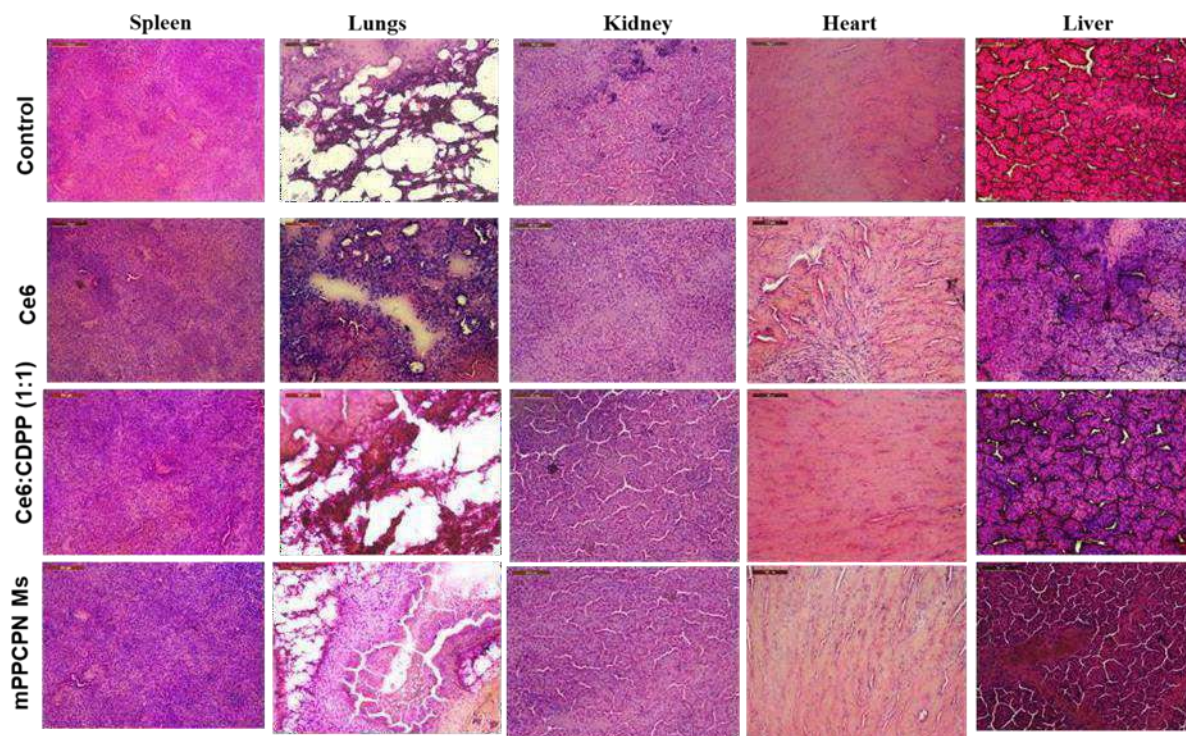
Figure 4.31 H&E stain of organs (FaDu HTB-43 tumor-bearing mice) after PBS, Ce6, Ce6:CDPP (1:1) and mPPCPN Ms administrated with irradiation (magnification $\times$ 200). Scale bar = 100 μm.

The neovascularization supplies the nutrient need of growing tumors. CD31, an upregulated biomarker in cancer, is a microvessel density marker and a clear indicator of neo-angiogenesis, located around the surfaces of hematopoietic stem cells, T-cells, endothelial cells of tiny blood vessels. The results indicated the ability of mPPCPN Ms to reduce the CD31 level, indicating hypoxia reversal (Figure 4.37 a).
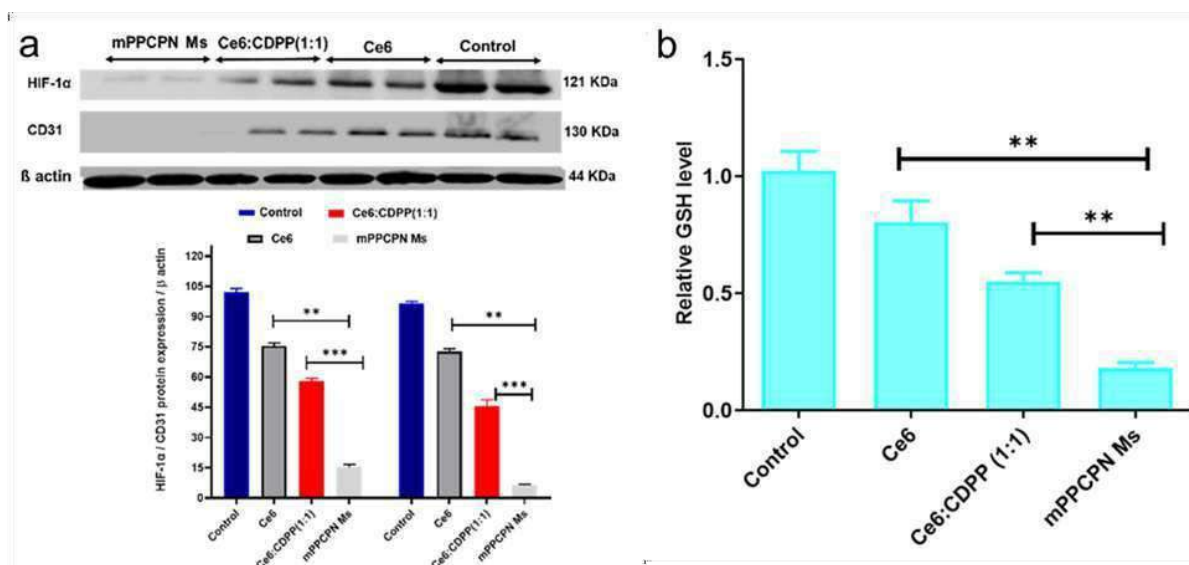
Figure 4.32 Western blotting of HIF-1α, CD31 (a); In vivo GSH level analysis by GSH Assay Kit in FADU HTB-43 tumor tissues (b).

4.3.4.9 Glutathione level in tumor tissues and Western blotting

Moreover, The decrease in the GSH level indicated the shifting of the cancer cell's redox balance towards more oxidative equilibrium. The GSH-dependent intracellular conversion of Pt(IV)-derivative to an active chemotherapeutic agent, Pt(II)-species, reduced the GSH level in the tumor. The decreased GSH level increased the oxidative stress by PDT, leading to enhanced treatment outcomes. (Figure 4.37b). The mPPCPN Ms treatment upregulated the apoptotic marker proteins, caspase-3 and -7, and down- regulated the epidermal growth factor receptor (EGFR) and proliferation marker, Ki-67, significantly more than the other treatment groups, as judged by the western blot experiment (Figure 4.38). Therefore, there is strong evidence that the improved

therapeutic efficacy is due to the apoptosis induction via the intrinsic pathway leading to tumor cell killing.
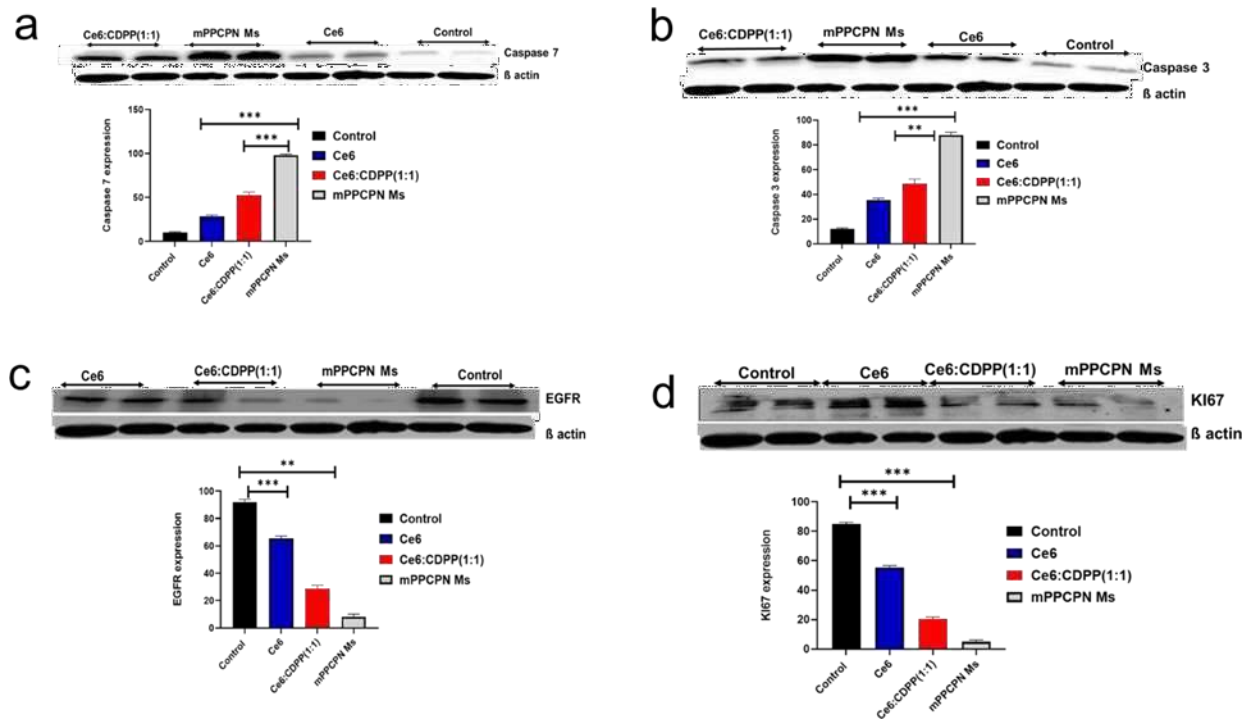
Figure 4.33 Western blot analysis of tumor tissues of mice from the treatment groups of saline, Ce6, Ce6:CDPP (1:1), and mPPCPN Ms. grey values for caspase-3, caspase-7, EGFR, KI67. β-actin was used as the internal standard. Bar graphs represent grey values of the protein bands. Significance of difference was analyzed by paired t-test, **p < 0.01 and ***p < 0.001.

4.4 Conclusion

A NIR-light degradable nanomicellar PDT-chemotherapy system decorated with photosensitizer Ce6 and chemotherapeutic moiety Pt(IV) was synthesized as a combination chemo-photodynamic therapy with the ability to generate molecular oxygen. Under 660 nm laser irradiation, the mPPCPN Ms convert Pt(IV)-prodrug to a more cytotoxic Pt(II) species by consuming GSH. The oxygen generated upon irradiation from Pt(IV) diazide is converted to ROS via activated Ce6 (type II reaction), which tilts the redox homeostasis of the cancer cells towards an oxidative state, thereby reversing hypoxia. After thorough characterization of mPPCPN polymer conjugate and micelles to determine their structure, morphology, ability to generate ROS, and molecular oxygen, the in vitro and in vivo studies were carried out. The in vitro study results demonstrated that the mPPCPN Ms were effectively internalized and decreased the cell viability by arresting the cell division, inducing apoptosis, generating ROS, and damaging the cellular DNA. The in vivo study corroborated the in vitro results and successfully suppressed the tumor growth, elevated/down-regulated apoptotic markers/anti-apoptotic proteins, reduced GSH level, and reversed hypoxia towards a more oxidative environment. Therefore, the established hypoxia-reversing chemo-photodynamic therapy could be a powerful treatment strategy for oropharyngeal carcinoma or other superficial solid tumors.

Chapter 5

NIR-Light Degradable Chlorin e6 Pro-DrugMicelles for Oral Cancer Treatment
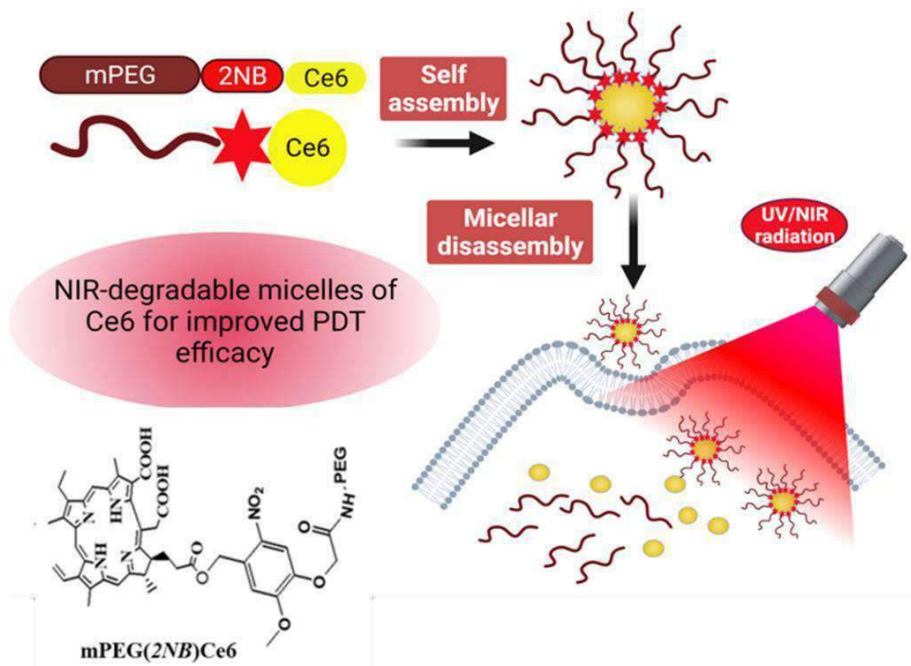
5.1 Introduction

Cancer is the primary cause of death in affluent nations and the second most common cause of death in developing nations. Head and Neck Squamous cell cancer (HNSCC) is anticipated to impact around 600,000 individuals globally, resulting in an annual mortality rate of 40-50 percent (Mirzaei S, Duan H 2022).   Oral cancer has a high fatality rate, especially when diagnosed at an advanced stage.   Over the past few decades, the survival rates for oral cancer have only shown a slow and steady improvement despite advancements in treatment. Chemotherapy, also known as the administration of chemotherapeutic medications or antitumor agents through oral ingestion or intravenous injection, is a highly prevalent approach in the treatment of cancer and inhibiting tumor growth that has been extensively utilized in recent decades. As a consequence of limited tumor selectivity during extended blood circulation, conventional chemotherapy medications are dispersed throughout the entire body, including normal tissues and organs. This leads to unwanted toxicity, severe side effects, and potential harm to the immune system (Goel A, Singla A, Prabhash K 2020). In recent years photodynamic therapy emerged as a potential anti-cancer therapeutic modality due to minimal invasiveness and less adverse effects. Photodynamic therapy (PDT) is a new anticancer treatment that uses photosensitizers to convert surrounding oxygen molecules into lethal reactive oxygen species (ROS) when exposed to particular laser irradiation. Consequently, Photodynamic Therapy (PDT), a treatment that does not require surgery, has generated significant attention for its potential in treating superficial cancers like oral squamous cell carcinoma (Saini R et al. 2016). Due to their hydrophobic nature, tendency to aggregate easily, and insignificant payloads, photosensitizers have limited ability to accumulate and target tumors. As a result, their therapeutic effect is inadequate. However, the PDT therapy process is accompanied by continuous oxygen consumption, which exacerbates the degree of

hypoxia at the tumor site, resulting in a loss in PDT efficacy. In addition, hypoxia enhances tumor metastasis and resistance to many treatments. As a result, one of the keys to improving PDT efficacy is to overcome the hypoxia limitation at the tumor site (Mosaddad SA et al. 2023).

In order to address the difficulties associated with inadequate solubility, limited permeability, and propensity for aggregation, it is necessary to develop appropriate drug delivery systems. Nano-drug delivery systems are specifically engineered to enclose pharmaceuticals within their core, enhancing the solubility, stability, and permeability of the drug being carried. Furthermore, appropriately engineered nanocarriers possess the ability to remain in the bloodstream for an extended period of time, leading to their eventual accumulation in the tumor microenvironment through the Enhanced Permeability and Retention (EPR) effect. In this regard a wide range of nanocarriers, including polymeric micelles, liposomes, nanogels, dendrimers, and polymer-drug conjugates, have been designed for delivering photosensitizers. The use of polymeric micelles for drug delivery applications has been extensively investigated (Ghezzi M et al. 2021).

In this study, we have developed a polymeric system consisting of a pro-drug of PEGylated Ce6. Specifically, Ce6 is chemically conjugated to mPEG to obtain mPEG-2NB-Ce6 (referred to as mPNCe6). mPEG provides extended blood circulatory potential. mPNCe6 has the ability to spontaneously assemble itself into micelles, preventing the clustering of Ce6 molecules, ensuring the durability of Ce6, and enabling the passive targeting of Ce6 to the tumor through the enhanced permeability and retention (EPR) effect. The polymer and micelles have undergone physicochemical characterization, and their therapeutic efficacy has been assessed in the context of cancer.

5.2 Materials and methods

5.2.1. Materials

Vanillin, anhydrous N,N-dimethyl formamide (DMF), Sodium borohydride, 4-dimethyl aminopyridine, propidium iodide, Paraformaldehyde, and DAPI (4,6-diamidino-2-phenylindole) were procured from Sigma-Aldrich(Mumbai, India). Chlorin e6 (Ce6) was bought from Frontier Scientific, Inc. (USA). Annexin V-FITC Apoptosis Detection Kit was purchased from Invitrogen Co. (USA). Spectra/Por dialysis membranes were procured from Spectrum Laboratories, Inc. (USA). Singlet oxygen sensor green (SOSG) and Calcein Blue AM, Trypan Blue solution was purchased from Thermo Fisher Scientific (USA). Trypan blue solution and Fluoromount-G were purchased from Himedia Laboratories (India).

Mouse Oral Squamous Cell Carcinoma (MOC2) was purchased from the National Center for Cell Sciences (NCCS, Pune, India). The Hypopharyngeal carcinoma cell line (FaDu HTB-43) was received from the American Type Culture Collection (ATCC, USA). Dulbecco's modified Eagle's medium (DMEM), Minimum Essential Medium Eagle (MEM), Penicillin Streptomycin, fetal bovine serum (FBS), and Trypsin-EDTA were obtained from Himedia Labs (India). The cells were cultured in a controlled environment with a humidity level and temperature of 37 °C, and a CO_2 concentration of 5 %.

C57 mice weighing 18-20 grams and aged 4-6 weeks were acquired from the National Centre for Laboratory Animal Sciences, National Institute of Nutrition, Hyderabad, India, for the purpose of studying the efficacy of antitumor treatments. The pharmacological experiments were approved by the Institutional Animal Ethics Committee of BITS-Pilani, Hyderabad. The mice were housed in standard mouse/rat cages, with 5 animals per cage, and kept in a temperature-controlled room

at 23- 24 °C with a relative humidity of 50-60%. They were exposed to a 12-hour light/dark cycle and provided with unrestricted access to food and water.

5.2.2 Preparation and characterization of mPNCe6 micelles

5.2.2.1 Synthesis of Ethyl 2-(4-formyl-2-methoxyphenyl) acetate

The scheme in Figure 4.2 is as follows to prepare the NIR-light cleavable amphiphilic polymer. A mixture of sodium carbonate (Na2CO3) (3.5 g, 25 mmol), vanillin (2.5 g, 16 mmol), and ethyl bromoacetate (2 mL, 3 g, 18 mmol) was prepared using dimethylformamide (DMF) (15 mL) as a solvent and stirred for 24 h at room temperature. The above mixture was partitioned using a separating funnel between ethyl acetate and saturated sodium chloride solution. The aldehyde ester with 90% yield was obtained after drying and evaporating the organic phase with anhydrous sodium sulfate.

5.2.2.2 Synthesis of 2-(4-formyl-2-methoxy-5-nitrophenoxy) acetic acid

A mixture was prepared using acetic anhydride (10 mL) and aldehyde ester 1 (3.5 g, 15 mmol). Into the solution, cool 70% HNO3 (10 mL) and acetic anhydride (15 mL) were added, maintaining the temperature at 4 °C. The above mixture was kept for stirring for 2 h and then allowed to warm up to room temperature. After the temperature is set, stir the mix for an additional 4 h and then add cold water to it. The pH was adjusted to 13-14 using sodium hydroxide and then changed to pH 2-3 using 36% HCl. The aqueous phase was extracted with ethyl acetate, while the organic phase was dried and evaporated. After evaporation, the yellow-colored solid product is obtained. This product was recrystallized using methanol/water to get the product with an 80% yield.

5.2.2.3 Synthesis of 2-(4-hydroxymethyl)-2-methoxy-5-nitrophenoxy) acetic acid

Into the solution of 2-(4-formyl-2-methoxy-5-nitrophenoxy) acetic acid (1 g) in THF (20 mL), sodium borohydride (NaBH4) was added at room temperature and stirred for 24 h. Next, 1 M HCl was added to adjust the pH in the range of 2-3. The organic phase was dried and evaporated, and the aqueous phase was extracted with ethyl acetate. A pale-yellow solid was obtained with a 95% yield.

5.2.2.4 Synthesis of PEG-NH2-(4-hydroxymethyl)-2-methoxy-5-nitrophenoxy) acetic acid

PEG-NH2 (0.4 g, 0.54 mmol), triethylamine (0.075 mL, 0.055 g, 0.54 mmol), EDC (0.1 g, 0.52 mmol), and 2-(4-hydroxymethyl)-2-methoxy-5-nitrophenoxy) acetic acid were mixed with DMF at room temperature and were stirred for 24 h. The resultant mixture was then partitioned between the saturated solution of sodium chloride and ethyl acetate. The organic phase was dried and evaporated to obtain the product (71% yield).

5.2.2.5 Synthesis of mPEG-2NB-Ce6

Chlorin e6 (20mg) was dissolved into the solution of DCC and DMAP in DMF to activate the carboxylic group of Chlorin e6. After 3 h, PEG-NH2-(4-hydroxymethyl)-2-methoxy-5-nitrophenoxy) acetic acid was slowly added. The reaction mixture was kept under stirring for 24 h at room temperature. DMF was evaporated using a rotary evaporator. Further, Milli-Q water was added and dialyzed using cellulose ester membrane (24 h, 1KDa). The product was lyophilized to obtain a solid powder with a 79% yield.
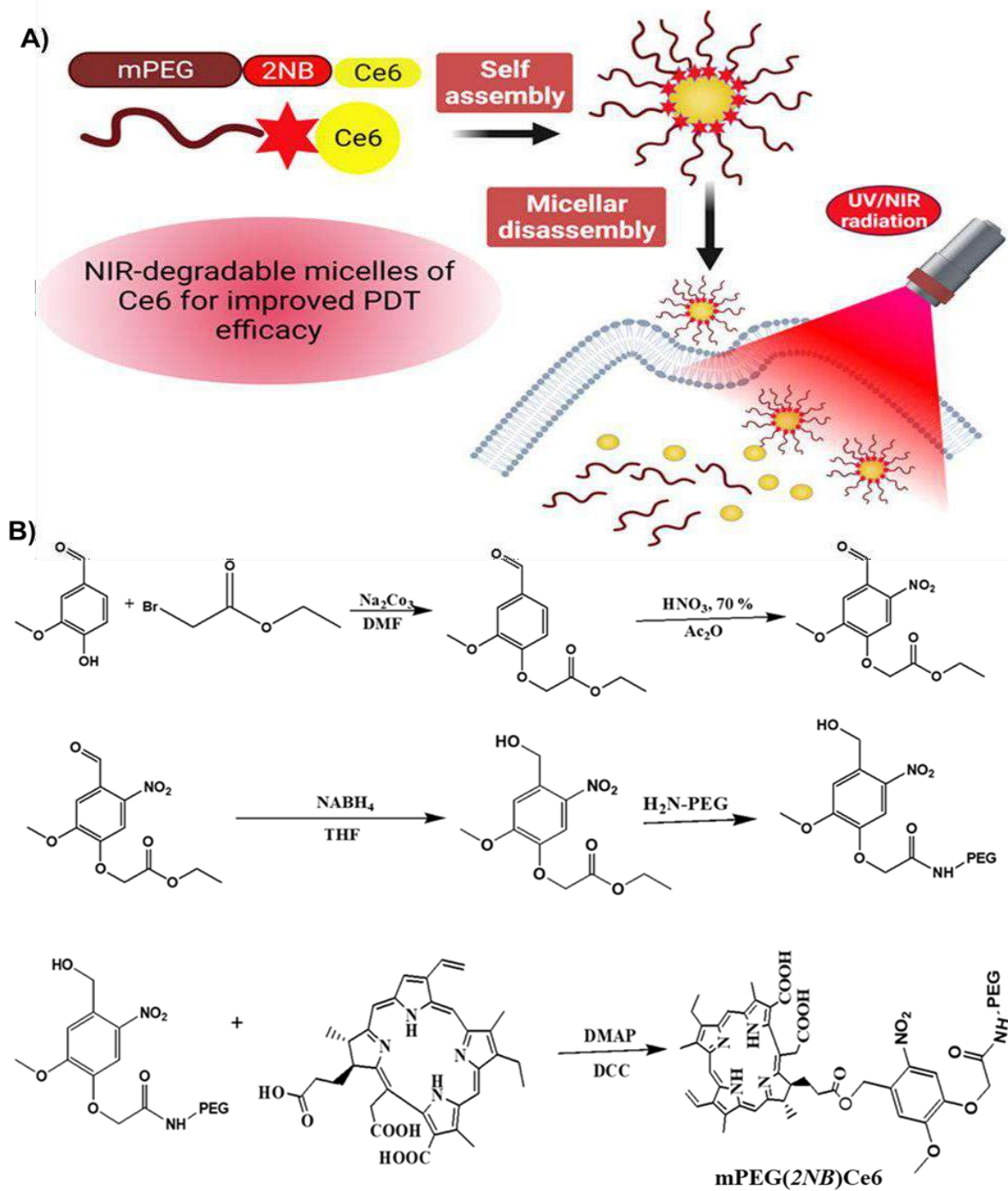
Figure 5.1 Preparation of mPNCe6 micelles (A); Synthesis of methoxy (polyethylene glycol)-2-nitrobenzyl-chlorin e6 (mPEG-2NB- Ce6) conjugate (B).

5.2.2.6 Preparation of mPEG-2NB-Ce6 (mPNCe6 micelles) and mPEG-Ce6 (mPCe6) micelles (used as control)

The mPEG-2NB-Ce6 (mPNCe6) conjugate of mPCe6 was dissolved in DMF (10.0 mg/ml). The organic solvent was removed by a rotary evaporator, then freeze-dried. The polymer film was hydrated in PBS 7.4 (500 µL), stirring for 5 h at 37°C. The micellar solution, mPNCe6 Ms, was centrifuged (13,000 RPM, 20 min, 4 °C) and filtered through a 0.45 µm filter to remove the un-encapsulated Ce6.

5.2.3 Physiochemical Characterization of mPNCe6/mPCe6 micelles

5.2.3.1 Particle Size and Zeta Potential

Samples were diluted with deionized water and placed into a cuvette of 10mm diameter at 25 °C. Dynamic light scattering was used to evaluate the particle size and zeta potential of mPNCe6 micelles using a Zetasizer™ ZEN 3600 instrument (Malvern Instruments Ltd., UK). The samples were analyzed for particle size and zeta potential.

5.2.3.2 Critical Micellar Concentration

The critical micelle concentration of the mPNCe6 micelles was determined using pyrene as the hydrophobic probe and a microplate reader (SpectramaxTM, Molecular Devices, USA). The excitation wavelength of the solution was set to an excitation wavelength of 339 nm and a slit width of 5 nm for both excitation and emission. Pyrene solution (50 L; 10 mg/mL in chloroform) was combined with a micellar solution at concentrations ranging from 3.125 to 100 g/mL. The graph was plotted using log concentrations of mPNCe6 micelles and the fluorescence intensities at ratios of $I338/I390$ at the X and Y axis, respectively (Paul M et al. 2023).

5.2.3.3 Scanning Electron microscopy (SEM)

Field Emission Scanning Electron Microscopy was used to examine the surface morphology of mPNCe6 micelles. A thin layer of nanoparticles was uniformly distributed over an adhesive carbon tape connected to aluminum stubs to prepare the sample. Further, nitrogen purging was done, and the stubs were sputter-coated with gold in the desired thicknesses and examined at 20 kV (Gothwal A, Khan I, Gupta U 2016).

5.2.3.4 Storage Stability

The stability of mPNCe6 micelles was tested at 4°C. Before measuring particle size, the NPs were examined for stability in physiological conditions by incubating them for 72 hours at 37°C in a DMEM medium containing 10% FBS (Muddineti et al., 2017b). The formulations in DMEM (10 L) were diluted with 1.5 mL MilliQ water, and particle size and zeta potential were measured using a Malvern zeta sizer.

5.2.3.5 X-ray diffraction

mPNCe6 micelles were taken for powder XRD analysis Using an X-ray diffractometer (ULTIMA-IV, Rigaku). The instrument had a Cu anode (1.54 mm) with a voltage of 40 kV and a current of 30 mA. At a 5°/min rate, the scanned angle was set at 2 from 5° to 100° (Hou W et al. 2016).

5.2.3.6 Differential scanning calorimetry (DSC)

A Differential Scanning Calorimeter (DSC 60, Shimadzu, Japan) and thermogravimetric analyzer at 10 °C/min from 25 to 800 °C in a nitrogen atmosphere conducted the thermo-analytical Characterization of Ce6 and mPNCe6.

5.2.3.7 Singlet Oxygen Generation (SOG)

The singlet oxygen generation by mPNCe6/mPCe6 micelles in distilled water was also measured using a green singlet oxygen sensor (SOSG) as described previously. 2.5 mM SOSG was combined

with mPNCe6/mPCe6 micelles in a quick experiment. A 633 nm laser source was used to irradiate the mixture. The sample was irradiated, which produced 1O2, which interacted with SOSG to produce SOSG endoperoxide (SOSG-EP). A fluorescence spectrophotometer was used to measure the fluorescence of SOSGEP (Ex. 510 nm; Em. 525–536 nm) (Li X et al. 2017).

5.2.3.8 In vitro drug release studies

The dialysis bag method was used to investigate in-vitro Ce6 release from mPNCe6/mPCe6 micelles at 37 °C in PBS pH-7.4. The dialysis bags with MW 3.5 kDa have three distinct ratios of mPNCe6/mPCe6 micelles, and free Ce6 (at a concentration of 50 µg/ml) were inserted. The bags were placed in a beaker with PBS, pH 7.4, at 37 °C with continual stirring at 300 rpm. 1 mL of aliquots from the outer phase were taken at predefined intervals and replaced with 1 mL of fresh PBS. A UV–Visible spectrophotometer set to 480 nm was used to calculate the amount of released Ce6 (Bobde Y, Biswas S, Ghosh B 2021).

5.2.4   Cell based study

5.2.4.1 Time-dependent Ce6 uptake

FaDu HTB-43, and MOC2 cells were grown in 12-well tissue culture plates on cover slips (50,000 cells/well). The cells were treated with free Dox and Dox-mPEG-PLA-OA micellesat DTP weight ratios of 1:5/10/15 at Dox concentration of 6 µg/mL for 1-4 h. The cells were washed with PBS, stained with DAPI and fixed with 4 % paraformaldehyde. The cells were mounted on a glass slide using Fluoromount G and visualized under confocal microscope. For flow cytometry studies, cells were seeded in 6 well plate (0.5X106 cells/well). The next day, cells were treated the same way as the confocal microscopy study. Following treatment, cells were washed with PBS, trypsinized,

centrifuged, washed, and re-suspended in PBS, pH7.4. The cellular uptake was analyzed by measuring the fluorescence of 10000 viable cells by flow cytometer (Amnis Flowsight, EMD Millipore, USA). The data was processed using IDEAS software (Cheng L et al. 2016).

5.2.4.2 Phototoxicity study

An in vitro phototoxicity experiment with free Ce6, mPCe6, and mPNCe6 micelles was carried out on FaDu HTB-43 and MOC2 cells. 5*104 cells/well were plated in 96-well plates for cell adhesion and kept at 37°C overnight. After rinsing the cells in PBS, each well was filled with 100 µL of free Ce6, mPCe6, and mPNCe6 micelles, which were incubated for 12 hours. Following the incubation time, the cells were exposed to a 660 nm laser at a power of 0.5 W/cm2 for 2 minutes. Irradiated cells were then incubated in the dark for additional 12 hours at 37°C. After that, the culture medium was withdrawn, and 50 µl of 5 mg/mL MTT in serum/phenol red-free medium was added to eachwell. After 3 hours of incubation, the MTT solution was discarded, and 150 µl of DMSO was addedto each well to dissolve the purple formazan crystals formed by MTT reduction by live cells' mitochondria. The absorbance at 570 nm was measured and then subtracted from the background absorbance at 630 nm (Zeng YP et al. 2016).

Following equation was consideredto determine the percent cell viability: Cell viability (%) = $(Absorbance\ of\ sample)/(Absorbance\ of\ control) \times 100$.

5.2.4.3 Annexin V Assay

FaDu HTB-43 and MOC2 cells were seeded and cultured overnight in a 12-well plate. The cells were treatedwith free Ce6, mPCe6, and mPNCe6 micelles at a Ce6 concentration of 6 µg/mL. The

cells were rinsed in PBS with a pH of 7.4 and centrifuged to get a cell pellet after an 18-hour incubation period. The pellet was resuspended in 100 µl of binding buffer and stained with 1 µl of Annexin-V FITC and 10 µl of PI, as described in the TACS® Annexin V-FITC Apoptosis Detection Kit. After 15 minutes of incubation, the binding buffer was added to all test samples and control tubes,and cells were analyzed by flow cytometry (Flowsight Amnis, Millipore, USA) by gating 10,000 live cells.

5.2.4.4 Cell cycle

Free Ce6, mPCe6, and mPNCe6 micelles were incubated overnight with seeded cells (0.5× 106 cells/well) at Ce6 concentration 6 µg/mL. Trypsin was used to harvest the cells, and the cell pellet was washed in ice-cold PBS. The cells were fixed in 70% ethanol with gentle agitation. Overnight, the samples were maintained at 20° C. The fixed cells were centrifuged for 7 minutes at 1000 rpm at 4 °C the next day. Finally, the cells were resuspended in 500 mL of staining solution containing 20% w/v RNAase, 2% w/v PI, and 0.1 percent v/v Triton X-100 in pH 7.4 PBS. The samples were incubated at room temperature for 30 minutes in the dark before being analyzed using flow cytometry (BDAriaTMIII). A dot plot of the PI width against the PI area was made. A histogram of the PI area was shown on the X-axis, with counts on the Y-axis (Bobde Y et al. 2021).

5.2.4.5 Mitochondria membrane potential

For this experiment, FaDu HTB-43 and MOC2 cells were seeded at a density of (1×105 cells/well) per well in complete media on 6-well assay plates. The cells were treated with free Ce6, mPCe6, and mPNCe6 micelles at a Ce6 concentration of 10 µM and incubated for 24 hours at 37 °C. The cells were then rinsed in cold PBS and stained for 30 minutes in a CO2 incubator with 2 M of 5,5′,6,6′- Tetrachloro- 1,1′,3,3′ tetraethyl benzimidazole carbocyanine iodide (JC1 dye). The cells were then visualized under fluorescence microscopy with 530 for green fluorescence and 630 for

red fluorescence. Green and red co-localization were represented by the yellow signal after processing the pictures using Image J software.

5.2.4.6 ROS Generation in cells

FaDu HTB-43 and MOC2 cells were seeded at a cell density (1×10^4 cells /well in 6 well plates) in the complete media. The following day, the cells were treated with free Ce6, mPCe6, mPNCe6 Ms at a Ce6 concentration of 50 µg/ml for 24 h. Afterward, the cells were irradiated with or without a 660 nm laser at a power density of 50 mW/cm2 for 5 min. Following that, confocal images were collected before and after irradiation. At the beginning and finish of the photoreaction, the changes in fluorescence intensity were also recorded (Kumbham S et al. 2022).

5.2.5 In vivo studies

5.2.5.1 Pharmacokinetic study and immunohistochemistry

The pharmacokinetic profile of the formulations was assessed in male Wistar rats aged 5-8 weeks, following the previously reported approach. In summary, rats that had fasted overnight were separated into three groups (n=3) and given either saline, mPCe6, or mPNCe6 micelles with a single intravenous injection (via the tail vein) at a dosage of 5 mg/kg. Heparinized tubes were used to collect blood samples at specific time intervals (0.5, 1, 3, 6, 12, 24, 36, 48, 72, and 96 hours) after injection. The blood samples were obtained using retro-orbital puncture. The plasma was isolated from the blood samples using centrifugation at a speed of 3000 rpm per minute for a duration of 5 minutes at a temperature of 5°C. The isolated plasma was then stored at a temperature

of -20°C until it was ready for analysis. The plasma samples were analyzed via reverse-phase high-performance liquid chromatography (RP-HPLC) with a C18 column (150nm × 4.4nm, 5µm). The mobile phase consisted of acetonitrile (ACN) and water, with a pH of 2.6 adjusted using orthophosphoric acid (25:75, v/v). The analysis was performed at a column temperature of 40°C and a flow rate of 0.6 mL/min. The statistical significance of the results was assessed using a paired t-test, with significance defined as p values below 0.05. The rats were subjected to euthanasia 96 hours following the injection of the medication. The different tissues were sliced into sections of 5µm thickness using a cryostat (Leica biosystem, Germany). These sections were then treated with 4% (v/v) paraformaldehyde to preserve them and subsequently stained with hematoxylin and eosin (H&E) for visualization (Kumbham S et al. 2022).

5.2.5.2 In vivo tumor inhibition study

The study utilized male C57BL/6J mice weighing between 18 and 20 grams, which were acquired from the National Institute of Nutrition (NIN) in Hyderabad, India. The mice were housed in a controlled environment with a temperature range of 19-23°C and a 12-hour light-dark cycle. The relative humidity was maintained at 50-60%. The mice were given one week to acclimate to these circumstances before the start of the experiment. Animals have unrestricted access to food and water. The experimental protocols were approved by the institute's Animal Ethics Committee. The mouse oral cancer model was established by subcutaneously injecting MOC2 cells into the right hind leg of mice at a cell density of 1×10^6 cells per 100µL of sterile phosphate buffer saline with a pH of 7.4. A tumor inhibition study was conducted once the tumor volume reached around 70 mm3. The investigation was conducted by randomly assigning the mice to 4 groups: control (saline), Ce6, mPCe6, and mPNCe6, with five mice in each group. Following the intravenous tail injection of the drug/formulations at a dosage of 5mg/kg, each mouse underwent laser irradiation

using a diode emitting light at a wavelength of 660 nm with a power density of 0.5 W/cm2 for a duration of 5 minutes after 12 hours. The tumor volume and body weight of the mice were regularly checked every other day for a period of 21 days. At the completion of the study period, mice were euthanized by cervical dislocation, and the tumor mass was surgically excised and quantified by weighing (Wen Y et al. 2017).

5.2.6 Statistics

All the above experiments were performed in triplicates and the data are shown as mean and standard deviation (mean ± SD). The significance of difference between all the groups was evaluated by one- way ANOVA using Graph Pad prism software (GraphPad, Inc., California, USA). The p-values < 0.05 reflected statistical significance. *, **, *** illustrates p-values < 0.05, 0.01 and 0.001, respectively.

5.3 Results and Discussion

5.3.1 Synthesis and characterization of the polymers

The mPEG-2NB-Ce6 conjugate was synthesized using the procedure illustrated in Figure 5.1. The 1H nuclear magnetic resonance (1H NMR) spectrum of mPNCe6 conjugate is shown in Figure 5.1 f, 1H-NMR (400 MHz, CDCl3) δ 9.83 (s, 1H), 7.41 (d, J=1.9, 1H), 7.39 (dd, J=8.1, 1.9, 1H), 6.86 (d,J=8.1, 1H), 4.75 (s, 2H), 4.24 (q, J=7.1, 2H), 3.92 (s,3H),1.26 (t, J=7.1,3H);

The 1H nuclear magnetic resonance (1H NMR) spectrum of Ethyl 2-(4-formyl-2-methoxyphenoxy) acetate is shown in Figure 5.1 a , 1H-NMR (400 MHz, CDCl3) δ 10.24 (s, 1H), 7.40 (s, 1H), 7.24 (s, 1H), 4.66 (s, 2H), 3.86 (s, 3H); The 13C nuclear magnetic resonance (1H

NMR) spectrum of Ethyl 2- (4-formyl-2-methoxyphenoxy) acetate is shown in Figure 5.1 a 13C-NMR (100 MHz, CDCl3) δ 187.4, 168.9, 153.3, 150.4, 143.1, 126.0, 110.1, 108.7, 65.6, 56.5.

The 1H nuclear magnetic resonance (1H NMR) spectrum of 2-(4-formyl-2-methoxy-5-nitrophenoxy) acetic acid is shown in figure 5.1 b 1H-NMR (400 MHz, CO(CD3)2) δ 7.73 (s, 1H), 7.54 (s, 1H),

4.99 (s, 2H), 4.87 (s, 2H), 4.00 (s, 3H); The 13C nuclear magnetic resonance (13C NMR) spectrum of 2-(4-formyl-2-methoxy-5-nitrophenoxy) acetic acid is shown in Figure 5.2 b. 13C-NMR (100 MHz, CO(CD3)2) δ 169.8, 155.4, 146.8, 139.7, 136.0, 111.5, 111.2, 66.5, 61.8, 56.7.

The 1H nuclear magnetic resonance (1H NMR) spectrum of 2-(4-hydroxymethyl)-2-methoxy-5-nitrophenoxy) acetic acid is shown in figure 5.1 c 1H-NMR (400 MHz, CO(CD3)2) δ 7.79 (s, 1H), 7.59 (s, 1H), 4.99 (s, 2H), 4.63 (s, 2H), 4.04 (s, 3H), 3.68-3.52 (m, 68H), 3.29 (s, 3H); The 1H nuclear magnetic resonance (13C NMR) spectrum of 2-(4-hydroxymethyl)-2-methoxy-5-nitrophenoxy) acetic acid is shown in figure 5.2 c 13C NMR (100 MHz, CO(CD3)2) δ 168.0, 155.5, 146.5, 136.6, 126.0, 112.4, 111.2, 72.63, 71.2 (x29), 71.0 (x2), 70.2, 70.0, 61.6, 58.8, 56.9, 39.4.

The peaks at 2988, 1720 cm−1 belong to the C−H vibrations and C=O stretch of PEG-NH2, while the band at 1079 and 1248 cm-1 is due to the –C- O-C- stretch of PEG and PLA on the mPNCe6 chain, respectively. (Figure 5.3 a). The characteristic peak at 1722 cm-1, 1248 cm-1 which corresponds to the ester bond (O=C-O), confirmed the successful conjugation of mPEG and Ce6. GPC analysis revealed that 4 moles of mPEG-NH2 were attached to Ce6 polymer at the specified reaction condition.

5.3.2 Physicochemical Characterization of mPNCe6 micelles

The particle size of mPCe6 and mPNCe6 micelles was 105.8 ± 2.58, and 135.32± 3.48, respectively, as measured by the dynamic light scattering technique. (Figure 5.4 a) The zeta potential was -8.8 ± 1.23 for blank and -10.21 ± 3.25 mV for mPCe6, mPNCe6 micelles. (Figure 5.4 b) The morphology of the prepared micelle was found to be spherical. The EE and %DL in mPNCe6 micelles were found to be 76.01 ± 2.53. Because of the low CMC concentration, self-assembled micelles developed quickly and remained stable in dilute conditions. (Figure 5.4 c)

The average particle size of mPNCe6 micelles was 150 nm, and their shape was spheroidal. The best nanomaterial size for obtaining the EPR effect has been shown to be between 10 nm and 200 nm, indicating that mPNCe6 micelles can target tumor tissues passively. The remarkable peak in UV/Vis absorption spectra at around 330 nm of mPEG-NH2-Ce6, free Ce6, mPCe6 and 2-(4-hydroxymethyl)- 2-methoxy-5-nitrophenoxy) acetic acid further confirmed the successful mPN-Ce6 micelle formation. (Figure 5.4 d). The particle size and drug loading were 212.32 ± 2.61 for mPNCe6 micelles on storage at 4 °C, compared to 655.40 ± 2.1 at room temperature. (Figure 5.4 e) The chemical components of the mPNCe6 micelles were also characterized by XPS analysis. An increase in oxygen (7.4%) was observed in mPNCe6 micelles compared to free Ce6. (Figure 5.4 f)
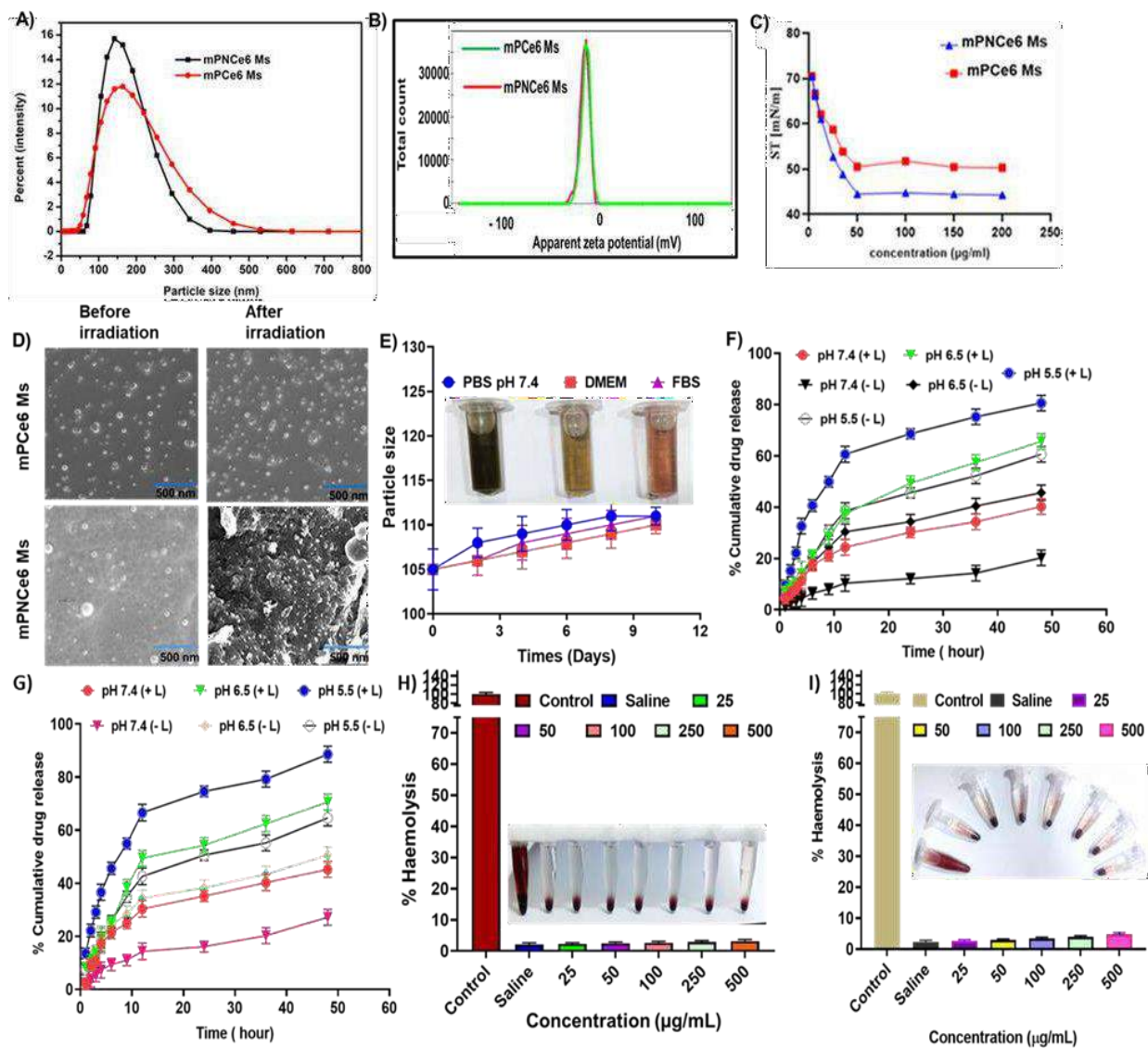
Figure 5.2 Particle size analysis of mPCe6 Ms, mPNCe6 Ms (A); Zeta potential of mPCe6 Ms, mPNCe6 Ms (B); Surface tension of mPCe6 Ms, mPNCe6 Ms (C); Scanning electron microscopic (SEM) images of mPCe6Ms, mPNCe6 Ms (D); Stability study of mPNCe6 Ms (E); In-vitro drug release study of mPCe6Ms, mPNCe6 Ms (F & G). Haemolysis study of mPCe6Ms, mPNCe6 Ms (H &I).

The XRD analysis of the mPNCe6 micelles revealed the amorphous nature of the formulation. Looking into the diffraction pattern obtained for mPNCe6 micellar formulation, we observe two characteristic peaks at 11.8º and 25.6º, ensuring the encapsulation of the drug in the desired micelles. (Figure 5.5 a). The DSC thermograms were plotted simultaneously to compare the thermal characteristics of newly formed mPNCe6 Ms. The diffractogram for Ce6 and mPNCe6 Ms showed clear peaks that demonstrated the presence of crystalline phase in the native form, whereas mPNCe6 Ms showed identical peaks in the diffractogram, confirming the conjugation of mPNCe6 miceller system (Figure 5.5 b). The stability testing data are illustrated graphically in Figure S1C. The particle size and drug loading of the mPNCe6 Ms did not change significantly in a 30-day stability study at 4 °C, however, at room temperature, an increase in particle size and a decrease in drug loading were observed (Figure 5.5 c). As shown in Figure 5.5 d the Ce6 release from mPNCe6 Ms was analyzed at different pH values (pH 7.4, 6.5, and 5) using the dialysis method. The amounts of Ce6 released from the micelles were all less than 50% after 48 h at pH 7.4, indicating that these systems were generally stable, and the release rate of Ce6 was rather slow under physiological conditions with or without laser. The released Ce6 from the mPNCe6 Ms were increased to 65.12 %, significantly greater than at pH 6.5 with laser. The total Ce6 release from mPNCe6 Ms was 82.41% for 48 h at pH 5.5. These Ce6-loaded micelles demonstrated considerable pH-dependent release behavior. When RBCs were treated with micelle solutions with polymer concentrations ranging from 0 to 500 µg/mL, the percentage of hemolysis was around 2.32 % (Figure S2). These findings indicated that the mPNCe6 Ms did not cause hemolysis.

In assessing mPCe6 Ms' reaction to NIR-activation, scanning electron microscopy (SEM) was utilized to analyze the microstructures of the polymeric micelles (Figure 5.6). Following laser irradiation, the polymeric micelles underwent a transformation into a spherical morphology due to

their osmotic swelling property. This transformation resulted in a marginally reduced surface charge of approximately -20.7 mV and an increased average hydrodynamic diameter of around 1230 nm after 30 minutes of laser exposure.

Upon exposure to a NIR laser mPCe6Ms, mPNCe6 Ms, and an ROS probe underwent irradiation, as depicted in Figure 5.7. The increase in DCF absorption at 500 nm with extended irradiation time suggests a light dose-dependent generation of reactive oxygen species (ROS), even when these species are loaded onto mPCe6Ms and mPNCe6 Ms. To assess the production of singlet oxygen ($1O_2$), crucial in photo-oxidative damage induced by PDT, Ce6 in mPCe6Ms and mPNCe6 Ms was evaluated by monitoring the reduction in 9,10-dimethylantracene (DMA) absorption at 378 nm. In the presence of $1O_2$, DMA transforms into a non-fluorescent endoperoxide derivative. As anticipated, the solution containing mPCe6Ms, mPNCe6 Ms, DMA, and irradiated with a tungsten lamp at 660 nm (0.5 W) for up to 10 minutes displayed a progressive decrease in DMA absorbance. This reduction solely attributes to the $1O_2$ action generated upon Ce6 irradiation.

5.3.3 Cellular Uptake study of mPNCe6 Ms

According to the flow cytometry histogram, the fluorescence peak of mPNCe6 shifted to the right as the incubation time increased, indicating that mPNCe6 internalization was more readily than free Ce6 (Figure 5.8). Confocal micrographs of cells treated with the formulations confirmed the findings. Free Ce6 showed a weak intensity of red signal after 1 hour of incubation, indicating low internalization. After 4 hours of treatment, mPNCe6 micelle treated cells showed a much higher power of the red signal, followed by mPCe6 and finally free Ce6. At 1, 4, hours, the geomean fluorescence of FaDu cells treated with ce6, mPCe6, and mPNCe6 micelles was 826±121.32,

2526±251.32, 3826±281.32 and MOC2 cell treated with ce6, mPCe6, and mPNCe6 micelles showed geo mean fluorescence 826±121.32, 2526±251.32, 3826±281.32.
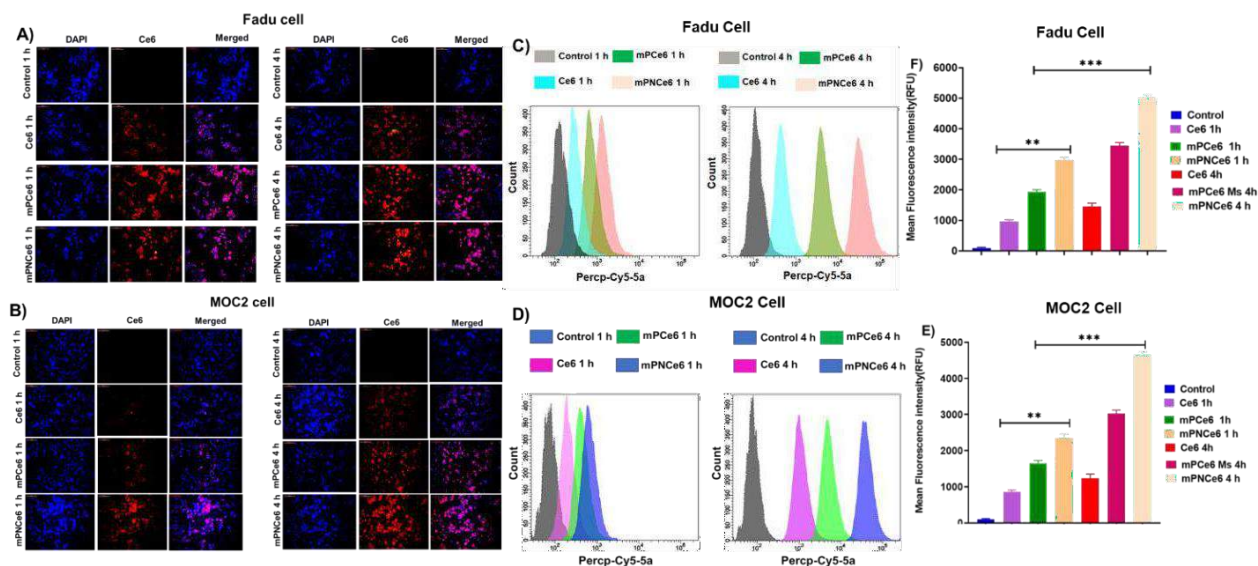
Figure 5.3 Uptake of free Ce6, mPCe6, mPNCe6 Ms by FADU and MOC2 cell lines after incubation for 1 h, 4 h at 37°C. Scale bar, 100 mm (A & B); Flow cytometry data of Free Ce6, mPCe6, mPNCe6 Ms. (C & D).

5.3.4   Cell viability study/Phototoxicity of mPNCe6 Ms

In the MTT experiment conducted on the FaDu cell line, treating with free Ce6, mPCe6, and mPNCe6 micelles led to a concentration and time-related decline in cell viability. Post-irradiation, the IC50 values for Ce6, mPCe6, and mPNCe6 micelles against the FaDu cell line were determined as 15.73 µg/ml, 11.50 µg/ml, and 9.32 µg/ml respectively after 24 hours and IC50 values for Ce6, mPCe6, and mPNCe6 micelles against the FaDu cell line were determined as 17.73 µg/ml, 14.50 µg/ml, and 10.32 µg/ml respectively (Figure 5.9). Notably, the mPNCe6 micelles exhibited

superior cell penetration, accumulating at higher Ce6 concentrations within the tumor cells, demonstrating enhanced cytotoxicity compared to free Ce6 across all concentrations in the cell viability assay. These formulations induced a more pronounced level of apoptosis relative to free Ce6, likely owing to the increased cellular uptake of Ce6 facilitated by the nanocarrier systems, consequently resulting in a higher degree of apoptosis induction.
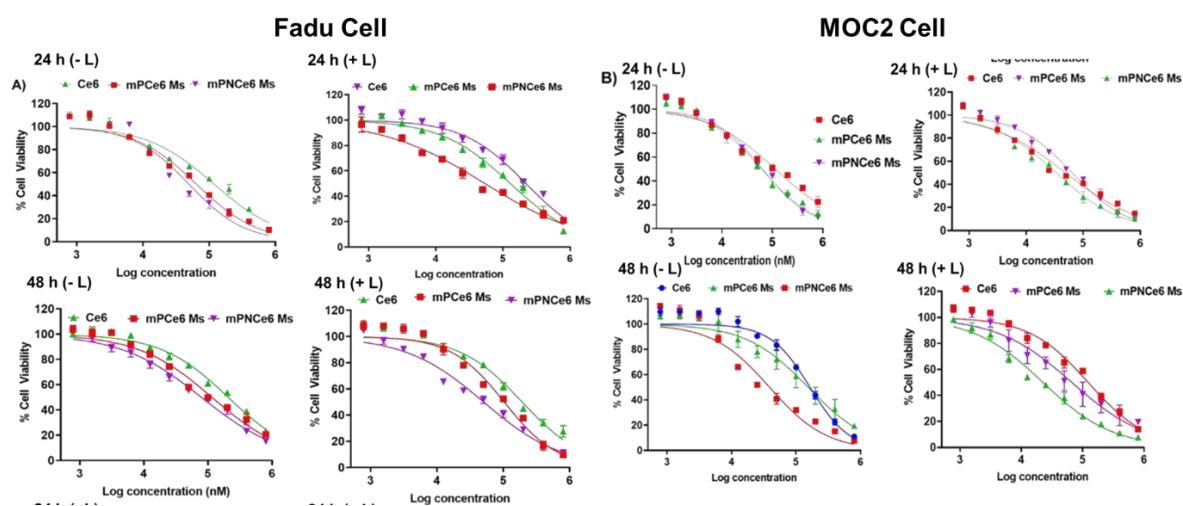
Figure 5.4 In vitro cell cytotoxicity of free Ce6 and mPCe6 Ms, mPNCe6 Ms against FADU and MOC2 cells after incubation for 24 h, 48 h (without irradiation 24 h and with irradiation 24 h b) or (without irradiation 48 h; and with irradiation 48 h) under light irradiation (660 nm, 0.5 W/cm2 5 min) in the dark (A, B, and C, D)

5.3.5 Apoptosis

When the cells undergo treatment, triggering the apoptotic pathway, phosphatidylserine (PS) relocates from the inner to the outer side of the plasma membrane, drawing in macrophages and instigating the creation of apoptotic bodies. AnnexinV, acting as a distinct ligand for PS, selectively

attaches to PS, a binding event detectable through its tagged fluorescence. Additionally, the assay employs propidium iodide (PI), which binds specifically to necrotic cells.

Annexin V assay measured the extent of cellular apoptosis following treatment with free Ce6, mPCe6, and mPNCe6 micelles at the fixed dose of Ce6 10 µg/mL. As indicated in (Figure 5.10) cells treated with free Ce6 exhibited total apoptosis of 20.6±1.2 % in FaDu cells and 52.6 ± 3.2 % for mPCe6 Ms, 75.6 ± 7.2 % for mPNCe6 Ms respectively with laser irradiation. mPNCe6 Ms without Laser exhibited total apoptosis of 50.6±1.6 %, whereas mPNCe6 Ms with Laser produced total apoptosis of 79.3±1.27% MOC2 cell lines.
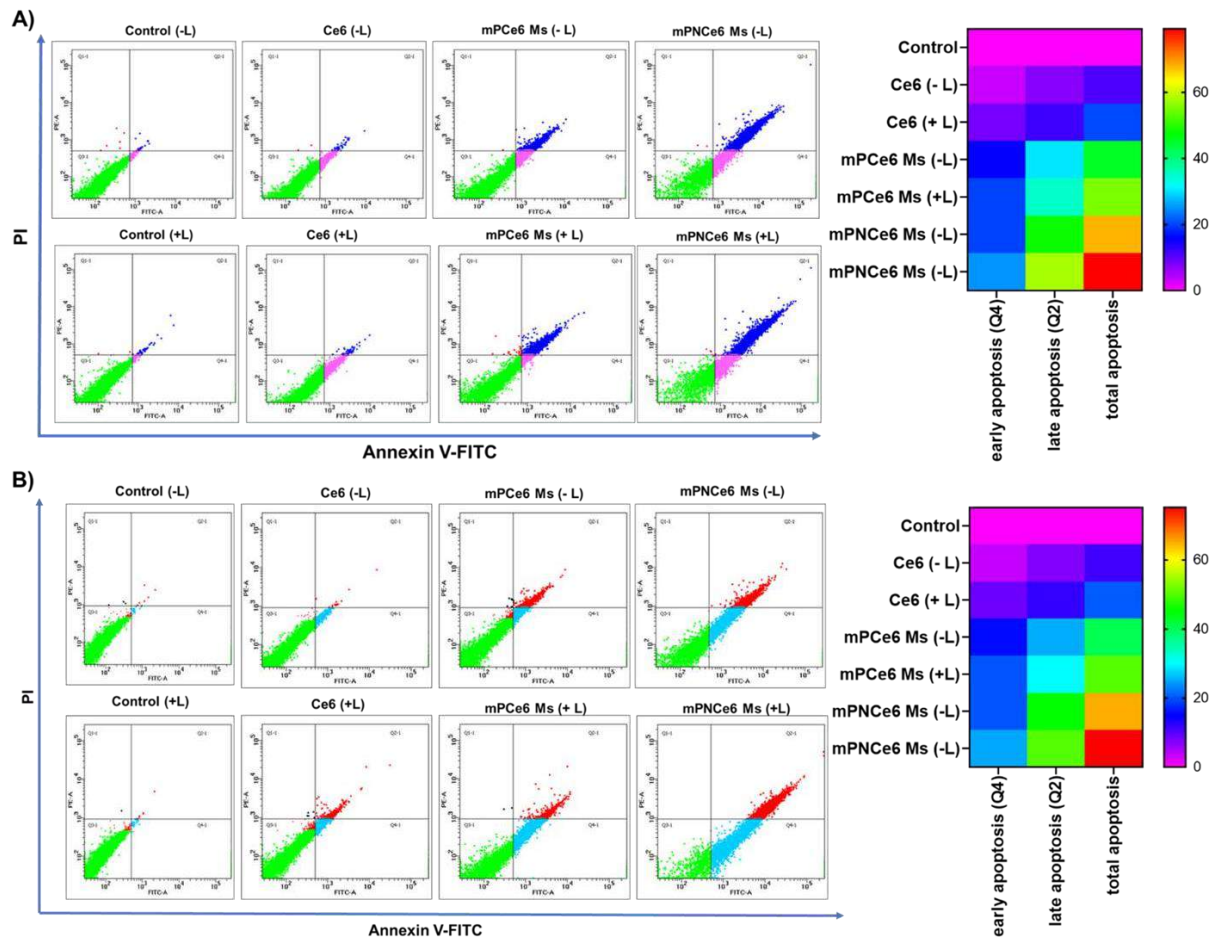
Figure 5.5 Apoptosis assay of cells using Annexin V/PI double staining method. Apoptotic populations of FADU and MOC2 cells after exposure to different formulations: culture medium, culture medium plus NIR irradiation, Ce6 solution, Ce6 solution plus NIR irradiation, mPCe6 Ms, mPCe6 Ms plus NIR irradiation, mPNCe6 Ms, mPNCe6 Ms plus NIR irradiation. Cell counts (%) of necrotic cells (Q1), late apoptotic cells (Q2), early apoptotic cells (Q3), normal cells (Q4), and total apoptotic cells (Q2 & Q3) after different treatments. (A and B).

5.3.6 Cell cycle analysis

The cell cycle analysis plot shows that all formulations have the most arrest in the G2-M phase, consistent with Ce6's mechanism of action, which is to arrest the cell in the early anaphase stage (M- phase). In comparison to free Ce6, mPNCe6 micelles treated FaDu cell lines in the G2-M phase 5 fold more. (Figure 5.11)
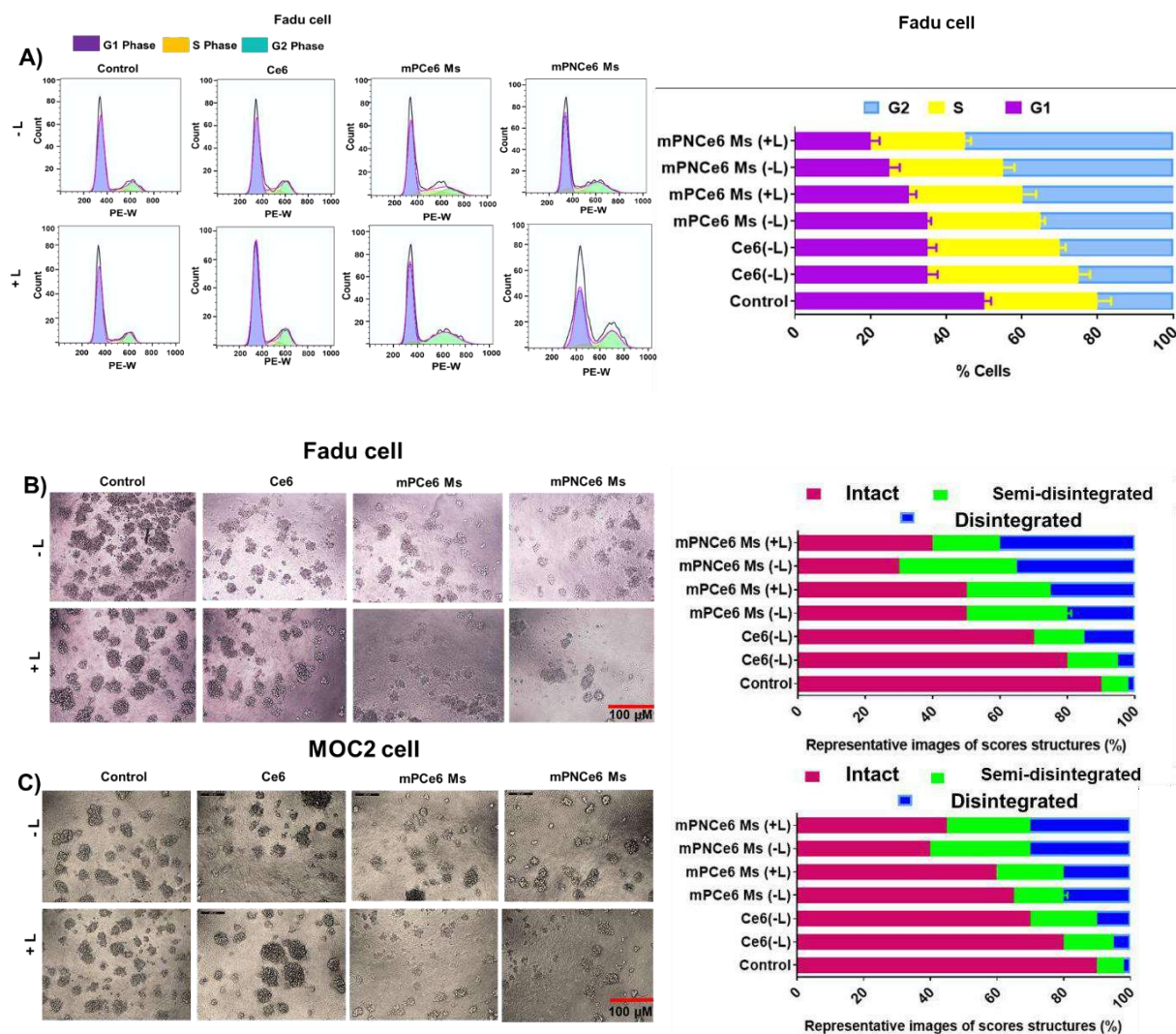
Figure 5.6 Cell cycle analysis of free Ce6 and mPCe6 Ms, mPNCe6 Ms against FADU cell lines.

5.3.7 Mitochondrial membrane potential assay

Intracellular cytotoxic ROS can damage cells' mitochondria, resulting in cell death. Our findings showed that mPNCe6 micelles are an effective drug delivery mechanism for Ce6. In our investigation, the mitochondrial membrane potential of our formulation mPNCe6 micelles treated group showed more severe collapse than mPCe6 and free Ce6. High levels of ROS can osmotically

inflate the mitochondrial matrix and disrupt the mitochondrial permeability transition pore, compromising the integrity of the mitochondrial membrane and causing the mitochondrial transmembrane potential to dissipate fast. The fluorescence images of the cells treated with free Ce6, mPCe6, and mPNCe6 micelles and tagged with JC 1 dye are shown in Figure 5.12. The dye exhibits red fluorescence for control cells, an intermediate between green and red fluorescence for free Ce6, and a bright green fluorescence for mPNCe6 micelles. According to the findings, the treatment of FaDu and MOC2 cells with mPNCe6 micelles resulted in a disruption of mitochondrial membrane potential. Furthermore, mitochondrial dysfunction could be implicated in the mPNCe6 micelles-induced apoptosis process.
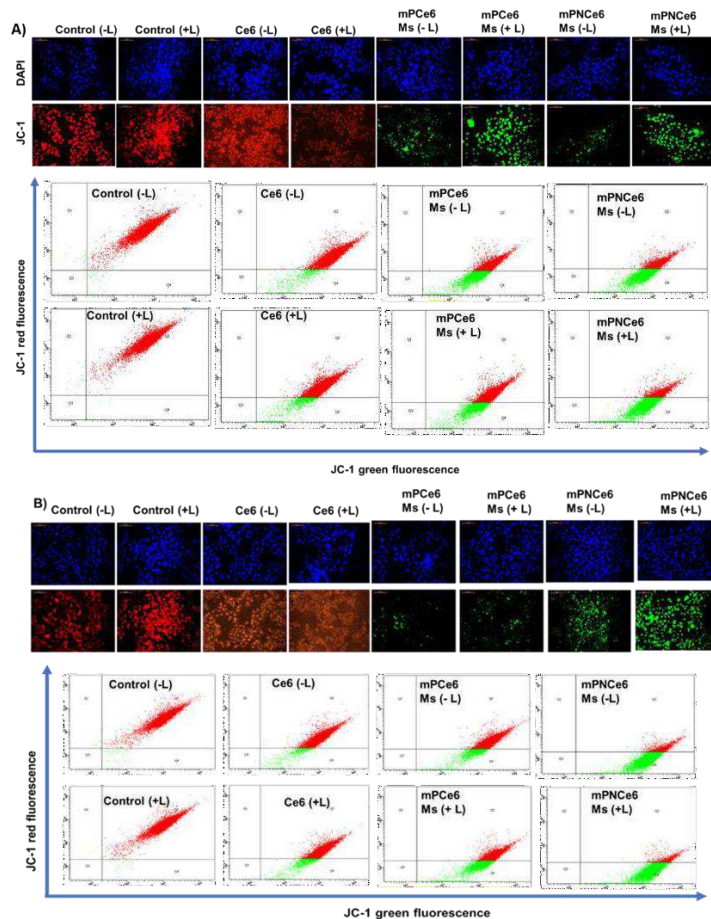
Figure 5.7 Analysis of mitochondrial membrane potential FaDu and MOC2 cells in different groups by fluorescence microscopy and flow cytometry

5.3.8 Reactive oxygen generation assay

Afterward, the ROS generation ability of mPCe6 and mPNCe6 Ms in FaDu HTB-43 cells was measured by a cell-permeable ROS-detecting fluorescent probe DCFH-DA. As shown in Figure 5.13 mPCe6, mPNCe6 Ms the group plus laser irradiation generated abundant ROS inside cells and exhibited strong green fluorescence when compared with other control groups (without Ce6), indicating the efficient delivery of Ce6 by mPNCe6 Ms and its excellent ROS generation ability inside cells upon laser irradiation. Based on the above results, the resulting mPPCPN Ms could enter into cells and generate ROS efficiently upon irradiation and, therefore, will facilitate the inducing of cancer cell apoptosis upon irradiation.
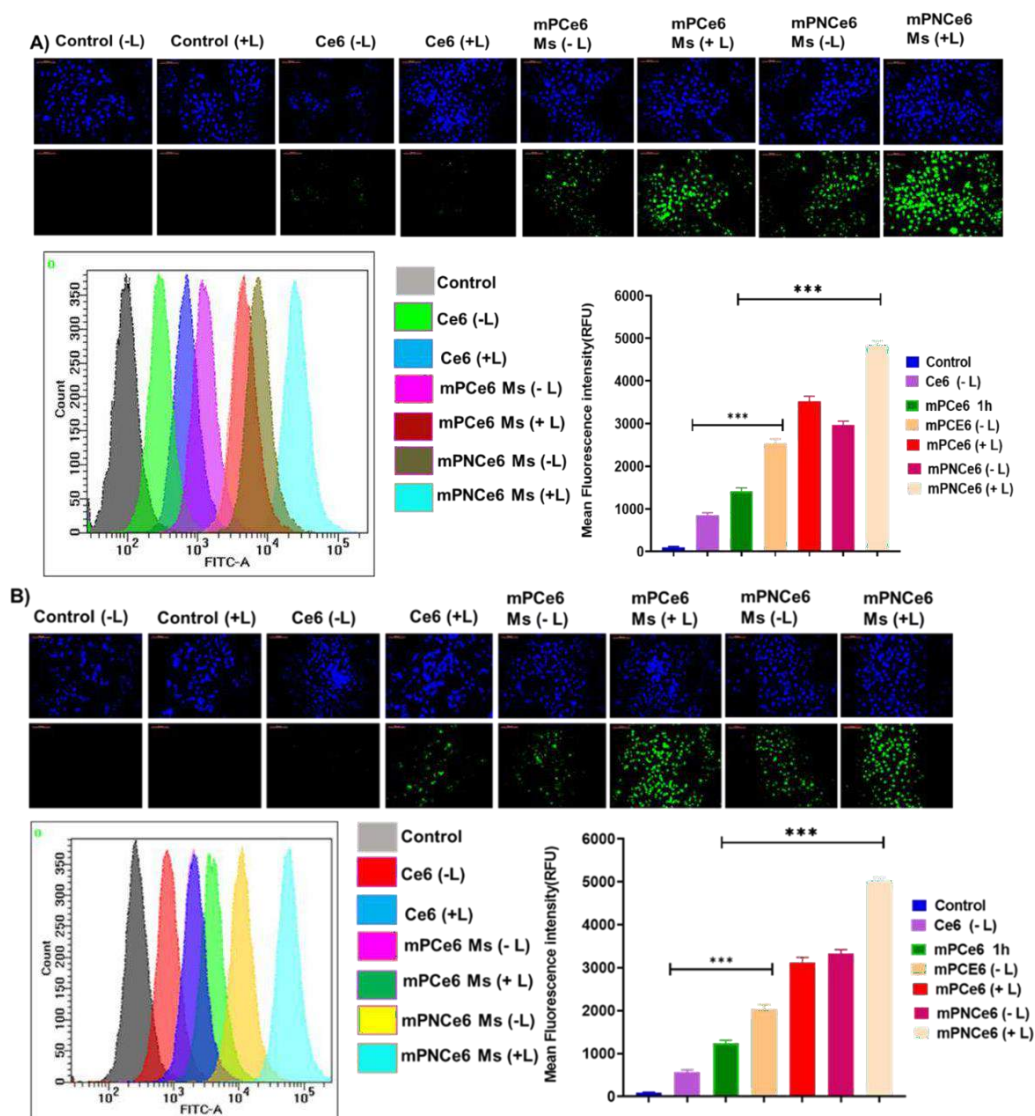
Figure 5.8 Determination of cellular ROS by DCFH-DA assay. Fluorescence microscopic image of FaDu and MOC2 treated cells using free Ce6 and mPCe6, mPNCe6 Ms with/ without Laser a); Fluorescence intensity measurement using flow cytometry (A & B).

5.4. Tumor inhibition assay

Motivated by promising in vitro therapeutic results, we investigated the potential anticancer effects of Ce6 and mPCe6, mPNCe6 Ms in vivo. Intravenous administration of PBS, Ce6, and mPCe6, mPNCe6 Ms was conducted in MOC2 tumor-bearing mice, initially presenting a tumor volume of 70 mm3. Notably, the rapid tumor growth in untreated mice was evident, with the tumor volume in the PBS- treated group reaching 998.6 ± 42.1 mm3 by the end of 21 days, as shown in Figure 9B While both free Ce6 and mPCe6, mPNCe6 Ms exhibited a slight suppression of MOC2 tumor growth within the initial 10 days of treatment, the tumor volume resumed its increase post-Ce6 treatment (reaching 998.4 ± 57.2 mm3 by 21 days) and mPCe6, mPNCe6 Ms treatment (measuring 256.3 ± 23.4 , 160.3 ± 12.4 mm3 at 21 days). Over the treatment period, there was only a marginal increase in mouse body weight, as depicted in Figure 5.14d. The average tumor weights for the control, free Ce6, and mPCe6, mPNCe6 Ms groups were recorded as 3.95 ± 0.21 g, 1.88 ± 0.14 g, and 0.45 ± 0.08 g, 0.20 ± 0.08 g respectively (Figure 5.14 e).
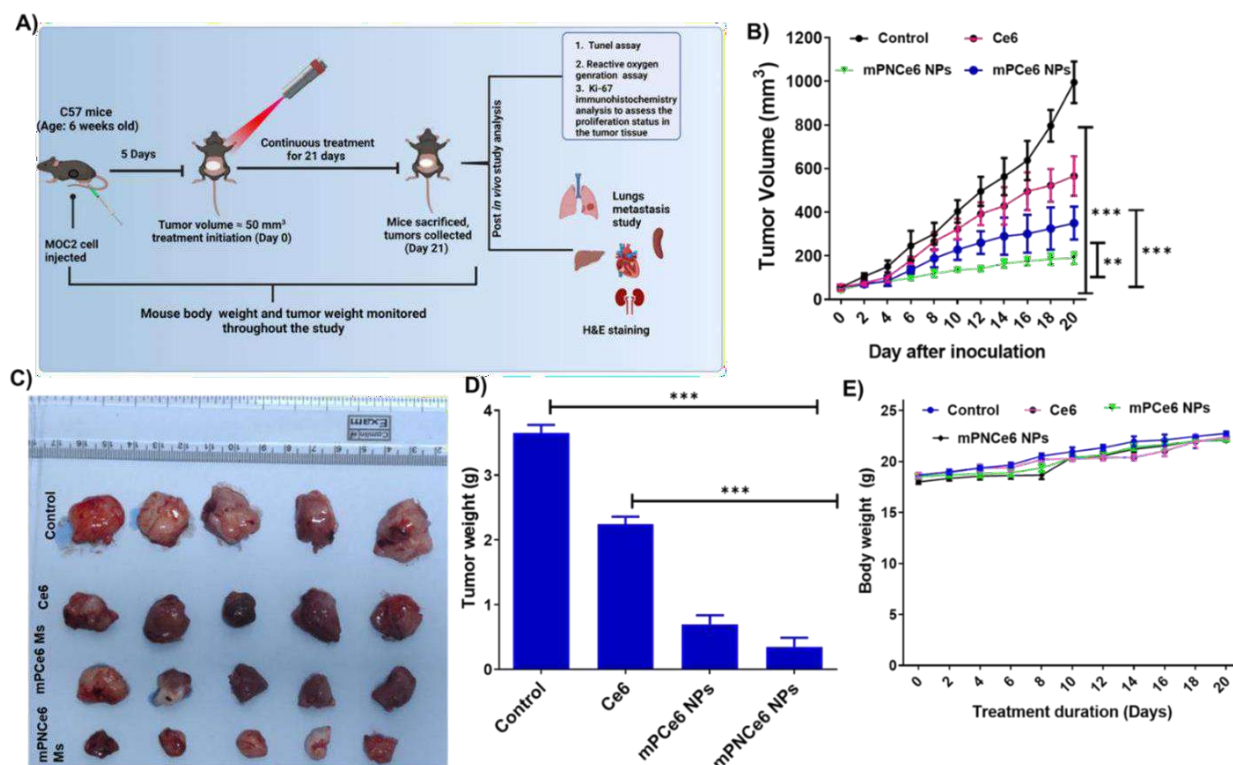
Figure 5.9 Schematic representation of the experimental protocol followed for the in vivo antitumor therapeutic efficacy of free Ce6 and mPCe6, mPNCe6 Ms in the MOC2 cell implanted tumor-bearing mouse model (A); Tumor volume inhibition assay (B); Graphical representation image of MOC2 tumor-bearing mice(C); Tumor weight of B16F10 tumor-bearing mice (D). Body weight of B16F10 tumor-bearing mice (E).

5.4.2 Biodistribution study

Live imaging biodistribution studies on animals revealed a non-specific distribution of mPCe6, mPNCe6 Ms in the excretory organs, which were cleared off more quickly than the Ce6 accumulated in the tumour (Figure 5.15). Ex vivo fluorescence analysis of tumor tissue and dissected organs (heart, liver, spleen, lung, and kidney) at 36 hours after injection further

demonstrated that mPCe6, mPNCe6 Ms significantly increased tumour accumulation compared to free Ce6.
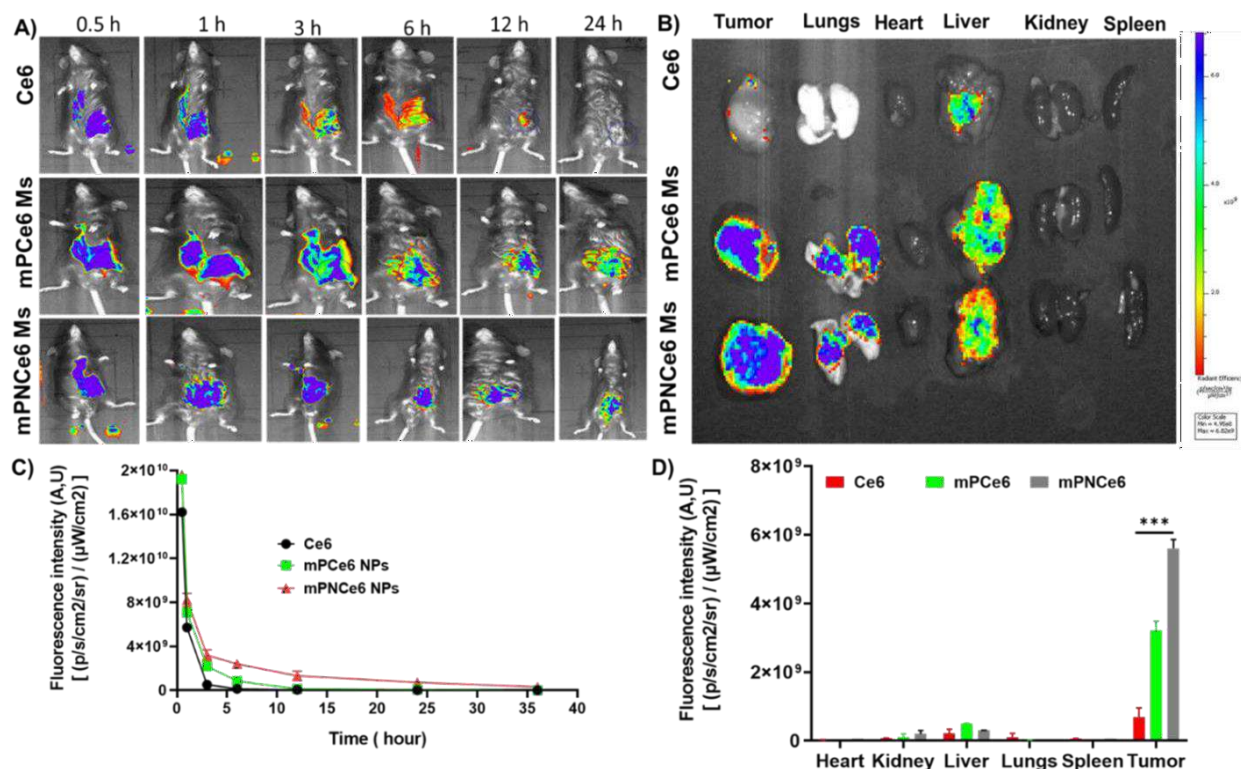
Figure 5.10 In-vivo biodistribution study of MOC2 tumor-bearing mice using Ce6, mPCe6 Ms and mPNCe6 micelles.

5.4.2   Immunohistochemistry

The mice treated with mPNCe6 displayed the most intense green fluorescence when assessed by the DCFH-DA probe, a tool used to gauge oxidative stress level (Figure 5.16 B). Once internalized into cells, the dye undergoes oxidation via intracellular reactive oxygen species (ROS), leading to the creation of 7'-dichlorodihydrofluorescein (DCF) and subsequent emission of green

fluorescence. Chemotherapy and photodynamic treatment (PDT) induce the generation of various reactive oxygen species (ROS), such as superoxide anion, hydrogen peroxide, and hydroxyl radicals, causing damage to cancer cells. The nano formulations triggered a higher production of ROS within tumor tissues compared to administering the unbound Ce6 medication. PDT primarily eradicates cancer cells by significantly increasing ROS production. The study revealed that mPNCe6 demonstrated a four-fold increase in ROS generation compared to all other examined formulations. This therapy heightened oxidative stress, leading to increased apoptosis in cancer cells, evident through the presence of TUNEL-positive cells emitting green fluorescence (Figure 5.16 A). Cells treated with the nanoformulation exhibited higher TUNEL-positive cell expression than those treated with free medicines, with mPNCe6 showing the highest population of apoptotic cells among the nanoformulations. Furthermore, analysis of tumor sections aimed to identify Ki-67 expression, a proliferation marker (Figure 5.16 C). Untreated tumor tissue displayed notably elevated Ki-67 expression, indicating rapid cell division and potential metastatic capacity. Conversely, the formulations exhibited reduced signals, consistent with ROS and TUNEL results, suggesting their ability to generate ROS, induce apoptosis, and suppress cell growth rates. Histological examination of tumor sections after treatment, using H&E staining (refer to Figure xx), revealed no observable damage in major organs like the heart, liver, spleen, lungs, and kidneys across all formulations. H&E staining provided a qualitative safety profile assessment, indicating that the combination nanoformulation did not induce inflammation or immunological reactions. These findings suggest its potential for safe utilization in cancer treatment.
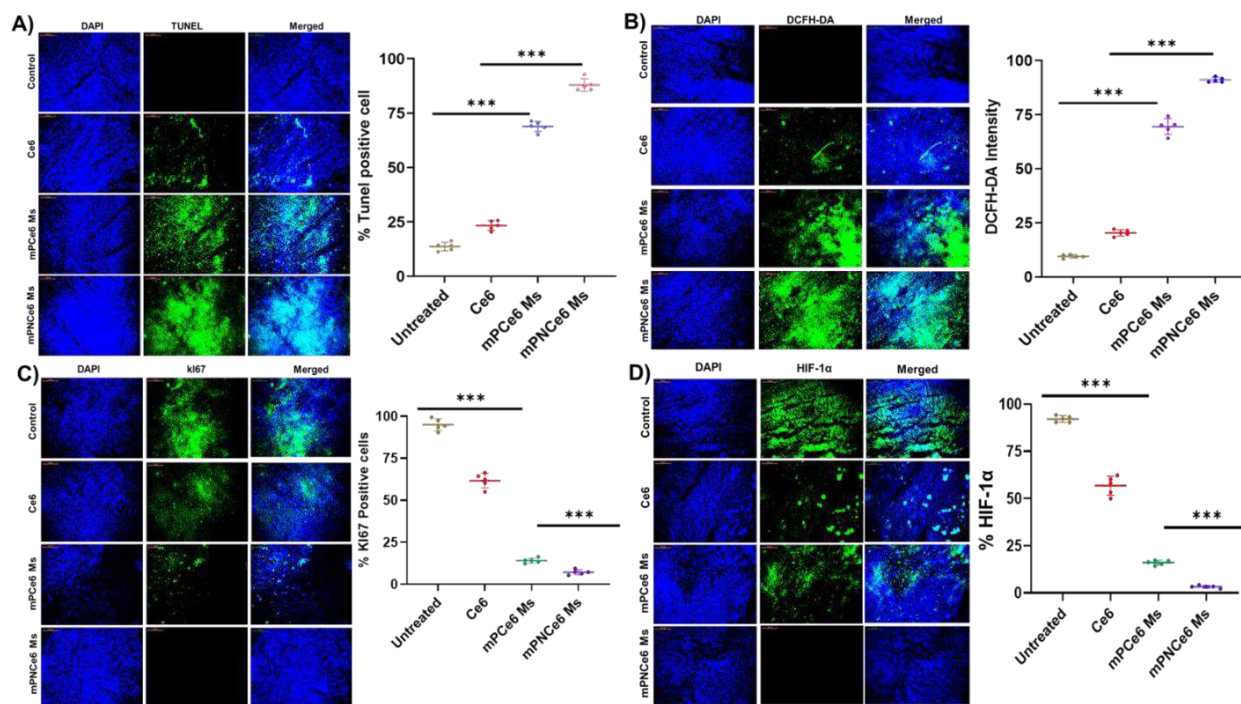
Figure 5.11 Immunohistochemistry analysis. Representative images of TUNEL assay in the tumor sections of isolated tumors (A); Ki67 assay (B); ROS generation assay (C); HIF 1 alpha assay (D).

BrdU, a nucleoside thymidine analog, plays a pivotal role as a marker in the BrdU assay, aiding in identifying proliferating cells. Upon microscopic examination of BrdU-stained lung sections, a significant observation emerged: there was a notably higher count of proliferating endothelial cells in metastasized lungs within the untreated and Ce6-treated groups in contrast to mPCe6, mPNCe6 Ms (Figure 5.18A). This disparity might be attributed to cancer cell entrapment within vessels, leading to the development of metastatic regions in the lungs. Another striking observation in lung tissue was the presence of lung metastasis upon the mice's demise. Subcutaneous injection of approximately 1.5 million melanoma cells induced skin melanoma, resulting in visible melanoma

nodules on the lungs in the control and Ce6 groups, as illustrated in Figure 11A. However, the proliferation of cancer cells on the lungs notably diminished in the treatment groups, as evidenced by the reduced fluorescence intensity observed in the BrdU assay.

Furthermore, there was a discernible reduction in collagen levels in the mPCe6, mPNCe6 -treated group compared to the untreated group. The weights of the lungs were documented as 1.25 ± 0.02 g, 0.55 ± 0.02 g, and 0.28 ± 0.04 g, 0.16 ± 0.04 g in the saline-treated, Ce6, and mPCe6, mPNCe6 groups, respectively. (Figure 5.17 b).
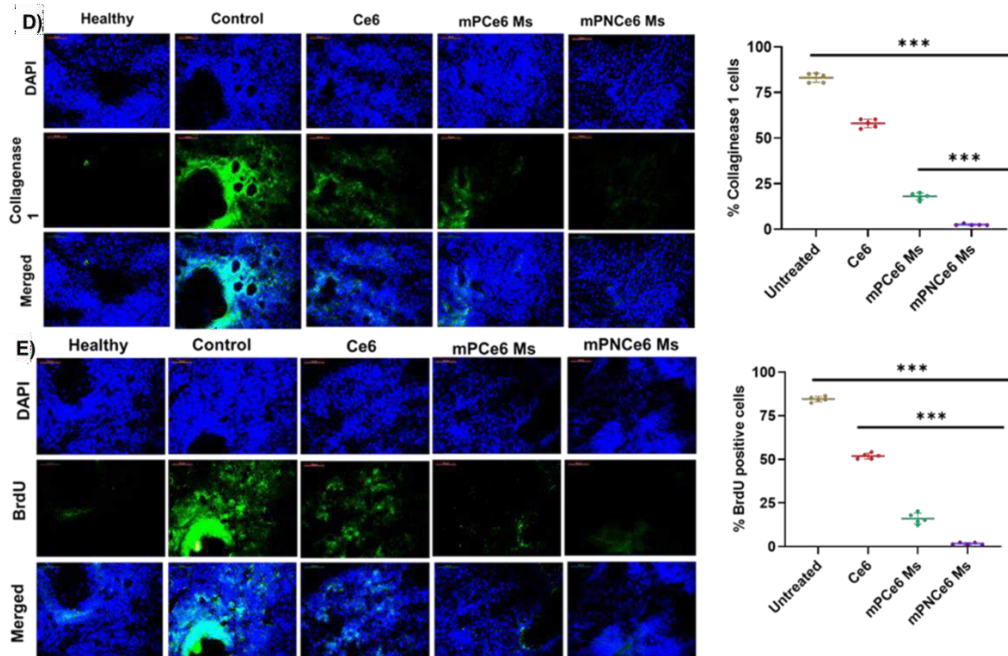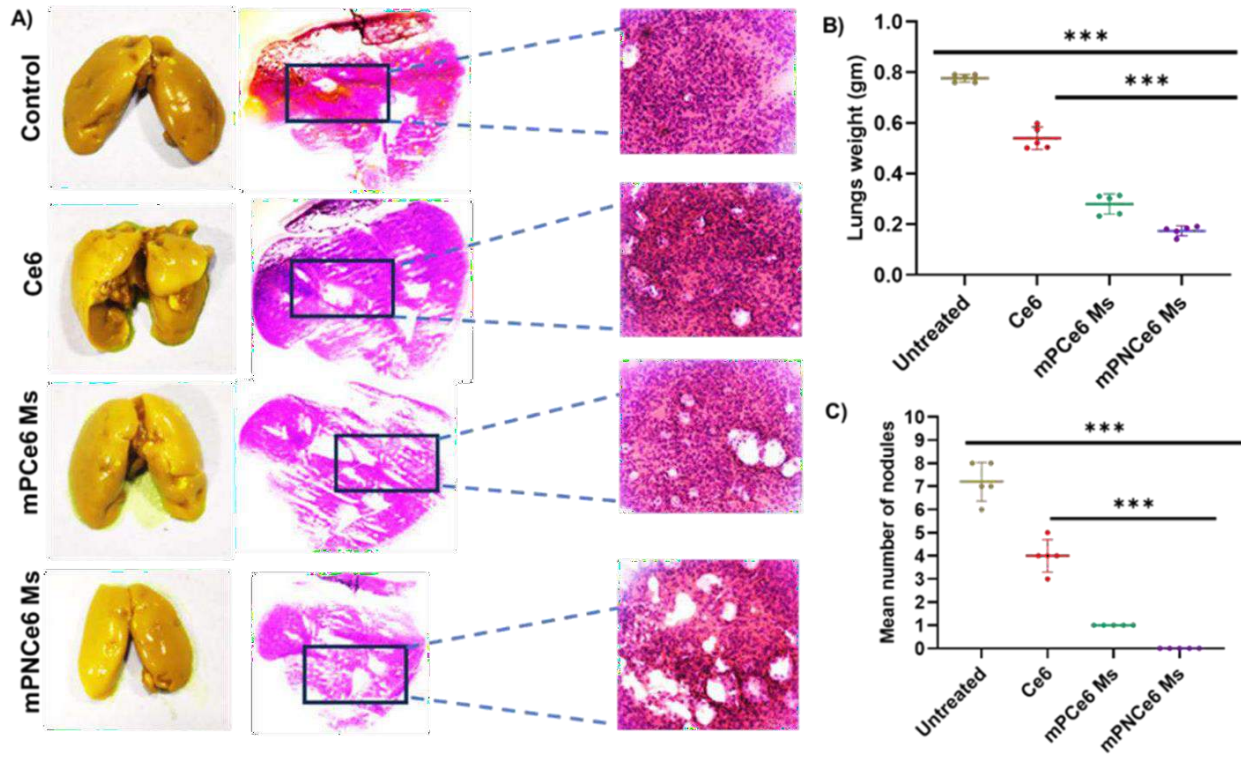
Figure 5.12 Suppression of lung metastasis. H&E staining of the lung section showed more proliferation of cells compared to treatment groups (A); Bar graph of lungs weight and lungs nodules (B &C); The proliferation of the metastatic cells in lung tissue was detected by injecting BrdU into the tail vein, followed by lung resection 2 h and stained with anti-BrdU antibody (D); The section was stained with collagen1 antibody to see the collagen level in the lung (E).

5.4.3 Blood biochemistry

Photodynamic therapy presents itself as a minimally invasive and highly precise treatment approach, overcoming the limitations associated with surgery, radiation, and chemotherapy. To evaluate the safety of our developed photodynamic therapy, we conducted an analysis of various serum biochemical markers, including blood urea nitrogen, creatinine, alkaline phosphatase, alanine aminotransferase, and total proteins, as illustrated in Figure 5.19. Our findings indicate that all measured serum biochemical parameters following treatment remained within normal ranges, affirming the non-toxic nature of the intravenous formulations to the liver and kidneys.
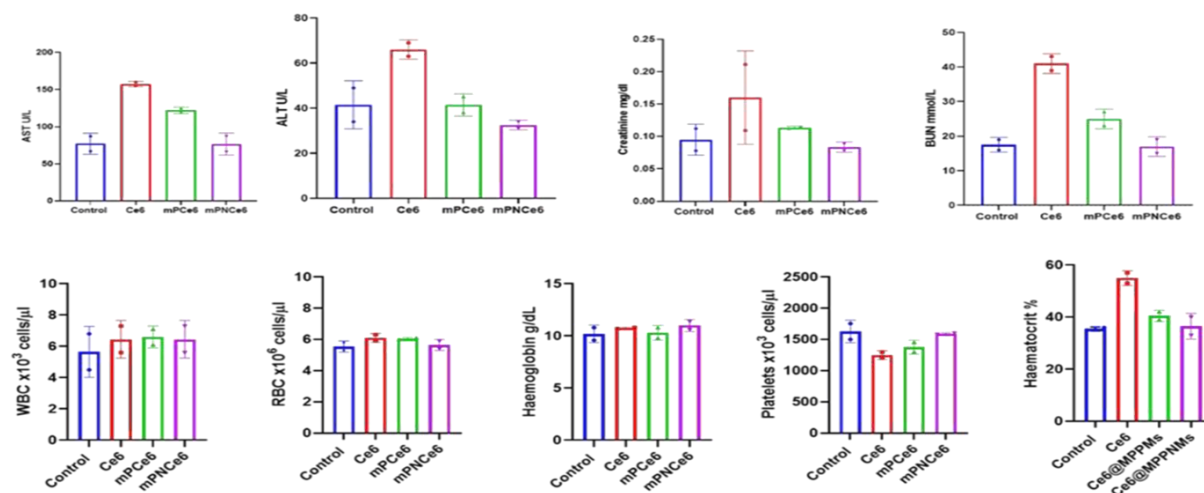
Figure 5.13 Blood biochemistry analysis of Ce6 and Ce6@F127 Ms

5.4 Conclusion

In this case, 2-nitrobenzyl-chlorin e6 (2NB-Ce6) was coupled with methoxy(polyethylene glycol) (mPEG) to create nanomedicine-mediated photodynamic therapy. The conjugated micelles functioned as carriers for Ce6. The polymeric micelles exhibited stability at a temperature of 4 °C, displayed ideal physicochemical properties regarding their spherical size, and had low critical micelles concentrations (CMC). The micelles entered the FaDu and MOC2 cells over time, resulting in a considerably greater cell death than free Ce6 or mPCe6 micelles. The findings revealed that the micelles exhibited a remarkable efficacy in triggering apoptosis, DNA damage, ROS formation, and mitochondrial membrane depolarization, ultimately leading to a greater extent of cellular demise than unbound Ce6. The presence of micelles reduced the rate at which Ce6 was removed from the bloodstream, as compared to when Ce6 was administered in its free form. Furthermore, the micelles' non-toxic nature was confirmed through immunohistochemistry data analysis. Furthermore, the created nano-micelles exhibited minimal penetration and cytotoxicity towards the normal cells. Hence, the utilization of mPNCe6-micelles as a therapeutic approach holds great potential for treating solid tumors, particularly in the context of oral cancer.

Chapter 6

Developing micelles containing a NIR light degradable of Chlorin e6 for the treatment of oral cancer
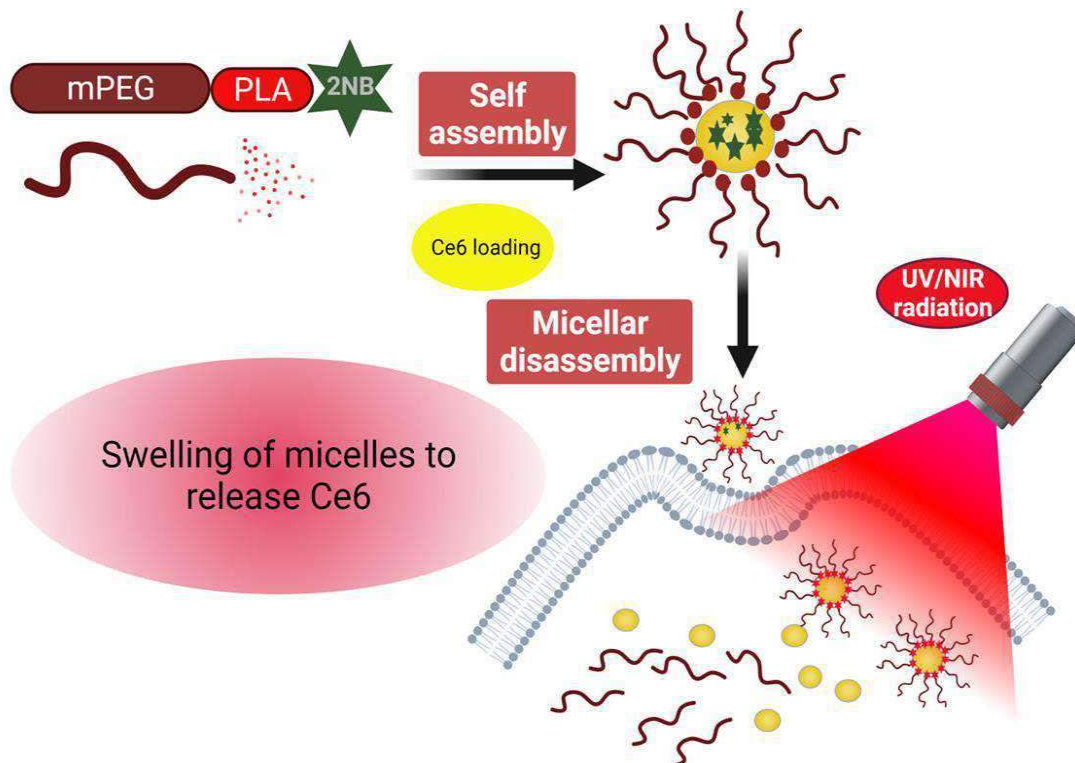
6.1 Introduction

Photodynamic therapy (PDT) has become increasingly prevalent in cancer treatment in recent years. PDT involves using photosensitizers (PSs) that become triggered by specific wavelengths of light, resulting in a sequence of photochemical processes generating phototoxicity. Photons are absorbed by PSs, causing them to transition from the ground singlet state to the excited singlet state. This excited singlet state is then converted to a longer-lasting excited triplet state through inter-system crossing. The excited triplet state undergoes two types of reactions: Type I and Type II. Reaction type I primarily occurs in conditions of low oxygen concentration or in a polar environment. However, it has been shown that Type II reaction is predominant in photodynamic therapy, and singlet oxygen ($1O_2$) is primarily recognized as cytotoxic, leading to cellular damage (Maharjan PS, Bhattarai HK 2022). Despite being highly cytotoxic, photosensitizers (PSs) face several limitations that hinder their successful usage in cancer treatment. These limitations include the hydrophobicity of the porphyrin moieties, restricted tissue penetration, the requirement of a specific wavelength of light source to activate the PSs, the need for the presence of oxygen, and the non-specific localization of photosensitizers to non-tumor tissues (Lan M et al. 2019). In order to overcome these problems, many nano-carrier platforms, including liposomes, polymeric micelles, dendrimers, and self-assembled polymeric nanoparticles, have been studied (Zhao X et al. 2021). Another significant issue in PDT is the reduction of surrounding tumor oxygen due to the quick and ongoing conversion of O_2 to $1O_2$ at high fluence rates (Zhao J, et al. 2020). This can lead to immediate local hypoxia and interfere with the photo-dynamic process, ultimately diminishing the effectiveness of the treatment.

In order to address the difficulties posed by inadequate solubility, limited permeability, and a propensity for aggregation, it is necessary to develop appropriate drug delivery systems. Nano-

drug delivery systems are specifically engineered to enclose pharmaceuticals within their core, enhancing the solubility, stability, and permeability of the drug being carried (Mohapatra S et al. 2018).

Furthermore, appropriately engineered nanocarriers possess the ability to remain in the bloodstream for a longer duration, leading to their eventual concentration in the tumor microenvironment through the Enhanced Permeability and Retention (EPR) effect. A wide range of nanocarrier systems, such as polymeric/lipid-based micelles, liposomes, polymeric nanoparticles, and drug-polymer conjugates, have been investigated for the transportation of Ce6 in cancer treatment (Ding C, Li Z. 2017).

In this study, we have developed drug-loaded polymeric micelles, Ce6@mPPN, by conjugating mPEG- PLA with 2NB followed by drug loading into the polymeric micelles. The purpose of this drug-loaded micelle is to enhance the solubility of Ce6, improve its circulatory stability by minimizing aggregation, selectively accumulate in cancer cells through the EPR effect, and release the drug in a stimuli-sensitive manner inside the cancer cells. This will ultimately enhance the effectiveness of the therapy. mPEG- PLA-2NB will enhance the pharmacokinetic profile of the micelle and also provide extended blood circulatory potential. These drug-loaded polymeric micelles have undergone physicochemical characterization, and their therapeutic efficacy has been assessed in the context of oral cancer.

6.2 Materials and methods

6.2.1 Materials

2-nitrobenzaldehyde, anhydrous N, N-dimethyl formamide (DMF), Sodium borohydride, Methanol, propidium iodide, Paraformaldehyde, and DAPI (4,6-diamidino-2-phenylindole) were procured from Sigma-Aldrich(Mumbai, India). Chlorin e6 (Ce6) was bought from Frontier Scientific, Inc. (USA). Annexin V-FITC Apoptosis Detection Kit was purchased from Invitrogen Co. (USA). Spectra/Por dialysis membranes were procured from Spectrum Laboratories, Inc. (USA). Singlet oxygen sensor green (SOSG) and Calcein Blue AM, Trypan Blue solution were purchased from Thermo Fisher Scientific (USA). Trypan blue solution and Fluoromount-G were purchased from Himedia Laboratories (India).

The Mouse Oral Squamous Cell Carcinoma (MOC2) was acquired from the National Center for Cell Sciences (NCCS) in Pune, India. The FaDu HTB-43 cell line, derived from Hypopharyngeal cancer, was obtained from the American Type Culture Collection (ATCC, USA). The following items were acquired from Himedia Labs (India): Dulbecco's modified Eagle's medium (DMEM), Minimum Essential Medium Eagle (MEM), Penicillin Streptomycin, fetal bovine serum (FBS), and Trypsin- EDTA. The cells were maintained under controlled conditions with a humidity level, temperature of 37°C, and a CO_2 concentration of 5%. C57 mice, weighing between 18 and 20 grams and aged between 4 and 6 weeks, were obtained from the National Centre for Laboratory Animal Sciences, National Institute of Nutrition, Hyderabad, India. These mice were acquired for the specific aim of investigating the effectiveness of anticancer therapies. The pharmacological tests performed received approval from the Institutional Animal Ethics Committee at BITS-Pilani, Hyderabad. The mice were kept in normal mouse/rat cages, with five animals per cage, in a temperature-controlled room that was maintained at 23–24 °C and 50–60% relative humidity. The

animals were subjected to a 12-hour alternating light and dark cycle and given unrestricted availability to food and water.

6.2.2 Preparation and characterization of Ce6@mPPN micelles

6.2.2.1 Synthesis of 2 nitrobenzyl alcohol

The scheme in Figure 2.1 was followed to prepare the NIR-light cleavable amphiphilic polymer. A mixture of 2 nitrobenzaldehyde (500 mg, 3.31 mmol) and sodium borohydride (125.21 mg, 3.31 mmol), was prepared using methanol (5 mL) as a solvent and stirred for 3 h at 0°C to room temperature. After the completion of the reaction, the solvent was evaporated under reduced pressure. The crude reaction mixture was diluted with ethyl acetate (30 mL) and washed with water three times (3×10 mL). (yield: 92 %)

6.2.2.2 Synthesis of 5-(2 nitrophenyl)- 4 oxopentonoic acid

5-(2 nitrophenyl)- 4 oxopentonoic acid was synthesized by dissolving (2 nitrobenzyl alcohol) amount of DMAP in 3 mL of DMF. For the next 20 min, the reaction mixture was agitated. After 20 min, succinic anhydride (1.533 mg; 0.0153 mmol) was added. Then allowed the reaction to proceed for 24 h at room temperature. After 24 h, evaporated the DMF from the reaction mixture and precipitated using cold diethyl ether. (yield: 75 %).

6.2.2.3 Synthesis of mPEG-PLA-2NB

5-(2 nitrophenyl)- 4 oxopentonoic acid (100 mg) was dissolved into the solution of DCC and DMAP in DMF to activate the carboxylic group of 5-(2 nitrophenyl)- 4 oxopentonoic acid . After 3 h, mPEG-PLA was slowly added. The reaction mixture was kept under stirring for 24 h at room temperature. DMF was evaporated using a rotary evaporator. Further, Milli-Q water was added

and dialyzed using a cellulose ester membrane (24 h, 1 KDa). The product was lyophilized to obtain a solid powder with a 79% yield.

6.2.2.4 Preparation of Ce6@mPPN/Ce6@mPP Ms

Polymer conjugate was dissolved in DMF at the concentration of 10.0 mg/mL, and also the Ce6 dissolved in DMF (1 mg/ml) and the organic solvent was removed by a rotary evaporator. The polymer film was hydrated in PBS 7.4 (500 µL) and stirred at 5 h at 37 ˚C. The micellar solution was centrifuged (13,000 RPM, 20 min, 4 ˚C) and filteredthrough a 0.45 µm filter to remove the un-encapsulated Ce6.

6.2.3   Physiochemical Characterization of Ce6@mPPN/Ce6@mPP micelles

6.2.3.1 Particle Size and Zeta Potential

The samples were diluted using deionized water and then transferred into a cuvette with a diameter of 10mm at a temperature of 25 °C. The particle size and zeta potential of Ce6@mPPN micelles were assessed using dynamic light scattering with a Zetasizer™ ZEN 3600 instrument (Malvern Instruments Ltd., UK). An analysis was conducted on the samples to determine their particle size and zeta potential.

6.2.3.2 Critical Micellar Concentration

The critical micelle concentration of the micelles Ce6@mPPN Ms, and Ce6@mPP Ms was determined using pyrene as the hydrophobic probe and a microplate reader (SpectramaxTM, Molecular Devices, USA). The excitation wavelength of the solution was set to an excitation wavelength of 339 nm and a slit width of 5 nm for both excitation and emission. Pyrene solution (50 µL; 10 mg/mL in chloroform) was combined with a micellar solution at concentrations ranging from 3.125 to 100 g/mL. The graph was plotted using log concentrations of Ce6@mPPN micelles

and the fluorescence intensities at ratios of I338/I390 at the X and Y axis, respectively (Li J et al. 2018) (Tseng TH et al. 2021) (Deng K et al. 2021).

6.2.3.3 Scanning transmission electron microscope (STEM)

Field Emission Scanning Electron Microscopy was used to examine the surface morphology of Ce6@mPPN Ms, Ce6@mPP Ms. A thin layer of nanoparticles was uniformly distributed over an adhesive carbon tape connected to aluminum stubs to prepare the sample. Further, nitrogen purging was done, and the stubs were sputter-coated with gold in the desired thicknesses and examined at 20 kV. Transmission electron microscopy was used to investigate the micelles ' morphology (TEM, JEM- 1200EX, JEOL, and Tokyo, Japan).

6.2.3.4 Storage Stability

The stability of Ce6@mPPN Ms, and Ce6@mPP Ms was tested at 4°C. Before measuring particle size, the NPs were examined for stability in physiological conditions by incubating them for 72 hours at 37°C in a DMEM medium containing 10% FBS. The formulations in DMEM (10 L) were diluted with 1.5 mL MilliQ water, and particle size and zeta potential were measured using a Malvern zeta sizer (Huang X et al. 2021).

6.2.3.5 X-ray diffraction

For powder X-ray diffraction (XRD) investigation, Ce6@mPPN micelles were used. Employing an X- ray diffractometer of the ULTIMA-IV model, manufactured by Rigaku. The device utilized a copper anode of 1.54 millimeters in diameter, operating at a voltage of 40 kilovolts and a current of 30 mA. The scanning angle was set at 2 from 5° to 100°, at a rate of 5° per minute.

6.2.3.6 Differential scanning calorimetry (DSC)

The thermo-analytical characterization of Ce6 and Ce6@mPPN was undertaken using a Differential Scanning Calorimeter (DSC 60, Shimadzu, Japan) and a thermogravimetric analyzer. The analysis was performed in a nitrogen environment, with a heating rate of 10 °C/min, ranging from 25 to 800 °C (Cheng L et al. 2016).

6.2.3.7 Singlet Oxygen Generation (SOG)

The singlet oxygen generation by Ce6@mPPN Ms, Ce6@mPP Ms in distilled water was also measured using a green singlet oxygen sensor (SOSG) as described previously. 2.5 mM SOSG was combined with Ce6@mPPN Ms, Ce6@mPP Ms in a quick experiment. A 633 nm laser source was used to irradiate the mixture. The sample was irradiated, which produced $1O_2$, which interacted with SOSG to produce SOSG endoperoxide (SOSG-EP). A fluorescence spectrophotometer was used to measure the Fluorescence of SOSGEP (Ex. 510 nm; Em. 525–536 nm) (Wu L et al. 2016).

6.2.3.8 In vitro drug release studies

The dialysis bag method was used to investigate in-vitro Ce6 release from Ce6@mPPN/ Ce6@mPP micelles at 37 °C in PBS pH-7.4. ITheialysis bags with MW 3.5 kDa have three distinct ratios of Ce6@mPPN Ms, Ce6@mPP Ms at a concentration Ce6 of 100 µg/ml were inserted. The bags were placed in a beaker with PBS, pH 7.4, at 37 °C with continual stirring at 300 rpm. 1 mL of aliquots from the outer phase were taken at predefined intervals and replaced with 1 mL of fresh PBS. A UV–Visible spectrophotometer set to 480 nm was used to calculate the amount of released Ce6.

6.2.3.9 Hemolysis assay

5 mL of rat blood was collected using heparinized tubes. The blood was subjected to centrifugation at 3000 rpm for 30 minutes at a temperature of 4 °C in order to separate the red blood cells (RBCs). Following a comprehensive washing process, the liquid portion containing unwanted substances was eliminated, and the cells were reintroduced into a solution by diluting with PBS, resulting in a 5 percent volume-to-volume suspension. During the subsequent stage, a 5 percent volume/volume red blood cell (RBC) solution was subjected to incubation. The RBC solution utilized PBS as the negative control and Triton-X 100 (1 percent solution) as the positive control. After the incubation period, all samples were subjected to centrifugation at a speed of 7000 revolutions per minute for a duration of 20 minutes. The amount of hemoglobin (Hb) in the supernatant was measured using a Spectramax microplate reader from Molecular Devices, USA. The % hemolysis of the formulation was then calculated using the formula

$$Hemolysis\,(\%) = AbSample - Ab\,(-)Control\,/Ab(+)Control - Ab\,(-)Control\,X100$$

where: Abs sample is the absorbance of the sample Abs -ve is the absorbance of negative control Abs +ve is the absorbance of positive control

6.2.4 Cell-based study

6.2.4.1 Time-dependent Ce6 uptake

FaDu and MOC2 cell lines were grown in 12-well tissue culture plates on coverslips at a density of 50,000 cells per well. The cells were exposed to both free Ce6 and Ce6@mPPN/ Ce6@mPP micelles containing 6 µg/mL of Ce6 for 1-4 hours. Subsequently, they were washed with PBS, stained with DAPI, and fixed using a 4% paraformaldehyde solution. Affixing the cells to glass slides with Fluoromount G allowed for their examination under a confocal microscope. The cells

were transferred to a 6-well plate at a seeding density of 0.5X106 cells per well for flow cytometry experiments. The next day, the cells underwent the same treatment as in the confocal microscopy analysis. Post-treatment, the cells were washed with PBS, detached using trypsin, centrifuged, rewashed, and finally suspended in PBS with a pH of 7.4. Cellular internalization was evaluated by measuring the Fluorescence emitted by 10,000 live cells using an Amnis Flowsight flow cytometer (EMD Millipore, USA). The resulting data was analyzed using IDEAS software.

6.2.4.2 Phototoxicity study

An in vitro phototoxicity assessment was carried out using free Ce6, Ce6@mPP, and Ce6@mPPN micelles on FaDu and MOC2 cells. A seeding of 5 x 10^4 cells per well was done in 96-well plates for cell adhesion, followed by an overnight incubation at 37°C. Post-washing the cells in PBS, 100 µL of free Ce6, Ce6@mPP, and Ce6@mPPN micelles were added to each well and incubated for 12 hours. After this incubation, the cells were exposed to a 660 nm laser with a power of 0.5 W/cm2 for 2 minutes. Following laser exposure, the cells were placed in darkness and further incubated for 12 hours at 37°C. Removal of growth material was followed by the introduction of 50 µl of 5 mg/mL MTT in serum/phenol red-free medium into each well. After a 3-hour incubation, 150 µl of DMSO was added to dissolve the purple formazan crystals produced by the reduction of MTT by viable cell mitochondria. Absorbance at 570 nm was measured and background absorbance at 630 nm was subtracted. Cell viability percentage was calculated using the equation: Cell viability (%) = (Sample Absorbance) / (Control Absorbance) ×100. (Kumari P et al. 2020).

6.2.4.3 Annexin V Assay

FaDu and MOC2 cells were cultured overnight in a 12-well plate. Exposure to free Ce6, Ce6@mPP, and Ce6@mPPN micelles at a concentration of 6 µg/mL of Ce6 followed. After an 18-hour incubation, cells were washed with PBS (pH 7.4) and centrifuged to form a cell pellet. This

pellet was suspended in 100 µl of binding buffer and treated with 1 µl of Annexin-V FITC and 10 µl of PI according to the TACS® Annexin V-FITC Apoptosis Detection Kit instructions. Following a 15-minute incubation, binding buffer was added to both test and control tubes. Cell analysis was performed via flow cytometry (Flowsight Amnis, Millipore, USA), gating a total of 10,000 viable cells.

6.2.4.4 Cell cycle

Cells were seeded at 0.5×10^6 cells/well density and treated overnight with Free Ce6, Ce6@mPP, and Ce6@mPPN micelles at a 6 µg/mL concentration. Post-treatment, trypsin was used to harvest the cells, and the resulting cell pellet was washed with ice-cold PBS before immersion in 70% ethanol with gentle stirring. These samples were then kept overnight at 20°C. On the subsequent day, the repaired cells underwent centrifugation at 1000 revolutions per minute for 7 minutes at 4°C. Following this, a staining solution consisting of 20% w/v RNAase, 2% w/v PI, and 0.1% v/v Triton X-100 in pH 7.4 PBS was added to the cells. After a 30-minute incubation in the absence of light at room temperature, flow cytometry (BDAriaTMIII) was used for examination. A scatter plot illustrating the relationship between PI width and area was generated alongside a histogram displaying the distribution of PI area, where the X-axis represented the area and the Y-axis indicated frequency counts.

6.2.4.5 Mitochondria membrane potential

In this particular experiment, FaDu and MOC2 cells were seeded in full medium on 6-well assay plates at a density of 1×10^5 cells per well. These cells encountered Free Ce6, Ce6@mPP, and Ce6@mPPN micelles with a concentration of 10 µM Ce6 and were subsequently incubated for 24 hours at 37°C. Following this, the cells underwent cold PBS washing and a 30-minute staining procedure within a CO2 incubator using a 2 M concentration of 5 ,250′4, 6 , 6 ′ - Tetrachloro-

1,1′,3,3′ tetraethyl benzimidazole carbocyanine iodide (JC1 dye). The cells were then observed under fluorescence microscopy, specifically at wavelengths of 530 nm for green Fluorescence and 630 nm for red Fluorescence. The colocalization of green and red signals was represented by the appearance of a yellow signal, identified through image processing using Image J software.

6.2.5 In vivo studies

6.2.5.1 In vivo tumor inhibition study

Male C57BL/6J mice, weighing between 18 and 20 grams, were sourced from the National Institute of Nutrition (NIN) in Hyderabad, India, for this study. They were housed in a temperature-controlled environment with a 12-hour light-dark cycle, maintaining a temperature range of 19-23°C and relative humidity between 50-60%. Prior to the experiment, a week-long acclimatization period was allotted for the mice to adjust to these conditions, ensuring their comfort. The animals had free access to water and food throughout the study.

Ethical approval for the experimental procedures was obtained from the institute's Animal Ethics Committee. The mouse oral cancer model was established by subcutaneously injecting xx cells into the right hind leg of each mouse at a cell density of 1×10^6 cells per 100μL of sterile phosphate-buffered saline (pH 7.4). Tumor inhibition studies commenced when the tumor volume reached approximately 75 mm3.

For the experiment, mice were randomly allocated into four groups: control (saline), Ce6, Ce6@mPP, and Ce6@mPPN, each comprising five mice. Post intravenous tail injection of the drug/formulations at a dosage of 5 mg/kg, each mouse underwent laser irradiation. The utilized Laser emitted light at a wavelength of 660 nm with a power density of 0.5 W/cm2, lasting 5 minutes and administered 12 hours after injection. Throughout 21 days, the mice's tumor volume

and body weight were methodically monitored every other day. At the study's conclusion, euthanasia was conducted via cervical dislocation. The tumor mass was surgically removed and weighed for measurement (Liang H et al. 2018).

6.2.5.1 Immunohistochemistry

The excised tumor tissues were preserved in an optimal cutting temperature medium and frozen. Tissue sections, 5 μm thick, were prepared using a cryotome (Leica CM1950, Leica Biosystems, Germany). These sections were analyzed under a fluorescence microscope to assess the expression of cancer extracellular matrix (ECM) proteins, including TUNEL, Ki-67, and ROS (Chang MH et al. 2018).

6.2.5.2 Detection of KI67 and Tunel assay

For Ki-67 assessment, tumor sections were fixed in methanol, blocked in 3% BSA, and incubated overnight with the Ki-67 primary antibody (Rabbit mAb # A21861) at 4°C. After PBS washing, sections were incubated with the secondary antibody Alexa Fluor® 488, followed by DAPI staining. The sections were observed using a fluorescence microscope.

The TUNEL assay (Click-iT™ Plus TUNEL Assay Kits for In Situ Apoptosis Detection Kit, ThermoFisher) followed the manufacturer's protocol. The tumor tissues underwent specific treatments and staining before observation under a fluorescence microscope (Hu C et al. 2020).

6.2.5.3 ROS generation in tumor tissue

In B16F10 tumor-bearing mice, Ce6, Ce6@mPP, and Ce6@mPPN Ms were intravenously injected, followed by laser application and DCFH-DA injection. After euthanasia, tumor tissues were collected, embedded in OCT media, cryo-sectioned, and examined under a fluorescence microscope to detect ROS.

6.2.5.4 Lung metastasis - BrdU assay, collagen1A1 and H&E in lung tissue

For BrdU assay in identifying proliferating cells, specific procedures were followed using BrdU solution and immunostaining techniques. Collagen I and H&E staining were also performed on lung tissue sections to analyze metastasis and tissue structure (Chibh S et al. 2020).

6.2.5.5 Potential toxicity assessment of Ce6, Ce6@mPP, and Ce6@mPPN

Systemic toxicity assessment of Ce6, Ce6@mPP, and Ce6@mPPN Ms was conducted through hematological and serum analyses. Blood samples were collected for various studies, and histological evaluations of tissues were performed to assess potential toxicity effects.

6.3 Statistics

The aforementioned tests were conducted in triplicate, and the results are shown as the mean value and standard deviation (mean ± SD). The statistical significance of the differences between all the groups was assessed using one-way analysis of variance (ANOVA) with GraphPad Prism software (GraphPad, Inc., California, USA). The p-values below 0.05 indicate statistical significance. *, **, and *** represent p-values that are less than 0.05, 0.01, and 0.001, respectively.

6.4 Results and Discussion

6.4.1 Synthesis and characterization of the polymers

The di block polymeric conjugate was successfully synthesized by conjugating 2NB to mPP by esterification reaction in Figure 6.1. The findings are evident that the conjugation of 2NB to mPP was verified by 1H NMR and FT-IR. In 1H NMR spectrum peak at 5.1 ppm represents the O2-attached secondary proton of the mPP. Peaks at 1.51 &1.96 ppm represent methylene protons of the NB in mPP- NB (Figure 6.2 A&B). In the IR spectrum, the presence of a peak at 1749.13 cm-1 indicated successful conjugation between mPP and NB. The other peaks representative of mPEG

-CH2 peak at 1464.67 cm- 1 NB aromatic -OH peak at 3426.89 cm-1, and acid -OH peak at 2885.95 cm-1 were seen in the spectrum (Figure 6.2B). The quantification of NB in mPP was also determined. This confirms the successful conjugation of nitrobenzyl to mPP. A sharp increase in pyrene fluorescence intensity was observed at 40 µg/mL of mPP-RA (Figure 6.2C). Similarly, a similar sharp decrease in the surface tension of mPP- NB was observed at 40 µg/mL (Figure 6.2C).
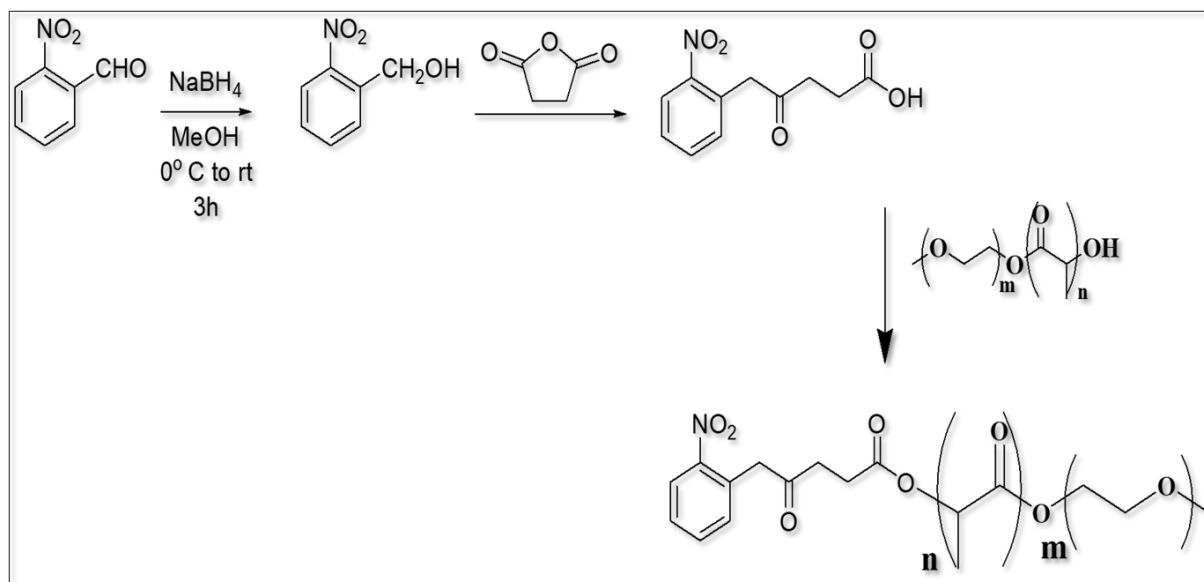
Figure 6.1 Synthetic route of mPEG-PLA-2NB conjugate preparation.

Moreover, the 1H NMR spectra of 2 nitrobenzyl alcohol are shown in Figure 6.2
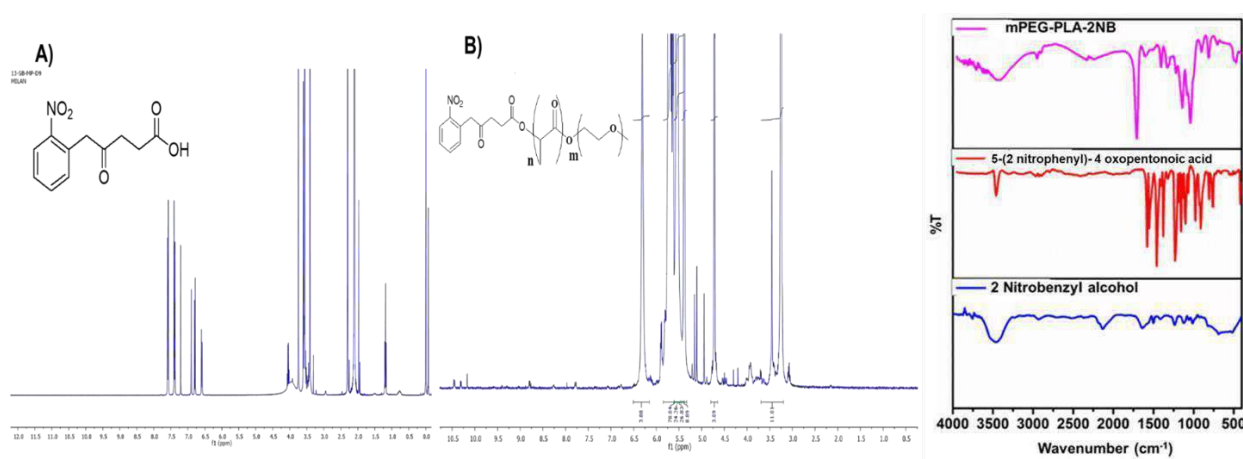
Figure 6.2 1H NMR spectra and FTIR spectra of 2NB and mPEG-PLA-2NB

6.4.2 Preparation and characterization of the formulation

The micelles synthesized underwent thorough characterization through particle size analysis, zeta potential measurements, differential scanning calorimetry (DSC), and X-ray diffraction spectroscopy (XRD). The sizes of Ce6@mPP and Ce6@mPPN Ms were measured at 127.85 ± 2.42 nm and 147.85 ± 2.52 nm, respectively, with detailed distribution curves depicted in Figure 6.2A from Malvern zeta sizer analysis. SEM images showcased in Figure 6.2B aligned with the dynamic light scattering (DLS) data for Ce6@mPP and Ce6@mPPN Ms, demonstrating a narrow polydispersity index of 0.12–0.14 and a negative zeta potential. The Ce6 loading in the micelles ranged between 10.91% and 12.36%, with Ce6@mPPN Ms showing an encapsulation efficiency of 82.5%. DSC thermograms (Figure 6.2C) indicated distinct endothermic peaks at varying temperatures for free Ce6, Ce6@mPP, and Ce6@mPPN Ms, ranging from 60.35 to 247.89 oC, highlighting their different thermal characteristics. Wide-angle X-ray powder diffraction was utilized to study the crystal properties of Ce6@mPPN Ms and better understand the interaction between mPEG-2NB conjugate. Stability testing data (Figure 6.2D and E) over 30 days at 4 °C showed minimal changes in particle size and drug loading, whereas room temperature conditions led to increased particle size and reduced drug loading. Ce6 release behavior from Ce6@mPPN Ms was observed at different pH values (pH 7.4, 6.5, and 5) using the dialysis method, showing less than 50% release after 60 hours at pH 7.4. However, at lower pH levels, a significant increase in Ce6 release was noted, with a total release of 78.41% at pH 5.5 over 60 hours. This pH-dependent release behavior indicated substantial potential for controlled release under varying physiological conditions.

Moreover, hemolysis tests conducted with RBCs treated with micelle solutions (0 to 6 mg/mL polymer concentrations) exhibited a low percentage of hemolysis (around 2.32%), confirming the

polymer's non- hemolytic nature (Figure 6.2H). These observations underscored the biocompatibility and stability of the synthesized micelles in various conditions and their potential as controlled-release delivery systems.
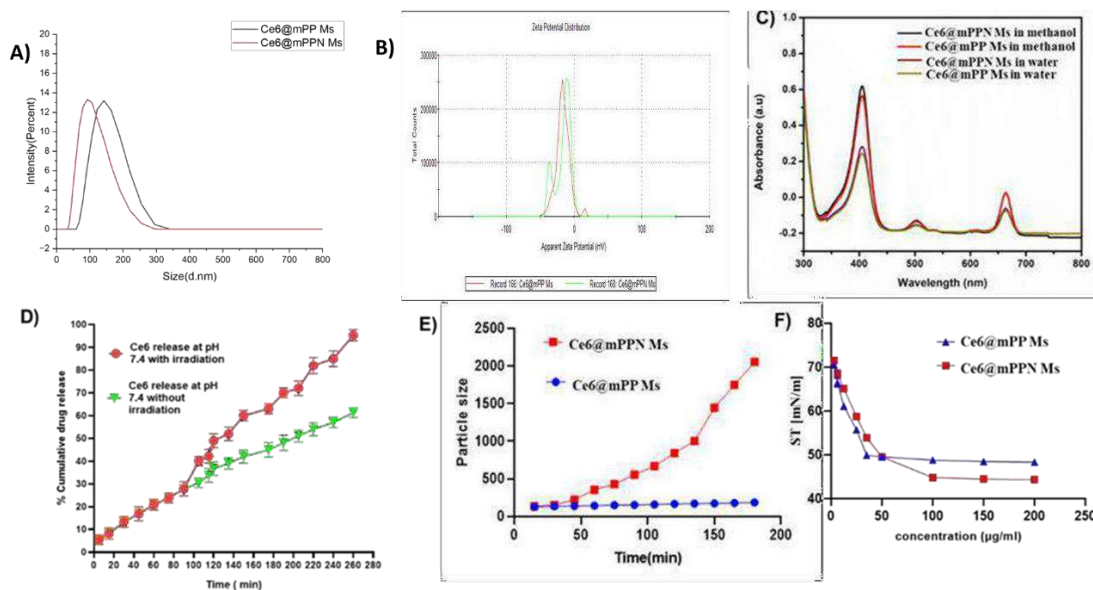
Figure 6.3 Characterization of Ce6@mPPN Ms. Size distribution a) ; Zeta-potential b) ; Uv spectra of two different micelles c) : drug release of micelles using UV/Vis absorbance spectra d); particles size with laser e); surface tension analysis f).
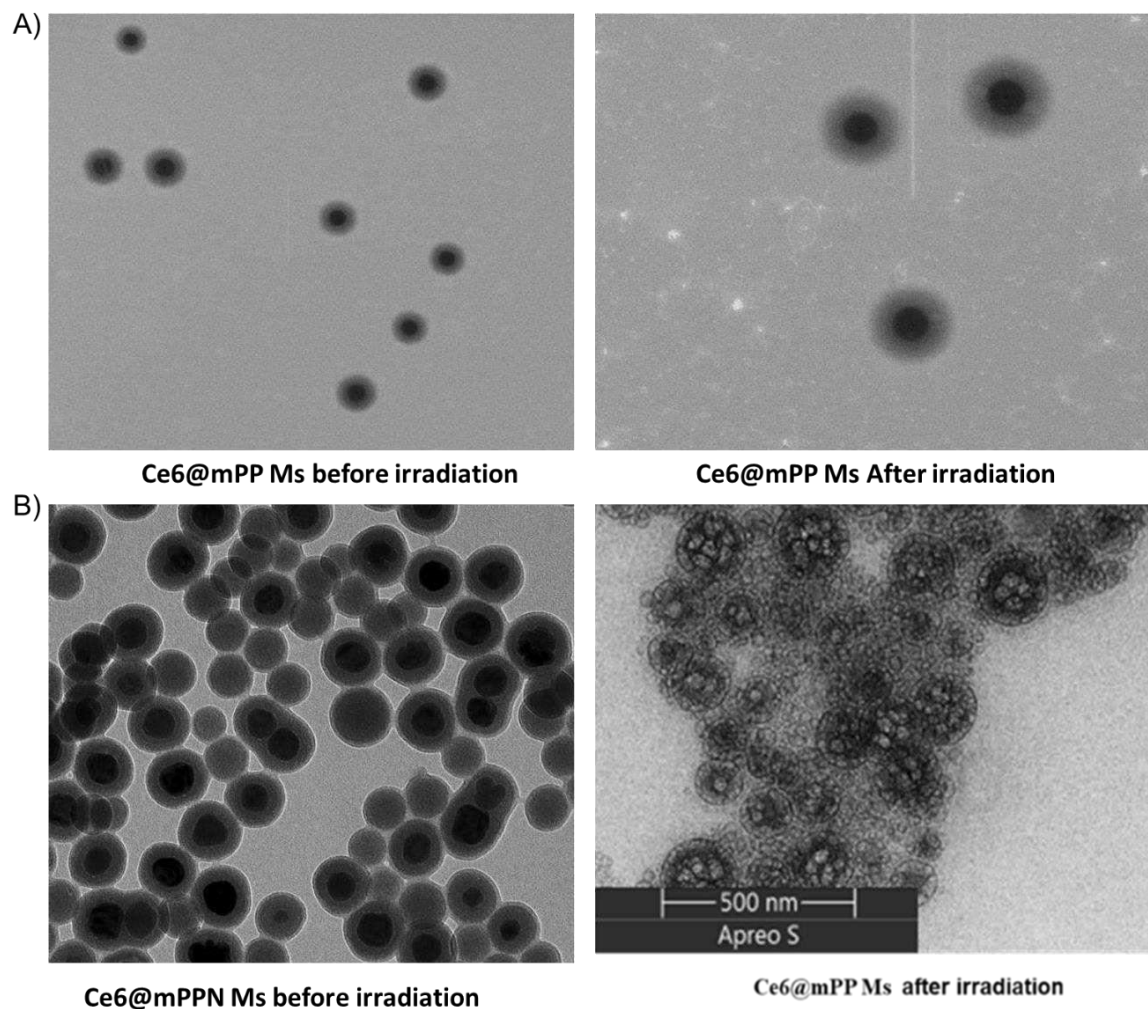
Figure 6.4 STEM image of Ce6@mPP, and Ce6@mPPN Ms

6.4.3 Cellular Uptake Study of Ce6@mPPN Ms

Cellular uptake was thoroughly examined both qualitatively and quantitatively using confocal microscopy. The fluorescence images revealed heightened Ce6 fluorescence within the cytoplasm and nuclei when exposed to NIR light at different time intervals. This observation suggested swift

internalization of the micelle formulation and rapid Ce6 release within the intracellular environment.

Notably, a substantial increase in bright red Fluorescence was observed in groups treated with free Ce6, Ce6@mPPN Ms, and Ce6@mPP Ms along with laser application (660 nm, 0.5 W/cm2) over 1 to 4 hours, indicating a time-dependent uptake by MOC2 and FaDu cells.Furthermore, Figure 6.5 demonstrates a significant surge in red fluorescence intensity specifically in the Ce6@mPP Ms group upon laser exposure, compared to free Ce6 without laser treatment. This finding strongly suggests laser- dependent cellular uptake in MOC2 cells.
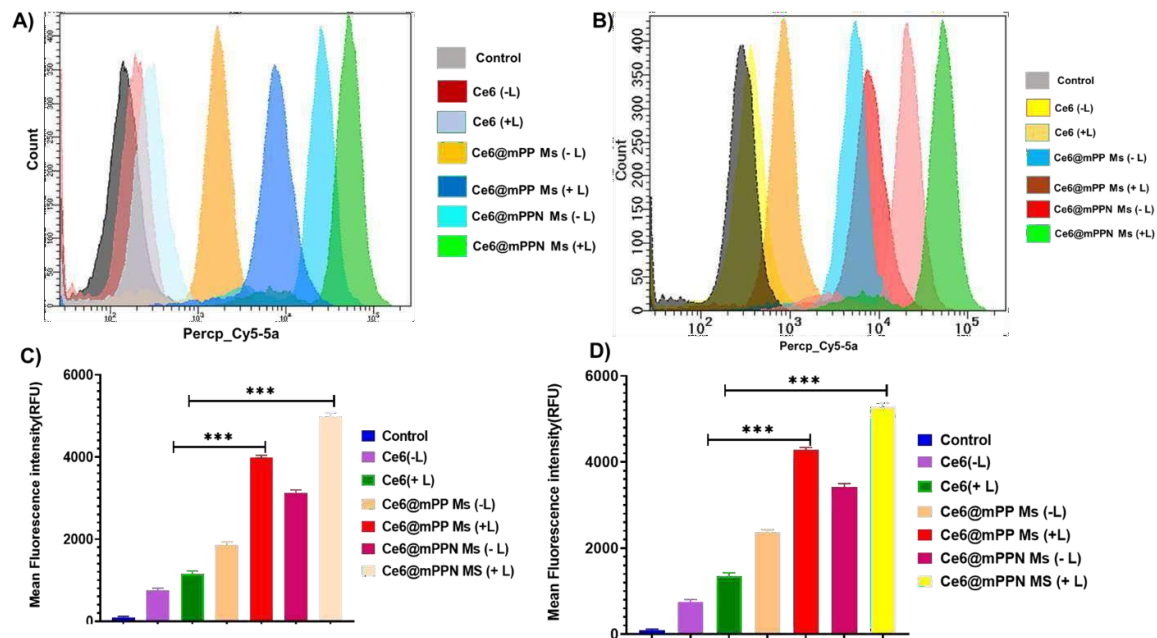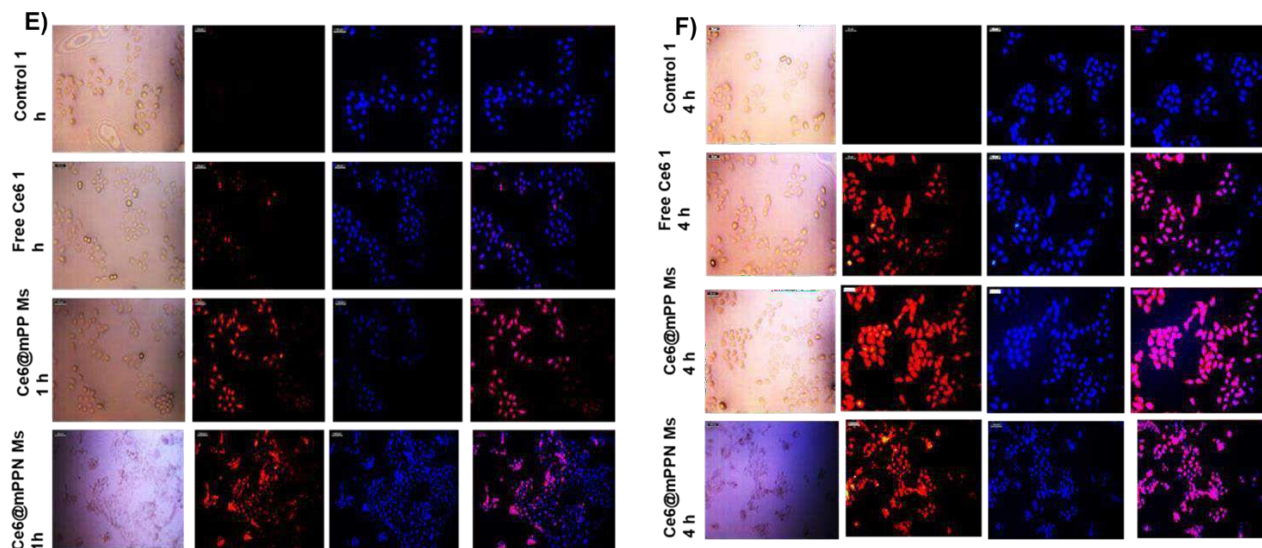
Figure 6.5 Uptake of free Ce6, Ce6@mPP, Ce6@mPPN Ms by FADU HTB 43 after incubation for 1 h, 4 h at 37°C. Scale bar, 100 mm (A); Flow cytometry data of free Ce6, Ce6@mPP, Ce6@mPPN Ms. (B).

6.4.4 Cell viability study/Phototoxicity of Ce6@mPPN Ms

Moreover, the cytotoxic impact of the Ce6 group, Ce6@mPPN Ms, and Ce6@mPP Ms on MOC2 and FaDu cells was assessed via a 24-hour and 48-hour MTT assay in vitro. Cells were seeded in 96-well plates following the addition of Ce6 group, Ce6@mPPN Ms, and Ce6@mPP Ms with or without 660 nm diode laser irradiation (0.5 W/cm2) across varied radiation durations. The antitumor efficacy of these nanoplatforms was evaluated in vitro. Figure 6.6 illustrates that the cell viability of the positive control group (laser only) resembled that of the negative control group (PBS), indicating non-toxicity due to laser irradiation alone. However, the viability of Ce6@mPPN Ms and Ce6@mPP Ms (at 3.25 μg/mL) without laser decreased to 67.5%.

As the concentration, duration, and laser irradiation time of Ce6@mPPN Ms and Ce6@mPP Ms increased, the surviving cell count continued to decrease, highlighting a dose, time, and laser-duration- dependent relationship. The substantial inhibition effect observed in Ce6@mPPN Ms and Ce6@mPP Ms without laser exposure could be attributed to the release of Ce6. Post laser irradiation, the inhibitory efficacy of Ce6@mPPN Ms was notably enhanced, demonstrating the potential of combined PDT and chemotherapy to improve treatment outcomes. An investigation into cell viability revealed that the Ce6@mPPN Ms formulation facilitated greater cellular internalization, resulting in lower cell viability compared to free Ce6. This indicated the formulation's efficacy in promoting cellular uptake and potentially enhancing therapeutic impact.
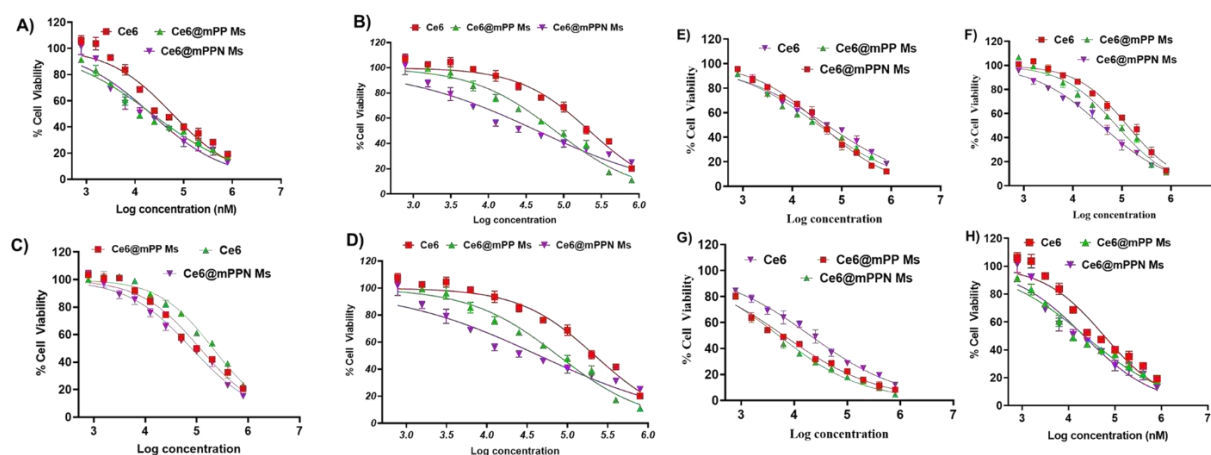
Figure 6.6. In vitro cell cytotoxicity of free Ce6, Ce6@mPP, and Ce6@mPPN Ms against FADU HTB 43 after incubation for 24 h , 48 h (without irradiation 24 h ; a and with irradiation 24 h b) or (without irradiation 48 h ; d and with irradiation 48 h e) under light irradiation (660 nm, 50 mWcm -2 5 min) in the dark. Various irradiation time (c & f) -L: without irradiation, +L: with irradiation

6.4.5 Apoptosis study

The assessment of viable cell apoptosis relied on Annexin V–FITC/PI staining. In the control group (without Ms), approximately 99.6% of cells were classified as normal (lower left quadrant). However, the percentage of live cells notably decreased when cells were co-incubated with free Ce6 or Ce6@mPPN Ms, Ce6@mPP Ms, with or without laser irradiation. As shown in (Figure 6.7), cells treated with free Ce6 displayed a total apoptosis rate of 20.6±1.3% in MOC2 cells. Ce6@mPPN Ms and Ce6@mPP Ms without laser exhibited total apoptosis rates of 41.6±1.3% and 48.23±1.3%, respectively. Meanwhile, Ce6@mPPN Ms and Ce6@mPP Ms with laser exhibited higher total apoptosis rates of 56.3±1.57% and 62.35±1.6%, respectively, in MOC2 cells.
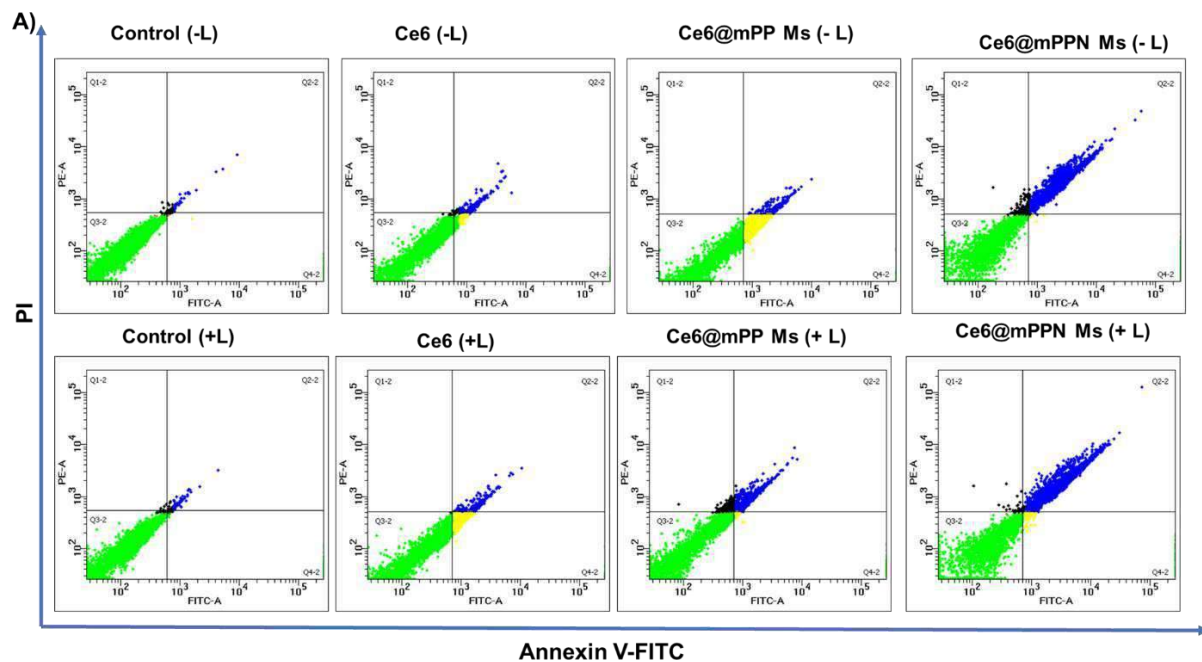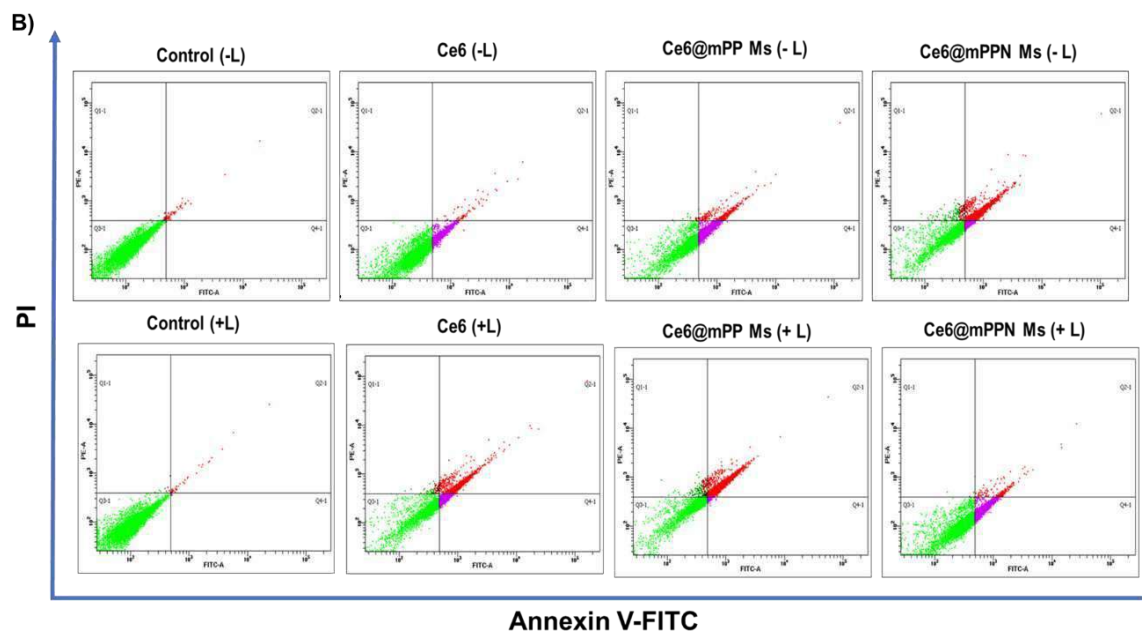
Figure 6.7 Apoptosis assay of FADU HTB 43 cells using Annexin V/PI double staining method. Apoptotic populations of FADU HTB 43 cells after exposure to different formulations: culture medium, culture medium plus NIR irradiation, Ce6 solution, Ce6 solution plus NIR irradiation, Ce6@mPP Ms, Ce6@mPPN Ms plus NIR irradiation, Ce6@mPP Ms, Ce6@mPPN Ms plus NIR irradiation. Cell counts (%) of necrotic cells (Q1), late apoptotic cells (Q2), early apoptotic cells (Q3), normal cells (Q4), and total apoptotic cells (Q2 & Q3) after different treatments. a);

6.4.6 Cell cycle analysis

To explore the potential correlation between cell growth inhibition and cell cycle alterations, cell cycle analysis was conducted on MOC2 cells. Following treatment with Ce6@mPPN Ms and Ce6@mPP Ms, both with and without Laser, there was a noticeable rise in the percentage of cell

populations in the G1 phase, increasing from 50.7% to 62% and 55.1%, respectively. This escalation was accompanied by a decrease in the percentage of cells in the G2/M and S phases for Ce6@mPPN Ms and Ce6@mPP Ms, respectively. The graphical representation (Figure 6.8) demonstrates a significant G2-M phase arrest for Ce6@mPPN Ms and Ce6@mPP Ms with Laser compared to free Ce6, regardless of laser exposure. This aligns with Ce6's mechanism of action, known for arresting cells in the early anaphase stage (M-phase).

6.4.7 Mitochondrial Membrane Potential Assay

Under fluorescence microscopy, control cells treated with JC-1 displayed intense red fluorescence, which combined with the green fluorescence from Ce6-treated cells, resulting in the emergence of orange and yellow signals in cells treated with Ce6, Ce6@mPPN Ms, and Ce6@mPP Ms, respectively (Figure 6.9). Notably, cells treated with Ce6@mPPN Ms and Ce6@mPP Ms showcased vivid green signals, indicating the presence of depolarized mitochondria.

6.5 In- vivo pharmacokinetic study

Live imaging biodistribution studies on animals revealed a non-specific distribution of Ce6@mPP, and Ce6@mPPN, as Ms in the excretory organs, which were cleared off more quickly than the Ce6 accumulated in the tumour (Figure 6.10). Ex vivo fluorescence analysis of tumor tissue and dissected organs (heart, liver, spleen, lung, and kidney) at 36 hours after injection further demonstrated that mPCe6, mPNCe6 Ms significantly increased tumour accumulation compared to free Ce6.
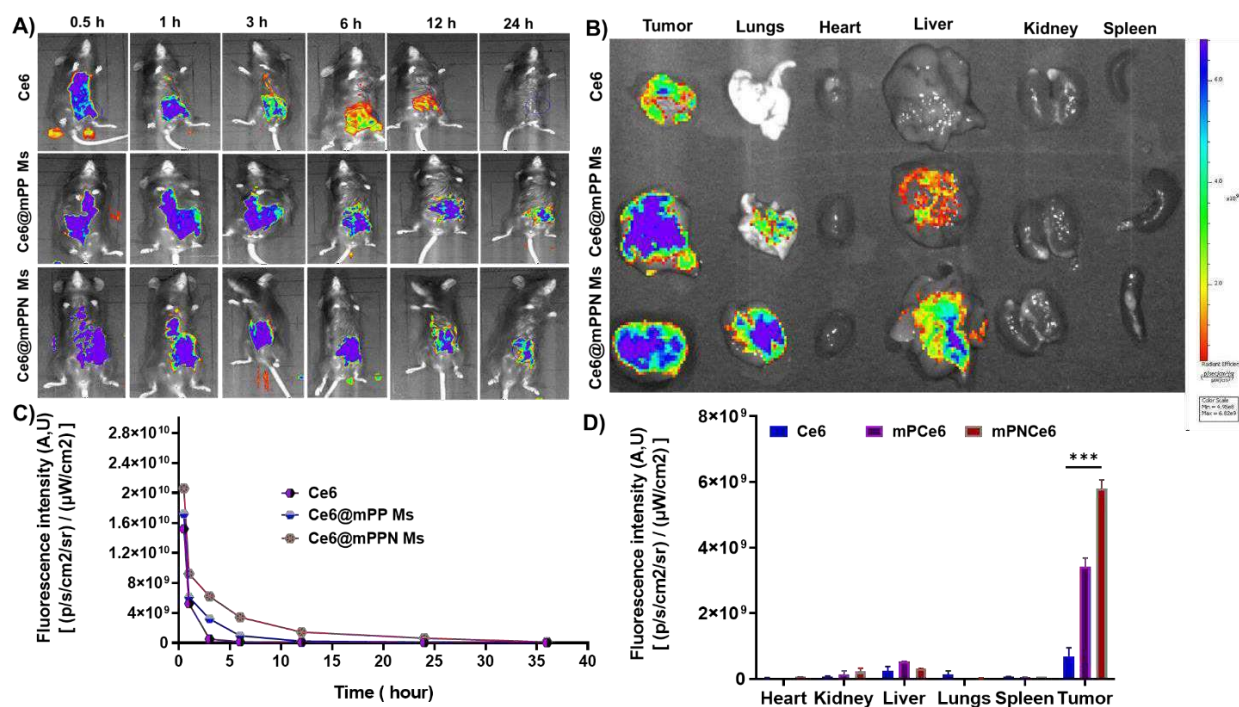
Figure 6.8 In vivo biodistribution study MOC2 tumor bearing mice using IVIS lumina.

6.5.1 Tumor inhibition assay

The tumor volumes on the 21st day after treatment initiation were measured to be 456 ± 23, 256 ± 35 and 180 ± 20 mm3 for the groups treated with saline, free Ce6, Ce6@mPP, and Ce6@mPPN, as shown in Figure 6.11c. The mean weights of the tumors in mice treated with saline, free Ce6, Ce6@mPP, and Ce6@mPPN were 2.5 gm, 0.56 gm, 0.20 gm. respectively (Figure 6.11 d). This investigation also indicated that the formulations are non-toxic to mice, as no decrease in weight was detected over time.
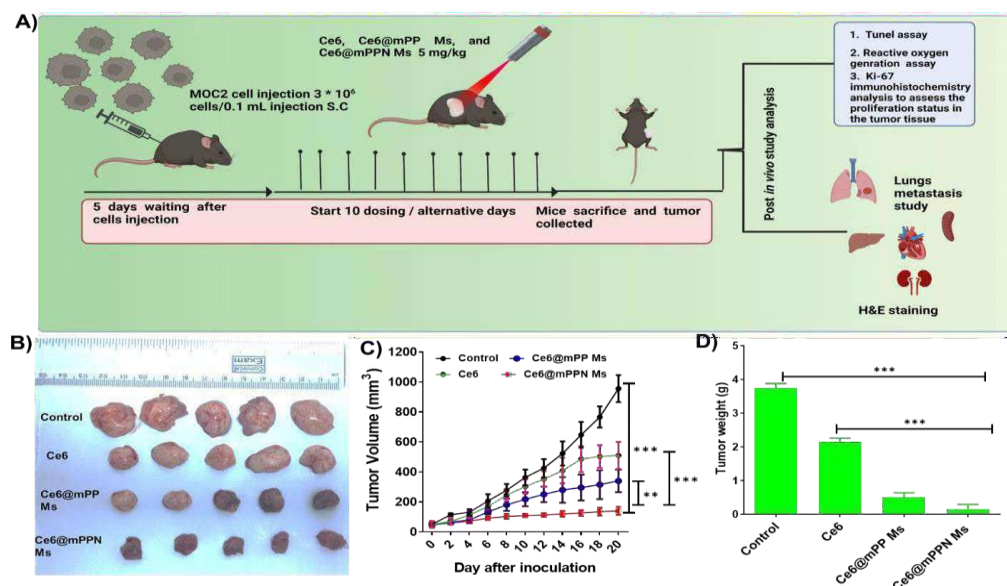
Figure 6.9 Schematic representation of the experimental protocol followed for the in vivo antitumor therapeutic efficacy of free Ce6 and Ce6@mPP, and Ce6@mPPN Ms in the MOC2 cell implanted tumor- bearing mouse model (A); Tumor volume inhibition assay (B); Graphical representation image of MOC2 tumor-bearing mice(C); Tumor weight of B16F10 tumor-bearing mice (D). Body weight of B16F10 tumor-bearing mice (E)

6.5.2 Immunohistochemistry

The mice who underwent Ce6@mPPN treatment exhibited the most intense green Fluorescence as measured by the DCFH-DA probe, which is used to assess oxidative stress levels (Figure 6.12 b). Upon cellular internalization, the dye undergoes oxidation by intracellular reactive oxygen species (ROS), resulting in the formation of 7'-dichlorodihydrofluorescein (DCF) and the emission of green Fluorescence. The reactive oxygen species (ROS) produced as a result of chemotherapy and photodynamic treatment (PDT) damage to the cancer cells include superoxide anion, hydrogen peroxide, and hydroxyl radicals. The nano formulations elicited more reactive oxygen species

(ROS) production in the tumor tissues compared to the administration of the unbound Ce6 medication. The primary method by which PDT eradicates cancer cells is by the production of an abundance of reactive oxygen species (ROS). The study demonstrated that the Ce6@mPPN was highly successful in generating a four-fold greater quantity of reactive oxygen species (ROS) compared to all other formulations that were examined. The therapy resulted in elevated oxidative stress, which in turn caused an upsurge in apoptosis in cancer cells. This was confirmed by the presence of TUNEL-positive cells exhibiting green Fluorescence (Figure A). According to the DCFH-DA results, the cells treated with the nanoformulation showed a higher expression of TUNEL-positive cells compared to the cells treated with the free medicines. Among the nanoformulations, Ce6@mPPN had the highest population of apoptotic cells. Moreover, tumor sections are examined to identify the presence of the proliferation marker Ki-67 expression (Figure 6.12 d). The tumor tissue that has not been treated exhibits the most elevated level of expression, suggesting its rapid pace of cell division and its capacity to spread to other parts of the body. The formulations exhibited a reduced signal, consistent with the ROS and TUNEL results, suggesting that the nanoformulations had the capacity to generate ROS, trigger apoptosis, and suppress the rate of cell growth. The tumor sections were subjected to histological inspection following treatment with the formulations and the free medication.
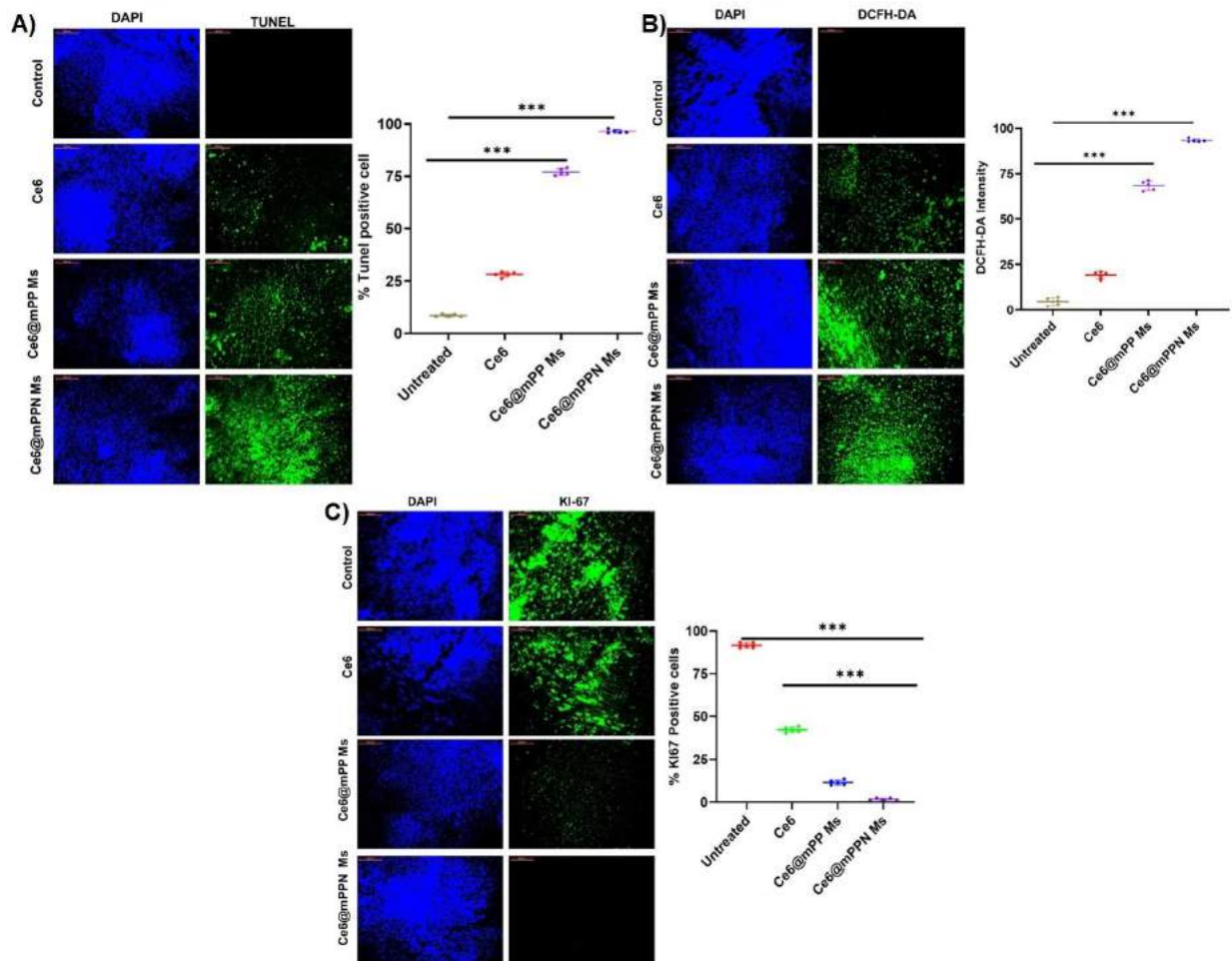
Figure 6.10 Immunohistochemistry analysis. Representative images of TUNEL assay in the tumor sections of isolated tumors (A); (ROS generation assay, B); HIF 1 alpha assay (C); Ki67 assay (D).

6.5.3 Lung metastasis - BrdU assay, collagen, and H&E in lung tissue

BrdU, an analog of thymidine, is utilized in the BrdU assay to determine proliferating cells. Consequently, it serves as a crucial marker for detecting cell proliferation. The lung sections labeled with BrdU were examined using a microscope. It was found that the untreated and free

Ce6 groups had a considerably higher number of proliferating endothelial cells in the metastasized

lungs compared to the other treatment groups (Figure 6.14). The potential cause may be the

obstruction of cancer cells within the blood arteries, resulting in the formation of metastatic regions in the lungs.
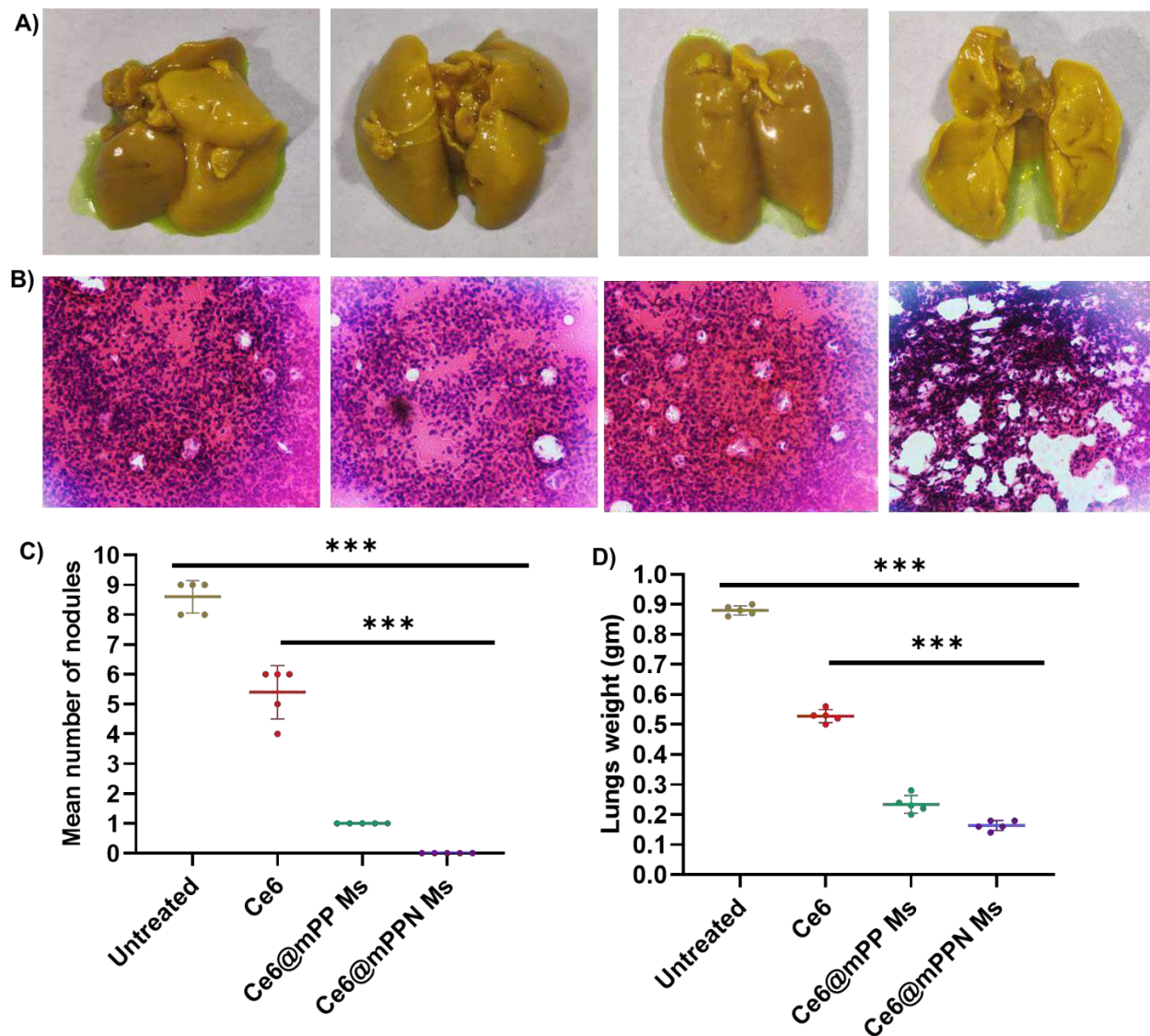
Figure 6.11 Suppression of lung metastasis. H&E staining of the lung section showed more proliferation of cells compared to treatment groups (A); Bar graph of lungs weight and lungs nodules (B &C).

Another notable finding in the lung tissue was the presence of lung metastases upon the mice's demise. Subcutaneous injection of approximately 1.5 million MOC2 cells was performed to promote the development of oral cancer. The control group and free Ce6 group both exhibited visible nodules on the lungs, as depicted in Figure 6.13.

The therapy groups, including Ce6@mPP and Ce6@mPPN, exhibited a substantial reduction in the proliferation of cancer cells on the lungs, as evidenced by a drop in fluorescence intensity in the BrdU assay. The collagen level in the Ce6@mPPN treated group was significantly lower compared to the untreated group. The mouse tumor was subjected to laser irradiation, resulting in the release of reactive oxygen species (ROS) and nano-sized Ce6@mPPN into the bloodstream. These substances reached the lungs, leading to a reduction in metastatic nodules inside the lung. This observation aligns with the biodistribution data, which indicates that the nanoparticle also accumulated in the lungs. Furthermore, the dimensions and mass of the lungs in each treatment were augmented in direct correlation with the infiltration of cancer cells throughout the lungs. The lungs' weight was measured to be 0.95 g, 0.50 g, 0.22 g, and 0.12 g in the saline treated, free Ce6, Ce6@mPP and Ce6@mPPN groups, respectively.
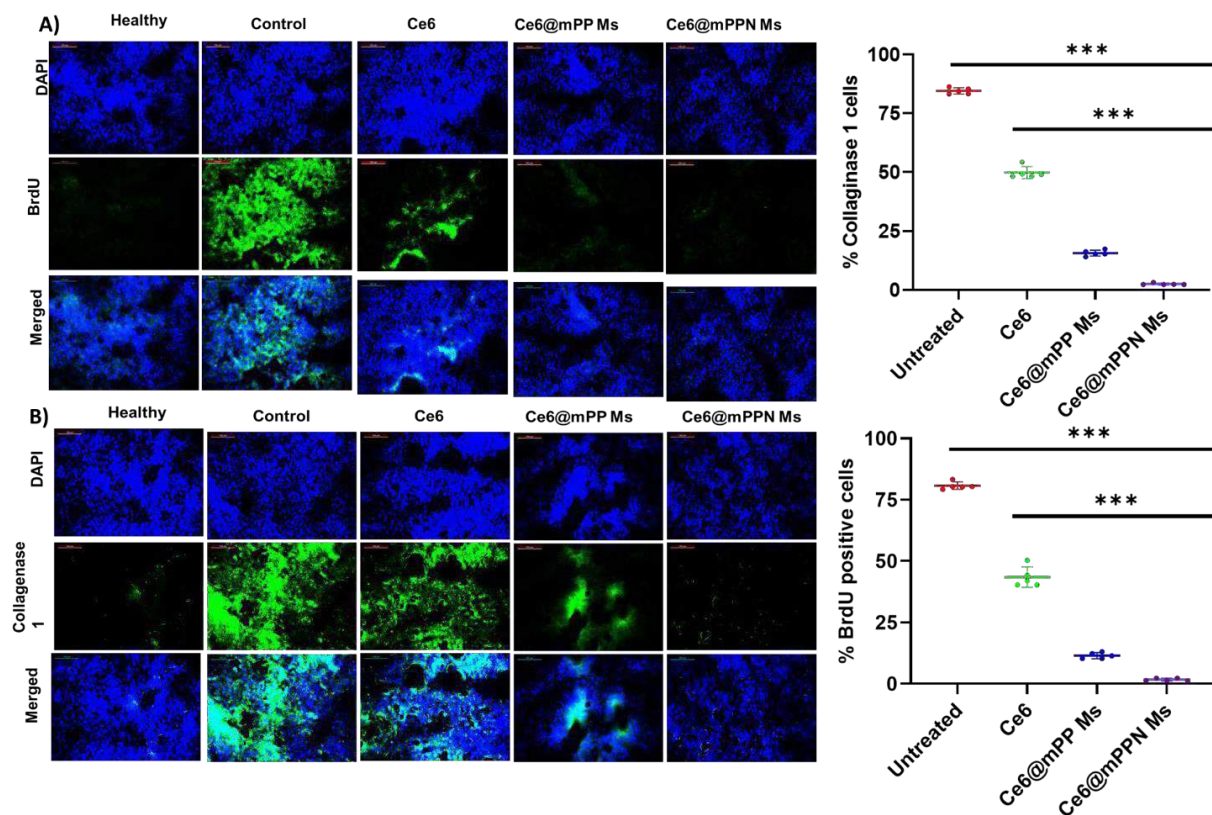
Figure 6.12 The proliferation of the metastatic cells in lung tissue was detected by injecting BrdU into the tail vein, followed by lung resection 2 h and stained with anti-BrdU antibody (A); The section was stained with collagen1 antibody to see the collagen level in the lung (B);

6.6 Conclusion

In order to develop nanomedicine-mediated photodynamic therapy, in this instance, 2-nitrobenzyl was coupled with methoxy(polyethylene glycol)-poly(D,L-lactide) (mPEG-PLA) and then loaded with Ce6. The drug-loaded micelles served as carriers for Ce6. The micelles demonstrated stability at a temperature of 4 °C, exhibited optimal physicochemical properties in relation to their spherical

size, and possessed low critical micelles concentrations (CMC). Over time, the micelles infiltrated the FaDu HTB-43 and MOC2 cells, leading to a much higher level of cell mortality in comparison to free Ce6 or Ce6@mPP micelles. The results showed that the micelles had a significant ability to induce apoptosis, DNA damage, ROS production, and mitochondrial membrane depolarization. As a result, there was a higher level of cellular death compared to when Ce6 was not bound. The existence of micelles led to a decrease in the pace at which Ce6 was cleared from the bloodstream, in contrast to when Ce6 was given in its unbound state. Moreover, the nontoxic properties of the micelles were verified by analyzing immunohistochemical data. In addition, the nano-micelles that were formed showed insufficient ability to enter and harm normal cells. As a result, the use of Ce6@mPPN micelles as a therapeutic strategy has considerable promise for the treatment of solid tumors, particularly oral cancer.

Chapter 7

Comparison of

Polymeric Micelles

7.1 Introduction

Combining several mechanisms into a single medication delivery system is an effective therapy method for oral cancer. Methoxy polyethylene glycol-poly lactic acid (mPEG-PLA) coupled to Ce6 or loaded with Ce6 and PTX were used in this study to create polymeric micelles. This Conjugation aided in the release of the drugs at the target site, i.e., the tumor microenvironment. Numerous physicochemical characterization investigations were carried out on the polymer and polymeric micelles loaded with Ce6 and PTX. The polymers underwent analyses using UV, IR, NMR spectroscopy, and gel permeation chromatography; the micelles underwent studies on hemolysis, stability, drug release kinetics, critical micelle concentration, percent drug loading, encapsulation efficiency, and dynamic light scattering, DSC, and XRD techniques. The drug-loaded micelles showed a narrower size distribution and smaller particle sizes.

In vitro tests on drug release and cellular uptake of this drug delivery system revealed effective cellular absorption and simultaneous drug release. Moreover, the polymeric micelles demonstrated noticeably greater cytotoxicity in tumor cells at different time intervals when compared to other nanoformulations or free medicines, suggesting that Ce6 and PTX work well together. When these micelles were applied to cells, there was an increase in apoptosis and cell cycle arrest (G2/M phase). Compared to free Ce6, polymeric micelles significantly increased the amount of DNA fragmentation, nuclear condensation, ROS production, and mitochondrial membrane permeabilization in cancer cells. In 3D spheroids, the polymeric micelles also demonstrated significant cell death and improved Ce6 penetration.

In pharmacokinetic studies, the plasma clearance and volume of distribution (Vd) of the Ce6-loaded polymeric micelles were significantly lower ($p<0.05$) than those of free Ce6.

The PEG-coating allows long circulation and accumulation to the tumor site by passive targeting. The polymer carries a photosensitizer, Ce6, and a chemotherapeutic moiety, Pt(IV).The polymer allows conversion of Pt(IV) to Pt(II) intracellularly upon irradiation and demonstrates NIR-light mediated cytotoxicity. The Pt(IV)-azido group in the polymer cause generation of oxygen, which alleviates hypoxia. The concept of incorporating Pt(IV)-azido species and the photosensitizer moiety in the drug delivery system to promote oxygenation in the hypoxic tumor has been validated in the proposal as an effective treatment strategy for oral cancer.The formulation can be tested in other tumor indications. In addition, other photosensitizer delivery can be attempted following the stated approach. In our next attempt, we validated the process of preparing NIR-degradable micelles for the on-demand release of the photosensitizer. The development strategy is unique as we introduced the NIR-cleavable moiety as the linker between hydrophobic and hydrophilic segments. The NIR light degradable micelles showed very effective MOC2 tumor bearing mice.

In the context of NIR-degradable micelles, chlorin e6 can be incorporated into the micellar structure to create a system that responds to near-infrared light for controlled drug release. The idea is to use the unique properties of chlorin e6, which is sensitive to light in the near-infrared range, to trigger the disassembly or degradation of the micelles when exposed to NIR light. The micelles are designed to encapsulate chlorin e6 along with methoxy polyethylene glycol, When these chlorin e6-loaded micelles are exposed to NIR light, chlorin e6 can absorb the light energy and induce photothermal or photochemical effects. This absorption can generate heat or reactive oxygen species, leading to the disruption or breakdown of the micellar structure and subsequent release of the encapsulated contents. Our results indicated that the developed mPPCPN micelles

could demonstrate a chemo-photodynamic therapeutic effect and produces molecular oxygen intracellularly, resulting in the alleviation of hypoxia.

7.2 Comparison of physicochemical characteristics

The particle size, zeta potential, EE% and DL% of the optimized formulations are given Table 6.1. The micelles were spherical in shape and the particle dispersion indexes (PDI,) revealed that the micelles had an acceptable size distribution and negative zeta potential that may stabilize micelles.

Table 7.1: Physicochemical characteristics of Polymeric micelles.

Compound name	Particle size (nm)	PDI	Zeta Potential	Encapsulation efficiency (%)	Drug loading (%)
Ce6@F127	135.25 ± 2.35	0.185 ± 3.21	-8.56 ± 1.23	78.25 ± 3.21	8.63 ± 1.20
Ce6/PTX-H/P NPs	165.32 ± 0.325	0.195 ± 0.08	-11.56 ± 1.23	70.25 ± 3.21	9.63 ± 1.20
mPPCPN Ms	115.32 ± 0.325	0.125 ± 0.01	-12.56 ± 1.23	78.25 ± 3.21	8.63 ± 1.45
mPNCe6 NPs	132.32 ± 0.325	0.20 ± 0.08	-10.02± 1.23	79.25 ± 3.21	11.20 ± 1.52
Ce6@mPPN Ms	156.32 ± 0.652	0.195 ± 0.04	-12.56 ± 1.23	78.25 ± 3.21	10.85 ± 1.63

Table 7.2: In vitro cytotoxicity study of various micelles.

Compound name	MTT IC$_{50}$ (μM)		% Apoptosis	Cell cycle
	24 h	48 h		
Ce6@F127	9.36 μg/ml	4.36 μg/ml	70.32 ± 3.20 %	35.32 ± 3.20 % (G2/M phase)
Ce6/ PTX-H/P	8.32 μg/ml	3.63 μg/ml	73.32 ± 3.20 %	41.25 ± 3.21 % (G2/M phase)
mPPCPN Ms	7.47 μg/ml	3.12 μg/ml	74.32 ± 3.20 %	44.32 ± 3.54 % (G2/M phase)
mPNCe6 NPs	7.42 μg/ml	2.53 μg/ml	78.32 ± 3.20 %	49.32 ± 2.85 % (G2/M phase)
Ce6@mPPN	8.20 μg/ml	3.96 μg/ml	74.32 ± 3.20 %	39.32 ± 3.52 % (G2/M phase)

The CMC concentration of mPEG-PLA, mPEG-PLA-2NB and mPEG-PLA-Ce6 was found to be 50, 35 and 40 μg/mL, respectively. These copolymers exhibited thermodynamic stability due to the low CMC of the micelles, and they were able to maintain micellar form after dilution. Given that, conjugation of Ce6 could add to the hydrophobic interactions between the polymer chains in the micelle core and stabilize the structure. Conjugation of Ce6 could add to the hydrophobic interactions between the polymer chains in the micelle core and stabilize the structure. Low CMCsof mPNCe6/ Ce6@mPP micelles might therefore have some advantages, such as stability against dissociation and precipitation in the blood due to dilution.

Table 7.3: In vivo study of various polymeric micelles.

Compound name	Tumor volume	%Tumor growth inhibition rate	% Lung metastasis inhibition rate
Ce6@F127	220.32 ± 10	42.32 ± 3.25	92.32 ± 2.36
Ce6/ PTX-H/P	185.32 ± 10	56.32 ± 3.25	_
mPPCPN Ms	180.32 ± 10	62.32 ± 3.25	_
mPNCe6 NPs	180.32 ± 10	72.32 ± 3.25	99.36 ± 2.95
Ce6@mPPN	230.32 ± 10	52.32 ± 3.25	95.02 ± 2.74

6.1 Conclusion

The above-mentioned physicochemical characteristics of all of the polymer-based micelles revealed that mPPCPN Ms and mPNCe6 Ms is relatively better in terms of particle size, PDI, drug loading(%), and in vitro release, in vitro study and in vivo study. However, all the polymeric micelles based nanocarriers have showed better performance compared to conventional formulations of the drug.

Chapter 8

Conclusion

Conclusion

Nanoparticulate drug delivery systems have addressed the limitations of conventional methods for delivering drugs. Emerging nanotechnology strategies are being applied to improve anti-cancer drug delivery by overcoming the non-specificity, adverse effects, and poor physiochemical properties associated with traditional chemotherapeutic agents. The design of nanocarriers is pivotal in achieving specific and targeted drug delivery systems. In anti-cancer drug delivery, diverse nanocarriers have been extensively studied to enhance drug properties and effectiveness.

Among the noteworthy amphipathic polymers, PEG-polylactide (PLA) stands out as it is highly suitable for constructing micelles. PLA, a biodegradable polyester derived from renewable sources and approved by the FDA for clinical use, is combined with PEG, a popular hydrophilic agent with several advantages including linearity, lack of charge, low polydispersity, and easy activation for conjugation. PEG–PLA micelles have been widely used in cancer therapy due to their exceptional physicochemical and biological properties such as nontoxicity, reduced protein adsorption, and limited uptake by the reticuloendothelial system (RES) post intravenous injection.

Protein-based nanoparticles using albumin or gelatin have emerged as versatile carriers for anti-cancer drugs. Human serum albumin (HSA) particularly stands out due to its biodegradability, lack of toxicity, and minimal immunogenicity. Albumin-bound paclitaxel (Abraxane) has proven both safe and effective, although the drug encapsulation efficiency and sustained release of crosslinked albumin NPs require improvement. These albumin-based nanoparticles readily accumulate in tumor tissues owing to the enhanced permeability and retention (EPR) effect. Studies indicate that these nanoparticles accumulate within tumor tissues through transcytosis, facilitated by the binding of albumin to the 60- kDa glycoprotein (gp60) receptor, resulting in the

formation of transcytosis vesicles. Considering these factors, HSA appears to be an appropriate material for nanoparticle synthesis.

Combination therapy, utilizing multiple therapeutic agents with distinct mechanisms, has the potential to induce more beneficial therapeutic responses compared to monotherapy. Limited data exists on combination chemotherapy for oral/breast cancer cells, especially concerning Chlorin e6/ Paclitaxel (Ce6/PTX) and Chlorin e6/ Cisplatin (Ce6/Pt). Nonetheless, research has demonstrated that the combination treatment of Chlorin e6/ Paclitaxel (Ce6/PTX) and Chlorin e6/ Cisplatin (Ce6/Pt)enhances G2/M cell cycle arrest and apoptosis in human and mouse oral/breast cancer cells, highlighting their potent effect in combination therapy and potential clinical significance.

The current study initially focused on improving the delivery of Ce6, which faces limitations due to its poor physicochemical properties and toxicity. Modification of the mPEG-PLA block copolymer by conjugating with Chlorin e6/ Paclitaxel (Ce6/PTX) and Chlorin e6/ Cisplatin (Ce6/Pt)aimed to enhance the anti-tumor effect of Ce6. Additionally, Ce6 was physically entrapped in the micellar core of pluroni F127 copolymers to prolong blood circulation. Physicochemical characterizations confirmed the developed polymers, and in vitro and in vivo studies demonstrated the therapeutic efficacy of the formulations in various cancer cell lines.

Chlorin e6/ Paclitaxel (Ce6/PTX) and Chlorin e6/ Cisplatin (Ce6/Pt) have shown photodynamic and chemotherapeutic activity in various cancers by influencing cell cycle arrest, differentiation, and apoptosis. Consequently, their potential against multiple cancers raises the prospect of their application in albumin-based drug delivery systems. The investigation reported the development of Ce6/PTX- loaded albumin nanoparticles.

 In the first objective, Ce6@F127 Ms were prepared and their physicochemical characteristics, such as a solubility and photoactivity in aqueous media, cellular internalization and tumor targeting

efficiency, were investigated. Ce6@F127 Ms exhibited high solubility and fluorescence intensity in aqueous media compared to free Ce6. Moreover, the ability of Ce6@F127 Ms to generate singlet oxygen was maintained in aqueous media. Ce6@F127 Ms demonstrated enhanced cytotoxicity against B16F10 and FaDu cells in vitro compared to free Ce6 due to its enhanced internalization rate. Moreover, due to its high tumor targeting efficiency, Ce6@F127 Ms strongly suppressed B16F10 xenograft tumor growth in after i.v. injection. On the basis of these results, we conclude that this Ce6@F127 Ms overcomes many of the problems associated with photosensitizers, such as poor solubility, cellular internalization and tumor targeting efficiencyis towards late apoptosis side (almost 3-fold higher compared to free Ce6 treatment).

In the second objective, Here, we have developed human serum albumin/poly(lactide)-co-glycolide (H/P) nanoparticles capable of incorporating dual drugs, the chemotherapeutic agent, paclitaxel and a photosensitizer, Chlroin e6 for a combination chemo-photodynamic therapy. The NPs were prepared by using emulsification technique, using PLGA and HSA as the corona and corona, respectively. The NPs were characterized thoroughly for various physicochemical parameters, including particle size, surface morphology, charge, drug release rate, entrapment, loading efficiencies, protein integrity, and the ability for PDT-mediated generation of ROS in biochemical assays. The effectiveness of formulations in killing murine melanoma and human oral squamous carcinoma cells was assessed by performing various in vitro and in vivo experiments. The cellular uptake data demonstrated the HSA- mediated active tumor targetability in both cancer cell lines.

 The combination nanoformulations, Ce6/PTX-H/P NPs demonstrated the lowest IC50 and synergistic effect both the cell lines upon irradiation. Ce6/PTX delivery to cancer cells induced apoptosis and cell cycle arrest in G2/M phase, causing DNA fragmentation and mitochondrial

depolarization by inducing ROS. The in vivo study performed using B16F10 tumor- bearing mice indicated that the combination therapy effectively reduced the tumor volume and induced apoptosis and antiproliferative effect in the tumor. The newly developed laser-activatable nanoformulation could be an efficient chemotherapy and photodynamic treatment option for superficial cancers, including melanoma or head and neck cancer.

In the third objective, A NIR-light degradable nanomicellar PDT-chemotherapy system decorated with photosensitizer Ce6 and chemotherapeutic moiety Pt(IV) was synthesized as a combination chemo-photodynamic therapy with the ability to generate molecular oxygen. Under 660 nm laser irradiation, the mPPCPN Ms convert Pt(IV)-prodrug to a more cytotoxic Pt(II) species by consuming GSH. The oxygen generated upon irradiation from Pt(IV) diazide is converted to ROS via activated Ce6 (type II reaction), which tilts the redox homeostasis of the cancer cells towards an oxidative state, thereby reversing hypoxia. After thorough characterization of mPPCPN polymer conjugate and micelles to determine their structure, morphology, ability to generate ROS, and molecular oxygen, the in vitro and in vivo studies were carried out. The in vitro study results demonstrated that the mPPCPN Ms were effectively internalized and decreased the cell viability by arresting the cell division, inducing apoptosis, generating ROS, and damaging the cellular DNA.

The in vivo study corroborated the in vitro results and successfully suppressed the tumor growth, elevated/down-regulated apoptotic markers/anti-apoptotic proteins, reduced GSH level, and reversed hypoxia towards a more oxidative environment. Therefore, the established hypoxia-reversing chemo- photodynamic therapy could be a powerful treatment strategy for oropharyngeal carcinoma or other superficial solid tumors.

In the fourth objective, In this case, 2-nitrobenzyl-chlorin e6 (2NB-Ce6) was coupled with methoxy(polyethylene glycol) (mPEG) to create nanomedicine-mediated photodynamic therapy. The conjugated micelles functioned as carriers for Ce6. The polymeric micelles exhibited stability at a temperature of 4 °C, displayed ideal physicochemical properties regarding their spherical size, and had low critical micelles concentrations (CMC). The micelles entered the FaDu and MOC2 cells over time, resulting in a considerably greater cell death than free Ce6 or mPCe6 micelles. The findings revealed that the micelles exhibited a remarkable efficacy in triggering apoptosis, DNA damage, ROS formation, and mitochondrial membrane depolarization, ultimately leading to a greater extent of cellular demise than unbound Ce6. The presence of micelles reduced the rate at which Ce6 was removed from the bloodstream, as compared to when Ce6 was administered in its free form. Furthermore, the micelles' non-toxic nature was confirmed through immunohistochemistry data analysis. Furthermore, the created nano-micelles exhibited minimal penetration and cytotoxicity towards the normal cells. Hence, the utilization of mPNCe6-micelles as a therapeutic approach holds great potential for treating solid tumors, particularly in the context of oral cancer.

In the fifth objective, In order to develop nanomedicine-mediated photodynamic therapy, in this instance, 2-nitrobenzyl was coupled with methoxy(polyethylene glycol)-poly(D,L-lactide) (mPEG- PLA) and then loaded with Ce6. The drug-loaded micelles served as carriers for Ce6. The micelles demonstrated stability at a temperature of 4 °C, exhibited optimal physicochemical properties in relation to their spherical size, and possessed low critical micelles concentrations (CMC). Over time, the micelles infiltrated the FaDu HTB-43 and MOC2 cells, leading to a much higher level of cell mortality in comparison to free Ce6 or Ce6@mPP micelles. The results showed

that the micelles had a significant ability to induce apoptosis, DNA damage, ROS production, and mitochondrial membrane depolarization. As a result, there was a higher level of cellular death

compared to when Ce6 was not bound. The existence of micelles led to a decrease in the pace at which Ce6 was cleared from the bloodstream, in contrast to when Ce6 was given in its unbound state. Moreover, the nontoxic properties of the micelles were verified by analyzing immunohistochemical data. In addition, the nano-micelles that were formed showed insufficient ability to enter and harm normal cells. As a result, the use of Ce6@mPPN micelles as a therapeutic strategy has considerable promise for the treatment of solid tumors, particularly oral cancer.

Chapter 9

Summary

Summary

Nanoparticulate drug delivery systems have revolutionized drug delivery by overcoming the limitations of conventional methods. In particular, emerging nanotechnology strategies hold promise for enhancing anti-cancer drug delivery, addressing issues like non-specificity, adverse effects, and poor drug properties associated with traditional chemotherapeutic agents. The design of nanocarriers plays a crucial role in achieving targeted drug delivery, with various amphipathic polymers, notably PEG-polylactide (PLA), standing out for their efficacy in constructing micelles. These micelles, combining PLA's biodegradability and PEG's hydrophilicity, exhibit exceptional physicochemical and biological properties, making them widely utilized in cancer therapy.

Protein-based nanoparticles, utilizing albumin or gelatin, have also emerged as versatile carriers for anti-cancer drugs. Human serum albumin (HSA), in particular, offers biodegradability, low toxicity, and minimal immunogenicity. Noteworthy is albumin-bound paclitaxel (Abraxane), which has shown safety and efficacy, although improvements in drug encapsulation efficiency and sustained release are needed. These albumin-based nanoparticles leverage enhanced permeability and retention (EPR) effects for efficient accumulation in tumor tissues.

Combination therapy, incorporating multiple therapeutic agents with distinct mechanisms, holds promise for more effective therapeutic responses. Limited data exists on combination chemotherapy for oral/breast cancer cells, especially concerning Chlorin e6/ Paclitaxel (Ce6/PTX) and Chlorin e6/ Cisplatin (Ce6/Pt). However, research demonstrates their potent effect in enhancing G2/M cell cycle arrest and apoptosis, indicating their potential clinical significance.

The current study focuses on enhancing Ce6 delivery, addressing its limitations through modification of mPEG-PLA block copolymers and physical entrapment in pluroni F127 copolymers. Physicochemical characterizations confirm the efficacy of the developed polymers, with in vitro and in vivo studies demonstrating their therapeutic efficacy across various cancer cell lines.

Chlorin e6/ Paclitaxel (Ce6/PTX) and Chlorin e6/ Cisplatin (Ce6/Pt) show both photodynamic and chemotherapeutic activity in various cancers, suggesting their potential in albumin-based drug delivery systems. Newly developed formulations demonstrate effectiveness in killing cancer cells and reducing tumor volume, presenting a promising treatment option for superficial cancers like melanoma or head and neck cancer.

The combination of nanotechnology and drug delivery offers a potent strategy for improving cancer treatment efficacy while minimizing adverse effects, paving the way for more effective and targeted therapies.

Chapter 10

Future scope of work

Future scope of work

Over the past decade, polymeric nanocarriers have undergone extensive exploration as adaptable and effective systems for delivering drugs in cancer therapy. Advancements in polymer structure design aim to boost drug-loading capacity, enhance tumor-specific uptake, and augment the anti-cancer impact. Various techniques have been devised to heighten the drug-carrying ability by improving interactions between the drug and the carrier within these polymeric nanocarriers. Additionally, there's a focus on developing dual-functional carriers with biologically active components to amplify their anticancer effects.

Incorporating combination therapeutics involving molecularly targeted biologics and conventional small molecule anti-cancer drugs into these developed nanocarriers holds promise. However, formulating combination therapies is notably more intricate than monotherapies, demanding sophisticated optimization strategies to select cargoes that synergize effectively. These polymeric nanoparticle-based approaches have mitigated immunogenicity and tumorigenesis, elevating drug safety, enabling controlled drug release, and refining targeted efficacy.

Novel approaches in combination therapy exemplify emerging trends in therapeutics. Simultaneously administering multiple drugs has the potential to target various signaling pathways involved in tumor growth, fostering a synergistic therapeutic effect. Yet, these approaches are in their nascent stages, carrying theoretical and technical limitations, alongside challenges related to dose-dependent toxicity and side effects that require resolution. Additionally, refining innovative in vitro evaluation systems is crucial for accurately predicting the pharmacokinetics of drugs in human subjects, as small animal models, although utilized, fall short in mimicking human responses. These ongoing investigations aim to develop an improved nanocarrier system to advance cancer treatment further.

Chapter 11

References

A

Agarwal SK. Lifestyles and Their Impact on Cancer. cardiovascular diseases. 2021;38:39. Alberts B. Molecular biology of the cell. Garland science; 2017 Aug 7.

Ahuja R, Jamal A, Nosrati N, Pandey V, Rajput P, Saxena N, Sidhu K, Kumar V. Human oncogenic viruses and cancer. Current science. 2014 Sep 10:768-85.

Akram N, Imran M, Noreen M, Ahmed F, Atif M, Fatima Z, Bilal Waqar A. Oncogenic role of tumor viruses in humans. Viral immunology. 2017 Jan 1;30(1):20-7.

Allison RR, Sibata CH. Oncologic photodynamic therapy photosensitizers: a clinical review. Photodiagnosis and photodynamic therapy. 2010 Jun 1;7(2):61-75.

Andreadis D, Pavlou AM, Sotiriou E, Vrani F, Ioannides D, Kolokotronis A. Utility of photodynamic therapy for the management of oral potentially malignant disorders and oral cancer. Translational Research in Oral Oncology. 2016 Nov 9;1:2057178X16669161 Allison RR, Downie GH, Cuenca R, Hu XH, Childs CJ, Sibata CH. Photosensitizers in clinical PDT. Photodiagnosis and photodynamic therapy. 2004 May 1;1(1):27-42.

Alakhov V, Lemieux P, Klinski E, Kabanov A, Pietrzynski G. Block copolymeric biotransport carriers as versatile vehicles for drug delivery. Expert opinion on biological therapy. 2001 Jul 1;1(4):583-602.

A. Hak, V. Ravasaheb Shinde, A.K. Rengan, A review of advanced nanoformulations in phototherapy for cancer therapeutics, Photodiagnosis and Photodynamic Therapy, 33 (2021) 102205.

A. Chlenski, M. Dobratic, H.R. Salwen, M. Applebaum, L.J. Guerrero, R. Miller, G. DeWane,

E. Solomaha, J.D. Marks, S.L. Cohn, Secreted protein acidic and rich in cysteine (SPARC) induces lipotoxicity in neuroblastoma by regulating transport of albumin complexed with fatty

B

Bugshan A, Farooq I. Oral squamous cell carcinoma: metastasis, potentially associated malignant disorders, etiology and recent advancements in diagnosis. F1000Research. 2020;9. Baddour JA, Sousounis K, Tsonis PA. Organ repair and regeneration: an overview. Birth Defects Research Part C: Embryo Today: Reviews. 2012 Mar;96(1):1-29.

Bradshaw TD. Chemotherapeutic Allg/lating Agents in Cancer Treatment. DNA Repair and Cancer: From Bench to Clinic. 2013 Jan 22:137.

Baskaran R, Lee J, Yang SG. Clinical development of photodynamic agents and therapeutic applications. Biomaterials research. 2018 Dec;22(1):1-8.

Biswas AK, Islam MR, Choudhury ZS, Mostafa A, Kadir MF. Nanotechnology based approaches in cancer therapeutics. Advances in Natural Sciences: Nanoscience and Nanotechnology. 2014 Nov 4;5(4):043001.

Bhatia S, Bhatia S. Nanoparticles types, classification, characterization, fabrication methods and drug delivery applications. Natural Polymer Drug Delivery Systems: Nanoparticles, Plants, and Algae. 2016:33-93.

Bailly C, Thuru X, Quesnel B. Combined cytotoxic chemotherapy and immunotherapy of cancer: modern times. NAR cancer. 2020 Mar;2(1):zcaa002.

Bobde Y, Biswas S, Ghosh B. PEGylated N-(2 hydroxypropyl) methacrylamide-doxorubicin conjugate as pH-responsive polymeric nanoparticles for cancer therapy. Reactive and Functional Polymers. 2020 Jun 1;151:104561.

Bonnett R. Photosensitizers of the porphyrin and phthalocyanine series for photodynamic therapy. Chemical Society Reviews. 1995;24(1):19-33.

Batrakova EV, Li S, Elmquist WF, Miller DW, Alakhov VY, Kabanov AV. Mechanism of sensitization of MDR cancer cells by Pluronic block copolymers: Selective energy depletion. British journal of cancer. 2001 Dec;85(12):1987-97.

Batrakova EV, Li S, Brynskikh AM, Sharma AK, Li Y, Boska M, Gong N, Mosley RL, Alakhov VY, Gendelman HE, Kabanov AV. Effects of pluronic and doxorubicin on drug uptake, cellular metabolism, apoptosis and tumor inhibition in animal models of MDR cancers. Journal of controlled release. 2010 May 10;143(3):290-301.

Batrakova EV, Han HY, Alakhov VY, Miller DW, Kabanov AV. Effects of pluronic block copolymers on drug absorption in Caco-2 cell monolayers. Pharmaceutical research. 1998 Jun;15:850-5.

Bhatt H, Ghosh B, Biswas S. Cell-penetrating peptide and α-tocopherol-conjugated poly (amidoamine) dendrimers for improved delivery and anticancer activity of loaded paclitaxel. ACS Applied Bio Materials. 2020 Apr 20;3(5):3157-69.

Bhatt H, Kiran Rompicharla SV, Ghosh B, Biswas S. α-tocopherol succinate-anchored PEGylated Poly (amidoamine) dendrimer for the delivery of paclitaxel: assessment of in vitro and in vivo therapeutic efficacy. Molecular Pharmaceutics. 2019 Feb 28;16(4):1541-54.

C

Chamoli A, Gosavi AS, Shirwadkar UP, Wangdale KV, Behera SK, Kurrey NK, Kalia K, Mandoli A. Overview of oral cavity squamous cell carcinoma: Risk factors, mechanisms, and diagnostics. Oral oncology. 2021 Oct 1;121:105451.

Choudhari SK, Chaudhary M, Gadbail AR, Sharma A, Tekade S. Oxidative and antioxidative mechanisms in oral cancer and precancer: a review. Oral oncology. 2014 Jan 1;50(1):10-8.

Cohen Y, Goldenberg-Cohen N, Shalmon B, Shani T, Oren S, Amariglio N, Dratviman Storobinsky O, Shnaiderman-Shapiro A, Yahalom R, Kaplan I, Hirshberg A. Mutational analysis of PTEN/PIK3CA/AKT pathway in oral squamous cell carcinoma. Oral oncology. 2011 Oct 1;47(10):946-50

Chen F, Qi S, Zhang X, Wu J, Yang X, Wang R. lncRNA PLAC2 activated by H3K27 acetylation promotes cell proliferation and invasion via the activation of Wnt/β-catenin pathway in oral squamous cell carcinoma. International journal of oncology. 2019 Apr 1;54(4):1183-94.

Castel H, Denouel A, Lange M, Tonon MC, Dubois M, Joly F. Biomarkers associated with cognitive impairment in treated cancer patients: potential predisposition and risk factors. Frontiers in pharmacology. 2017 Mar 21;8:138.

Calixto GM, Bernegossi J, De Freitas LM, Fontana CR, Chorilli M. Nanotechnology-based drug delivery systems for photodynamic therapy of cancer: a review. Molecules. 2016 Mar 11;21(3):342.

Cheng L, Wang C, Liu Z. Upconversion nanoparticles and their composite nanostructures for biomedical imaging and cancer therapy. Nanoscale. 2013;5(1):23-37.

Chidambaram M, Manavalan R, Kathiresan K. Nanotherapeutics to overcome conventional cancer chemotherapy limitations. Journal of pharmacy & pharmaceutical sciences. 2011 Feb 16;14(1):67-77.

Cameron AC, Touyz RM, Lang NN. Vascular complications of cancer chemotherapy. Canadian Journal of Cardiology. 2016 Jul 1;32(7):852-62.

Cheng L, Kamkaew A, Sun H, Jiang D, Valdovinos HF, Gong H, England CG, Goel S, Barnhart TE, Cai W. Dual-modality positron emission tomography/optical image-guided photodynamic cancer therapy with chlorin e6-containing nanomicelles. ACS nano. 2016 Aug 23;10(8):7721-30.

Chang MH, Pai CL, Chen YC, Yu HP, Hsu CY, Lai PS. Enhanced antitumor effects of dermal growth factor receptor targetable cetuximab-conjugated polymeric micelles fo photodynamic therapy. Nanomaterials. 2018 Feb 22;8(2):121.

Chibh S, Mishra J, Kour A, Chauhan VS, Panda JJ. Recent advances in the fabrication and bio-medical applications of self-assembled dipeptide nanostructures. Nanomedicine. 2020 Dec;16(2):139-63.

Chen K, Preuß A, Hackbarth S, Wacker M, Langer K, Röder B. Novel photosensitizer-protein nanoparticles for photodynamic therapy: photophysical characterization and in vitro investigations. Journal of Photochemistry and Photobiology B: Biology. 2009 Jul 17;96(1):66-

C.R. Park, J.H. Jo, M.G. Song, J.Y. Park, Y.-H. Kim, H. Youn, S.H. Paek, J.-K. Chung, J.M. Jeong, Y.-S. Lee, K.W. Kang, Secreted protein acidic and rich in cysteine mediates active targeting of human serum albumin in U87MG xenograft mouse models, Theranostics, 9 (2019) 7447-7457.

C.S. Lee, W. Park, S.J. Park, K. Na, Endolysosomal environment-responsive photodynamic nanocarrier to enhance cytosolic drug delivery via photosensitizer-mediated membrane disruption, Biomaterials, 34 (2013) 9227-9236.

Chlenski A, Dobratic M, Salwen HR, Applebaum M, Guerrero LJ, Miller R, DeWane G, Solomaha E, Marks JD, Cohn SL. Secreted protein acidic and rich in cysteine (SPARC) induces lipotoxicity in neuroblastoma by regulating transport of albumin complexed with fatty acids. Oncotarget. 2016 Nov 11;7(47):77696.

Chen Q, Wang X, Wang C, Feng L, Li Y, Liu Z. Drug-induced self-assembly of modified albumins as nano-theranostics for tumor-targeted combination therapy. ACS nano. 2015 May 26;9(5):5223-33.

Chen Q, Chen J, Liang C, Feng L, Dong Z, Song X, Song G, Liu Z. Drug-induced co-assembly of albumin/catalase as smart nano-theranostics for deep intra-tumoral penetration, hypoxia relieve, and synergistic combination therapy. J Control Release. 2017 Oct 10;263:79-89.

D

Dhillon PK, Mathur P, Nandakumar A, Fitzmaurice C, Kumar GA, Mehrotra R, Shukla DK, Rath GK, Gupta PC, Swaminathan R, Thakur JS. The burden of cancers and their variations across the states of India: the Global Burden of Disease Study 1990–2016. The Lancet Oncology. 2018 Oct 1;19(10):1289-306.

Danhier F, Feron O, Préat V. To exploit the tumor microenvironment: passive and active tumor targeting of nanocarriers for anti-cancer drug delivery. Journal of controlled release. 2010 Dec 1;148(2):135-46.

Desai N. Nanoparticle albumin-bound paclitaxel (Abraxane®). Albumin in medicine: Pathological and clinical applications. 2016:101-19.

Dasari S, Tchounwou PB. Cisplatin in cancer therapy: molecular mechanisms of action. European journal of pharmacology. 2014 Oct 5;740:364-78.

Ding C, Li Z. A review of drug release mechanisms from nanocarrier systems. Materials Science and Engineering: C. 2017 Jul 1;76:1440-53.

Deng K, Yu H, Li JM, Li KH, Zhao HY, Ke M, Huang SW. Dual-step irradiation strategy to sequentially destroy singlet oxygen-responsive polymeric micelles and boost photodynamic cancer therapy. Biomaterials. 2021 Aug 1;275:120959.

Das S, Paul M, Ghosh B, Biswas S. Synergistic Anticancer Response via Docetaxel-and Oleanolic Acid-Loaded Albumin/Poly (lactide) Nanoparticles in Triple-Negative Breast Cancer. ACS Applied Nano Materials. 2023 Oct 30.

D. Knauer, L. Hwang, C. Lowe, J. Hwang, M. Norng, V. Trieu, N. Desai, Albumin-Binding and Angiogenic Domains of SPARC Located at Its C-Terminus, Cancer Research, 69 (2009) 2144-2144.

E

Elzoghby AO, Samy WM, Elgindy NA. Albumin-based nanoparticles as potential controlled release drug delivery systems. Journal of controlled release. 2012 Jan 30;157(2):168-82.

E. Miele, G. Spinelli, E. Miele, F. Tomao, S. Tomao, Albumin-bound formulation of paclitaxel (Abraxane® ABI-007) in the treatment of breast cancer, International journal of nanomedicine, 4 (2009) 99-105.

F

Fouad YA, Aanei C. Revisiting the hallmarks of cancer. American journal of cancer research. 2017;7(5):1016.

Furness S, Glenny AM, Worthington HV, Pavitt S, Oliver R, Clarkson JE, Macluskey M, Chan KK, Conway DI. Interventions for the treatment of oral cavity and oropharyngeal cancer: chemotherapy. Cochrane Database of Systematic Reviews. 2011(4).

Fauzee NJ, Dong Z, Wang YL. Taxanes: promising anti-cancer drugs. Asian Pac J Cancer Prev. 2011 Jan 1;12(4):837-51.

G

Gunjal S, Pateel DG, Yang YH, Doss JG, Bilal S, Maling TH, Mehrotra R, Cheong SC, Zain RB. An overview on betel quid and areca nut practice and control in selected Asian and South East Asian Countries. Substance use & misuse. 2020 Jun 1;55(9):1533-44.

Gollin SM. Cytogenetic alterations and their molecular genetic correlates in head and neck squamous cell carcinoma: a next generation window to the biology of disease. Genes, Chromosomes and Cancer. 2014 Dec;53(12):972-90.

Greish K. Enhanced permeability and retention (EPR) effect for anticancer nanomedicine drug targeting. Cancer nanotechnology: Methods and protocols. 2010:25-37.

Green AE, Rose PG. Pegylated liposomal doxorubicin in ovarian cancer. International journal of nanomedicine. 2006 Sep;1(3):229.

Ghosh B, Biswas S. Polymeric micelles in cancer therapy: State of the art. Journal of Controlled Release. 2021 Apr 10;332:127-472. 46

Ghezzi M, Pescina S, Padula C, Santi P, Del Favero E, Cantù L, Nicoli S. Polymeric micelles in drug delivery: An insight of the techniques for their characterization and assessment in biorelevant conditions. Journal of Controlled Release. 2021 Apr 10;332:312-36.

Goel A, Singla A, Prabhash K. Neoadjuvant chemotherapy in oral cancer: Current status and future possibilities. Cancer Research, Statistics, and Treatment. 2020 Jan 1;3(1):51-9.

Gothwal A, Khan I, Gupta U. Polymeric micelles: recent advancements in the delivery of anticancer drugs. Pharmaceutical research. 2016 Jan;33:18-39.

Gupta N, Gupta R, Acharya AK, Patthi B, Goud V, Reddy S, Garg A, Singla A. Changing Trends in oral cancer-a global scenario. Nepal journal of epidemiology. 2016 Dec;6(4):613.

H

Hanahan D, Weinberg RA. Hallmarks of cancer: the next generation. cell. 2011 Mar 4;144(5):646-74.

Huang SH. Oral cancer: Current role of radiotherapy and chemotherapy. Medicina oral, patologia oraly cirugia bucal. 2013 Mar;18(2):e233.

Hu J, Tang YA, Elmenoufy AH, Xu H, Cheng Z, Yang X. Nanocomposite-based photodynamic therapy strategies for deep tumor treatment. Small. 2015 Nov;11(44):5860-87. Huang P, Li Z, Lin J, Yang D, Gao G, Xu C, Bao L, Zhang C, Wang K, Song H, Hu H. Photosensitizer-conjugated magnetic nanoparticles for in vivo simultaneous magnetofluorescent imaging and targeting therapy. Biomaterials. 2011 May 1;32(13):3447- 58.

Hassanin I, Elzoghby A. Albumin-based nanoparticles: A promising strategy to overcome cancer drug resistance. Cancer Drug Resistance. 2020;3(4):930.

Hou W, Xia F, Alves CS, Qian X, Yang Y, Cui D. MMP2-targeting and redox-responsive PEGylated chlorin e6 nanoparticles for cancer near-infrared imaging and photodynamic therapy. ACS applied materials & interfaces. 2016 Jan 20;8(2):1447-57.

Huang X, Chen T, Mu N, Lam HW, Sun C, Yue L, Cheng Q, Gao C, Yuan Z, Wang R. Supramolecular micelles as multifunctional theranostic agents for synergistic photodynamic therapy and hypoxia-activated chemotherapy. Acta biomaterialia. 2021 Sep 1;131:483-92.

Hu C, Zhuang W, Yu T, Chen L, Liang Z, Li G, Wang Y. Multi-stimuli responsive polymeric prodrug micelles for combined chemotherapy and photodynamic therapy. Journal of Materials Chemistry B. 2020;8(24):5267-79.

Hamblin MR, Miller JL, Rizvi I, Ortel B, Maytin EV, Hasan T. Pegylation of a chlorin e6 polymer conjugate increases tumor targeting of photosensitizer. Cancer research. 2001 Oct 1;61(19):7155-62.

He Z, Jiang H, Zhang X, Zhang H, Cui Z, Sun L, Li H, Qian J, Ma J, Huang J. Nano-delivery vehicle based on chlorin E6, photodynamic therapy, doxorubicin chemotherapy provides targeted treatment of HER-2 negative, αvβ3-positive breast cancer. Pharmacological research. 2020 Oct 1;160:105184.

Hak A, Shinde VR, Rengan AK. A review of advanced nanoformulations in phototherapy for cancer therapeutics. Photodiagnosis Photodyn Ther. 2021 Mar 1;33:102205.

I

Imon AA, Rahman QB, Sabrina F, Haque N, Islam MR. Carcinoma of oral cavity causative and risk factors: A review. EC Dental Science. 2019;18(10):2424-30.

Iyama T, Wilson III DM. DNA repair mechanisms in dividing and non-dividing cells. DNA repair. 2013 Aug 1;12(8):620-36.

Itoo AM, Paul M, Padaga SG, Ghosh B, Biswas S. Nanotherapeutic intervention in photodynamic therapy for cancer. ACS omega. 2022 Dec 6;7(50):45882-909.

Itoo AM, Paul M, Ghosh B, Biswas S. Polymeric graphene oxide nanoparticles loaded with doxorubicin for combined photothermal and chemotherapy in triple negative breast cancer. Biomaterials Advances. 2023 Oct 1;153:213550.

Itoo AM, Paul M, Ghosh B, Biswas S. Oxaliplatin delivery via chitosan/vitamin E conjugate micelles for improved efficacy and MDR-reversal in breast cancer. Carbohydrate Polymers. 2022 Jan 11:119108.

J

Johnson NW, Amarasinghe HK. Epidemiology and aetiology of head and neck cancers. Head and neck cancer: multimodality management. 2016:1-57.

Jurel SK, Gupta DS, Singh RD, Singh M, Srivastava S. Genes and oral cancer. Indian journal of human genetics. 2014 Jan;20(1):4.

Johnson TL, Lai MB, Lai JC, Bhushan A. Inhibition of cell proliferation and MAP kinase and Akt pathways in oral squamous cell carcinoma by genistein and biochanin A. Evidence-Based Complementary and Alternative Medicine. 2010 Sep 1;7:351-8.

Jungmann KP. Aspects of fundamental muon physics. InMuon Science 2017 Nov 1 (pp. 405- 461). Routledge.

Jain R, Paul M, Padaga SG, Dubey SK, Biswas S, Singhvi G. Dual-Drug-Loaded Assisted Topical Delivery of Photodynamically Active Lipid-Based Formulation for Combination Therapy of Cutaneous Melanoma. Molecular Pharmaceutics. 2023 Jun 1.

J.E. Schnitzer, gp60 is an albumin-binding glycoprotein expressed by continuous endothelium involved in albumin transcytosis, Am J Physiol, 262 (1992) H246-254.

K

Kyrgidis A, Antoniades K. Oral Cancer: Biomarkers, Hallmarks, Stem Cell Origin and Clinical Implications. CANCER ETIOLOGY, DIAGNOSIS AND TREATMENTS. 2010:1.

Keagle MB. DNA, chromosomes, and cell division. In The Principles of Clinical Cytogenetics 2012 Aug 30 (pp. 9-21). New York, NY: Springer New York.

Kondo T. Radiation-induced cell death and its mechanisms. Radiat Emerg Med. 2013 Feb;2(1):1-4.

Kim KW, Roh JK, Wee HJ, Kim C, Kim KW, Roh JK, Wee HJ, Kim C. Alkylating anticancer drugs. Cancer Drug Discovery: Science and History. 2016:71-94.

Khdair A, Chen D, Patil Y, Ma L, Dou QP, Shekhar MP, Panyam J. Nanoparticle-mediated combination chemotherapy and photodynamic therapy overcomes tumor drug resistance. Journal of Controlled Release. 2010 Jan 25;141(2):137-44.

Kanwal U, Irfan Bukhari N, Ovais M, Abass N, Hussain K, Raza A. Advances in nano- delivery systems for doxorubicin: an updated insight. Journal of drug targeting. 2018 Apr 21;26(4):296-310.

Kumari P, Ghosh B, Biswas S. Nanocarriers for cancer-targeted drug delivery. Journal of drug targeting. 2016 Mar 15;24(3):179-91.

Kumari P, Paul M, Bhatt H, Rompicharla SV, Sarkar D, Ghosh B, Biswas S. Chlorin e6 conjugated methoxy-poly (ethylene glycol)-poly (d, l-lactide) glutathione sensitive micelles for photodynamic therapy. Pharmaceutical Research. 2020 Feb;37:1-7.

Kumari P, Jain S, Ghosh B, Zorin V, Biswas S. Polylactide-based block copolymeric micelles loaded with chlorin e6 for photodynamic therapy: in vitro evaluation in monolayer and 3D spheroid models. Molecular Pharmaceutics. 2017 Nov 6;14(11):3789-800.

Kumari P, Paul M, Bobde Y, Soniya K, Kiran Rompicharla SV, Ghosh B, Biswas S. Albumin-based lipoprotein nanoparticles for improved delivery and anticancer activity of curcumin for cancer treatment. Nanomedicine. 2020 Oct;15(29):2851-69.

Kumbham S, Paul M, Itoo A, Ghosh B, Biswas S. Oleanolic Acid-conjugated human serum albumin nanoparticles encapsulating doxorubicin as synergistic combination chemotherapy in oropharyngeal carcinoma and melanoma. International journal of pharmaceutics. 2022 Jan 15:121479

Kumari P, Rompicharla SV, Bhatt H, Ghosh B, Biswas S. Development of chlorin e6- conjugated poly (ethylene glycol)-poly (d, l-lactide) nanoparticles for photodynamic therapy. Nanomedicine (Lond). 2019 Apr;14(7):819-34.

Knauer D, Hwang L, Lowe C, Hwang J, Norng M, Trieu V, Desai N. Albumin-Binding and Angiogenic Domains of SPARC Located at Its C-Terminus. Cancer Res. 2009 Dec 15;69(24_Supplement):2144.

Kumbham S, Ghosh A, Ghosh B, Biswas S. Human serum albumin-poly (Lactide)-conjugated self-assembly NPs for targeted docetaxel delivery and improved therapeutic efficacy in oral cancer. Int. J. Biol. Macromol. 2022 Dec 1;222:1287-303.

L

Lee SY, Ju MK, Jeon HM, Jeong EK, Lee YJ, Kim CH, Park HG, Han SI, Kang HS. Regulation of tumor progression by programmed necrosis. Oxidative medicine and cellular longevity. 2018 Oct;2018.

Lahtz C, Pfeifer GP. Epigenetic changes of DNA repair genes in cancer. Journal of molecular cell biology. 2011 Feb 1;3(1):51-8.

Leemans CR, Braakhuis BJ, Brakenhoff RH. The molecular biology of head and neck cancer. Nature reviews cancer. 2011 Jan;11(1):9-22.

Lakshminarayana S, Augustine D, Rao RS, Patil S, Awan KH, Venkatesiah SS, Haragannavar VC, Nambiar S, Prasad K. Molecular pathways of oral cancer that predict prognosis and survival: A systematic review. Journal of carcinogenesis. 2018;17.

Livshits Z, Rao RB, Smith SW. An approach to chemotherapy-associated toxicity. Emergency Medicine Clinics. 2014 Feb 1;32(1):167-203.

Lan M, Zhao S, Liu W, Lee CS, Zhang W, Wang P. Photosensitizers for photodynamic therapy. Advanced healthcare materials. 2019 Jul;8(13):1900132.

Lucky SS, Soo KC, Zhang Y. Nanoparticles in photodynamic therapy. Chemical reviews. 2015 Feb 25;115(4):1990-2042.

Li L, Bae BC, Tran TH, Yoon KH, Na K, Huh KM. Self-quenchable biofunctional nanoparticles of heparin–folate-photosensitizer conjugates for photodynamic therapy. Carbohydrate polymers. 2011 Aug 15;86(2):708-15.

Li X, Gao M, Xin K, Zhang L, Ding D, Kong D, Wang Z, Shi Y, Kiessling F, Lammers T, Cheng J. Singlet oxygen-responsive micelles for enhanced photodynamic therapy. Journal of Controlled Release. 2017 Aug 28;260:12-21.

Lan M, Zhao S, Liu W, Lee CS, Zhang W, Wang P. Photosensitizers for photodynamic therapy. Advanced healthcare materials. 2019 Jul;8(13):1900132.

Li J, Meng X, Deng J, Lu D, Zhang X, Chen Y, Zhu J, Fan A, Ding D, Kong D, Wang Z. Multifunctional micelles dually responsive to hypoxia and singlet oxygen: enhanced photodynamic therapy via interactively triggered photosensitizer delivery. ACS applied materials & interfaces. 2018 May 3;10(20):17117-28.

Liang H, Zhou Z, Luo R, Sang M, Liu B, Sun M, Qu W, Feng F, Liu W. Tumor-specific activated photodynamic therapy with an oxidation-regulated strategy for enhancing anti- tumor efficacy. Theranostics. 2018;8(18):5059.

Lee SJ, Koo H, Lee DE, Min S, Lee S, Chen X, et al. Tumor-homing photosensitizer- conjugated glycol chitosan nanoparticles for synchronous photodynamic imaging and therapy based on cellular on/off system. Biomaterials 2011;32:4021e9.

Lukyanov AN, Torchilin VP. Micelles from lipid derivatives of water-soluble polymers as delivery systems for poorly soluble drugs. Advanced drug delivery reviews. 2004 May 7;56(9):1273-89.

Lee CS, Park W, Park SJ, Na K. Endolysosomal environment-responsive photodynamic nanocarrier to enhance cytosolic drug delivery via photosensitizer-mediated membrane disruption. Biomaterials. 2013 Dec 1;34(36):9227-36.

Lee WT, Yoon J, Kim SS, Kim H, Nguyen NT, Le XT, Lee ES, Oh KT, Choi HG, Youn YS. Combined Antitumor Therapy Using In Situ Injectable Hydrogels Formulated with Albumin Nanoparticles Containing Indocyanine Green, Chlorin e6, and Perfluorocarbon in Hypoxic Tumors. Pharmaceutics. 2022 Jan 8;14(1):148.

M

More Y, D'Cruz AK. Oral cancer: review of current management strategies. The National medical journal of India. 2013 May 1;26(3):152-8.

Monsuez JJ, Charniot JC, Vignat N, Artigou JY. Cardiac side-effects of cancer chemotherapy. International journal of cardiology. 2010 Sep 24;144(1):3-15.

Master A, Livingston M, Gupta AS. Photodynamic nanomedicine in the treatment of solid tumors: perspectives and challenges. Journal of controlled release. 2013 May 28;168(1):88- 102.

Majumder N, G Das N, Das SK. Polymeric micelles for anticancer drug delivery. Therapeutic delivery. 2020 Oct;11(10):613-35.

Mokhtari RB, Homayouni TS, Baluch N, Morgatskaya E, Kumar S, Das B, Yeger H. Combination therapy in combating cancer. Oncotarget. 2017 Jun 6;8(23):38022.

Ma P, Mumper RJ. Paclitaxel nano-delivery systems: a comprehensive review. Journal of nanomedicine & nanotechnology. 2013 Feb 2;4(2):1000164.

Mustafa G, Hassan D, Ruiz-Pulido G, Pourmadadi M, Eshaghi MM, Behzadmehr R, Tehrani FS, Rahdar A, Medina DI, Pandey S. Nanoscale drug delivery systems for cancer therapy using paclitaxel—A review of challenges and latest progressions. Journal of Drug Delivery Science and Technology. 2023 May 16:104494.

Mirzaei S, Duan H. Radioimmunotherapy and Targeted Radiotherapy of Squamous Cell Carcinoma of the Head and Neck. Nuclear Medicine and Immunology. 2022:457-69.

Mosaddad SA, Namanloo RA, Aghili SS, Maskani P, Alam M, Abbasi K, Nouri F, Tahmasebi E, Yazdanian M, Tebyaniyan H. Photodynamic therapy in oral cancer: A review of clinical studies. Medical Oncology. 2023 Feb 7;40(3):91.

Maharjan PS, Bhattarai HK. Singlet oxygen, photodynamic therapy, and mechanisms of cancer cell death. Journal of Oncology. 2022;2022.

Mohapatra S, Ranjan S, Dasgupta N, Kumar R, Thomas S, editors. Applications of targeted nano drugs and delivery systems: nanoscience and nanotechnology in drug delivery. Elsevier; 2018 Oct 5.

 Miele E, Spinelli GP, Miele E, Tomao F, Tomao S. Albumin-bound formulation of paclitaxel (Abraxane® ABI-007) in the treatment of breast cancer. Nanomed. J. 2009 Apr 20:99-105.

N

Nathanson JW, Yadron NE, Farnan J, Kinnear S, Hart J, Rubin DT. p53 mutations are associated with dysplasia and progression of dysplasia in patients with Crohn's disease. Digestive diseases and sciences. 2008 Feb;53:474-80.

Negi AS, Gautam Y, Alam S, Chanda D, Luqman S, Sarkar J, Khan F, Konwar R. Natural antitubulin agents: Importance of 3, 4, 5-trimethoxyphenyl fragment. Bioorganic & medicinal chemistry. 2015 Feb 1;23(3):373-89.

Nakamura H, Jun F, Maeda H. Development of next-generation macromolecular drugs based on the EPR effect: challenges and pitfalls. Expert opinion on drug delivery. 2015 Jan 2;12(1):53-64.

O

Oliveira AC. Development of a non-invasive approach for oral squamous cell carcinoma diagnosis (Doctoral dissertation).

Ohnishi Y, Yasui H, Kakudo K, Nozaki M. Regulation of cell migration via the EGFR signaling pathway in oral squamous cell carcinoma cells. Oncology Letters. 2017 Feb 1;13(2):930-6.

Omura K. Current status of oral cancer treatment strategies: surgical treatments for oral squamous cell carcinoma. International journal of clinical oncology. 2014 Jun;19:423-30.

Oerlemans C, Bult W, Bos M, Storm G, Nijsen JF, Hennink WE. Polymeric micelles in anticancer therapy: targeting, imaging and triggered release. Pharmaceutical research. 2010

P

Paul M, Itoo AM, Ghosh B, Biswas S. Hypoxia alleviating platinum (IV)/chlorin e6-based combination chemotherapeutic-photodynamic nanomedicine for oropharyngeal carcinoma. Journal of Photochemistry and Photobiology B: Biology. 2023 Jan 1;238:112627

Pellosi DS, De Jesus PD, Tedesco AC. Spotlight on the delivery of photosensitizers: different approaches for photodynamic-based therapies. Expert Opinion on Drug Delivery. 2017 Dec 2;14(12):1395-406.

Patel T, Itoo AM, Paul M, Kondapaneni LP, Ghosh B, Biswas S. Block HPMA-based pH- sensitive gemcitabine pro-drug nanoaggregates for cancer treatment. European Polymer Journal. 2023 Mar 15;186:111843.

Pulya S, Patel T, Paul M, Adhikari N, Banerjee S, Routholla G, Biswas S, Jha T, Ghosh B. Selective inhibition of histone deacetylase 3 by novel hydrazide based small molecules as therapeutic intervention for the treatment of cancer. European Journal of Medicinal Chemistry. 2022 Aug 5;238:114470.

Pulya S, Himaja A, Paul M, Adhikari N, Banerjee S, Routholla G, Biswas S, Jha T, Ghosh B. Selective HDAC3 Inhibitors with Potent In Vivo Antitumor Efficacy against Triple-Negative Breast Cancer. Journal of Medicinal Chemistry. 2023 Sep 3;66(17):12033-58.

P. Kumari, S. Jain, B. Ghosh, V. Zorin, S. Biswas, Polylactide-Based Block Copolymeric Micelles Loaded with Chlorin e6 for Photodynamic Therapy: In Vitro Evaluation in Monolayer and 3D Spheroid Models, Mol Pharm, 14 (2017) 3789-3800.

P. Kumari, S.V.K. Rompicharla, H. Bhatt, B. Ghosh, S. Biswas, Development of chlorin e6-conjugated poly(ethylene glycol)-poly(d,l-lactide) nanoparticles for photodynamic therapy, Nanomedicine (Lond), 14 (2019) 819-834.

Park CR, Jo JH, Song MG, Park JY, Kim YH, Youn H, Paek SH, Chung JK, Jeong JM, Lee YS, Kang KW. Secreted protein acidic and rich in cysteine mediates active targeting of human serum albumin in U87MG xenograft mouse models. Theranostics. 2019;9(24):7447.

Q

Qie S, Diehl JA. Cyclin D1, cancer progression, and opportunities in cancer treatmReenfte. Jroeunrcneasl of molecular medicine. 2016 Dec;94:1313-26.

Q. Chen, X. Wang, C. Wang, L. Feng, Y. Li, Z. Liu, Drug-Induced Self-Assembly of Modified Albumins as Nano-theranostics for Tumor-Targeted Combination Therapy, ACS Nano, 9 (2015) 5223-5233.

Q. Chen, J. Chen, C. Liang, L. Feng, Z. Dong, X. Song, G. Song, Z. Liu, Drug-induced co-assembly of albumin/catalase as smart nano-theranostics for deep intra-tumoral penetration, hypoxia relieve, and synergistic combination therapy, J Control Release, 263 (2017) 79-89.

R

Ram H, Sarkar J, Kumar H, Konwar R, Bhatt ML, Mohammad S. Oral cancer: risk factors and molecular pathogenesis. Journal of maxillofacial and oral surgery. 2011 Jun;10:132-7.

Rafique R, Kailasa SK, Park TJ. Recent advances of upconversion nanoparticles in theranostics and bioimaging applications. TrAC Trends in Analytical Chemistry. 2019 Nov 1;120:115646.

Rabiee N, Yaraki MT, Garakani SM, Garakani SM, Ahmadi S, Lajevardi A, Bagherzadeh M, Rabiee M, Tayebi L, Tahriri M, Hamblin MR. Recent advances in porphyrin-based nanocomposites for effective targeted imaging and therapy. Biomaterials. 2020 Feb 1;232:119707.

Regina A, Demeule M, Che C, Lavallee I, Poirier J, Gabathuler R, Béliveau R, Castaigne JP. Antitumour activity of ANG1005, a conjugate between paclitaxel and the new brain delivery vector Angiopep-2. British journal of pharmacology. 2008 Sep;155(2):185-97.

Rivera C. Essentials of oral cancer. International journal of clinical and experimental pathology. 2015;8(9):11884.

S

Sriharikrishnaa S, Suresh PS, Prasada K S. An Introduction to Fundamentals of Cancer biology. InOptical Polarimetric Modalities for Biomedical Research 2023 Jul 23 (pp. 307- 330). Cham: Springer International Publishing.

Sung H, Ferlay J, Siegel RL, Laversanne M, Soerjomataram I, Jemal A, Bray F. Global cancer statistics 2020: GLOBOCAN estimates of incidence and mortality worldwide for 36 cancers in 185 countries. CA: a cancer journal for clinicians. 2021 May;71(3):209-49.

Sharma S, Satyanarayana L, Asthana S, Shivalingesh KK, Goutham BS, Ramachandra S. Oral cancer statistics in India on the basis of first report of 29 population-based cancer registries. Journal of oral and maxillofacial pathology: JOMFP. 2018 Jan;22(1):18.

Sándor GK, Carmichael RP, Ylikontiola LP, Jan A, DuVal MG, Clokie CM. 15 Healing of Large Dentofacial Defects. Oral Wound Healing: Cell Biology and Clinical Management. 2012 Mar 7:347.

Sroussi HY, Epstein JB, Bensadoun RJ, Saunders DP, Lalla RV, Migliorati CA, Heaivilin N, Zumsteg ZS. Common oral complications of head and neck cancer radiation therapy: mucositis, infections, saliva change, fibrosis, sensory dysfunctions, dental caries, periodontal disease, and osteoradionecrosis. Cancer medicine. 2017 Dec;6(12):2918-31.

Saini R, Lee NV, Liu KY, Poh CF. Prospects in the application of photodynamic therapy in oral cancer and premalignant lesions. Cancers. 2016 Sep 2;8(9):83.

Shen Y, Shuhendler AJ, Ye D, Xu JJ, Chen HY. Two-photon excitation nanoparticles for photodynamic therapy. Chemical Society Reviews. 2016;45(24):6725-41.

Samy NA, Salah MM, Ali MF, Sadek AM. Effect of methylene blue-mediated photodynamic therapy for treatment of basal cell carcinoma. Lasers in medical science. 2015 Jan;30:109-15. Stavrovskaya AA, Rybalkina EY. Recent advances in the studies of molecular mechanisms regulating multidrug resistance in cancer cells. Biochemistry (Moscow). 2018 Jul;83:779-86.

Saha RN, Vasanthakumar S, Bende G, Snehalatha M. Nanoparticulate drug delivReeryfesryesntecmess for cancer chemotherapy. Molecular membrane biology. 2010 Oct 1;27(7):215-31.

Shen X, Liu X, Li T, Chen Y, Chen Y, Wang P, Zheng L, Yang H, Wu C, Deng S, Liu Y. Recent advancements in serum albumin-based nanovehicles toward potential cancer diagnosisand therapy. Frontiers in Chemistry. 2021 Nov 18;9:746646.

Singh S, Dash AK. Paclitaxel in cancer treatment: perspectives and prospects of its delivery challenges. Critical Reviews™ in Therapeutic Drug Carrier Systems. 2009;26(4).

Sharifi-Rad J, Quispe C, Patra JK, Singh YD, Panda MK, Das G, Adetunji CO, Michael OS, tar O, Polito L, Živković J. Paclitaxel: application in modern oncology and nanomedicine- based cancer therapy. Oxidative medicine and cellular longevity. 2021 Oct 18;2021.

Singer JW, Baker B, De Vries P, Kumar A, Shaffer S, Vawter E, Bolton M, Garzone P. Poly- (L)-Glutamic Acid-Paclitaxel (CT-2103)[XYOTAX™], a Biodegradable Polymeric Drug Conjugate: Characterization, Preclinical Pharmacology, and Preliminary Clinical Data. Polymer drugs in the clinical stage: advantages and prospects. 2003:81-99.

Sun Q, Liu C, Zhong H, Zhong B, Xu H, Shen W, Wang D. Multi-center phase II trial of weekly paclitaxel plus cisplatin combination chemotherapy in patients with advanced gastric and gastro-esophageal cancer. Japanese journal of clinical oncology. 2009 Apr 1;39(4):237- 43.

Surmont V, Aerts JG, Pouw E, Tan KY, Vernhout R, Gras J, Salomé J, Pronk T, Schmitz PI, Hoogsteden H, van Klaveren RJ. Oral UFT, etoposide and leucovorin in recurrent non-small cell lung cancer: A non-randomized phase II study. Lung Cancer. 2009 Dec 1;66(3):333-7.

Sahara S, Herzog AE, Nör JE. Systemic therapies for salivary gland adenoid cystic carcinoma. American Journal of Cancer Research. 2021;11(9):4092.

Saini R, Lee NV, Liu KY, Poh CF. Prospects in the application of photodynamic therapy in oral cancer and premalignant lesions. Cancers. 2016 Sep 2;8(9):83.

Shen L, Huang Y, Chen D, Qiu F, Ma C, Jin X, Zhu X, Zhou G, Zhang Z. pHR-erefseproennscivees aerobic nanoparticles for effective photodynamic therapy. Theranostics. 2017;7(18):4537.

Swetha KL, Paul M, Maravajjala KS, Kumbham S, Biswas S, Roy A. Overcoming drug resistance with a docetaxel and disulfiram loaded pH-sensitive nanoparticle. Journal of Controlled Release. 2023 Apr 1;356:93-114.

S. Zhou, X. Hu, R. Xia, S. Liu, Q. Pei, G. Chen, Z. Xie, X. Jing, A Paclitaxel Prodrug Activatable by Irradiation in a Hypoxic Microenvironment, Angew Chem Int Ed Engl, 59 (2020) 23198-23205.

Shen X, Li T, Chen Z, Xie X, Zhang H, Feng Y, Li S, Qin X, Yang H, Wu C, Zheng C. NIR- light-triggered anticancer strategy for dual-modality imaging-guided combination therapy via a bioinspired hybrid PLGA nanoplatform. Molecular Pharmaceutics. 2019 Feb 18;16(3):1367-84.

Son J, Yi G, Kwak MH, Yang SM, Park JM, Lee BI, Choi MG, Koo H. Gelatin–chlorin e6 conjugate for in vivo photodynamic therapy. Journal of Nanobiotechnology. 2019 Dec;17(1):1-2.

Shi G, Cui Y, Zhao J, Liu J, Wang Y, Yang Y, Han J, Cheng X, Chen L, Yuan Y, Mi P. Identifying TOPK and Hypoxia Hallmarks in Esophageal Tumors for Photodynamic/Chemo/Immunotherapy and Liver Metastasis Inhibition with Nanocarriers. ACS nano. 2023 Feb 28;17(7):6193-207.

Schnitzer JE. gp60 is an albumin-binding glycoprotein expressed by continuous endothelium involved in albumin transcytosis. Am. J. Physiol. - Heart Circ. Physiol. 1992 Jan 1;262(1):H246-54.

Shi Y, Shan S, Li C, Song X, Zhang C, Chen J, You J, Xiong J. Application of the tumor site recognizable and dual-responsive nanoparticles for combinational treatment of the drug- resistant colorectal cancer. Pharm. Res. 2020 Apr;37:1-4.

Shen X, Li T, Chen Z, Xie X, Zhang H, Feng Y, Li S, Qin X, Yang H, Wu C, Zheng C. NIR- light-triggered anticancer strategy for dual-modality imaging-guided combination therapy via a bioinspired hybrid PLGA nanoplatform. Mol. Pharmaceutics. 2019 Feb 18;16(3):1367-84.

Son J, Yi G, Kwak MH, Yang SM, Park JM, Lee BI, Choi MG, Koo H. Gelatin–chlorin e6 conjugate for in vivo photodynamic therapy. J. Nanobiotechnology. 2019 Dec;17(1):1-2.Shi G, Cui Y, Zhao J, Liu J, Wang Y, Yang Y, Han J, Cheng X, Chen L, Yuan Y, Mi P. Identifying TOPK and Hypoxia Hallmarks in Esophageal Tumors for Photodynamic/Chemo/Immunotherapy and Liver Metastasis Inhibition with Nanocarriers. ACS nano. 2023 Feb 28;17(7):6193-207.

T

Tilakaratne WM, Jayasooriya PR, Jayasuriya NS, De Silva RK. Oral epithelial dysplasia: Causes, quantification, prognosis, and management challenges. Periodontology 2000. 2019 Jun;80(1):126-47.

Towle R. The molecular characterization of the progression of oral squamous cell carcinoma. 2016 (Doctoral dissertation, University of British Columbia).

Torgovnick A, Schumacher B. DNA repair mechanisms in cancer development and therapy. Frontiers in genetics. 2015 Apr 23;6:157.

Tang D, Tao D, Fang Y, Deng C, Xu Q, Zhou J. TNF-alpha promotes invasion and metastasis via NF-kappa B pathway in oral squamous cell carcinoma. Medical science monitor basic research. 2017;23:141.

Tiwari M. Antimetabolites: established cancer therapy. Journal of Cancer Research & Therapeutics. 2012 Oct 1;8(4).

Torchilin VP. Multifunctional nanocarriers. Advanced drug delivery reviews. 2012 Dec 1;64:302-15.

Torchilin VP. Passive and active drug targeting: drug delivery to tumors as an exRamefpeler.eDnrcuegs delivery. 2010:3-53.

Tseng TH, Chen CY, Wu WC, Chen CY. Targeted and oxygen-enriched polymeric micelles for enhancing photodynamic therapy. Nanotechnology. 2021 Jun 17;32(36):365102

Tan P, Cai H, Wei Q, Tang X, Zhang Q, Kopytynski M, Yang J, Yi Y, Zhang H, Gong Q, Gu Z. Enhanced chemo-photodynamic therapy of an enzyme-responsive prodrug in bladder cancer patient-derived xenograft models. Biomaterials. 2021 Oct 1;277:121061.

U

Ulbrich K, Hola K, Subr V, Bakandritsos A, Tucek J, Zboril R. Targeted drug delivery with polymers and magnetic nanoparticles: covalent and noncovalent approaches, release control, and clinical studies. Chemical reviews. 2016 May 11;116(9):5338-431.

V

Vysyaraju NR, Paul M, Ch S, Ghosh B, Biswas S. Olaparib@ human serum albumin nanoparticles as sustained drug-releasing tumour-targeting nanomedicine to inhibit growth and metastasis in the mouse model of triple-negative breast cancer. Journal of Drug Targeting. 2022 Nov 21;30(10):1088-105.

W

Wacker M, Chen K, Preuss A, Possemeyer K, Roeder B, Langer K. Photosensitizer loaded HSA nanoparticles. I: Preparation and photophysical properties. International journal of pharmaceutics. 2010 Jun 30;393(1-2):254-63.

Wang C, Tao H, Cheng L, Liu Z. Near-infrared light induced in vivo photodynamic therapy of cancer based on upconversion nanoparticles. Biomaterials. 2011 Sep 1;32(26):6145-54.

Wang F, Porter M, Konstantopoulos A, Zhang P, Cui H. Preclinical development of drug delivery systems for paclitaxel-based cancer chemotherapy. Journal of Controlled Release. 2017 Dec 10;267:100-18.

 Wen Y, Zhang W, Gong N, Wang YF, Guo HB, Guo W, Wang PC, Liang XJ. Carrier-free, self-assembled pure drug nanorods composed of 10-hydroxycamptothecin and chlorin e6 for combinatorial chemo-photodynamic antitumor therapy in vivo. Nanoscale. 2017;9(38):14347-56.

Wu L, Cai X, Zhu H, Li J, Shi D, Su D, Yue D, Gu Z. PDT-driven highly efficient intracellular delivery and controlled release of CO in combination with sufficient singlet oxygen production for synergistic anticancer therapy. Advanced Functional Materials. 2018 Oct;28(41):1804324.

Wang M, Lu P, Wu B, Tucker JD, Cloer C, Lu Q. High efficiency and low toxicity ofpolyethyleneimine modified Pluronics (PEI–Pluronic) as gene delivery carriers in cell culture and dystrophic mdx mice. Journal of Materials Chemistry. 2012;22(13):6038-46.

W.T. Lee, J. Yoon, S.S. Kim, H. Kim, N.T. Nguyen, X.T. Le, E.S. Lee, K.T. Oh, H.G. Choi, Y.S. Youn, Combined Antitumor Therapy Using In Situ Injectable Hydrogels Formulated with Albumin Nanoparticles Containing Indocyanine Green, Chlorin e6, and Perfluorocarbon in Hypoxic Tumors, Pharmaceutics, 14 (2022).

Wen Y, Dong H, Li Y, Shen A, Li Y. Nano-assembly of bovine serum albumin driven by rare- earth-ion (Gd) biomineralization for highly efficient photodynamic therapy and tumor imaging. Journal of Materials Chemistry B. 2016;4(4):743-51.

Y

Yao Y, Dai W. Genomic instability and cancer. Journal of carcinogenesis & mutagenesis. 2014;5.

Yang M, Yang T, Mao C. Enhancement of photodynamic cancer therapy by physical and chemical factors. Angewandte Chemie International Edition. 2019 Oct 1;58(40):14066-80.

Yoon HY, Koo H, Choi KY, Lee SJ, Kim K, Kw Con IC, Leary JF, Park K, Yuk SH, Park JH, Choi K. Tumor-targeting hyaluronic acid nanoparticles for photodynamic imaging and therapy. Biomaterials. 2012 May 1;33(15):3980-9.

Y. Shi, S. Shan, C. Li, X. Song, C. Zhang, J. Chen, J. You, J. Xiong, Application of the Tumor Site Recognizable and Dual-Responsive Nanoparticles for Combinational Treatment of the Drug-Resistant Colorectal Cancer, Pharm Res, 37 (2020) 72.

Z

Zhang SZ, Xie L, Shang ZJ. Burden of oral cancer on the 10 most populous countries from of Environmental Research and Public Health. 2022 Jan 13;19(2):875.

Zeng YP, Luo SL, Yang ZY, Huang JW, Li H, Liu C, Wang WD, Li R. A folic acid conjugated polyethylenimine-modified PEGylated nanographene loaded photosensitizer: photodynamic

therapy and toxicity studies in vitro and in vivo. Journal of Materials Chemistry B. 2016;4(12):2190-8.

Zhao X, Liu J, Fan J, Chao H, Peng X. Recent progress in photosensitizers for overcoming the challenges of photodynamic therapy: from molecular design to application. Chemical Society Reviews. 2021;50(6):4185-219.

Zhao J, Duan L, Wang A, Fei J, Li J. Insight into the efficiency of oxygen introduced photodynamic therapy (PDT) and deep PDT against cancers with various assembled nanocarriers. Wiley Interdisciplinary Reviews: Nanomedicine and Nanobiotechnology. 2020 Jan;12(1):e1583.

Zhang W, Du XF, Liu B, Li C, Long J, Zhao MX, Yao Z, Liang XJ, Lai Y. Engineering supramolecular nanomedicine for targeted near infrared-triggered mitochondrial dysfunction to potentiate cisplatin for efficient chemophototherapy. ACS nano. 2021 Dec 28;16(1):1421-35.

Appendix

Publications

1. Paul M, Bhatt H, Kumbham S, Ghosh B, Biswas S. Concurrent Delivery of Paclitaxel and Chlorin e6 to Tumors Using Albumin/PLGA Nanoparticles for NIR Light-Triggered Chemo/Photodynamic Therapy. ACS Applied Nano Materials. 2023 Jul 10;6(14):13385-99.

2. Paul M, Itoo AM, Ghosh B, Biswas S. Hypoxia alleviating platinum (IV)/chlorin e6- based combination chemotherapeutic-photodynamic nanomedicine for oropharyngeal carcinoma. Journal of Photochemistry and Photobiology B: Biology. 2023 Jan 1;238:112627.

3. Paul M, Itoo AM, Ghosh B, Biswas S. Current trends in the use of human serum albumin for drug delivery in cancer. Expert Opinion on Drug Delivery. 2022 Nov 2;19(11):1449- 70.

Biography

Biography of Milan Paul

Mr. Milan Paul has completed his Bachelor of Pharmacy from Institute of Pharmacy, Jalpaiguri, India in 2017. He pursued his Master of Pharmacy in Pharmaceutics from, Dr. Harisingh Gour University, India in 2019. Mr. Milan Paul worked on "Polymeric/albumin- based nano micellar systems for the delivery of anticancer drugs to treat oral cancer". Moreover, Mr. Milan Paul has received a senior research fellowship (SRF) from the Indian Council of Medical Research (ICMR) to carry out the research work. He has published 4 peer- reviewed scientific publications as first author and 10 peer-reviewed scientific publications as joint first author and 19 peer-reviewed scientific publications as co-author in reputed international journals. Moreover, he has published two Indian Patent applications.

Biography of Prof. Swati Biswas

Prof. Swati Biswas is presently working as Professor, in Department of Pharmacy, Birla Institute of Technology and Science, Pilani, Hyderabad Campus. She received her B. Pharm degree (1998) and M. Pharm (2000) from Jadavpur University, India. She was awarded her Ph.D. in Pharmaceutical Sciences in the year 2008 from Wayne State University, USA. After completion of doctoral studies, she pursued her postdoctoral studies in Northeastern University, USA (2013). She has been involved in research for the last 15 years. She is the editorial advisory board member for the journal ACS publications, molecular pharmaceutics for the tenure 2021- 2023, and associate editor for the journal, frontiers in biomaterials Sciences in the specialty section of delivery systems and controlled release (since 2021). She has been featured among the world's top 2 % scientists in the year 2019, 2021, 2022 in pharmacology and pharmacy/nanoscience & nanotechnology/ clinical medicine. She has to her credit more than 85 research publications, two US patents and two Indian Patents. She has authored 4 book chapters in "Dendrimers: Synthesis, Applications and Role in Nanotechnology", "Drug Delivery Strategies for Poorly Water-Soluble Drugs", "Handbook of Polymers for Pharmaceutical technologies, Volume 2: Processing and Applications" and "RNA imaging". She has successfully completed many sponsored projects and currently handling projects sponsored by DST and ICMR. She has guided four Ph.D students and currently four students are pursuing their Ph.D. work under her guidance.